INVESTIGATION OF DEGRADATION IN BIO-BASED AND PETROLEUM BASED RESINS USED IN POLYESTER MELAMINE COIL COATINGS USING SPECTROSCOPY AND CHEMICAL FORCE MICROSCOPY

Neelam Siyab

School of Engineering and Materials Science

Queen Mary University of London

Supervisors:

Dr Asa Barber and Dr Emiliano Bilotti (QMUL)

James Maxted and Chris Lowe (Beckers Ltd, Liverpool)

April 2016

Submitted in partial fulfilment of the requirements of the Degree of Doctor of Philosophy

STATEMENT OF ORIGINALITY

I, Neelam Siyab, confirm that the research included within this thesis is my own work or that where it has been carried out in collaboration with, or supported by others, that this is duly acknowledged below and my contribution indicated. Previously published material is also acknowledged below.

I attest that I have exercised reasonable care to ensure that the work is original, and does not to the best of my knowledge break any UK law, infringe any third party's copyright or other Intellectual Property Right, or contain any confidential material.

I accept that the College has the right to use plagiarism detection software to check the electronic version of the thesis.

I confirm that this thesis has not been previously submitted for the award of a degree by this or any other university.

Signature:

Date:

Details of collaboration and publications:

This research was carried out in Collaboration with Becker Ltd, Liverpool, UK, who provided all the materials used in this research.

SIYAB. N, TENBUSCH. S, WILLIS. S, LOWE. C and MAXTED. J, Going Green: making reality match ambition for sustainable coil coatings, J. Coat. Technol. Res, 2016.

ABSTRACT

The degradation of polyester coatings of three different formulations on steel substrates were critically analysed using photo-acoustic fourier transform infrared spectroscopy (PA-FTIR), atomic force microscopy (AFM), scanning electron microscopy (SEM), focussed ion beam (FIB) and chemical force microscopy (CFM). NS01, a coating with standard polyester resin, NS02, a 100% bio-sourced resin and NS03, a partially bio-sourced resin were each cross-linked with hexamethoxymethyl melamine and oven cured to reach a peak metal temperature of 232˚C. The cured coatings were subjected to accelerated weathering using the QUVA machine and natural weathering in Florida. The extent of photo-oxidation, using the characteristic OH band in FTIR 3600-3200cm^{-1} was found to increase with respect to time and the gloss retention decreased. NS01 showed an expected trend of gradual increase whereas NS02 completely disintegrated by 1000 hours and NS03 out-performed NS01 until 1200 hours. The sudden degradation in NS03 is caused by the instability of the aliphatic chain in the resin backbone which is hindered after 1200 hours of exposure. The addition of Titanium dioxide, TiO_2 stabilises the coatings improving the durability of NS01 and NS03.

A chemical force microscopy method was adopted to evaluate the chemistry on the substrate surface and depth profile after milling into the sample using a focussed ion beam. This technique has helped further the understanding of how chemical changes upon degradation manifest into physical changes ultimately causing failure which has not been investigated before.

Acknowledgements

First and foremost, I would like to express my gratitude to my Lord, all praise be to God because of whom I could get through the on-going trials during the period of my research, my Mum, Dad and Temur-my husband, for their continuous love, support and encouragement and I would also like to thank all my family and friends for offering their kind words in support of my progress

I would like to sincerely thank my principal supervisors Prof. Asa Barber and James Maxted for all the help and advice throughout my research, along with Chris Lowe who was a consulting supervisor at Beckers, ltd and was able shed light on the research findings through his expertise in this industry. I am also grateful to Dr Emiliano Bilotti for stepping in as my supervisor during my last academic year.

Many thanks to Beckers, Ltd, Liverpool, for collaborating on this project and sponsoring my PhD. I shall be forever grateful for the warm welcome I got every time I visited the company.

I am very thankful to all of my peers in Barber research group for their kindness and will to help out especially, Filipe and Alex who kindly helped me with, synthesizing OH brushes and CFM respectively. Russell Bailey, was also very supportive when using FIB or CFM at the Nanovision center. I want to thank Krystelle Mafina who was the experimental officer in the characterisation lab, for dealing with any problems regarding the FTIR and finally, I would like to acknowledge all the staff in the SEMS office who have been very supportive during my time at Queen Mary, university of London.

Contents

ABSTRACT **3**

LIST OF ABBREVIATIONS **8**

LIST OF FIGURES **10**

LIST OF TABLES **16**

1. Introduction **17**

2. Background on polyester based coil coatings; the process, chemistry, weathering, durability and analysis techniques **19**

2.1 An introduction to the coil coating process **19**

2.2 Coil Coating chemistry **21**

2.2.1 An introduction to polymers 21

2.2.2 Composition of coil coatings 24

2.2.3 Crosslinking polyester resin with hexamethoxymethyl melamine 25

2.2.4 Addition of pigments 27

2.2.5 The role of solvents and other additives 28

2.3 Degradation of coil coatings **28**

2.3.1 Polymer irradiation 29

2.3.2 Photo-degradation and hydrolysis 31

2.3.3 Photo-oxidation 33

2.4 Weathering methods **34**

2.5 A background on the techniques used to analyse coil coatings **35**

2.5.1 Scanning probe Microscopy 35

2.5.1.1 Atomic force microscopy 36

2.5.1.2 Chemical force microscopy 41

2.5.2 Infrared Spectroscopy 43

2.5.2.1 Fourier Transformed Infrared Spectroscopy 45

2.5.2.2 Infrared and Raman spectroscopy 48

2.5.3 Measuring gloss retention 50

2.5.4 Scanning electron microscopy 51

2.5.5 Focussed ion beam microscopy 53

3. Materials and methods **58**

3.1 Sample preparation **59**

3.2 Weathering tests **60**

3.3 Characterisation techniques **61**

3.3.1 Gloss retention 61
3.3.2 Atomic Force Microscopy 61
3.3.3 Photo-acoustic FTIR 65
3.3.4 Scanning electron microscopy 66
3.3.5 Focused Ion Beam microscopy 67
3.3.6 Chemical force microscopy 69
4. Results from artificial weathering of NS01 and NS03 coatings using a QUVA machine 72
4.1 Investigating gloss retention 72
4.2 Analysis of the surface roughness using AFM 75
4.3 Analysis of the chemical make-up using photoacoustic Fourier transform infrared spectroscopy 79
4.3.1 Analysing PA-FTIR spectra 79
4.3.2 PA-FTIR Spectra analysis 85
4.3.3 PA-FTIR RESULTS FROM PEAK ANALYSIS 88
4.4 Surface analysis using scanning electron microscopy 92
4.5 Conclusion of experimental results 98
5. Results from natural weathering of NS01 and NS03 coatings in Florida 99
5.1 investigating gloss retention 99
5.2 Analysis of the surface roughness using AFM 101
5.3 Analysis of the chemical make-up using photoacoustic Fourier transform infrared spectroscopy 104
5.4 Surface analysis using scanning electron microscopy 113
5.5 Conclusion of experimental results 116
6. Degradation performance of polyester based coil coatings and partially bio-sourced polyester coatings 117
6.1 Conclusion 125
7. Development of techniques to spatially map chemical degradation in coil coatings using focused ion beam and chemical force microscopy 126
7.1 Preliminary work 132
7.2 Repeating measurements on the surface of the sample 135
7.3 Chemical force microscopy on the surface of the sample 136
7.4 Using the focus ion beam 150
7.5 Results and Discussion 158
7.6 Analysis of the technique 164

7.7 Concluding remarks 169

8. Summary and future work 172

References 176

LIST OF ABBREVIATIONS

PA-FTIR	Photo-acoustic Fourier Transform Infrared Spectroscopy
AFM	Atomic Force Microscopy
SEM	Scanning Electron Microscopy
FIB	Focused Ion Beam
CFM	Chemical Force Microscopy
T_g	Glass Transition Temperature
T_m	Melting Temperature
NPG	Neopentyl Glycol
HD	Hexane Diol
TMP	Trimethylol Propane
IA	Isophtalic Acid
TA	Terephthalic Acid
OA	Orthophthalic Acid
AA	Adipic Acid
HMMM	Hexamethoxymethyl Melamine
TMMM	Tris-methoxymethyl Melamine
TMCT	Tris-methyl Carbomoyl Triazine
HALS	Hindered Amine Light Stabiliser
UV	Ultra-violet
STM	Scanning Tunnelling Microscopy
PVDF	Polyvinylidene Fluoride
PMMA	Polymethyl Methacrylate
PE	Polyethylene
CRM	Confocal Raman Microscopy
RMS	Root Mean Squared
SSPR-FTIR	Step Scan Photo-Acoustic Fourier Transform Infrared Spectroscopy
PET	Polyethylene Terephthalate

SAM	Self-Assembly Monolayers

LIST OF FIGURES

Figure 1.1: Process of coil coating……..20

Figure 2.1: The structure of coil coatings..... 24

Figure 2.2: Common polyols used in the synthesis of polyester resin…… 26

Figure 2.3: The three structures of melamine, TMMM, HMMM and TMCT 27

Figure 2.4 Chemical structure of polyester/ melamine bonds 31

Figure 2.5: Hydrolysis of ether linkages forming melamine methylol groups 32

Figure 2.6: production of amine groups and formaldehyde due to decomposition of methylol groups (Batista et al,2011)……32

Figure 2.7: The probe deflection against the attractive and repulsive forces……37

Figure 2.8: contact mode (left), non-contact mode (middle) and tapping mode (right)..... 38

Figure 2.9: phase and height images using tapping mode AFM of an unweathered paint surface, Biggs et al, 2001……39

Figure 2.10: a) AFM images and b) force displacement curves, Gu et al(2004) ……..40

Figure 2.11: The interaction of a chemically modified tip with the surface chemical group.42

Figure 2.12: The generation of phase lag and delay in signal in AFM……..42

Figure 2.13: Cross section images of a) PET sample and b) PVDF sample, Zhang et al (2009,a)……47

Figure 2.14: Cross section examination using CRM by Zhang et al (2010)……49

Figure 2.15: Gloss loss over QUV-B exposure time, Biggs et al (2001)……...50

Figure 2.16: Components of the scanning electron microscope (Harris P, EM Lab……..52

Figure 2.17: The scanning electron microscopy and focused ion beam systems……54

Figure 2.18: A schematic demonstrating the dual beam system involving an electron beam and an ion beam……55

Figure 2.19: An illustration of the dual beam in a SEM-FIB system……56

Figure 2.20: Porous ceramic on Ni: strong curtaining due to rough surface (Reuteler. J 2016)……57

Figure 3.1 NT-MDT NTEGRA, the atomic force microscopy equipment……63

Figure 3.2: Mounting sample on the AFM stage……64

Figure 3.3: AFM sampling technique……65

Figure 3.4: SEM image of steps milled in a polymer coating……69

Figure 3.5: Fluid cell used in chemical force microscopy.....71

Figure 3.6: A set-up of the filled fluid cell on the AFM stage.....71

Figure 4.1: a) Gloss retention of clear coatings b) gloss retention of white coatings.....73

Figure 4.2: RMS value of NS01 clear using QUVA exposure.....75

Figure 4.3: RMS Value of NS03 clear using QUVA exposure 76

Figure 4.4: RMS value of NS01 white using QUVA exposure.....77

Figure 4.5: RMS value of NS03 white using QUVA exposure.....77

Figure 4.6: FTIR spectra of NS01 clear to demonstrate peak changes.....79

Figure 4.7: FTIR spectrum for NS01 clear showing the peaks used for analysis.....83

Figure 4.8: FTIR spectrum for NS03 clear showing the peaks used for analysis.....84

Figure 4.9: FTIR spectra of NS01 clear samples at various exposure hours.....85

Figure 4.10: Photo-oxidation of NS01 clear after QUVA exposure.....86

Figure 4.11: Melamine peak and CH peak spectral analysis for NS01 clear after QUVA exposure.....86

Figure 4.12: FTIR spectra of NS0 clear samples at various exposure hours.....87

Figure 4.13: The degradation of the melamine and CH peak in NS03 clear after QUVA exposure.....87

Figure 4.14: -OH,-NH peak analysis against time for NS01 and NS03 clear.....88

Figure 4.15: Melamine peak analysis against time for NS01 and NS03 clear.....89

Figure 4.16: Methylene peak analysis of NS01 and NS03 clear.....90

Figure 4.17: -Oh/-NH peak analysis of NS01 and NS03 white.....91

Figure 4.18: Melamine peak analysis of NS01 and NS03 white.....91

Figure 4.19: Methylene peak analysis of NS01 and NS03 white.....92

Figure 4.20: Surface analysis of a) NS01 clear unexposed and b) NS01 clear, exposed at 2981 hrs.....94

Figure 4.21: Surface analysis of a) NS03 clear unexposed and b) NS03 clear, exposed at 3113 hrs.....95

Figure 4.22: Surface analysis of a) NS01 white unexposed and b) NS01 white, exposed at 2206 hrs.....96

Figure 4.23: Surface analysis of a) NS03 white unexposed and b) NS03 white, exposed at 2206 hrs.....97

Figure 5.1: a) Gloss retention of clear coatings and b)Gloss retention of white coatings after Florida exposure.....100

Figure 5.2: RMS value of NS01 clear after Florida exposure.....101

Figure 5.3: RMS values of NS03 clear after Florida exposure.....102

Figure 5.4: RMS value of NS01 white after Florida exposure.....103

Figure 5.5: RMS value of NS03 white after Florida exposure.....103

Figure 5.6: PA-FTIR spectra off samples exposed in Florida for NS01 clear.....104

Figure 5.7: Changes in the –OH,-NH peak for NS01 clear sample.....105

Figure 5.8: Changes in the melamine peak for NS01 clear sample.....105

Figure 5.9: PA-FTIR spectra of all samples exposed in Florida for NS03 clear.....106

Figure 5.10: Changes in the OH peak for NS03 clear.....106

Figure 5.11: Changes in the melamine peak for NS03 clear.....107

Figure 5.12: -OH,-NH peak analysis against time for NS01 and NS03 clear.....108

Figure 5.13: melamine peak analysis of NS01 and NS03 clear.....108

Figure 5.14: Methylene peak analysis of NS01 and NS03 clear.....109

Figure 5.15: -Oh/-NH peak analysis of NS01 white and NS03 white.....110

Figure 5.16: Methylene peak analysis of NS01 and NS03 white.....110

Figure 5.17: Melamine peak analysis fro NS01 and NS03 white.....111

Figure 5.18: PA-FTIR spectra of all NS01 white samples exposed in Florida.....111

Figure 5.19: PA-FTIR spectra of all NS03 white samples exposed in Florida.....112

Figure 5.20: Surface analysis of a)NS01 clear and b) NS01 clear, exposed at 24 months....114

Figure 5.21: Surface analysis of a) NS03 clear, unexposed and b)NS03 clear, exposed at 24 months.....115

Figure 6.1: NS03 clear a) 0hrs exposure, b) 1007hrs exposure and c) 1227 hrs exposure.....118

Figure 6.2: SEM images of NS03 clear samples after a) 1007 hrs exposure and b) 1227hrs exposure.....119

Figure 6.3: How light is reflected fr a) a smooth surface and b) a rough surface.....120

Figure 6.4: 3D AFM image of NS03 clear exposed at a) 1007 hrs and b) 1227 hrs.....121

Figure 6.5: a) and b) 3D AFM image of NS03 clear exposed from different areas of the sample.....122

Figure 6.6: Proposed mechanism for NS03 clear degradation behaviour (Siyab et al, 2016).....124

Figure 6.7: 3D AFM image displaying the roughness of NS03 white after maximum exposure hours (2206).....124

Figure 7.1: PA-FTIR spectra of a photo-oxidised polymeric material fro modulation frequencies between 25 to 1000Hz, Gonan et al, (2001)…….127

Figure 7.2: Lateral force image of SAMs on gold substrate. (a) Force-displacement curve measured for the OH-tip and OH-terminated area, (b) Adhesion data on OH-terminated area, (c) Force-displacement curve measured for the OH-tip and CH_3-terminated area, (d) Adhesion data on CH_3-terminated area, Papastavrou and Akari (1999)……..129

Figure 7.3: (a)Condensation figure of a water droplet condensed onto the COOH terminated area (the darker area) surrounded by CH_3 terminated area, (b) Friction map obtained with COOH-terminated tip where area of high friction (COOH) are light and surrounding area of CH_3 is of low-friction therefore darker, (c) phase lag map of a COOH-terminated tip and (d) phase lag map of a CH_3-terminated tip- dark area corresponds to greater phase lag, Noy et al (1998)……130

Figure 7.4: A schematic drawing of the micro-patterned substrate with OH-terminated brushes……132

Figure 7.5: CFM Phase-imaging on OH-terminated sample using OH-terminated tip in air……133

Figure 7.6: A schematic drawing demonstrating how a ‘water layer’ can form over the OH brushes and mask the tip-sample interaction……134

Figure 7.7: CFM Phase-imaging on OH-terminated sample using OH-terminated tip in hexadecane……134

Figure 7.8: CFM phase-data on three separate areas of the same sample……135

Figure 7.9: An example of a a) plane corrected height image and b) phase image……136

Figure 7.10: a) Phase image on unexposed NS01 sample b) Data from the height image of the unexposed sample and c) Data from CFM on the surface of NS01 unexposed sample……137

Figure 7.11: CFM on surface of NS01 clear at 0, 1480 and 2981 hrs……138

Figure 7.12: Chemical force microscopy of NS03 0hrs a) 3D height image, b) average height data, c) 3D phase image and d) phase angle data to calculate the phase change……140

Figure 7.13: Chemical force microscopy of NS03 1227hrs a) 3D height image, b) average height data, c) 3D phase image and d) phase angle data to calculate the phase change….141

Figure 7.14: Chemical force microscopy of NS03 1227hrs a) 3D height image, b)3D phase image and c) phase angle data to calculate the phase change……..143

Figure 7.15: Chemical force microscopy of NS03 3113hrs, 20×20µm a) 3D height image, b)3D phase image and c) average height data d) phase angle data to calculate the phase change……144

Figure 7.16: X-cross section analysis of NS03 3113hrs a) height image and line analysis and b) phase image and line analysis……145

Figure 7.17: Y-cross section analysis of NS03 3113hrs a) height image and line analysis and b) phase image and line analysis……146

Figure 7.18: CFM on surface of NS03 clear at 0, 1227 and 3113hrs……148

Figure 7.19: Average phase data from CFM on sample surface of NS01 and NS03, with calculated error……149

Figure 7.20: A Plot showing the relationship between the beam energies used to FIB mill platinum coated polycarbonate and the resulting AFM phase shift angle and RMS roughness measurements from AFM. 0KeV represents the bulk polycarbonate material (Bailey et al, 2013)……151

Figure 7.21: Plot showing Ga+ content variation with ion beam energy used to mill PC surfaces. The main plot shows the weight % of Ga+ as calculated by the EDS software, taken from the EDS spectra insert for the different FIB milled surfaces showing the Ga peak at 1.1keV (Bailey et al, 2013)……153

Figure 7.22: Method of cutting steps into the sample using FIB……155

Figure 7.23: Steps in NS01 clear coating exposed at 2981hrs……157

Figure 7.24: CFM on first step, approximately 3µm deep a) phase image and b) phase data……159

Figure 7.25: CFM on middle/second step, approximately 6µm deep a) phase image and b) phase data……160

Figure 7.26: CFM on third step, approximately 9µm deep a) phase image and b) phase data……161

Figure 7.27: SEM images of a coating delaminated from the edges of the substrate……165

Figure 7.28: SEM image of the side profile of a coating showing the inconsistent thickness of the coating……166

Figure 7.29: SEM image of the steps milled under the surface of the sample……166

Figure 7.30: SEM image showing a method developed to overcome inconsistent thickness of a sample in to successfully mill steps……167

Figure 7.31: Data summary of NS01 clear a) SEM Images, b) AFM height images, c) RMS roughness data and d) Gloss retention data……170

Figure 7.32: Data summary of NS03 clear a) SEM Images, b) AFM height images, c) RMS roughness data and d) Gloss retention data……171

LIST OF TABLES

Table 1: A summary of the chemical make-up of each sample……59
Table 2: Advantages and disadvantages of using AFM……61
Table 3: Advantages and disadvantages of using PA-FTIR……65
Table 4: Advantages and disadvantages of using SEM……67
Table 5: Advantages and disadvantages of using FIB……68
Table 6: Advantages and disadvantages of using CFM……70
Table 7: FTIR band assignment for NS01 ((Larkin et al, 1988, Zhang. W,2009, Wang. X, 2012 and Marchewka et al, 2002)……80
Table 8: FTIR band assignment for NS03 ((Larkin et al, 1988, Zhang. W,2009, Wang. X, 2012 and Marchewka et al, 2002)……81
Table 9: NS01 peaks used for FTIR analysis……83
Table 10: NS03 peaks used for FTIR analysis……84
Table 11: A summary of CFM phase data on the surface of NS01 and NS03 clear samples..147
Table 12:Phase change with depth over 3 different exposure times for NS01 clear……162
Table 13: Phase change with depth over 3 different exposure times for NS03 clear……163

1. Introduction

Coatings can be defined as a covering purposefully applied to a surface in order to meet functional or decorative requirements, and in some cases both. They may be found on many products used daily. For example, cans, refrigerators, cars and wires. Each coating varies and is described either by its appearance (clear, pigmented, glossy or matte), its function (corrosion resistant and abrasion resistant etc.) or even by the deposition process (coil coating or dip coating). Here, the discussion is limited to coil coatings.

Coil coatings inherit their name from the production method in which the substrate, typically a metal is covered in various coating layers in order to protect and extend the lifetime of the substrate. They have been used in a variety of applications such as commercial as well as residential building products including roofing and building panels since the 1940s (Gu et al, 2004 and Zhang et al, 2009). The main purpose of coil coatings is to act as a barrier for corrosion protection of the underlying material but they also commonly incorporate visual appeal such as texture and colour for interior and exterior finishes. Critically, the integrity of the coil coating during their exposure in interior or, the typically more demanding exterior environments, is a significant concern for the buyer and the suppliers in the industry.

To protect the metal substrate, it is essential that the coating is highly durable yet flexible. However, when these coatings are used for outdoor applications they are subjected to various weather conditions which may lead to degradation of the coating due to ultra-violet radiation in sunlight, temperature and humidity (Gu et al, 2004), along with acid rain and pollution (Zhang et al, 2011). Degradation of the coating is a major concern in the coating industry as predicting a lifetime for the coating is an essential component required for a product guarantee. Hence, the coating industry requires analytical methods which help in assessing various characteristics of the coating. The formulation of the polymer coating may make the coating susceptible to various forms of degradation such as thermal oxidation, hydrolysis (Wicks Z.W, Jr et al, 1999) photo-oxidation processes such as chain scission (Gu et al, 2009) and thermal and moisture enhanced photo-oxidation. Analytical methods such as infrared spectroscopy and Raman spectroscopy have therefore become a useful tool for quantifying degradation of coatings to enable monitoring chemical changes (Almeida et al, 2009; Santos et al, 2007; Zhang et al,2010 and Zhang et al, 2011). Furthermore, macro-scale physical failure mechanisms are typically observed in coating degradation; including delamination (Rodriguez .F, 1996), chalking (Santos et al 2007), gloss loss (Biggs et al, 2001;

Faucheu et al, 2006 and Gu et al, 2009), colour change (Santos et al, 2007) and changes in the appearance of the coating (Zhang et al,2011) which are all influenced by the nature of the environment the coatings are subjected to. These changes usually take place over long periods of time and can be quantified via a range of tests. Accelerated weathering tests are commonly carried out in order to predict how the coating reacts in the natural environment, without requiring the extended lifetimes, hence speeding up the testing process.

This research is undertaken in collaboration with Becker Industrial Coatings Limited (Liverpool, UK). The purpose of the research is to examine the degradation of three (NS01, NS02 and NS03) industrial coil coatings based on a standard polyester resin and two novel bio-sourced resins crosslinked with a common hexamethoxymethyl melamine cross-linking agent. The degradation of the coatings is to be quantified using spectroscopic and imaging techniques to investigate the link between chemistry changes within the coil coating and external surface changes. As chemical changes are heterogeneous throughout the material, correlation between chemistry and microscopically observed structural changes will provide information beyond the current state-of-the-art in the spatial mechanism of degradation in coil coatings.

The specific objectives of this research are:

- To characterise the physical degradation of the coating by measuring gloss loss and other standard industry measures.
- To apply Fourier transform infra-red (FTIR) spectroscopy to quantify the chemistry of coil coatings. In particular, the use of photo-acoustic FTIR to analyse chemical changes in coil coatings before, during and after weathering. The use of these vibrational spectroscopy techniques will provide chemical information both at the coating surface and sub-surface.
- To use atomic force microscopy (AFM) and scanning electron microscopy (SEM) to analyse the surface changes of the coating during the course of weathering and after weathering and to correlate the finding to the chemical degradation.
- To then develop further techniques by which the changes in the surface morphology can be correlated to the changes in the coating chemistry during weathering which can be done by spatially mapping the chemical degradation.

2. Background on polyester based coil coatings; the process, chemistry, weathering, durability and analysis techniques

2.1 An introduction to the coil coating process

Coil coatings acquire their name from the coating process as the substrate material, typically a metal, is uncoiled during the process and coiled again once the application of the coating is complete. The process can be seen in figure 1.1.

Large sheets of metal are provided by manufacturers in a coiled form. The first stage of the process requires the metal to be uncoiled to be cleaned and pre-treated. Once uncoiled the process continues with the metal being degreased, cleaned, rinsed and chemically pre-treated with a liquid depending on the substrate material. For galvanized steel the pre-treatment usually used is zinc phosphate. Pre-treatments extend the corrosion resistance of the system also allowing the primer and coating to adhere to the metal. The pre-treated metal then goes through an oven for drying after which it is ready to be coated with the primer, the second stage of the process. The primer is applied to the metal using rollers for even distribution and thickness. Again, the metal goes through an oven for the primer to be cured. The third stage is the application of the top coat. The top coat is applied using rollers and cured via an oven. If the coating requires embossing or laminating, this is done after the top coat has been applied. The last stage is the recoiling of the coated metal, ready for shipment. As stated above, the preferred deposition method of the primer and the top coat is using rollers.

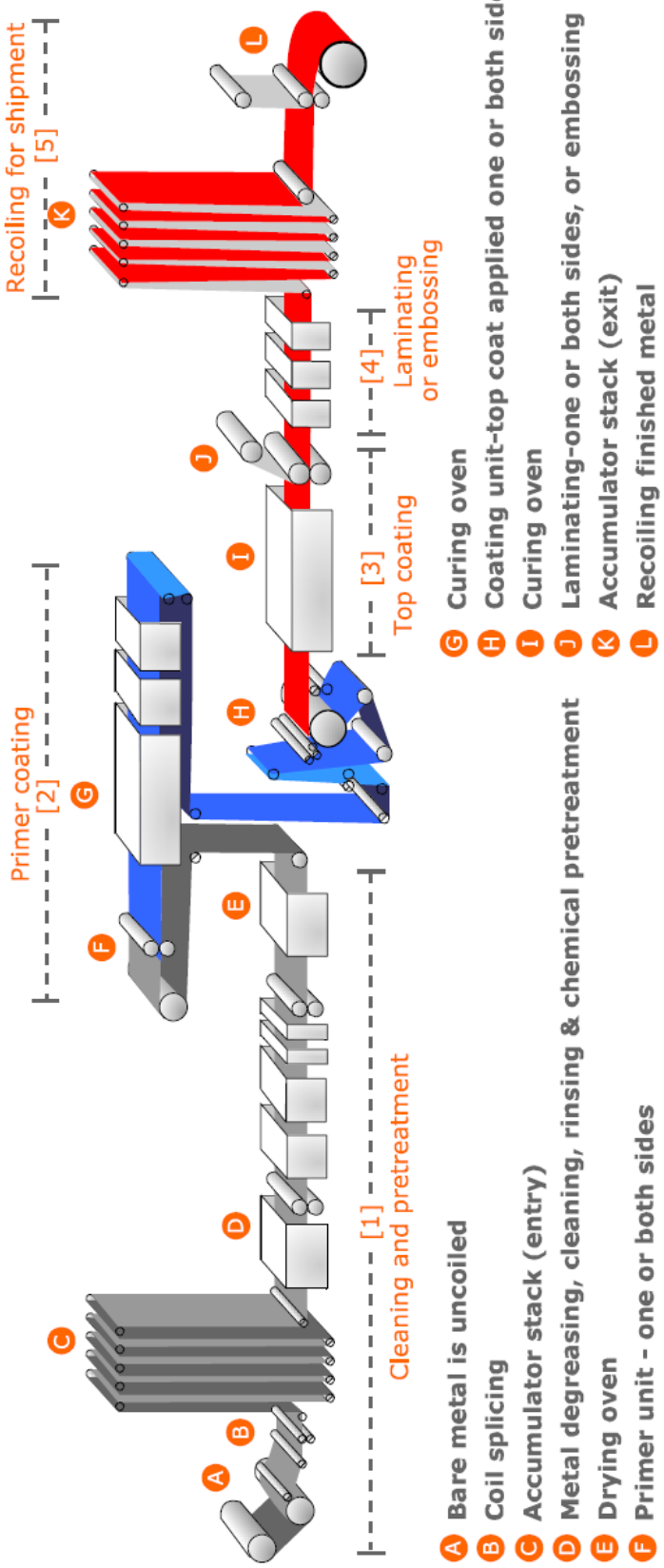

Figure 1.1: Process of coil coating (https://ambrometals.com/wp-content/uploads/2017/02/Coil-Coating-Diagram-ecca1.png)

2.2 Coil Coating chemistry

Coil coatings are polymeric coatings and the main resins used are copolymers based on aromatic and aliphatic diacids and aliphatic diols. Typically, such monomers are sourced from the petrochemicals and are synthetically produced. Their properties and degradation in the natural environment have been extensively studied and reported. However, with the volatility in the price of crude oil and concerns about long term sustainability, active efforts are now in hand to make full or partial replacement of these petrochemically sourced monomers with similar monomers sourced and/or derived from natural, biobased sources. Considerably less is known and reported about the chemistry and the degradation of these monomers once polymerised into coating resins particularly those designed for use in the coil coating market.

2.2.1 An introduction to polymers

Polymers can be classified by many different properties, most commonly by their structure and physical state. The end use of the polymer is dictated by the properties it possesses. Generally, a polymer is a structure of repeating monomer units held together by covalent bonds. The resultant polymer chain molecules form a network structure either linked via intermolecular forces such as van der Waals forces or covalently bonded together. The broad classification of polymers is related to the bonding within the network, with the weaker intermolecular forces found in thermoplastic polymers and stronger covalent cross-linking of polymer chains occurring in thermosetting polymers. The bonding between polymer chains is critical in defining resultant polymer material stability, especially when exposed to moisture, thermal stresses and UV irradiation. Thermoplastics can easily switch from a solid to a liquid phase during thermal processing as the thermal energy gained by the polymer chains during heating overcomes their weak intermolecular forces. Subsequent cooling allows the reformation of the solid polymer in a reversible manner. Typically, such coatings are soft and have a low glass transition, T_g temperature making them susceptible to damage. Thermosets are much more resistant to thermal processes as considerably more energy is required to break the covalent cross-linked bonds. However, at extreme temperatures thermosetting polymers degrade irreversibly. Being generally harder with a higher T_g than thermoplastic coatings, they are also more resistant to damage and degradation in hot environments. This general resistance of thermosetting polymers therefore make them particularly good candidates for coil coatings.

The physical properties of all polymers are dependent both on the chemical structures found within the polymer chains and the ordering of polymer chains in the material. The physical state of a polymer refers to the conformation of a polymer chain in free space. Each bond in the polymer chain is free to rotate when possessing enough thermal energy (i.e. >0 K). However, the bond angles and lengths within the polymer remain constant. The organisation of the bonds within the polymer chain can lead to a variety of different polymer chain organisations, ranging from linear to branched structures. Structural packing of these chains in a solid material is important in determining the physical properties of a polymer and can be generally ordered into whether the polymer is crystalline or amorphous. For thermosetting coil coatings, the structural organisation of the polymer chains is almost always amorphous, with the polymer chains having a random arrangement. Characterisation of polymeric materials with either amorphous or crystalline structures is typically achieved by recording temperatures at which the thermal energy is sufficient for polymer chains to overcome their interactions with neighbouring chains. Two main thermal transition temperatures characterise polymer structures; the glass transition temperature (T_g) and the melting temperature (T_m) of the polymer. T_g is the temperature below which *"free rotation ceases because of intra-molecular energy barriers"* (Rodriguez, 1996), hence the polymer is in its 'glassy' state. Crystalline polymers do not display a range in the change of state as amorphous polymers do. Upon heating a crystalline structure disintegrates and simply melts. However, when an amorphous polymer is heated the structure is not ordered into crystals and the energy supplied allows movement of the randomly packed chains leading to a noticeable temperature transition phase before melting. Hence T_g can only be measured for amorphous polymers or regions and T_m can be recorded for crystalline polymers only.

Measuring the T_g of a thermoset polymer system is typically used to determine the percentage crosslinking in the coil coating structure (Hill, 1992). In coil coating production, the coating is applied by roller coating and then heated typically up to 230°C peak metal temperature. As the temperature rises the solvents present in the coating evaporate and above a specification activation energy (typically 180°C) the crosslinking transesterification reaction commences between the functional OH groups on the main polyester resin backbone and the reactive (methoxy) sites on the aminoplast resin. As these crosslinking reactions proceed, a three-dimensional network is formed and the viscosity increases dramatically until an infinite network (gel) is formed and all the solvent driven off. The structure is then fixed by quenching the coil coating in cold water. Several factors determine the extent of crosslinking including the functionality of the polymer backbone (typically for

polyesters defined as the hydroxyl content), the use of an organic acid catalyst and the amount of energy going into the coating (a function of both the oven air temperature and the speed of the continuously coated strip going through the oven and dwell time).

Determining the T_g of the cured coil coating is therefore essential to guarantee the coil coating is properly cured and can withstand mechanical forming processes and exposure in outdoor environments. The second thermal transition of melting temperature, $T_{m,}$ describes the thermal energy required to separate polymer chains beyond their equilibrium intermolecular interaction distance when moving from the solid to liquid phase during melting. Thus, T_m in indicative of a crystalline structure although many commercially available thermoplastic materials are semi-crystalline, containing both crystalline and amorphous regions giving rise to both T_g and T_m.

Both T_m and T_g are significant in polymer coil coating applications. Ideally a coil coating system must have a T_m and T_g somewhat greater than the temperature of the environment it shall be exposed in to avoid the bonds in the polymer chain gaining sufficient energy to be able to rotate and re-orientate the thermoset structure. Since coil coatings can be subjected to harsh environments with high temperatures and humidity along with acid rain and intense UV exposure, so the coating needs to be well cross linked to withstand these extreme environments for the minimum period stated in its warranty. For this reason, it is important to study the chemistry of the coatings to better understand how it is affected by weathering. The most obvious changes in the coating are at the macro scale and occur at the exposed surface. These are typically expressed as changes in surface topography, gloss (gloss loss) and colour (Faucheu et al, 2006; Gu et al, 2004 and Gu et al, 2009). Therefore, the measurement of surface properties of polymer coatings is a very important means to characterise the coil coating's surface morphology, chemical heterogeneity and how these properties change with degradation.

2.2.2 Composition of coil coatings

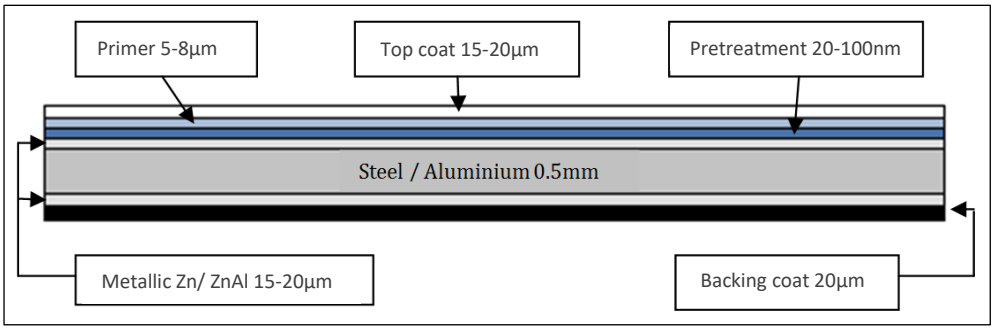

Figure 2.1: The structure of coil coatings

Figure 2.1 shows a cross section of a typical coil coated metal panel. Each layer acts as a protective coating for the metal substrate being used. The topcoat provides the external interface with the surrounding environment and acts as the principle barrier between the under layers and the external environment. The topcoat resinous binder comprises of a highly durable thermosetting polymer resin and an aminoplast crosslinking agent such as melamine. The thermosetting polymer resin is chosen according to the application of the coating and the requirements given by the customer for example, is it to be used as roofing material or as building panels. They range from polyurethanes, epoxies, acrylics, alkyds and polyester resins (Wicks, 1999). In the case of this work, a polyester resin is used as the reference and the bio-sourced resins are essentially modified polyester resins (bio-sourced monomers) hence they are discussed in greater detail.

Coil coatings consist of binders, pigments, solvents and additives. The binder is the bulk material of the coating which holds all the components together and allows the formulation to adhere to the substrate. In this case the binder is an organic polymer. Pigments provide colour and opacity to the coating and may be excluded if a clear coat is desired. The primary purpose of the solvents is to dissolve the binder components and aid the flow of the coating for smooth application. Once applied, these solvents evaporate. Additives are used to modify various properties of the coating for example, a catalyst for the polymerisation of the binder or a flow modifier.

2.2.3 Crosslinking polyester resin with hexamethoxymethyl melamine

Polyesters are prepared from polyols and organic acids via esterification and then cross-linked with a cross-linker such as melamine or isocyanate to prepare polyester based coatings. The esterification reaction is reversible, and a general equation is shown below along with a specific equation to produce polyesters.

Basic equation to form esters

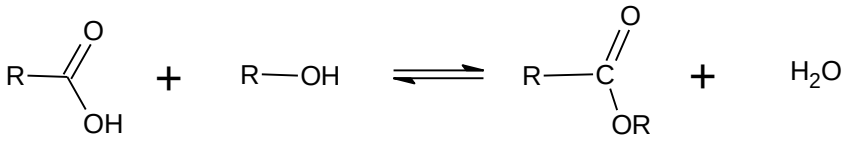

Acid + Alcohol = Ester + Water

Equation to produce polyesters

$$n.HOOC - R - COOH + n.HO - R' - OH \rightleftharpoons H(O - R' - O - OC - RCO)nOH + (2n - 1)H_20$$

(Eq 2. 1)

The polyols and acids are chosen in accordance to the requirements of the resin such as durability, flexibility, chain stiffness and adhesion to the substrate. A coil coating polyester paint therefore contains a polyester resin, an aminoplast cross linker such as hexamethoxymethyl melamine, various additives to catalyse the cross-linking reaction that promote good flow and levelling. The paint also contains solvents to attain optimum application viscosity and pigments to provide colour and desired visual effects.

There many polyols available to be used for the polyester synthesis but the most commonly used are diols for example, hindered diol neopentyl glycol (NPG), linear diol hexane diol (HD) and triols such as trimethylol propane (TMP), as seen in figure 2.2. NPG is used for superior exterior durability due to there being no labile β hydrogen in terms of hydroxyl functionality therefore, is less susceptible chemical attack. The presence of two methyl groups in NPG *"increase the steric hindrance that imparts chemical resistance, stability towards hydrolysis and corrosion resistance*,"(Wang, 2012).

The most common organic acids used in combination with the polyols are either aromatic or aliphatic. Aromatic di-acids include Isophtalic acid (IA), terephthalic acid (TA), orthophthalic acid (OA) amongst others. The most commonly used aliphatic acid is adipic acid (AA). Aromatic acids are used to increase the hardness of the polyester coating and an aliphatic acid can help the chemical resistance of the coating. The ester linkages formed via the esterfication reaction of the acids and polyols are susceptible to hydrolysis.

The susceptibility of the polyester to hydrolysis is dependent upon various factors such as; the concentration of ester bonds, the acidity of the polyols used, the hydrophobicity of the glycol/dicarboxylic acid and steric hindrance surrounding the ester groups (Wang, 2012).

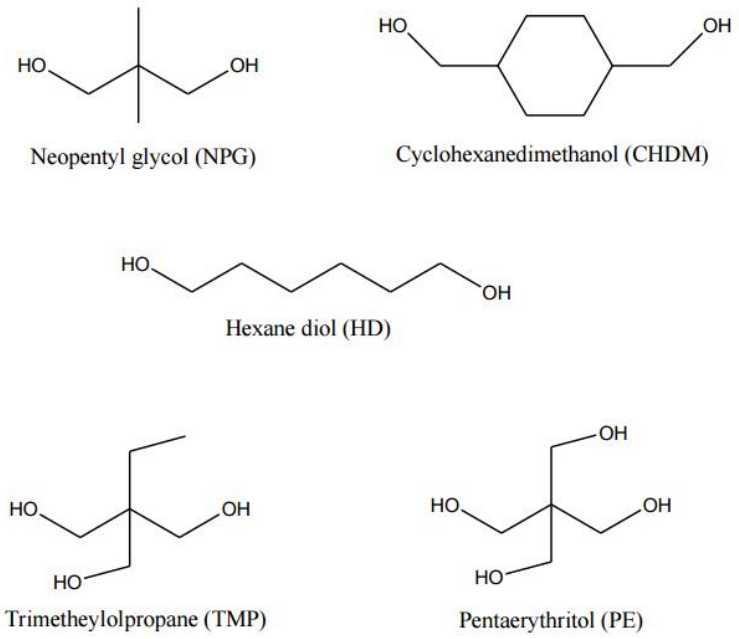

Figure 2.2: Common polyols used in the synthesis of polyester resin (Wang, 2012)

The polyester resin is co-condensed with a cross-linking agent to construct a polyester coating. Two of the most commonly used cross-linkers are melamines and blocked isocyanates. Melamine is a crosslinker resin actively used in the coil coating industry to crosslink polyesters which contain hydroxyl functional groups. Melamine is a robust crosslinker and is used in this research of polyester-melamine coatings. The melamine resin used is not only highly reactive with the polyester resin but provides high cross-link density which is advantageous to the properties of the resultant coating. There are various forms of

melamine as shown in the figure 2.3. However, the most stable melamine is hexa-methoxymethyl melamine (HMMM) and hence it is used widely.

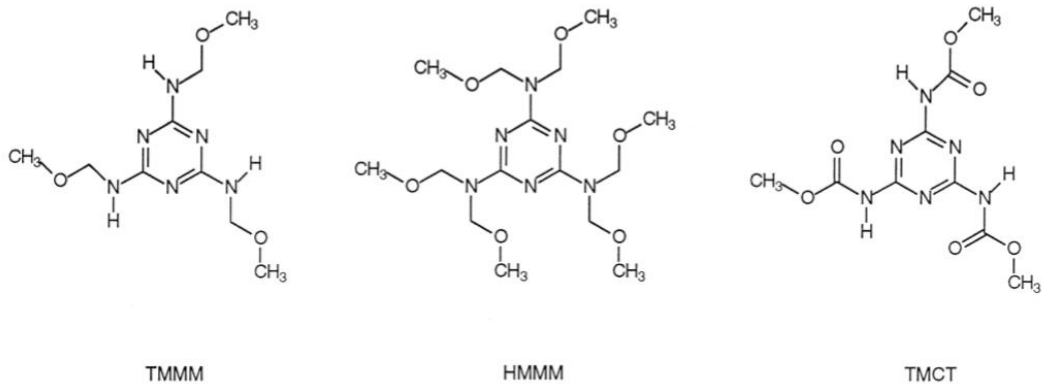

Figure 2.3: Three structures for melamine, TMMM(tris-methoxymethyl melamine), HMMM (hexamethoxymethyl melamine)- used in this study and TMCT (tris-methyl carbamoyl triazine). (Larkin et al, 1998)

2.2.4 Addition of pigments

Pigments have found great use in coil coatings. They may be organic or inorganic and are used to provide colour, improve performance properties such as weathering of coatings as well as reduce costs. The selection of the pigment depends on the application of the coating and the stability variation of the pigment and polymer phases (Zhang et al, 2012). Pigments used in the coil coating industry include titanium dioxide (TiO_2). This pigment provides white colour to the coating and also provides enhanced chemical stability if doped by pro-longing photo-oxidation. However, the photo-activity of TiO_2 can have a detrimental effect on the lifetime of the coating even though it may act as a UV stabiliser for another. Gesenhues (2001) described the basic reaction involved in photocatalysis by TiO_2. The first step involves the production of e- in the conduction band and h+ in the valance band of TiO_2 because of exposure to UV irradiation. Then both charge carriers can either recombine, become trapped by impurities and dopants within the surface or, initiate redox reactions of adsorbed molecules by crossing the particle surface. It is thought to be most likely that with paint polymers the h+ is transferred to a hydroxyl group present at the TiO_2 surface resulting in an OH radical, which then attacks the polymer. However, it is not known how the pigment will affect the bio-based coating, but it has been used greatly in the standard petroleum-based coating used in this research. The white coatings used in this study do use TiO_2, therefore keeping the clear coatings as a reference to understand the effect of this particular pigment on the bio-based formulation will be seen.

2.2.5 The role of solvents and other additives

There is a vast variety of solvents to choose from when considering them for coil coatings. The main reason for the use of solvents is the ease of application of the coating. It does so by controlling the viscosity of the paint hence aiding the spread of a smooth and even layer on the substrate. When the paint is cured the high temperatures cause the solvents to evaporate so it is thought there is no residual in the final coating.

Other additives used in coatings are generally used to either improve the performance of the coating or to aid the coating application. For instance, stabilisers may be added to improve the durability of the coating. One such stabiliser commonly used is a 'hindered amine light stabiliser' (HALS). Flow agents and dispersing agents are also used when needing to improve the dispersing pigments and paint flow.

2.3 Degradation of coil coatings

Over 60% of all coil coated materials are used for exterior applications in the construction industry. This means that the polymer system in such topcoats will be subject to degradation. This will attack both the cross linker and the crosslinked network but also the backbone polyester resin too. Degradation occurs where there is, in theory, enough energy to overcome the bond dissociation energies causing chemical scission of the backbone or crosslinked network and hence producing small fragments.

Degradation could be further subdivided into various categories; thermal, chemical, photochemical, radiation, mechanical and biological degradation (Zhang. Y, 2012). Thermal degradation is induced by exposure to high temperatures without the involvement of other compounds causing breakage in polymer bonds. Chemical degradation takes place in the presence of chemicals and/or catalysts which induce a chemical reaction leading to chain scission and free radicals being produced. Photochemical degradation is usually initiated by chemicals in the ozone and ultraviolet radiation. Degradation via radiation refers to high energy radiation such as X-rays and γ-rays which produces ionization and excitation in polymer molecules causing polymer alterations. Mechanical degradation is the macroscopic manifestation of external stresses and shear forces whereas biological degradation involves microbial attack on chemical species in the polymer, something polyurethanes are more susceptible to than polyesters.

In polyester coatings more than one form of degradation can take place. The most common forms of degradation are; hydrolysis, a form of chemical degradation, photo-degradation, initiated in the presence of UV radiation and photo-oxidation, a combination of both thermal and chemical degradation. The process of each degradation is highlighted in the following sections.

2.3.1 Polymer irradiation

Radiation is the emission of energy in the form of either waves or particles. Types of radiation include X-rays, γ-rays, electron beams, ultraviolet (UV) and infrared light which also determine the energy of the radiation. It is usually UV radiation or ionising radiation such as from gamma or neutron sources which can induce degradation in polymeric materials. In the case of ultraviolet radiation, the energy absorption takes place at specific molecular sites which may lead to electronically excited states, whereas, ionising radiation leads to the production of free radicals or ionic species (Reichmanis et al, 1993). In ionisation, an orbital electron from the outer shell of a specific atom is removed, converting it to a positively charged ion and consequently the covalent bond associated with that atom is broken. This leads to the rearrangement of an atom or a group of atoms and hence crosslinking or scission at the ionisation site. Irradiation of organic polymers can also induce molecular chain branching and degradation along with crosslinking and scissioning (Spadaro. G, 2017).

In both cases, subsequent events can result in the side group or main chain scission or crosslinking can take place. Scission refers to "*the severance or rupture of molecular chain bonds*" (Jr. W.D.C, 2007), causing chains to separate at the point of scission and hence reducing the molecular weight of the polymer. On the other hand, crosslinking and chain branching increase the molecular weight of the polymer. Many of the polymer's properties are dependent on the molecular weight of the polymer, such as the mechanical strength and the ability to resist chemical attack. If the molecular weight is reduced some physical and chemical properties are also affected. Bond rupture can also take place due to heat and chemical reaction.

The molecular modifications within polymers will vary depending on the environment the polymer is irradiated in. For example, during ionising radiation, the free radicals produced when the irradiation happens in air, can give rise to oxidative reaction as the radicals produced can also react with oxygen. The free radicals produce oxidised functional groups such as carbonyl, peroxides and hydroxyls to name a few. There will also be significant changes on the surface of the sample as oppose to the bulk due to availability of oxygen at

the surface (O'Donnell J.H, 1989). The effect would be different for irradiation taking place in vacuum or in the presence of inert gas (Spadaro et al, 2017).

The adsorption of radiation energy occurs spatially at random at a molecular level but the consequent chemical reactions are not arbitrary as some polymers may have chemical groups which are sensitive to radiation-induced reactions. Some of these chemical groups are COOH, C-Hal, NH_2 and C=C (O'Donnell. J.H, 1989). These chemical reactions can result from the resultant free radicals ions or from intramolecular or intermolecular migration of energy.

As discussed above, irradiation in vacuum would yield different effects on the polymer. For example, vacuum ultraviolet light can have photon energies greater than the binding energy of chemical bonds, hence leading to bond scissions. Some of the chemical bonds include, C-C, C-H and C-O (Li et al, 2006). Molecular modifications under vacuum irradiation usually depend on morphology and initial molecular structure. Unhindered main chains predominantly result in chain branching and crosslinking (Spadaro et al, 2017).

Li et al (2006) also found that aliphatic polyesters such as poly(butylene succinate), PBS degrade at a higher rate in comparison to poly(methyl methacrylate), PMMA and the active species propagating degradation upon Vacuum ultraviolet irradiation was negatively charged oxygen. Aromatics, however, have been known to provide irradiation resistance for organic molecules (Reichmanis et al, 1993).

Access to oxygen seems like the key to subsequent chemical/oxidative reactions after the onset of polymer irradiation. The readily available oxygen at the surface of the sample allows significant changes on the surface as oppose to the bulk (O'Donnell J.H, 1989). Reichmanis et al (1993) state that molecular modifications and the formation of physiochemical groups will not be uniform within the polymer material. They have observed "*The extent of the oxidative degradation phenomena is higher in the external layers of the polymers and a concentration gradient of oxidized groups, moving from the external surfaces toward the bulk."* It would be useful to see if this phenomenon takes place with the coatings in this research.

2.3.2 Photo-degradation and hydrolysis

Thermal energy and Ultra-violet (UV) radiation can initiate chemical reactions and cause bond breaking in organic polymers. The latter process is known as photo-degradation. A pre-requisite for this type of degradation is that the macromolecule should contain chromophoric groups (functional groups that absorbs UV light) to initiate a reaction (Schnabel, 1992). This fact plays an important part in analysis of organic coatings as most coatings are subjected to outdoor exposure and sunlight which contains a fraction of UV light. With enough energy from UV radiation this could lead to chain scission i.e. photolysis, photo-oxidation and crosslinking of shorter chain polymers. Organic coatings subjected to outdoor exposure usually show physical degradation in the form of cracking, chalking and colour changes (Zhang. Y, 2012).

Batista et al (2011) have compiled a set of schemes to demonstrate the photo-degradation of melamine based coatings when artificially weathered hence; the resultant schemes are based on the effect of controlled moisture and UV radiation.

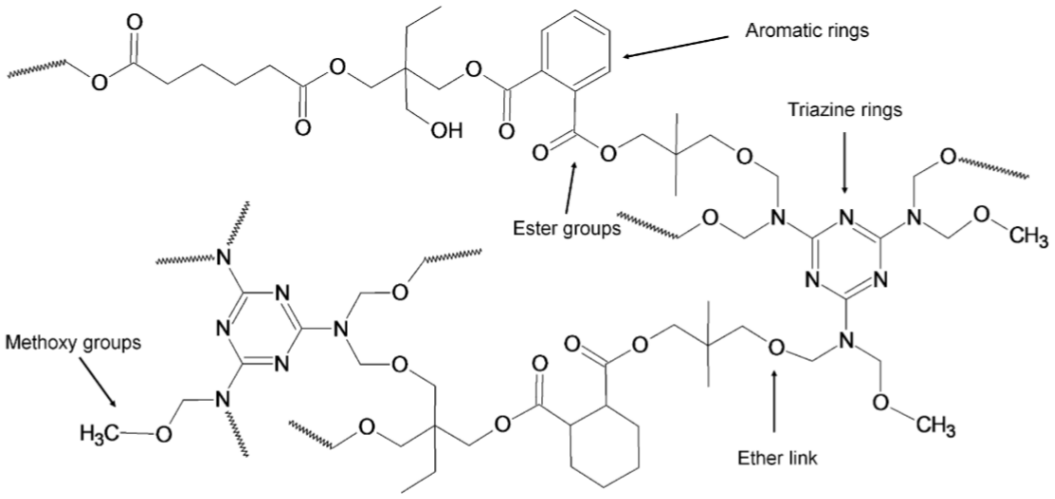

Figure 2.4: chemical structure of polyester/melamine bonds (Batista et al, 2011)

Figure 2.4 displays the chemical structure of the polymer/melamine coating highlighting the main chromophore groups present in the matrix. Chromophore groups absorb certain wavelengths of light exciting electrons. The main chromophore groups are: the ether links in methoxy groups, any aromatic rings in the polyester structure, ester groups within the polyester structure along with the triazine ring in the melamine structure.

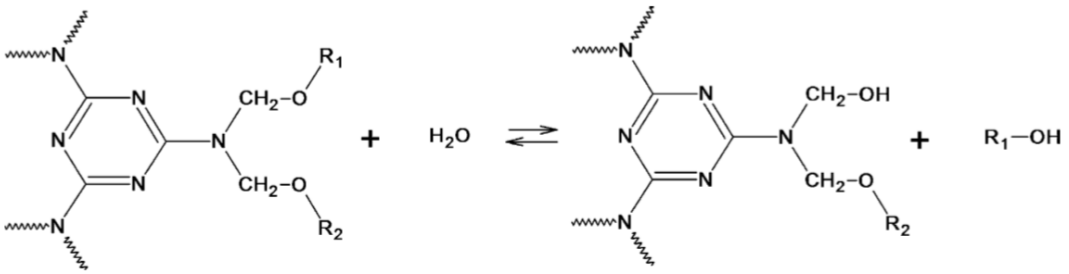

Figure 2.5: hydrolysis of ether linkages forming melamine methylol groups (Batista et al, 2011)

The degradation is initiated by hydrolysis of the ether linkages. Hydrolysis is the breakdown of bonds due to the addition of a water molecule. In this chemical reaction the molecule splits into 2 parts; one gains a hydrogen ion (H^+) from the additional water molecule. The other group collects the remaining hydroxyl group (OH^-). The nucleophile then attacks the carbon of the carbonyl group of either the ester or the amide.

In this case the hydrolysis of the ether linkages (Figure 2.5) in the polyester/melamine resin is thought to result in melamine methylol groups which then rapidly decay into amine groups and formaldehyde (figure 2.6).

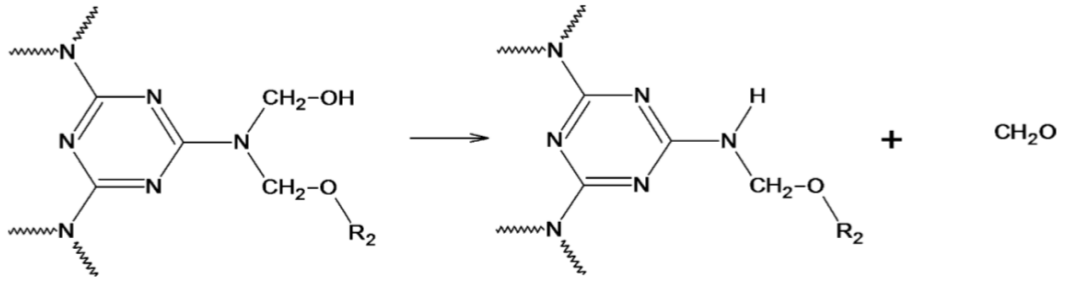

Figure 2.6: production of amine groups and formldehyde due to decomposition of methylol groups (Batista et al, 2011).

The production of amine groups can be observed by carrying out FTIR on the exposed sample and monitoring the –NH peak, an increase will then confirm this mechanism. It is stated that beyond this point and after the formation of formaldehyde the degradation can take two routes, one in the presence of UV, which results in the photolysis of formaldehyde and free radicals ready for attack, leading to peroxide free radicals and a continuation of the degradation cycle until the process is terminated by various chemical groups. The second is in the absence of UV in which formaldehyde may be oxidised into formic acid. Both

mechanisms were shown to take place as peak analysis by FTIR can show the production and reduction of certain chemical groups.

2.3.3 Photo-oxidation

Chain scission or photolysis induced via photo-degradation can initiate a reaction in which free radicals are produced. The free-radicals produced propagate further reactions with oxygen leading to photo-oxidation (or a continuation of reactions with oxygen i.e. auto-oxidation) resulting in unstable hydro peroxides and peroxides- which themselves further degrade to form a range of oxidised species, and (in the case of polyesters) acids, anhydrides, alcohols and amines. The free radicals can also react with each other due to which the series of photo oxidation reactions are terminated. Below, scheme 1(Wicks et al, 1999) represents this process.

Scheme 1 demonstrates that the initial step in photo-oxidation is photolysis, where UV breaks bonds within the polymer to start degradation after which free radicals continue to react with each other in the presence of oxygen. The series of reactions are terminated once the free radicals react with each other.

Initiation

Polymer (P) $\xrightarrow{\text{sunlight}}$ P* (where P* is P in its photo-excited state)

P* $\longrightarrow$ Free radicals (P•)

Propagation

P• + O_2 $\longrightarrow$ POO•

POO• + Polymer (P-H) $\longrightarrow$ POOH + P•

PO• (•OH) + Polymer (P-H) $\longrightarrow$ POH(H_2O) + P•

Termination

2POO• $\longrightarrow$ POOP + O_2

2P• $\longrightarrow$ P-P

POO• + P• $\longrightarrow$ POOP

(Scheme 1)

Another form of characterising failure of the coating is the delamination of the coating from the surface of the substrate. Phase separation within a mixture can lead to interfacial failure causing the coating to delaminate from the surface of the substrate. For instance, if a plasticizer is extracted from a system or migrates within the system to a heterogeneous area the integrity of the system is affected and the appearance is marred (Rodriguez,1996). The

surface as a result may be softened and 'peel' from the surface. Similarly, in coil coatings if the polymeric binder holding the system together degrades enough, the whole coating weakens and either results in the loss of previously bound pigments (a phenomenon known as chalking) or, if this degradation reaches the interface with a primer or metal surface, it can result in delamination.

2.4 Weathering methods

The lifetime and durability of a coating is of great concern to manufacturers of coil coatings as the product needs to retain a certain lifetime guarantee in the order of several years. Therefore, prior to making the product available on the market various tests and investigations are carried out to analyse the performance of the coating. It is well known, coatings degrade upon exposure to natural weathering events such as sunlight and moisture. The effects of weathering are noticeable only after many years of exposure when the coating has reached a critical point before failure and can include colour change, delamination, chalking, gloss loss and cracking and oxidation. However, it is difficult to predict how long it may take for the coating to reach its potential lifetime. Accelerated weathering devices have been used to replicate natural weathering even though it is apparent that the exact replication is not possible due the change on weather daily. After ten years of exterior durability tests on various accelerated devices, Cocuzzi and Pilcher (2013) concluded that "*the only reliable form of accelerated testing for coil coatings is to expose the coatings under real-time conditions as quickly as possible to build-up exposure time as quickly as possible*."

To simulate natural weathering a QUV machine is used in which materials are exposed to alternating cycles of humidity and UV light. The humidity and UV cycles are kept at intense conditions to accelerate the weathering by photo-degradation and hydrolysis. Simultaneously, natural weathering would be carried out to compare the test results. Once the weathering tests have been completed the samples undergo further tests which describe the level of physical degradation, such as testing for gloss loss, chalking, delamination and surface roughness, as well as chemical degradation via spectroscopy techniques.

2.5 A background on the techniques used to analyse coil coatings

Microscopes has been used from as early as the 17th century to give insight on a microscopic scale. From cells and bacteria strains, rocks and minerals, to imperfections in materials, a microscope has proven to be a useful tool to deepen our understanding of each.

Anthony van Leeuwenhoek (1632-1723) designed one of the earliest instruments to be able to image very small objects, and through which he discovered bacteria and was able to identify red blood cells by their shape. An adaptation to this instrument by adding another convex lens to be able to focus is what makes the basis of a light microscope today. However, whilst striving to achieve better resolution scientists came to the realisation that the number or the type of lens were not the sole limiting factor of the resolution of the microscope but the wavelength of light used for illumination also contributes. It was discovered that in vacuum, accelerated electrons behave like visible light by travelling in straight lines with wave-like properties, but a wavelength almost 100,000 times shorter. Furthermore, the path the electrons follow can be shaped using magnetic fields. (FEI, 2010)

There are three basic types of microscopes; optical, scanning probe and charged particle which encompass electrons and ions. Optical microscopes use visible light along with transparent lenses and can view small objects up to 1 micrometre (μm). On the other hand, electron and ion microscopes use electromagnetic or electrostatic lenses to focus charged particles instead of light. Such microscopes allow features in the nanometre scale to be seen for example, individual atoms. The final type is the scanning microscope which utilise a small probe to scan across a sample. The various forces and interactions between the sample and the probe are then used to create an image of the surface. For example, the atomic force microscope. Again, these have atomic scale resolution.

2.5.1 Scanning probe Microscopy

Scanning probe microscopy (SPM) is an imaging technique in which the interaction between a probe and the sample surface yields surface topographies. Scanning tunnelling microscopy (STM) first discovered by Binnig and Rohrer in 1982 is a technique in which the surface topography is constructed "*on an atomic scale directly in real space,*" (Binning G and Rohrer H, 1983). An accurate image is constructed due to the controlled movement of the probe attached to piezo-positions and the tunnelling current between the probe and the sample. To control the movement of the probe so it moves sequentially over the sample surface and to record the spatial co-ordinates, a set-point is fixed. This set point is maintained via the tunnelling current. Tunnelling is best described as the quantum mechanical behaviour of

electrons passing through a gap in between two conducting materials in close proximity of each other. When the potential energy barrier is overcome the electrons can tunnel through the gap producing a tunnelling current which can be detected. Tunnelling allows an image to be constructed without direct contact however can only be used in conjunction with conductive samples.

Atomic force microscopy (AFM) is also a form of SPM invented by Binnig, Quate and Gerber (Binning et al, 1986). Similar to STM, the interaction between the sample and the probe is the key to reconstructing images of the sample surface. In this case however, the tunnelling current is not measured; instead the force is measured by the cantilever system that is attached to the scanning probe, which makes it particularly useful to image non-conductive samples such as polymers. The AFM set-up typically consists of a cantilever, probe, a position sensitive detector, a piezoelectric actuator and a laser beam. The laser beam is reflected from the back of the cantilever which enables the position of the moving cantilever to be recorded and a feedback mechanism to be maintained, keeping the tip at a constant force or height.

2.5.1.1 Atomic force microscopy

AFM is operated in three different modes as shown in figure 2.7 below; the contact mode, non-contact mode and a tapping mode. In the contact mode the tip is in direct contact with the sample surface like a pencil to a paper during scanning of the probe over the sample surface. In the non-contact mode, the cantilever is oscillated at its resonance frequency and can detect van der Waals attractive and repulsive forces between the sample surface and the scanning probe. Other useful modes of AFM are: lateral force microscopy in which frictional forces are measured on the surface using AFM, force modulation where sample properties are investigated using repulsive forces between the sample and the tip and phase imaging which depends on the phase shifts influenced by sample-tip friction, adhesion, high elasticity or chemical interactions (detailed explanation follows) (Maver et al, 2016).

The AFM technique described above shows that the probe and sample interaction yield useful information regarding the mechanical properties of the surface of the sample. This is only possible due to the force curves that are produced from the probe and sample interaction. The force cannot be directly measured but is calculated from the deflection of the cantilever. When the probe is moving towards a sample surface, an attractive force

develops between the probe and the sample that causes a deflection of the cantilever towards the sample surface hence the attractive force becomes greater as the distance decreases between the probe and sample. Once the probe is in contact with the sample surface the cantilever begins to deflect back on itself as the interaction between the probe and the sample surface increases. So, this becomes a repulsive force between the probe and the sample surface and continues to increase until the set point value is reached and the approach is stopped. When the probe is removed from the sample, the force acting on the probe decreases until attraction followed by probe-sample separation is achieved. The complete van der Waals interaction force corresponding to AFM probe-sample interactions is shown in figure 2.7 below.

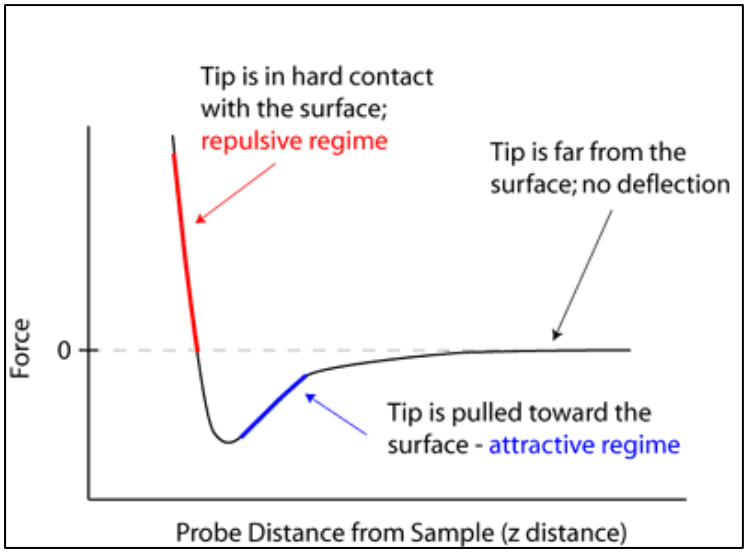

Figure 2.7: The probe deflection against the attractive and repulsive forces, (nanoscience)

This force acting on an AFM probe in contact causes a corresponding bending in the cantilever attached to the AFM probe. The force acting on the AFM probe is therefore measured from the cantilever deflection using a simple relationship, Hooke's law (Capella and Dietler, 1999).

$$F = -kd_c \qquad \text{(Eq 2.2)}$$

where; k= spring constant of the cantilever, F = force and dc = cantilever deflection.

The tapping mode is the preferable option for imaging soft samples when compared to contact mode imaging. Specifically, contact mode relies on the AFM probe contacting the sample while sequentially scanning over the sample and the contact pressure between the probe and the sample can result in sample damage. As figure 2.8 shows, non-contact mode

can be used to avoid any interaction with the sample, as the tip is oscillating above the sample and therefore does not damage the surface at all. Tapping mode on the other hand, relies on the interaction between the probe attached to an oscillating cantilever and the sample surface so that the probe is only intermittently in contact with the sample. The cantilever is first oscillated at its resonance frequency and then moved towards the sample surface. The resonance frequency shifts towards lower frequency as the repulsive regime of the interaction curve shown in figure 2.7 is approached. Practically, the amplitude of the oscillation at the resonance frequency drops as sample moves up towards the oscillating probe. A set-point amplitude is defined and maintained so that the oscillating probe lightly taps over the sample surface as the probe is scanned over the sample during the imaging process.

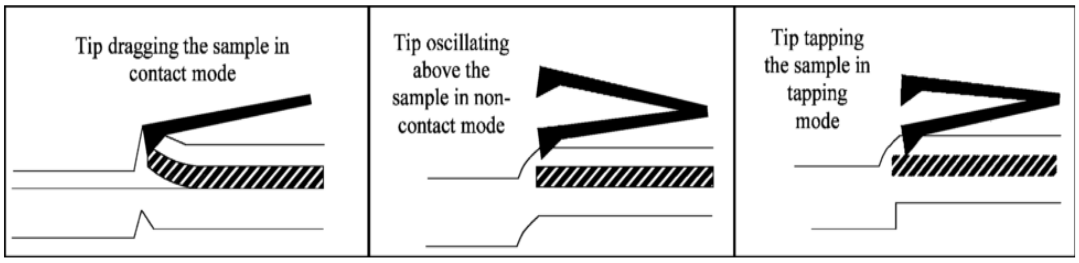

Figure 2.8: contact mode (left), non-contact mode (middle) and tapping mode (right).

AFM phase imaging is a further technique that is available in conjunction with tapping modes AFM and shows image contrast due to mechanical or chemical property variations at a sample's surface. Phase imaging AFM provides information on the contact area between a solid AFM probe that sequentially taps over the surface of a sample. The change in the probe-sample contact area provides a phase lag between the driving sinusoidal signal moving the AFM probe and the response of the probe after tapping on the sample surface. For example, flat samples will provide a constant contact area between the AFM probe and sample assuming the mechanical properties of the same are homogeneous. A heterogeneous sample containing mechanically soft domains will result in an increase in the contact area between the tapping probe and the sample. The AFM phase image therefore produces a map of the harder and the softer areas at the sample's surface.

Phase imaging was first carried out on coil coatings by Biggs et al (2001) and was highlighted as being a useful method of surface characterisation due to it being non-destructive. Phase imaging of unweathered samples as well as a standard topography image is shown in figure 2.9. Little image contrast was observed in the phase image for the unweathered sample,

suggesting that the mechanical properties of the coating are homogeneous across the areas examined.

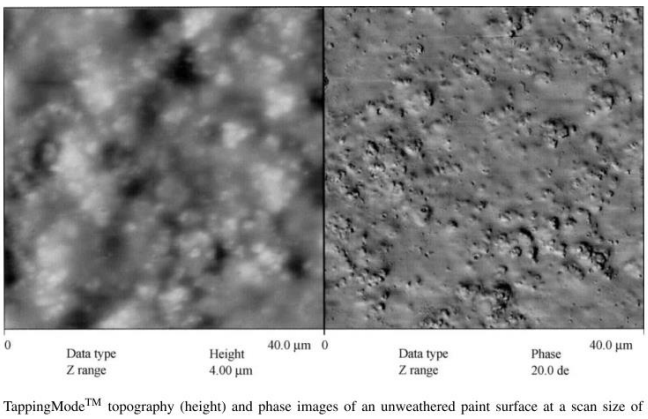

TappingMode™ topography (height) and phase images of an unweathered paint surface at a scan size of 4

Figure 2.9: phase and height images using tapping mode AFM of an unweathered paint surface, Biggs et al, (2001)

AFM has been used extensively to characterise surface morphology of polymeric coatings. Gu et al (2004) have used atomic force microscopy and chemical force microscopy to study the degradation and nano-chemical heterogeneity of polymeric coating surfaces. In their study, samples were imaged as a function of exposure time in various environments. Samples included polyester films, cross linked epoxies and blend films of polyvinylidene fluoride (PVDF) and polymethyl methacrylate (PMMA). Particular interest was paid to polyester films as these are the type of systems used in our current research. The AFM was used in tapping mode to evaluate surface topography and phase images were produced. The degradation of the surface of these coatings was monitored by AFM as it enables active imaging of the formation and evolution of pits in the sample surface as a function of exposure time. The increase in the pit dimensions in the coating was observed with degradation time and was correlated with the changes in the coating's external appearance, for example, chalking or loss of gloss. Force curves were used to describe the mechanical differences in the pitted and non-pitted regions within the sample (refer to figure 2.10).

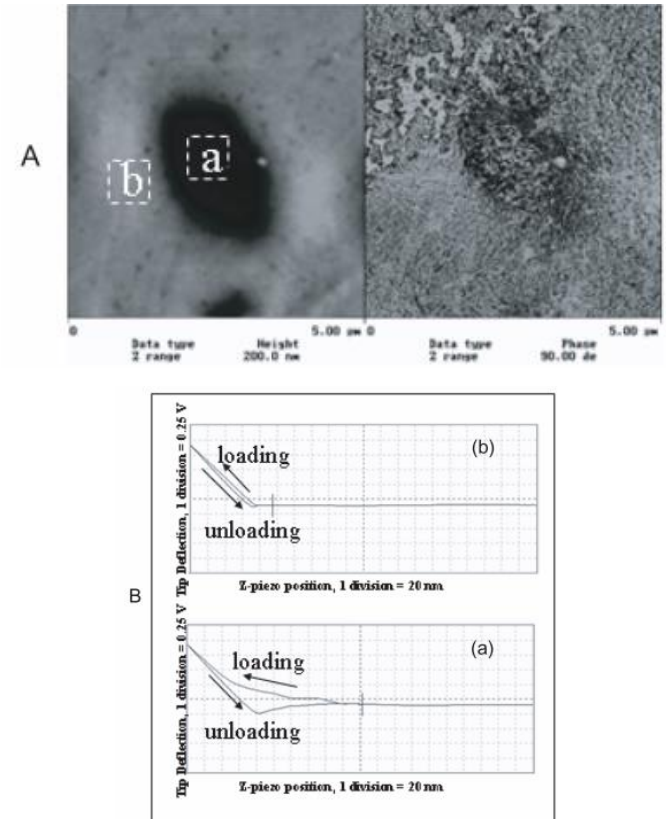

Figure 2.10: A) AFM images and B) force displacement curves, Gu et al (2004)

In another study (Biggs et al, 2001), AFM imaging was employed to examine the surface of a pigmented polyester-melamine thermoset coating area as a function of degradation time. This study involved marking corners of a 250µm square pattern on the coating sample surface using a micro-hardness indenter with a maximum load of 100g to relocate the same region following weathering. The indented pattern could only withstand 2 weeks of exposure in an artificial accelerated weathering (QUV) system. The scan size was used to obtain phase images with the AFM tapping mode to extract surface topography especially the evolution of surface roughness during degradation. Initially, three different scan sizes were employed; 1µm × 1µm, 40µm × 40µm and 200µm × 200µm. Of all three scan sizes, 1µm × 1µm, revealed minimal information about the surface topography. It was unable to show any changes in the surface structure for the small scan range as many artefacts on the surface could be excluded from the measured area. For this reason, it was not used further in the study. Therefore, it must be noted that the selection of an appropriate scan size is vital to get useful and representative information on coating degradation.

Many other studies have used AFM in a similar manner to correlate the surface topography changes to various property changes. For example, using AFM imaging, Gu et al (2009) found that the degradation process is not a homogenous process and that this may be due to the

presence of small degradation susceptible-regions across the surface. This heterogeneous degradation is supported by the formation of large pits over time on the surface of a polymeric coating that appears to occur by the coalescence of smaller pits initially prone to degradation. This change is surface topography was linked to the chemical changes using Fourier Transform Infrared Spectroscopy (FTIR). As the exposure time increased the coating surface changes became severe and the chemical degradation that was monitored using FTIR was also shown to increase. The production of amide groups in the coating was particularly prevalent, which suggests that the photo-oxidation products in the coating cause morphological changes.

2.5.1.2 Chemical force microscopy

Chemical force microscopy is another form of scanning probe microscopy and uses the same equipment as AFM, except the probe is chemically modified. It has been used to measure and image chemical interactions between the tip and a sample surface. It can be a useful experiment to measure the heterogeneity of chemical groups on the surface of a sample. This is done by modifying atomic force microscopy probes to detect a specific functional group. For example, in order to detect hydroxyl groups a bond must form between the chemical group on the probe and the surface.

OH modified AFM probes have been used in order to detect OH groups on the sample surface and enable chemical mapping in the form of a phase image. The phase image is produced due to the chemical interaction between the OH groups on the AFM probe and the OH groups on the sample (figure 2.11) surface. This interaction generates a phase lag resulting in the z-coordinate in phase imaging (Figure 2.12). A stronger interaction results in a larger phase lag so the phase difference describes the tip-sample contact. The tip and sample interaction can also be measure via adhesion and friction forces (Noy et al, 1995, Van der Vegte and Hadziioannou, 1997 and Papastavrou and Akari, 1999).

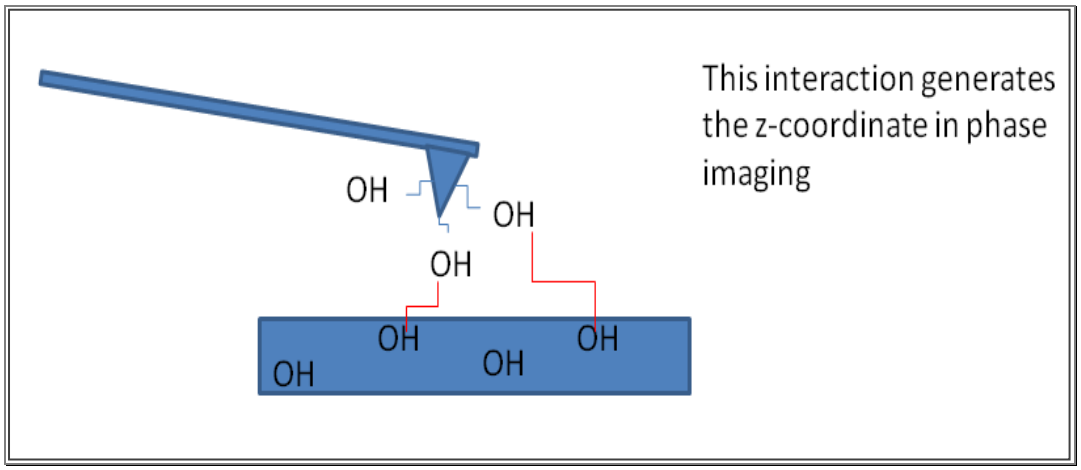

Figure 2.11: The interaction of a chemically modified tip with the surface chemical groups

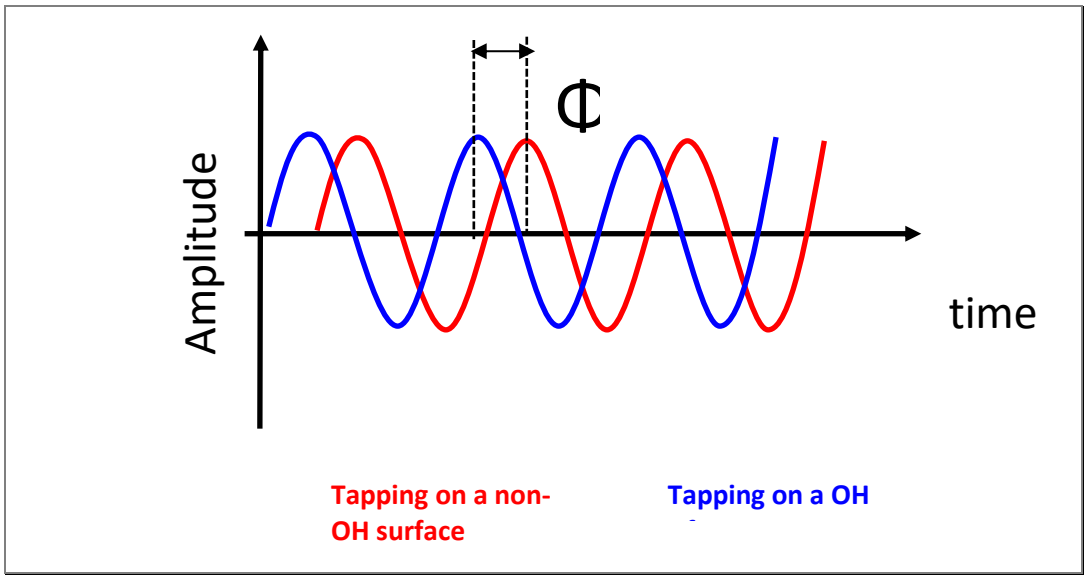

Figure 2.12: The generation of phase lag and delay in signal in CFM

A chemically homogeneous surface will generate a phase image in which most pixels will have the same phase value or friction and so the resultant phase histogram will display a strong adhesion force peak and a greater z-displacement, whereas a chemically heterogeneous surface generates many different phase values. CFM and FIB have been used in this study as a novel experimental combination on coil coatings to spatially map the photo-oxidation by mapping the production of hydroxyl groups. These techniques and their application in this study will be discussed further in chapter 7.

2.5.2 Infrared Spectroscopy

Infrared spectroscopy has long been used in the analysis of organic chemistry to help identify the different functional groups present in a compound. This can help in the determination of the structure of the compound. Transitions between molecular vibrational energy levels of chemical bonds upon excitation by infrared light can be detected and measured using a Fourier Transform Infrared Spectrophotometer. (Raman spectroscopy also relies on the perturbation of chemical entities on irradiation by mid infrared light to enable structural elucidation - details mentioned later). To be classified as an infrared transition i.e. for infrared absorption, the selection rule states that the molecule must have a dipole moment which must change during vibration. The molecule which satisfies this rule is termed 'infrared active' and that which does not is normally 'Raman active' as the ruling does not apply to vibrational spectroscopy using Raman spectroscopy.

A pair of atoms joined by covalent bonds can be thought of as masses on vibrating springs which vibrate at different energies depending on the mass of the atoms and the strength of the bond. A lighter atom will vibrate at a higher frequency compared to a heavier atom and a stronger bond also gives rise to higher frequency in comparison to a weaker bond. When radiation of the right frequency is supplied, the bonded atoms will absorb the energy and vibrate at a significantly enhanced amplitude. Bonds mainly absorb wavelengths of light at the infrared range of the spectrum which generally corresponds to heat. Since different types of bonded atoms absorb at different frequencies they can be easily identified.

An infrared spectrum is normally a plot of the percentage transmittance versus the wavenumber ($1/\lambda \equiv$ cm-1) which is a reciprocal of the wavelength ($\lambda \equiv$ cm). The frequency of the vibrations can be used to determine the wavelength of the absorbed energy and hence the wavenumber.

For example: calculating the wavenumber of a C-C single bond for Infrared spectroscopy.

To calculate the change in energy levels of a molecule, equation 2.3 is used.

$$\Delta E = h\nu \qquad \text{(Eq.2.3)}$$

Where, h = Planck's constant and v= frequency (Hz).

In order to calculate the wavelength of light transmitted equation 2.4 is re-arranged once the frequency is known.

$$\nu = \frac{c}{\lambda}$$

(Eq.2.4)

Where, c = speed of light (3×10^{10}cms^{-1}) and λ = wavelength of light.

To be able to utilise equation 2.4 the frequency must be calculated which can be done using the equation below.

$$\nu = \frac{1}{2\pi}\sqrt{\frac{k}{\mu}}$$

(Eq.2.5)

Where, k= force constant of the bond (Nm^{-1}) and μ = the reduced mass of the molecules (kg).

The reduced mass is calculated using equation 2.6.

$$\mu = \frac{m_1 \times m_2}{(m_1 + m_2)}$$

(Eq.2.6)

Where m_1 = relative atomic mass of molecule 1 / Avogadro's constant, $N_A = 6 \times 10^{23}$ and m_2= relative atomic mass of molecule 2 / Avogadro's constant, $N_A = 6 \times 10^{23}$.

So, since the wavelength the relative atomic mass of carbon is 12, μ can be calculated as follows:

$$\mu = \frac{\frac{12}{N_A} \times \frac{12}{N_A}}{(\frac{12}{N_A} + \frac{12}{N_A})}$$

$$\mu = \frac{144}{{N_A}^2} \times \frac{{N_A}^2}{24N_A}$$

$$\mu = \frac{6}{N_A}$$

Therefore, substituting the actual value of N_A we get;

$$\mu = 1 \times 10^{-23}$$

(Eq.2.7)

Substituting equation 2.7 along with k= 5 × 10^5 Nm^{-1} into equation 3 yields the frequency.

$$\nu = \frac{1}{2\pi}\sqrt{\frac{5 \times 10^5}{1 \times 10^{-23}}}$$

$$\nu = 3.5588 \times 10^{13}$$

(Eq.2.8)

Now, substituting equation 2.8 along with the known value c = 3×$10^{10}$$cms^{-1}$ into equation 2.4 (re-arranged) we are able to calculate the wavelength of the absorbed radiation.

$$\lambda = \frac{3 \times 10^{10}}{3.5588 \times 10^{13}} = 8.43 \times 10^{-4} cm$$

Hence, the wavenumber is:

$$\frac{1}{\lambda} = \frac{1}{8.43 \times 10^{-4}} = 1186\ cm^{-1}$$

(Eq.2.9)

From literature, it can be seen that C-C single bond absorptions occur over a wide range of wavenumbers in the fingerprint region 1600-1000cm^{-1}. The C-C single bond absorbs around 1200cm^{-1} and a double C=C bond absorbs around 1660cm^{-1}. Hence the wavenumber calculated for the C-C single bond is in close agreement to data found in literature and can be deemed valid.

A basic infrared spectrometer consists of an infrared light source (the energy source), a sample holder and a detector along with some external source used for plotting the results. Once all bonds are excited via the energy source the resulting spectrum is Fourier transformed to produce a standard spectrum. Hence the process is known as Fourier Transformed Infrared Spectroscopy (FTIR).

2.5.2.1 Fourier Transformed Infrared Spectroscopy

FTIR is used to analyse products to find their chemical make-up and perhaps the most significant analytical technique to examine degradation in coil coatings. FTIR is a popular method for analysing the chemical changes that take place with degradation as it examines both the coating and depth profiling of coil coatings. Photoacoustic FTIR (PA-FTIR) has been found to be a superior technique for following degradation of opaque (not transmitting materials) such as coatings with a conventional reflectance FTIR technique. This is because the latter relies in good surface physical contact between the germanium crystal and the

sample for good spectral response, whereas the former is a non-contact technique. As samples degrade and their surface roughens, achieving good physical surface contact becomes more difficult and so the quality of the spectral response diminishes.

Zhang et al (2009a) demonstrated the use of step-scan PA-FTIR (SSPA-FTIR) to monitor coil coating degradation at constant depth across the spectrum. The study involved the analysis of two different model coatings to investigate the accuracy of this technique. One of the coatings was a clear polyethylene (PET) laminate on top of a polyester-melamine coating whilst the other was a titanium dioxide pigmented polyvinylidene fluoride (PVdF) top coat. The cross-section thickness was measured using an optical microscope (figure 2.13) to compare the true thickness against the thickness obtained via SSPA-FTIR depth profiling. It was found that an accurate sampling depth was obtained via step-scan PA-FTIR depth profiling for the clear PET coating but depth profiling of the pigmented PVdF coating was slightly less accurate. Zhang et al suggested that the difference in accuracy was due to the inclusion of inorganic pigments in the PVdF coating. This variability is because inorganic pigments tend to have a higher thermal diffusivity compared to polymers and the thermal diffusion depth increases with an increase in thermal diffusivity. Hence, general measures used to calculate the thermal diffusion depth may introduce errors in calculations.

a

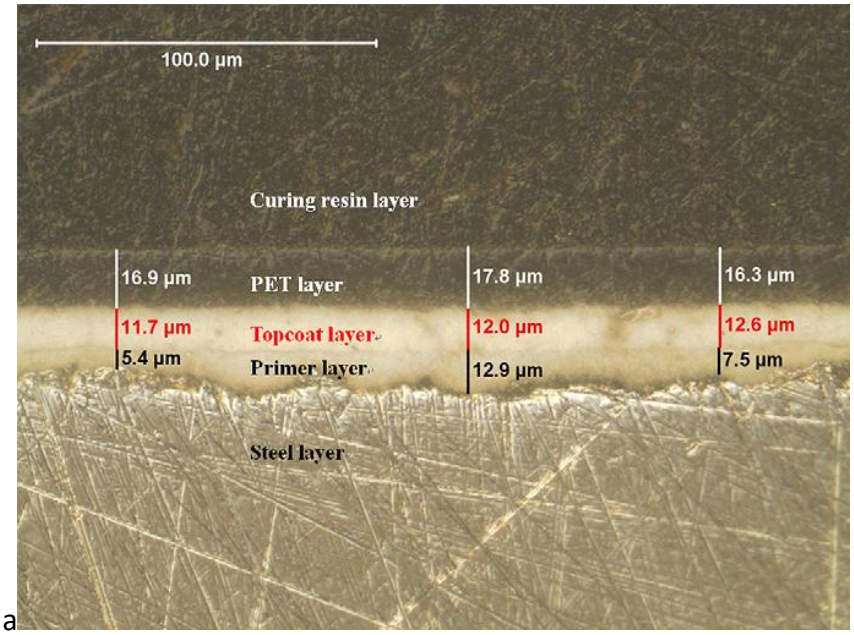

b

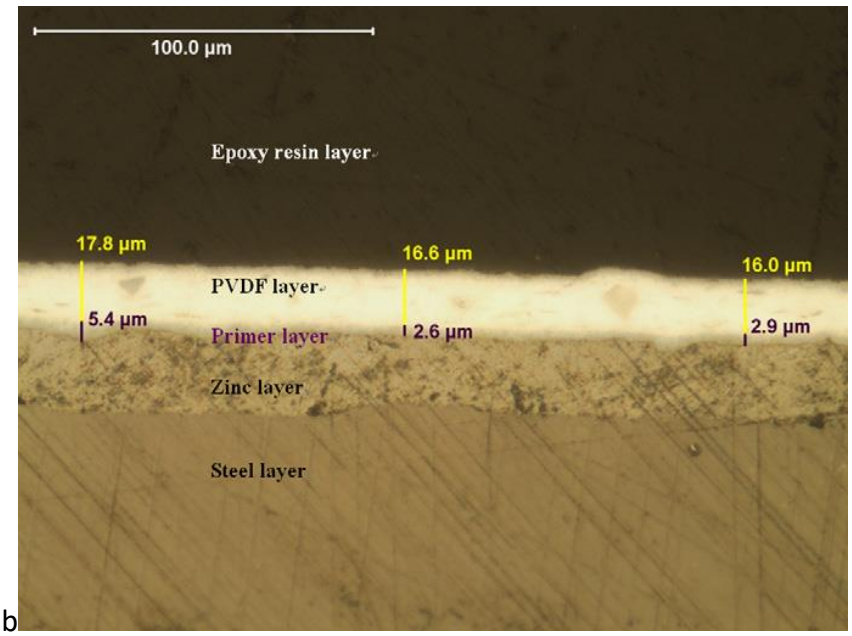

Figure 2.13: cross section images of a) PET sample and b) PVDF sample, Zhang et al (2009, a)

SSPA-FTIR was again used by Zhang et al (2011) and Zhang et al (2012a) to investigate changes in the bulk chemistry of a coil coating with respect to depth. It was found that the surface morphological changes do not always correlate to the bulk chemistry changes hence it is important to analyse both.

2.5.2.2 Infrared and Raman spectroscopy

This idea of depth profiling can be further explored using other techniques such as Confocal Raman microscopy (CRM). Raman spectroscopy is also able to provide useful information about the molecular bonds which help determine the structure of the molecule. However, the Raman selection rule differs from that of the infrared spectroscopy. For a material to be Raman active it must undergo a change in the polarizability on mid infrared absorption and vibration rather than a change in the dipole moment. This change in polarisation can be detected and a peak representing the vibration can be plotted on the Raman spectrum.

Scheepers et al (1995) showed that Raman imaging was a useful technique to study the heterogeneity of melamine within a melamine-formaldehyde cured resin. For analysis of multi-layered coil coatings, it is found that Confocal Raman microscopy (CRM) can provide depth profile information in a similar manner to SSPA-FTIR and it also allows chemical mapping via lateral scanning. A study by Zhang et al (2009b) demonstrates the usefulness of CRM and lateral scanning. Both techniques were applied to clear coil coatings firstly using a dry method with no sample preparation and secondly using oil immersion. It was found that the oil immersion objective yielded better depth resolution in comparison to the dry method, but it contaminated the sample in depth profiling and lateral scanning hence why the dry method is preferred as long as the objective lens chosen meet the profiling requirements for enhanced resolution.

Making use of both FTIR and Raman data requires considerable amount of expertise to interpret the spectrum. It is essential to be able to differentiate between many peaks which may be produced as a result of two separate components in the reactant or a change in products during degradation. Research has been carried out to consolidate data to classify certain functional group vibrations and molecular vibrations for certain compounds and components within the coating formulation, such as; melamine and polyester resins.

In the coil coating industry, melamine is the most commonly used cross-linker. It consists of a triazine ring surrounded by various functional groups. Due to the variation of functional groups on the melamine ring the vibration frequencies differ for each type. Larkin et al (1998) made detailed examinations of three types of popular melamine compounds and made assignments to selected IR active and Raman active vibrations.

Similar assignments were made for many molecular vibrations connected to melamine by Marchewka (2002) using infrared and Raman spectra. Any information regarding the behaviour of HMMM is particularly useful as it is the cross-linker used for this study and

previous works has shown it to behave in an unusual manner. For the cross-linker to work effectively in a film or coating it is essential it is distributed uniformly within the coating and hence across the surface. A recent study (Zhang et al, 2010) showed that melamine tends to co-condense to form melamine rich regions. Confocal Raman microscopy in conjunction with nano-indentation has been used to characterise areas of highly concentrated melamine as shown below in figure 2.14. The Raman intensity map in 2-D and 3-D is shown in figure 2.14 b) and c) respectively in which it can clearly be seen where the melamine enriched zone is.

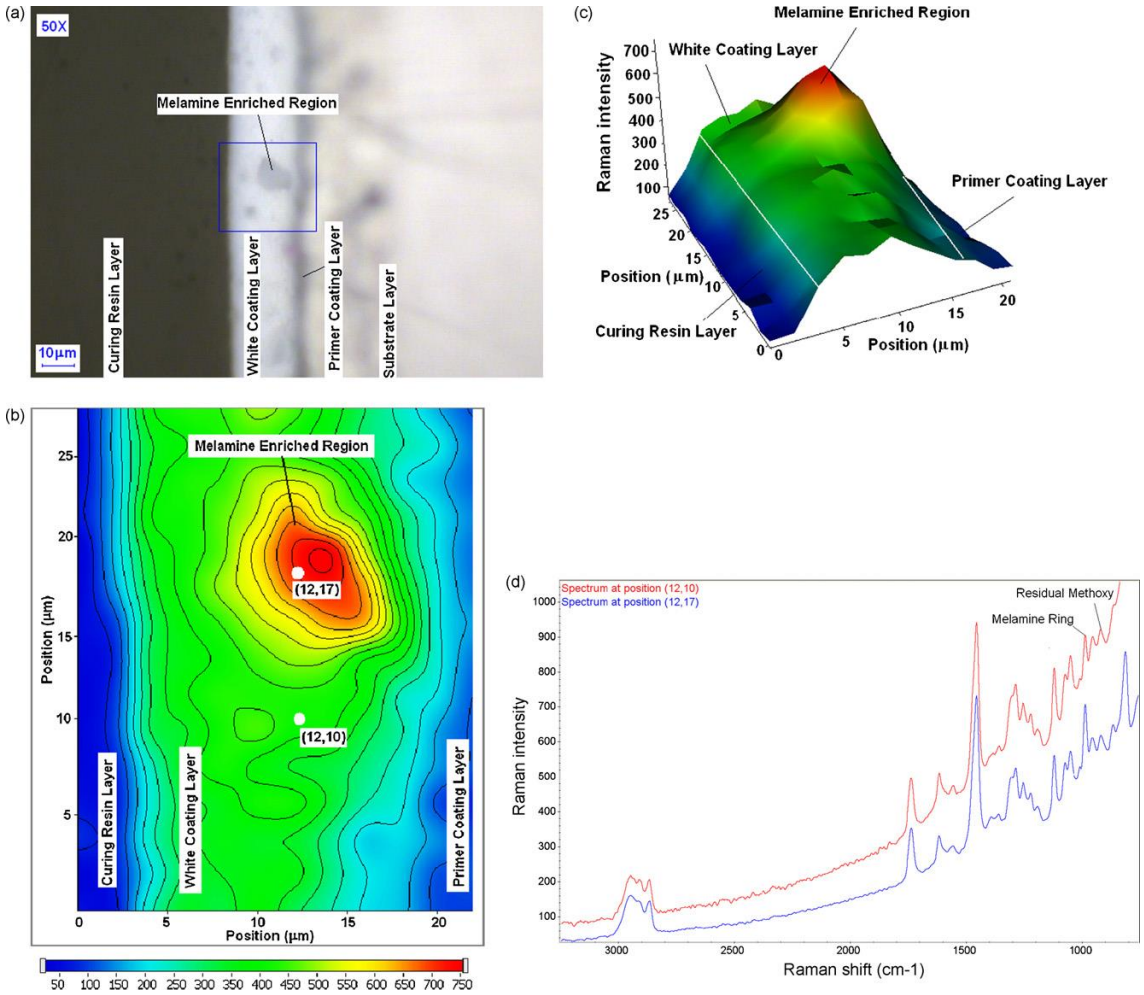

Figure 2.14: cross section examination using CRM by Zhang et al (2010)

Such self-condensation of melamine can be problematic as it gives mechanically varied zones within the coating as was shown via nano-indentation of these zones (Zhang et al, 2010). Specifically, melamine rich zones were shown to have increased hardness relative to non-melamine enriched zones. Having mechanically varied zones within any material makes it

susceptible to failure due to shear forces generated from strain mis-matches between the varied moduli of the separate regions.

2.5.3 Measuring gloss retention

Other means used in industry to measure the weatherability of a coating are gloss loss and colour retention, they are affected by changes in the sample surface topography on exposure (Gerlock et al, 2003). These two parameters are commonly quoted in product warrantees hence it is desirable to know the rate and extent at which changes in these macro properties occur. The gloss loss is measured using a standard gloss 60° meter which measures the gloss as a percentage of light reflected from the surface at an angle of 60° from the normal. Gloss loss is a purely independent measure and is not affected by sample size such as shown by Biggs et al (2001) regarding AFM imaging data. This study indicated a rapid gloss loss within the first week of weathering followed by a more gradual loss thereafter as shown in figure 2.15.

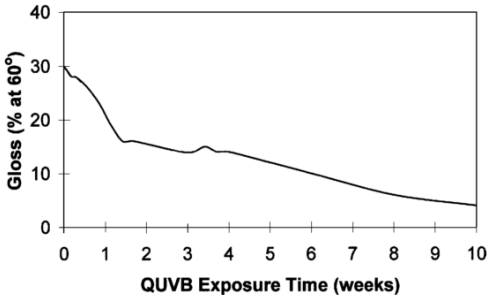

Figure 2.15: gloss loss over QUV-B exposure time, Biggs et al (2001)

It is known that to achieve a range of colours in paint many different pigments are used, some in combination whilst others being the sole providers of the colour we see. In an investigation carried out by Zhang et al (2011), it was found that the type and the concentration of the pigment used in the coating formulation had effects on the surface morphology, surface chemistry and the bulk chemistry not only after weathering but before weathering as well. The coatings in this study were formulated using different pigments (lead chromate, iron oxide and copper phthalocyanine) combined with the most common pigment used, titanium dioxide. They were then exposed in Hainan province, south eastern China for two years. Analysis of the samples before and after the 2-year exposure showed that each pigment gave rise to a different mechanism of degradation.

Faucheu et al (2006), were in agreement in regard to the observation of different degradation mechanisms as they also found that using different pigment grades showed dissimilar characteristics after exposure. Hence it is essential to look at the morphology changes with and without the pigment. This may help differentiate between changes occurring because of main resins or due to the influence of the pigments incorporated.

2.5.4 Scanning electron microscopy

Finally, scanning electron microscopy (SEM) has been further exploited to inspect the surface of a coating at high resolution. It uses an electron beam to raster scan the surface of the sample in a high vacuum chamber and is used excessively in the field of materials science. SEM is particularly useful for research of all types of coatings including coil coatings. Using SEM allows for the physical degradation to be observed. Over time, the physical degradation that takes place can be monitored and then compared to previous images to analyse the changes in the surface topography that manifest over exposure time.

SEM is used to obtain two-dimensional high-resolution images. Imaging using the SEM requires testing to be done under vacuum as the electrons cannot travel through air. Figure 2.16 demonstrates the basic components of a SEM system. The electron gun emits electrons which are accelerated typically by 20kV. The electrons then pass through the condenser lens, followed by the objective lens, scan coils and then an aperture, landing on the specimen. These electrons are emitted by the specimen and detected by the detector producing a signal which is amplified to produce an image.

The detection of the electrons is dependent upon the interaction of electrons with the specimen. A number of signals are generated when high energy electrons interact with the specimen including backscattered electrons, secondary electrons and x-rays. Backscattered electrons are high energy electrons from within the sample because of which they give compositional information in the image. On the other hand, secondary electrons provide topographical information as they do not originate deep within the sample, rather from the near surface of the sample hence are sensitive to the structure of the surface.

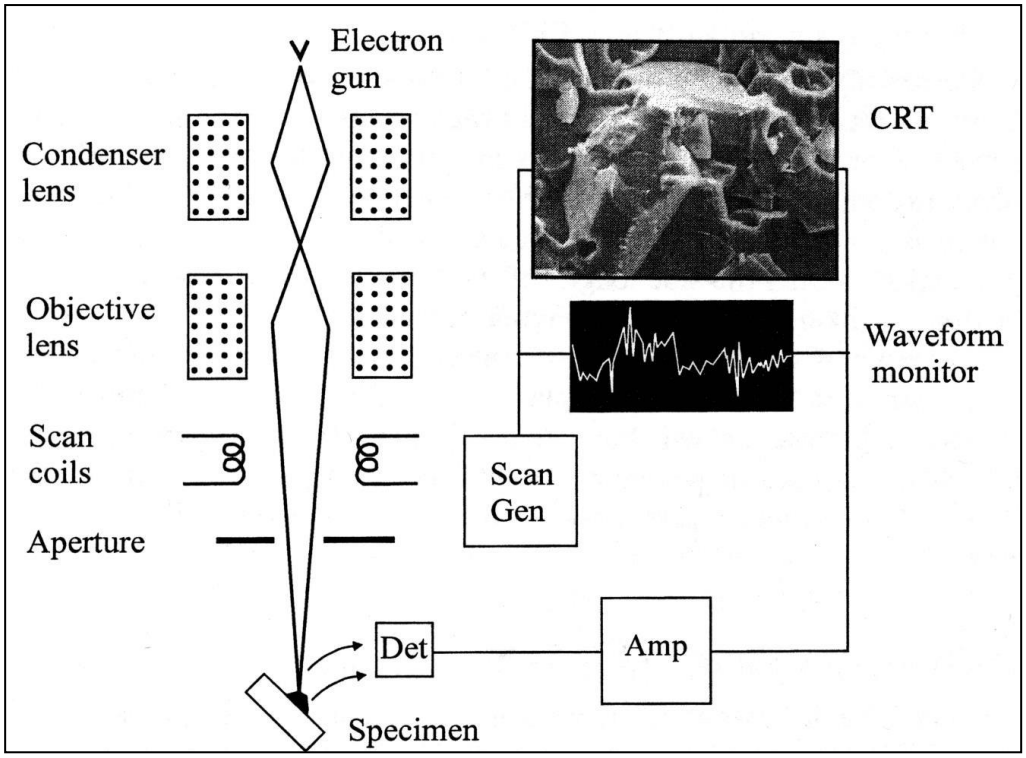

Figure 2.16: Components of the scanning electron microscope (Haris. P, EMLab)

The sample is mounted on the stage using a specimen stub and placed in the chamber. The surface of the sample must always be a specified working distance from the electron beam for it to focus, with FEI machines it is 10mm although each instrument may vary depending on the model.

When collecting SEM images, the resolution of the image is a key factor to be able to investigate and characterise features on a specimen. As mentioned earlier backscattered images are of lower resolution compared to images generated using secondary electrons. The resolution also depends on the accelerating voltage as less spherical aberration is experienced by higher energy electrons as they pass through the lens. (Harris. P, EMLab and Vernon-Parry. K.D, 2000)

Another factor which affects the quality of the images is charging of the surface. This tends to happen when the surface is a poor conductor and therefore it accumulates charge causing the incident electrons to be repelled by the charged areas. This can result in distorted images with the charged areas appearing very bright. During specimen preparation, the specimens are coated in conducting materials such as gold or carbon to avoid this problem.

SEM can find application in all parts of materials science where information regarding the surface is desired. It is conventional, time saving and suitable to image most materials. Some

specimens require no preparation, while others need to be cleaned and coated with a conducting material as stated earlier.

The SEM can also be used in conjunction with Focused Ion Beam (FIB) in a dual-beam system, where compatible. This is beneficial if one needs to remove material and requires high resolution imaging as well.

2.5.5 Focussed ion beam microscopy

The focussed Ion Beam (FIB) microscope has become a very useful tool in fundamental materials science research due to its ability to provide both imaging and micromachining at nanometre and micrometre scale. FIB has the capability for in-situ sectioning, making it an attractive instrument for materials characterisation.

The FIB has a system which is almost identical to the SEM as can be seen in Figure 2.17. The difference is the type of beam each uses. The SEM uses an electron beam whereas the FIB uses an Ion beam. Ions are atoms which have a positive charge due to the loss of an electron in the outermost shell. These charged ions have varied mass and the lightest mass is almost 2000 times that of an electron (Harris. P, EMLab) In a SEM the lighter electrons interact non-destructively with the sample which, produce secondary electrons thus providing a high-quality image when detected. The ion beam mills the surface directly by using the ions (of a higher mass in comparison to the electrons) to dislodge particles from the sample surface. This modification process is called sputtering. The milling is particularly useful as it can remove unwanted material from the sample or produce small components from the sample such as beams or pillars. It has nanometre precision. FIB secondary ion images and secondary electron images can also allow valuable material contrast, particularly useful for studying corrosion or grain boundary oxidation of metals (Phaneuf. M.W, 1999).

Another feature available using the FIB system is chemical vapour deposition, assisted by the ion beam. This enables the deposition of material, again with great level of precision and can be very useful when milling.

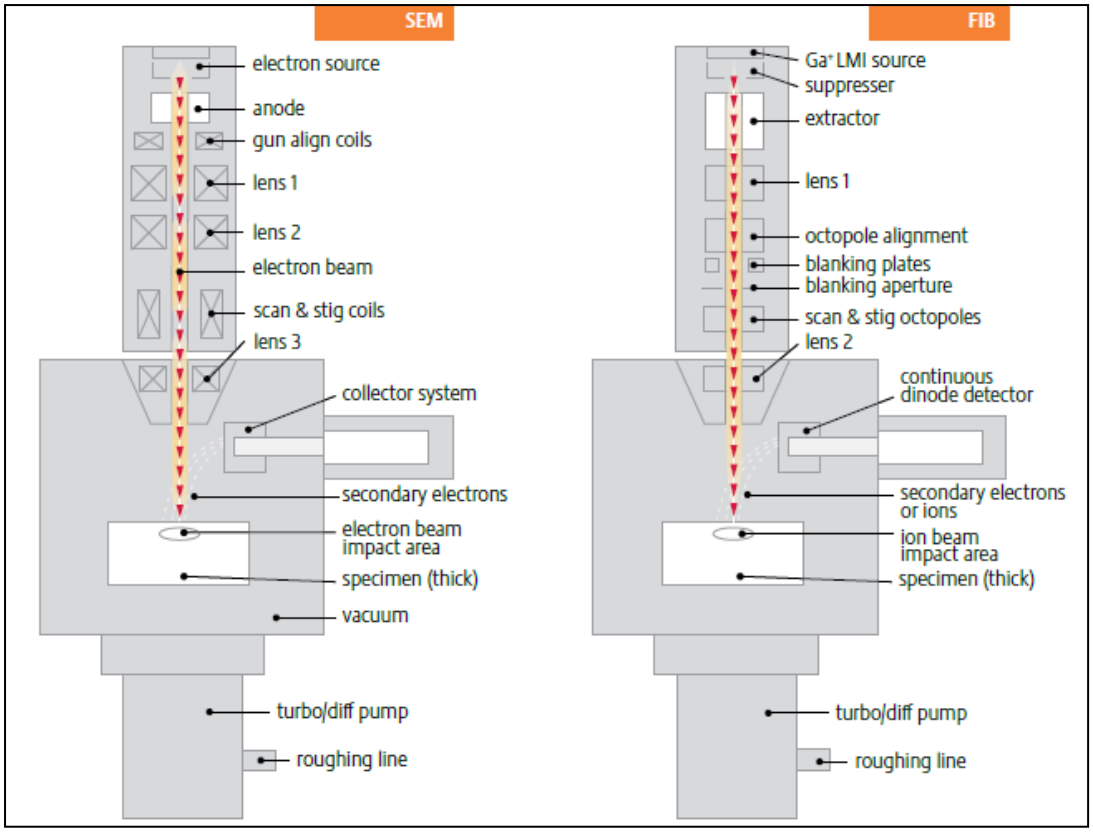

Figure 1.17: The scanning electron microscopy and focused ion beam systems.

The FIB system can be used in conjunction with the SEM system to make a powerful materials characterisation tool. In a dual beam system, the intersection of the two beams at a eucentric point of 52˚ is necessary. A schematic showing the configuration of the dual beam system can be seen in figure 2.18. Once the intersecting beams reach the eucentric point, immediate SEM imaging and FIB milling can be done.

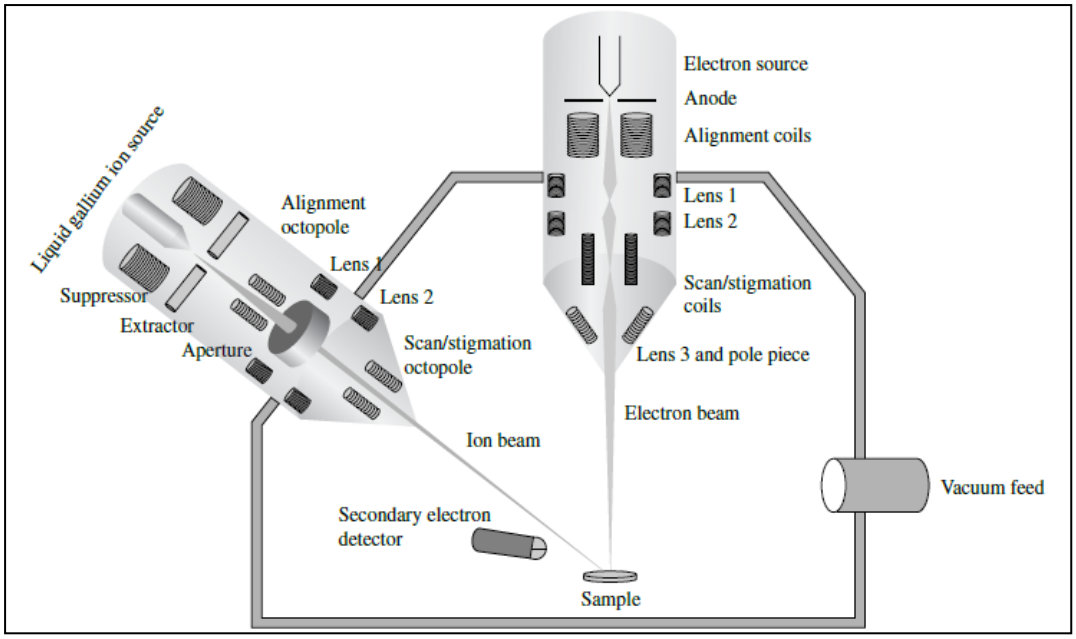

Figure 2.18: A schematic demonstrating the dual beam system involving an electron beam and an ion beam

The FIB column provides a beam of ions to image, analyse and modify a sample. For all three applications, a range of combinations of beam current to spot size is required. For example, for high resolution imaging low currents with a small spot size is preferred whereas if a sample needs to be modified, a range of currents are needed. Low currents will allow precise special control whilst milling and on the other hand high currents will allow one to remove great amount of material at a quicker rate.

A liquid metal ion source (LMIS) is required to provide the ions for the beam. The first LMIS was discovered in 1970s and there are various sources presently used but, Gallium (Ga) is most commonly used (Latif, 2000) due to its ease of use and a great combination of low vapour pressure and large atomic number. An LMIS comprises of a sharp tungsten needle coated with the liquid metal.

The FIB instrument can come with a dual beam system (figure 2.19) which enables imaging via the SEM column and material removal through the ion beam. To carry out the imaging and milling a highly focussed beam is required. Hence, a small effective source size is required to focus firmly which is provided by an equipped field ionisation source. In most FIB systems, the sputtering action of Gallium (Ga) ions is used to enable precise, surface-specific milling of samples. For example, milling into the sample to reveal the internal structure. Gallium being the liquid metal ion source commercially used has many advantages over other metals due to its low melting temperature which makes the source easy to design and operate, low volatility and vapour pressure (Volkert and Minor,2007).

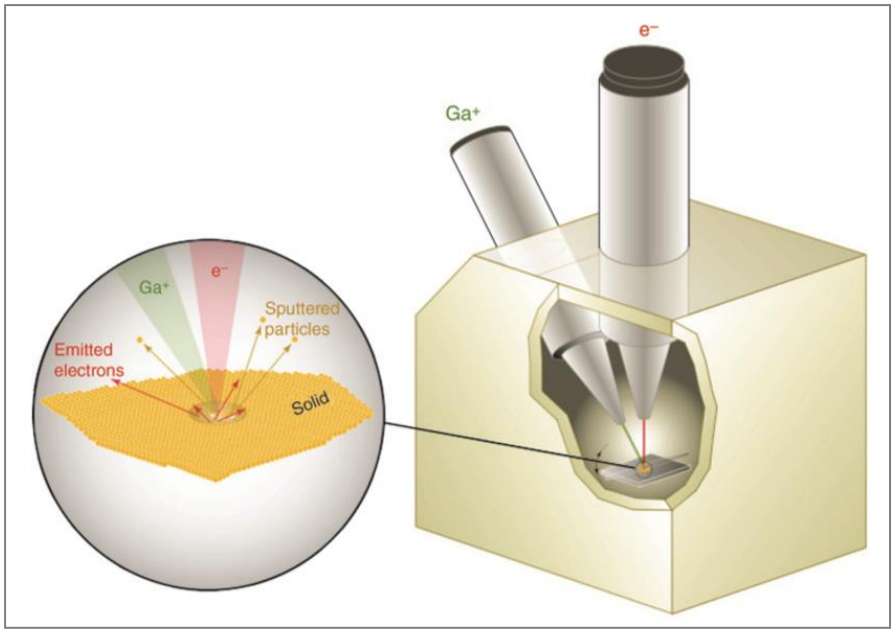

Figure 2.19: An illustration of the dual beam in a FIB-SEM system.

To carry out the milling the sample is mounted to the stage. A conductive coating is not always required as with SEM, however, when using a dual beam system, a conductive coating is used to image using SEM while milling using the focused ion beam. The stage not only has three-axis translation, but it also has tilt and rotation settings. These facilities enable it to have a eucentric point at where the two beams intersect. FIB is sample-dependant as the ultimate spatial resolution is limited by sputtering of the sample, and each sample behaves differently. In order to carry out the milling of the sample one must know how the sample reacts to the various factors as the ion beam can cause significant damage. This is due to the build-up of ions causing an overlap in disordered cascade regions forming a damaged layer on the surface. Depending on the sample, the ion damage can take the form of surface amorphization, creation of point defects, dislocation formation amongst others (Volkert and Minor,2007). The damage can be detrimental and in polymer composites, the damage is due to the polymer matrix characteristics. Among these adverse effects is heating damage, material redeposition and the curtain effect (Olea-Mejia et al, 2012).

When milling a sample for cross sectional analysis, the desired flat surface is not always achieved and instead lines appear on the milled surface or an irregular surface is created. This is known as the curtaining effect (Gianuzzi. A.L, 2004). See Fig 2.20.

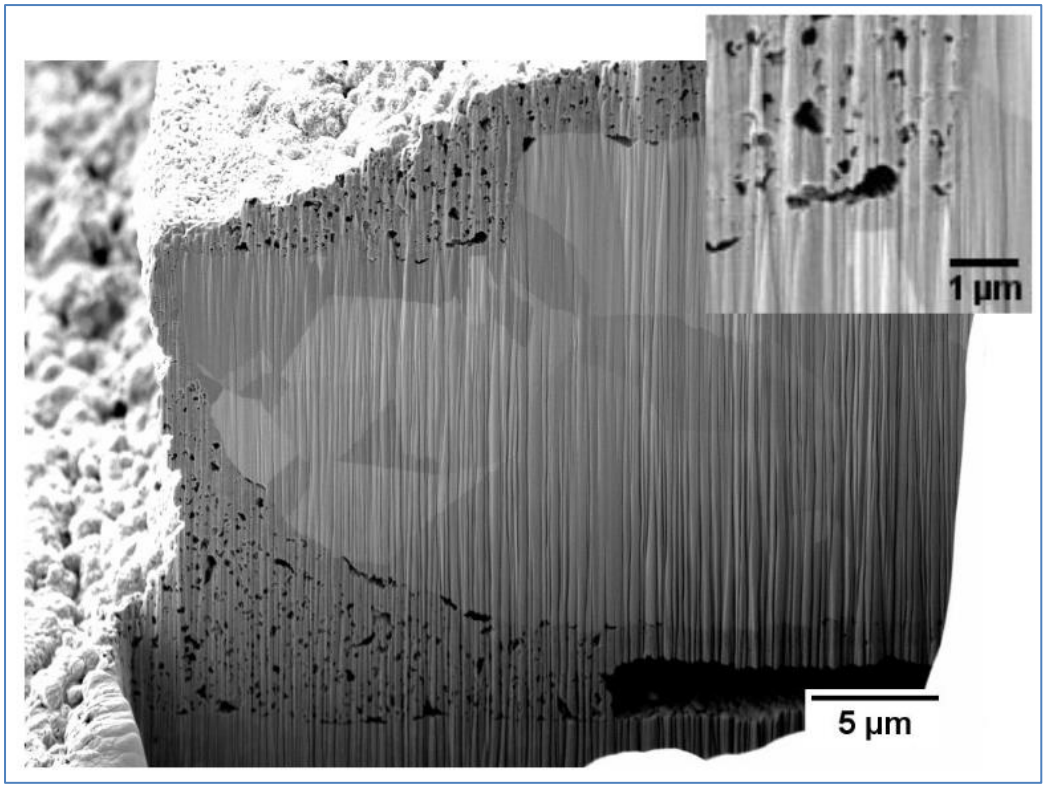

Fig 2.20: Porous ceramic on Ni: strong curtaining due to rough surface (Reuteler. J, 2016)

When a sample has uneven surface topography, a heterogeneous chemical structure, a surface composed of hard and soft materials or a porous surface, the ion dose and milling speed of the ions at the surface is modulated, hence, affecting the shape and roughness of the final milled face, leading to the curtain effect.

The preferred settings used for polymers and various other soft samples is the use of low current to avoid heat damage and depositing a layer of platinum to stay clear of the curtain effect.

3. Materials and methods

Chapter 2 outlined the background of this study. Following on from that; this chapter is dedicated to highlighting the materials used in this study including the sample preparation and the various techniques used along with the exact operating procedures utilised.

The resin is a vital component in the makeup of any coil coating, forming the backbone of the chemical structure. The resin is chosen according to the properties required for the specified performance as the resin may not behave in a similar manner in different environments. Natural weathering is the main cause of degradation in the coatings causing polymeric chain scission, photo-oxidation and hydrolysis which inevitably defines the lifetime of the coating. Therefore, it is imperative to study the effect the polyester chemical structure may have on the stability of the polyester-melamine coating being studied in this research.

In this research, three types of polyester resins were utilized. NS01, a standard petroleum sourced polyester resin was used, NS02, a resin obtained fully from bio-sources and NS03, where the polyester was partially bio-sourced. Bio-sourced products are products made from biological materials as oppose to their petroleum counterparts. Hence, the monomers which makeup the polyesters differ, although the crosslinker (melamine) and majority of additional components were the same. It is therefore not unexpected that each coating will possess different grades of resistance to the conditions the coating is subjected to. The summary of the chemical make-up is given in the table below. However, due to confidentiality purposes the exact formulation cannot be stated.

Table 4: A summary of the chemical make-up of each sample

Samples	Polyester Resin	Crosslinker	Pigment
NS01 clear	Petroleum based di-acids(aromatics and aliphatics) and diols	HMMM	None
NS02 clear	Fully bio-based di-acids (aliphatics and cycloaliphatics) and diols	HMMM	None
NS03 clear	di-acids (petroleum based aromatics and bio-based aliphatics) and fully bio-based diols	HMMM	None
NS01 white	Petroleum based di-acids(aromatics and aliphatics) and diols	HMMM	Coated rutile TiO_2
NS02 white	Fully bio-based di-acids (aliphatics and cycloaliphatics) and diols	HMMM	Coated rutile TiO_2
NS03 white	di-acids (petroleum based aromatics and bio-based aliphatics) and fully bio-based diols	HMMM	Coated rutile TiO_2

3.1 Sample preparation

Coil coatings typically are produced on a large scale. However, in order to carry out pilot studies on the performance of coatings after weathering, small scale productions is utilised out on the premises of Beckers Ltd, Liverpool, UK. In their laboratory the coil coating procedure is replicated. A fresh batch of paint was made for all three formulations. For confidentiality reasons the exact formulation cannot be listed. Each component used in the formulation was accurately weighed and the mixing time was carefully monitored to ensure all components were added at their prescribed time, as with any form of mixing, elements are added in stages per their use. Once the paint was made it applied to pre-treated galvanised steel substrates which were cut into panels. The application procedure is outlined below.

The 0.5mm galvanised steel panels were pre-treated with zinc. To remove any moisture retained through the pre-treatment, panels are heated for approximately 15 seconds in a preheated industrial oven at 275˚C. Then using a spiral wire drawdown applicator, a bar with 0.028 inch diameter was used to apply the paint to the coating. The aim was to deposit films

with a thickness between 18-20µm on the panels. The coated panels were then placed in another industrial oven which was preheated at peak metal temperature, approximately 232-241˚C. Samples were cured in the oven for 30 seconds, immediately removed and quenched in cold water and then pressure dried.

After preparing the panels the thickness of the coating was measured using an industrial thickness gauge. Prior to coating the panels, the initial thickness of the pre-treated steel panel is measured and subtracted from the final thickness to calculate the coating thickness. The gloss is also measured at this stage.

3.2 Weathering tests

2 types of weathering test were carried out which include the following conditions:

1) **QUV A accelerated weathering**. This is also termed the artificial weathering method as it is carried out in the laboratory at Beckers Ltd, Liverpool. The panels were placed in the accelerated weathering chambers and the tests commenced. The testing period was approximately 3000 hours. During the testing period the samples were exposed to alternating UV and condensation cycles to replicate the natural moisture induced weathering. When the UV cycle was in use the chamber temperature was maintained at 60˚C and the samples were exposed to UV-340 irradiance of 0.87 W/m² using fluorescent lamps for 8 hours. Then the sample is subjected to a dark condensation cycle at 50˚C. As said earlier the cycles are alternated for the duration of the tests. This method of carrying out artificial weathering of materials is an industry standard for coil coatings.
2) **Natural weathering test**. This type of test is carried out on an outdoor exposure site relevant to the research. In this case the exposure site was in Florida. The sample panels were placed 45˚ facing south for 2years.

During the testing period, at set intervals, the panels were removed and coupons 7mm in diameter were punched out using a special metal puncher. The idea was to get a close look at what happens in the initial hours/months of exposure, so the intervals in the first year were very close. For the QUVA samples the hours were monitored and for the Florida exposed samples coupons were punched every 2months in the first year and then every 6months for the second year.

3.3 Characterisation techniques

3.3.1 Gloss retention

The gloss retention refers to the coatings ability to retain a certain level of gloss as it is a vital property for the aesthetics of the coating. The gloss is measured by a gloss meter which initially is used to configure the required finish on the paint and used for quality control. It is one of the physical properties measured before and after exposure, hence a few gloss readings are taken per sample to gain an average measurement. The gloss meter works by shining light at a specified angle onto the surface of the paint and then measures the reflective light in gloss units. The gloss retention is measured as a ratio of the gloss of the exposed sample over the gloss of the unexposed sample. The resultant ratio is expressed as a percentage from which we can determine the amount of gloss loss taken place over a specific exposure period.

3.3.2 Atomic Force Microscopy

When considering AFM as an experimental technique for this study the advantages and disadvantages were carefully considered. AFM is a useful analysis tool to attain information about the surface topography which would limit the damage to the surface if used in tapping mode. As the analysis was predominantly on the surface of the coating the steepness of the sample was not a concern. To ensure mechanical damage to the surface would not affect any chemical analysis of the coatings, FTIR was carried out first.

Table 5: Advantages and disadvantages of using AFM

Advantages	Disadvantages
• 3D imaging • High resolution imaging • No sample prep involved (which may change or damage sample/surface) • Operates in air / liquid – possible to image biological macromolecules/ organisms • Non-contact and tapping mode available	• Single scan image size • Scanning speed is slow • Possibility of image artefacts • Scanning limitation over steep areas on sample. • Can scratch surface in contact mode

AFM was carried out using the NT-MDT NTEGRA-Spectra shown in figure 3.1. The phase images were generated in the semi-contact mode. The probes used were Silicon AFM cantilever probes bought from Bruker with a spring constant of 42 N/m. On the back side of the probe was an aluminium reflective coating to improve the laser signal. The data was collected and analysed using NOVA software.

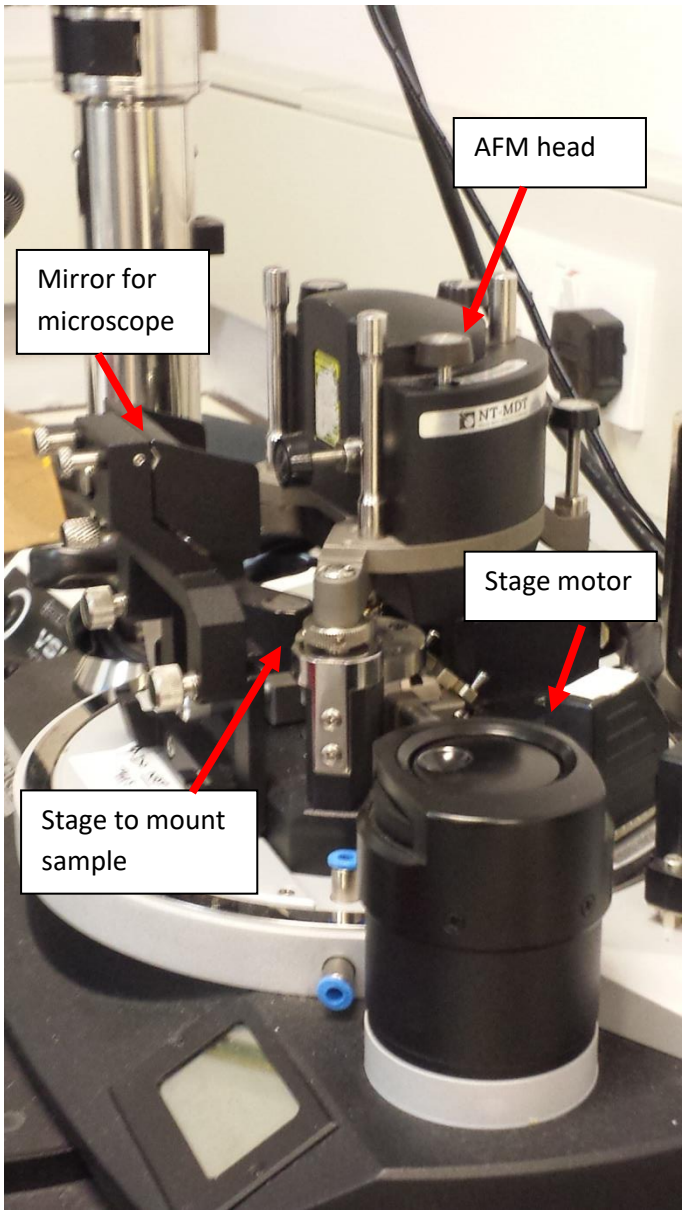

Figure 3.1: NT-MDT NTEGRA-SPECTRA, the atomic force microscopy equipment

Figure 3.2 shows how the sample is mounted and where the probe sits to scan the sample.

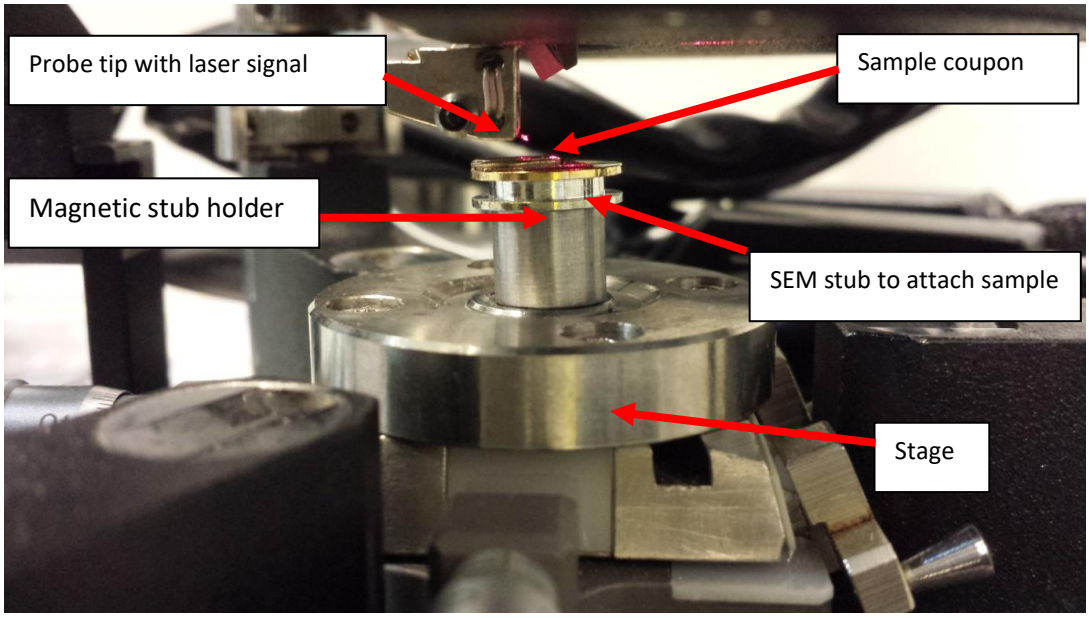

Figure 3.2: Mounting sample on AFM stage

The sample was mounted to a stub using carbon tape to minimise movement of the sample during measurements. The stub was then placed into a magnetised sample holder made at the Queen Mary University of London workshop. The stub holder then magnetically attaches to the AFM stage.

A cause for concern in using AFM on the coatings is the representation of the data. How can we avoid over-generalising the data obtained, yet know that conclusions drawn from this research are applicable to the real-life scenarios? To resolve this problem a few methods were considered. First and foremost, the data must be statistically valid hence, repeatable measurements are a must. Each technique will be repeated on every sample for a minimum number of five times. Once the extent of reproducibility of the data has been established and a method confirmed that minimises variability, the next focus will be to ensure that the optimum sampling size is determined, especially for AFM imaging. This is because, when using AFM to image a sample there are size limitations and the entire sample cannot be imaged at once. Analysing the surface at the micrometre level means locating the same area to sample each time is extremely difficult. To ensure the validity of the sampling method some correlation work was carried out. For each sample, the sampling data consisted of a

batch size of 5 (each large square), each with a sampling size of 5 (small squares measuring 10µm × 10µm) as can be seen in figure 3.3.

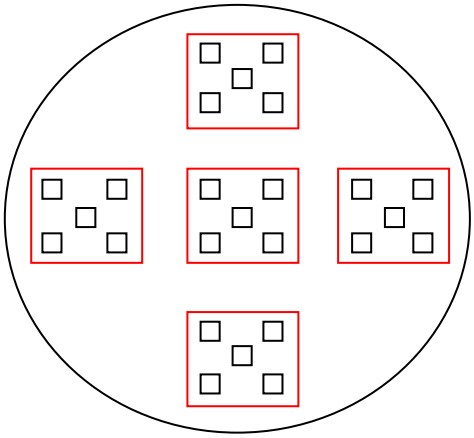

Figure 3.3: AFM sampling technique

After using the above method, it was found that the size of the imaging frame is important and having a frame which is too big or too small can neglect vital topography related information. A very small frame such as the 10µm × 10µm, may only image a small raised section of the surface and provide misleading information regarding the topography. On the other hand, if the imaging frame is rather big, for example 100µm × 100µm, the pickup of a small defect will be hidden in the majority topography data, again providing misleading results. After much trial and error, it was concluded that the sampling size would be 60µm × 60µm, and 5 areas will be tested per sample, in a systematic order in order to cover different areas of the sample (shown as red squares on the figure above).

3.3.3 Photo-acoustic FTIR

The advantages and disadvantages of using Fourier Transform Infrared spectroscopy have been listed in table 3. The coatings on metal substrate meant traditional FTIR could not be used as the samples were opaque. Hence, photo-acoustic FTIR was adopted to carry out chemical analysis on the samples.

Table 6: Advantages and disadvantages of using PA-FTIR

Advantages	Disadvantages
• High quality spectrum • Quick analysis • Accessories available for PA-FTIR . • Gas, solids and liquids can be analysed • No external calibration required and gives accurate results • Non-destructive technique	• Not suitable of opaque samples therefore require PA-FTIR • Small sample size required for PA-FTIR

PA-FTIR was done using a Bruker Tensor 27 instrument with a photo-acoustic cell, an accessory provided with the machine. The chamber was cooled with liquid nitrogen prior to testing hence helium was not required as with most FTIR machines. Sampling using any form of FTIR requires collecting of background noise. The background is collected to eliminate the noise in the spectrum which arises from the water and CO_2 in the air in the chamber by subtracting it from the sample spectra. To take a background measurement carbon black is placed in the chamber and a measurement is taken. Immediately after the carbon black is replaced and the chamber was closed. The following settings were used each time with a fresh background per sample.

- Resolution frequency: $4cm^{-1}$
- Sample scan number: 32 scans
- Background scan number: 32 scans
- Scanner velocity: 2.2kHz
- Range: $4000 – 400cm^{-1}$

The data was collected and analysed using the provided OPUS data analysis software.

3.3.4 Scanning electron microscopy

SEM was a vital experimental technique to investigate the surface changes taking place on samples degraded over time as well as using it in conjunction with FIB. However, the coatings were not conductive, and the sample needs to be conductive for imaging. This can be easily resolved if the sample is coated with a conductive material such as gold. The problem associated with coating the sample was that the conductive layer on top of the coating will

hinder other analysis methods. To overcome this issue, SEM was the last experimental technique used on the samples.

Table 7: Advantages and disadvantages of using SEM

Advantages	Disadvantages
• Suitable for most materials • Sample size is variable • High resolution imaging • Quick imaging • No sample damage	• Sample must be conductive • Otherwise need to coat with conductive materials • Requires vacuum environment • Delay in experiments if analysing the surface • Need to ensure tests are complete on surface (e.g. FTIR, AFM, CFM) or have extra samples

To observe the surface, a high-resolution microscope is required. The SEM used in this study is a FEI instrument. The details of how an SEM works can be found in chapter 2. In preparation of imaging, the samples are mounted on a specimen stub. The samples need to be coated with gold coating as they need to be electrically conductive. Once the samples are coated they are placed in the SEM chamber, ready to be raster scanned using the electron beam.

The settings used to image are listed below:

- Aperture: 30µm
- Current: 93PA
- Spot size: 5.0
- Voltage: 10kV
- Scan rate: 3µs

3.3.5 Focused Ion Beam microscopy

The advantages and disadvantages of using FIB microscopy have been detailed in table 5 and are further discussed in chapter 7. The main advantage of using FIB for my research was that it was one of the least destructive techniques to cross section and depth profile the coatings. Other mechanical methods to cross section the sample for example, cutting it with an instrument would require further polishing to get rid of any artefacts or smearing of the coating layers during the process. FIB however could alter the surface morphology due to

implantation of ions used to remove the excess material. This can be overcome by either using platinum to protect the area of interest or by altering the parameters used to remove the material. After careful research and trial and error the latter approach was adopted.

Table 8: Advantages and disadvantages of using FIB

Advantages	Disadvantages
• Ability to mill or cross section small samples • Fast and high quality imaging as dual beam with electron beam • Good grain contrast • Can use platinum to avoid Ga ions imbedding into sample during sputtering	• Sample preparation • Drifting • Vacuum • Residual Gallium ions • Imaging process may spoil subsequent analysis • Ion beam damage – lowered resolution • Slow milling process

FIB was implemented using another instrument by FEI to obtain areas with known depth to carry out depth profiling of the coating. This FIB instrument is dual beam with an electron beam and an ion beam. Similar to the SEM the samples need to be coated with a conductive material and in this case, they were coated with gold. The samples were placed on a sample holder which had a pre-tilted angle of 45˚. The FIB can be very damaging to the sample if the right settings are not used with soft samples such as polymers. With polymers it is ideal to use low currents especially when carrying out fine milling. An initial cut was made using a rectangular pattern approximately 120µm in length and 15µm in depth into the sample in order to get a uniform plane to mill the step-like (referred to as steps in this research) pattern for depth profiling with the voltage at 30kV and the current at 15nA. This was the ideal current to use as a relatively large amount of material was removed. After the initial cut was carried out the cut was refined using repetitive milling at smaller currents. This was done to obtain a uniform surface. Following this, three square patterns, each square measuring 30µm ×30µm with a difference of 3µm in depth were milled in parallel to obtain the 'steps' as shown in the figure below. The steps were milled using a current of 3nA (greater detail of how this technique was developed to carry out the required depth profiling is in chapter 7).

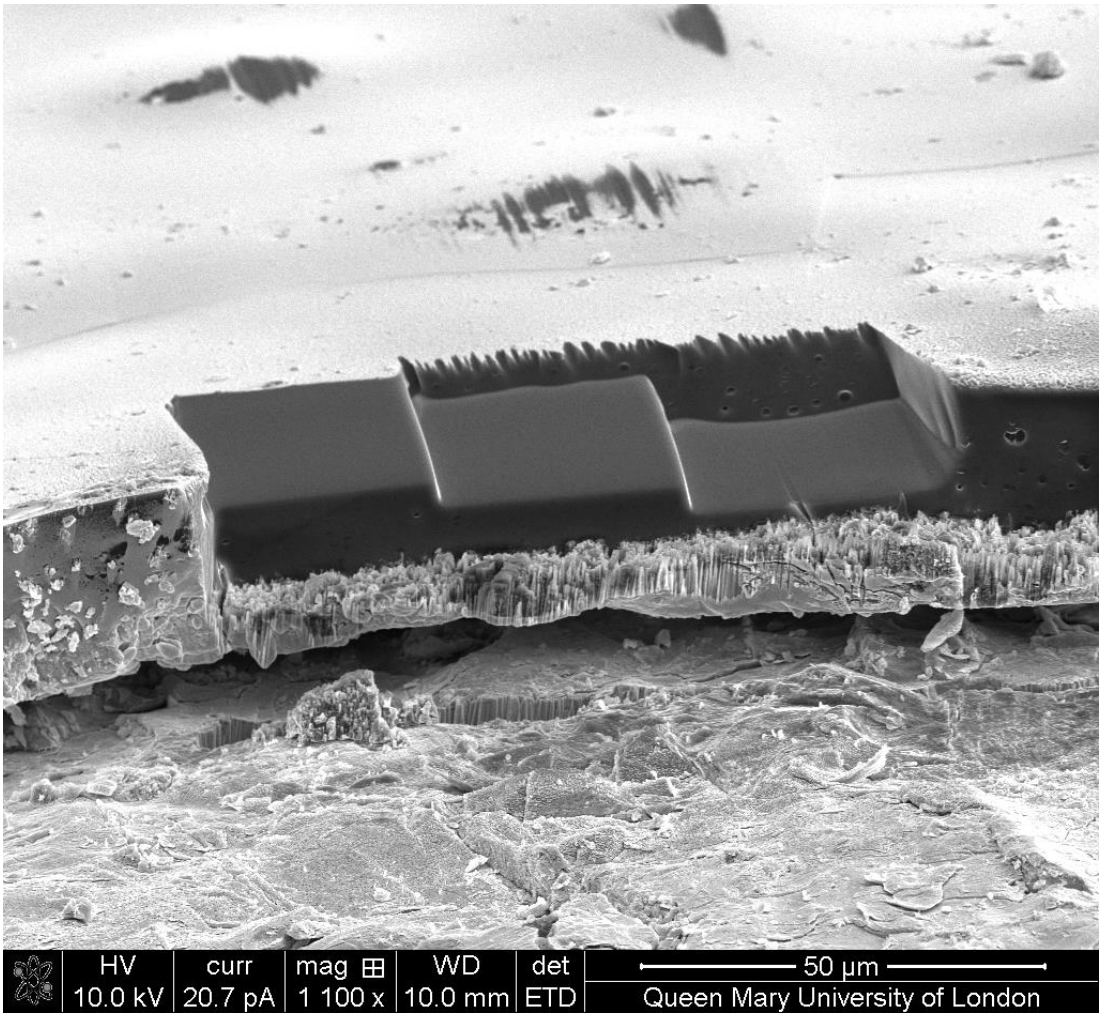

Figure 3.4: SEM image of steps milled in a polymer coating

3.3.6 Chemical force microscopy

Chemical force microscopy used in conjunction with FIB is a novel technique used to quantifying degradation in organic coatings. The disadvantages associated with CFM are mostly related to the technique being time or cost effective, see table 6. With the correct sample preparation and functionalised tips, it was a promising technique for depth profiling the coatings. The set-up of the experiment and the parameters used follow.

Table 9: Advantages and disadvantages of using CFM

Advantages	Disadvantages
• Able to determine chemical nature of surface • Chemical mapping • Differentiate between areas with particular chemical group • Can be used in conjunction with AFM to map chemical and mechanical changes	• Special functionalised probes required • Probes are expensive • Slow scanning • Sample must be free from impurities • Requires liquid medium e.g. hexadecane

CFM was also carried out on the NT-MDT NTEGRA-Spectra. The only difference being the probe used and the use of a liquid cell. The need for a liquid medium for CFM was found after extensive research (please refer to chapter 7). The liquid cell is pictured in the image below. The sample was placed under the supporting clips. The clips are present on the liquid cell to avoid floating of a sample. Once the sample was secured, a syringe was used to extract hexadecane and to fill the liquid cell. There is no specific measurement of the liquid required. The liquid cell was filled until a meniscus forms. This will ensure there is enough liquid to immerse the CFM crystal holding the probe. Once the liquid cell was filled it was placed on the sample holder as shown in figure 3.6.

The probes used for CFM were from Windsor Scientific. They are silicon nitride cantilevers with a 35 nm chromium / gold coating on the detector side. This is to ensure good reflective laser signal. The triangular cantilevers were equipped with two functionalised tips per side, in this case OH-modified probes. The tip used in this research was 100µm in length with a width of 13.5µm and a thickness of 0.6µm.. The force constant of the probe was 0.32N/m with an operating resonance frequency between 55-67kHz. The data was collected and analysed using NOVA software.

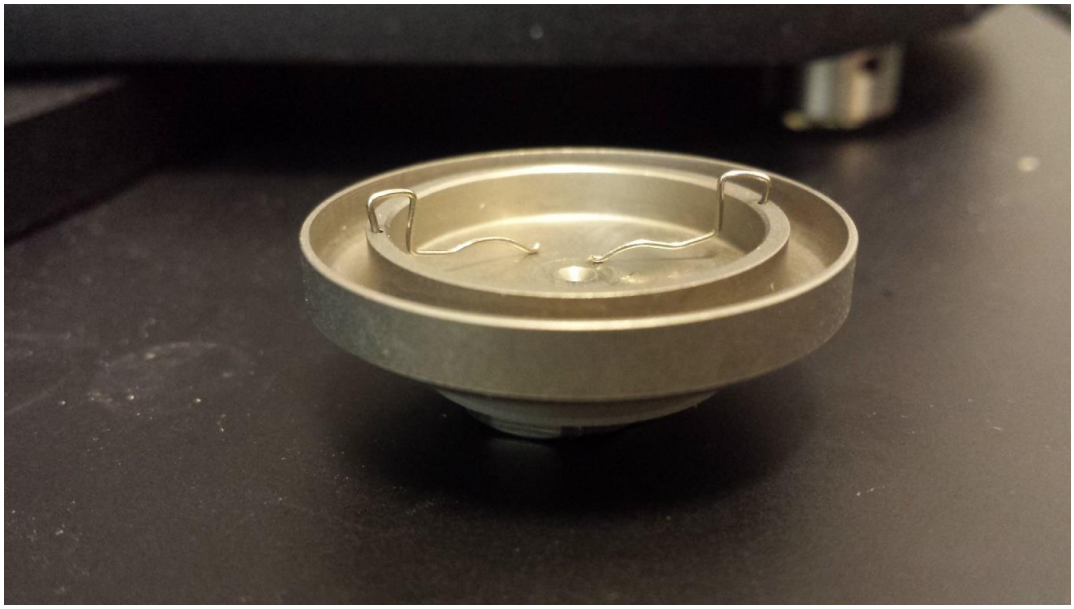

Figure 3.5: Fluid cell used in chemical force microscopy

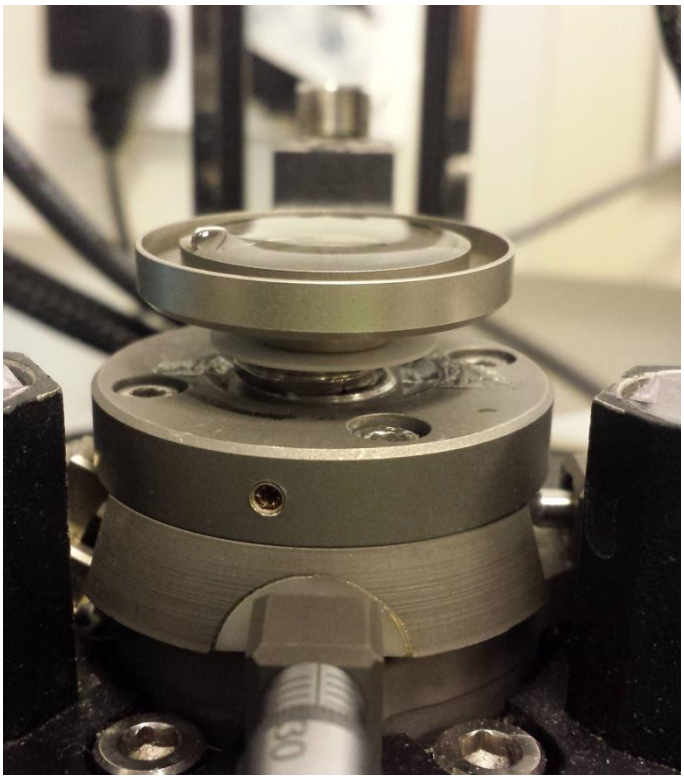

Figure 3.6: A set-up of the filled fluid cell on the AFM stage

4. Results from artificial weathering of NS01 and NS03 coatings using a QUVA machine

Artificial testing is used extensively in the coating industry to replicate the effects of natural weathering. This accelerates the process to transform a coating formulation into a final product which is ready to be used for various applications. Natural weathering can take many years to cause the coating to fail; this obviously is a desired prerequisite before selling the product. However, it is not feasible to wait so long to carry out the relevant analysis to improve or supply new products. Hence, the coatings are prepared as described in chapter 3 on to panels and the samples are weathered using an artificial weathering machine to replicate the natural weathering along with naturally weathering it in a location suitable for its end use. A detailed investigation is required to determine the lifetime of a coating and the causes of failure. The investigation begins with artificially weathered samples to be compared to the naturally weathered samples at a later stage. This has been a standard way of testing coatings for durability and causes of failure in the coil coating industry.

It will be seen in this chapter how the artificially weathered coatings perform in their lifetime. Various techniques have been utilised to explore the reason for failure starts and the manner in which it propagates. Much research has been carried out to characterise the failure of a coating, however it is not common practice to focus on the initial stages of failure to get a greater understanding of the relationship between the various mechanisms which cause the different modes of failure. This chapter will focus on these points before moving on to compare the results of the naturally weathered samples in the following chapter.

4.1 Investigating gloss retention

One of the first tests carried out to test the coating durability is measuring the amount of gloss loss or the ability of the coating to retain gloss. As can be seen in figure 4.1(a) NS01 being the control sample has a steady reduction in the amount of gloss retained. NS02 deteriorates rapidly demonstrating that the formulation is not fit to be used as a coating. NS03 on the other hand has surpassed the standard up until approximately 1200 hours after which there is a steep decline. The performance of NS03 clear in the initial hours makes it a competitor for NS01 clear if the formulation can be improved to increase the gloss retention.

a)

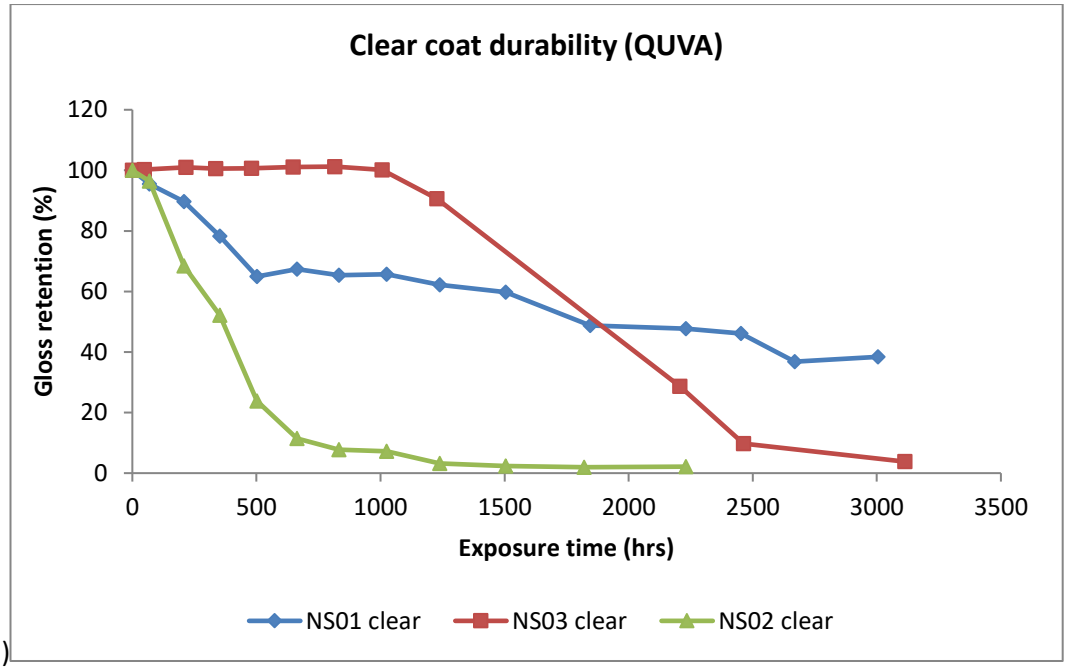

b)

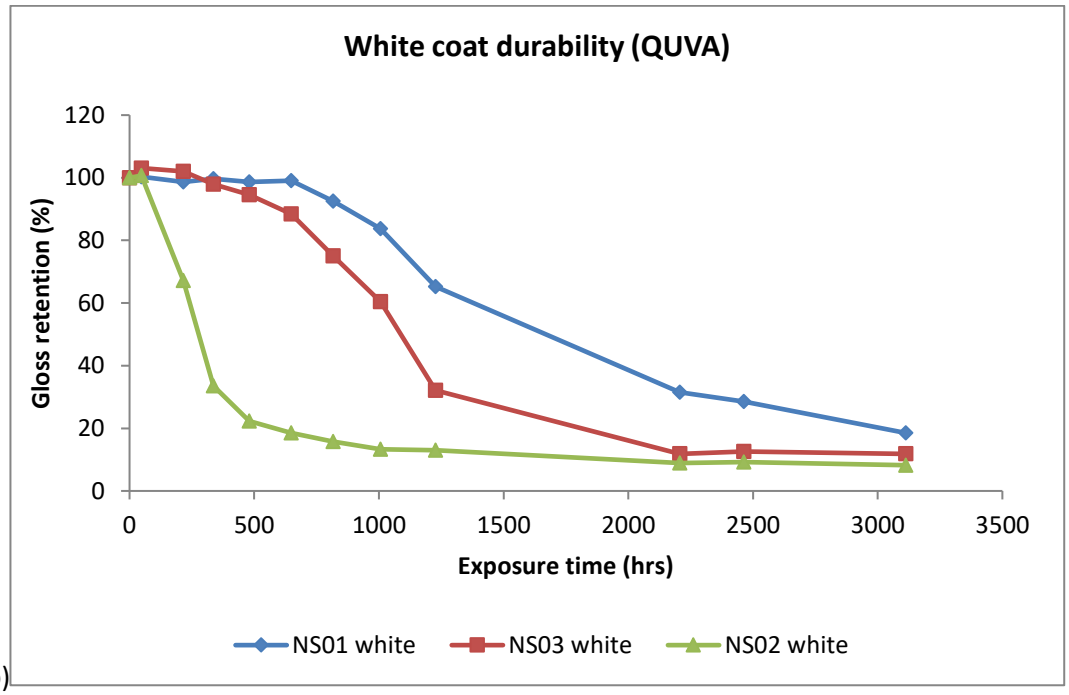

Figure 4.1: a) Gloss retention of clear coatings b) Gloss retention of white coatings

The clear coatings are coatings without any pigment and the white coatings have organic pigment, which is titanium dioxide in this case. Figure 4.1(b) shows that upon the addition of the pigment NS01 white retains gloss better than NS02 and NS03 white. NS02 white again deteriorates rapidly within 500 hours of exposure. Adding titanium dioxide to a coating formula normally stabilises the coating resulting in an extended lifetime of the coating. This

is because the titanium dioxide is able to absorb the wavelength of light in return shielding the bonds sensitive to the light in the binder (Gesenhues. U, 2000).

NS03 white shows a steadier reduction in gloss similar to that of NS01 white. This confirms that upon the addition of pigment, the formula has been stabilised. It is important to note that the coatings are not used as clear coatings in the industry but, the need for analysing clear coatings is equally significant to recognise the strengths and flaws of a certain formulations. It is vital to see how the coating functions without the addition of substances which will help improve its performance and perhaps mask the true performance.

After looking at the performance of the NS02 coatings in both clear and white it was deemed appropriate to only focus on NS01 and NS03 formulations. The NS02 coating could not withstand the weathering for a short amount of exposure, while the intention is to produce a coating formulation to last approximately 40 years. The formulation of a solely bio-sourced resin is flawed, and it is not fit for this purpose. Hence onwards, the research will focus on the NS01 and NS03 coatings, both clear and white.

4.2 Analysis of the surface roughness using AFM

Atomic force microscopy was used to analyse the topography of the samples. After exposure the coating slowly disintegrates which may cause the coating to eventually delaminate from the surface of the substrate. As the binder disintegrates the pigments may also loosen and fall off the surface forming pits and holes and hence roughening the surface. AFM is used to measure the root mean square (RMS) roughness of the sample.

Figure 4.2 demonstrates how the RMS value increases with exposure time for NS01 clear. It can be seen, between 0 to 45hrs there is an initial decrease in roughness due to the re-arrangement of the bonds. After this decrease in RMS value a steady increase is seen. However, with exposure the RMS value spreads further from the mean. This supports the idea of a chemically heterogeneous coating. It has been a reason for debate whether a cured coating is chemically homogenous or not and if this has any implications upon the degradation of the coating. Some say this is negligible however, the findings here suggest that the extent of degradation differs from one area to another on the sample hence why there is a greater deviation in the RMS value from the mean with longer exposure times. If the sample was chemically homogenous the topography of the sample surface at any given time would be very similar across the whole sample. These measurements were taken from five different areas on the same sample.

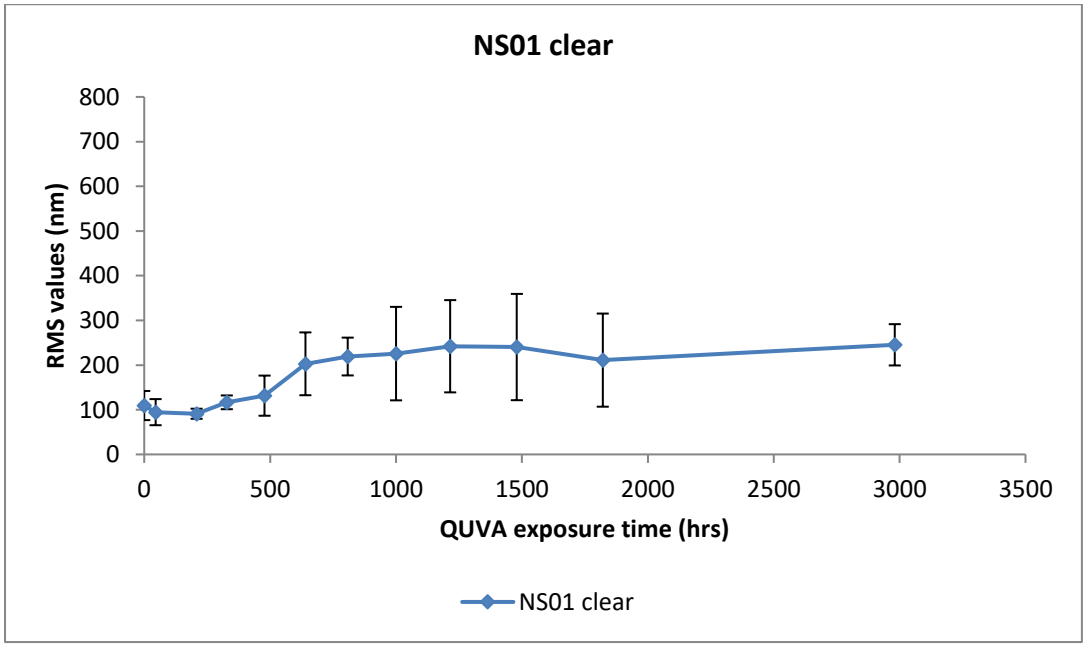

Figure 4.2- RMS value of NS01 clear using QUVA exposure

In comparison to NS01 clear, NS03 clearly shows a rather stable coating. Figure 4.3 displays the RMS values which remain near enough constant for the first 1200 hours after which, it increases dramatically. This correlates positively to the gloss loss that is seen in figure 4.1(a) up until 1200 hours. This is a critical marking for NS03 clear at which the coating degrades significantly after performing undoubtedly better than NS01 clear, our standard formulation. After 1200 hours the RMS values increase radically and after 2200hrs of QUVA exposure the RMS value begins to stabilise again. To determine if this change is evident on the surface of the coating scanning electron microscopy (SEM) was utilised.

After analysing the surface over the exposure period it became clear that the dramatic increase in RMS value was a manifestation of the surface roughness over time. The surface of NS03 clear is physically degrading at a faster rate than NS01 clear

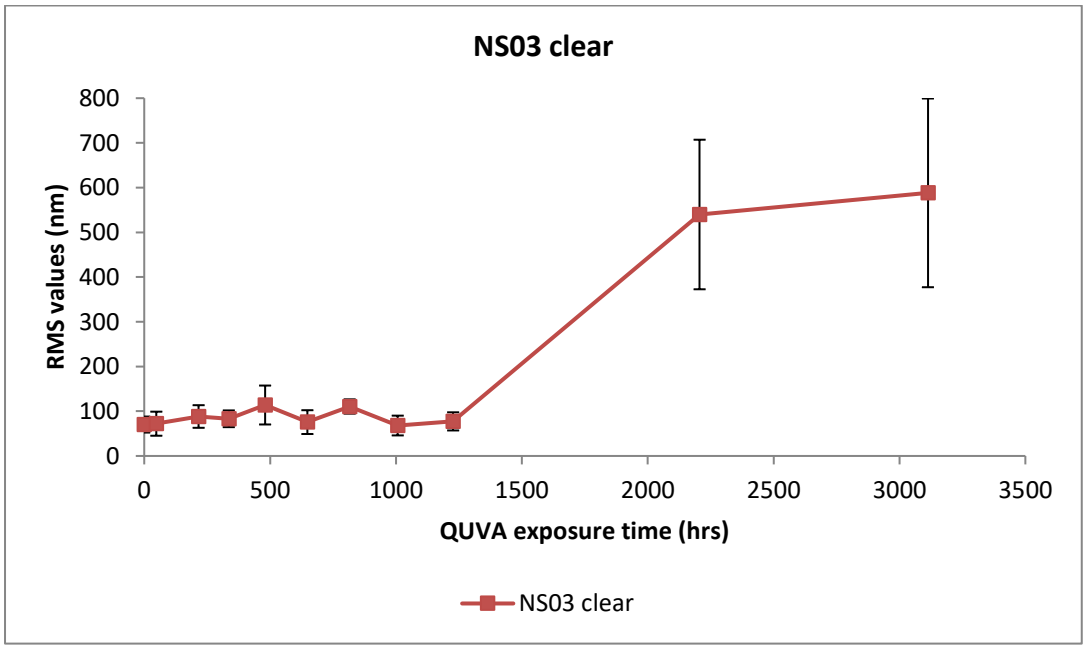

Figure 4.3 RMS value of NS03 clear using QUVA exposure.

As stated earlier, pigmented coatings were also analysed. The same techniques were applied to the two pigmented coatings, NS01 white and NS03 white. It was confirmed that the pigment stabilised the gloss retention of the coatings which, also reflects in the RMS data. As can be seen from figure 4.4, there is no dramatic increase in RMS values over increased exposure time. In fact, the RMS values fluctuate around the initial average RMS value i.e. at 0hrs exposure time. RMS data for NS03 white shows a similar trend to NS01 white (figure 4.5).

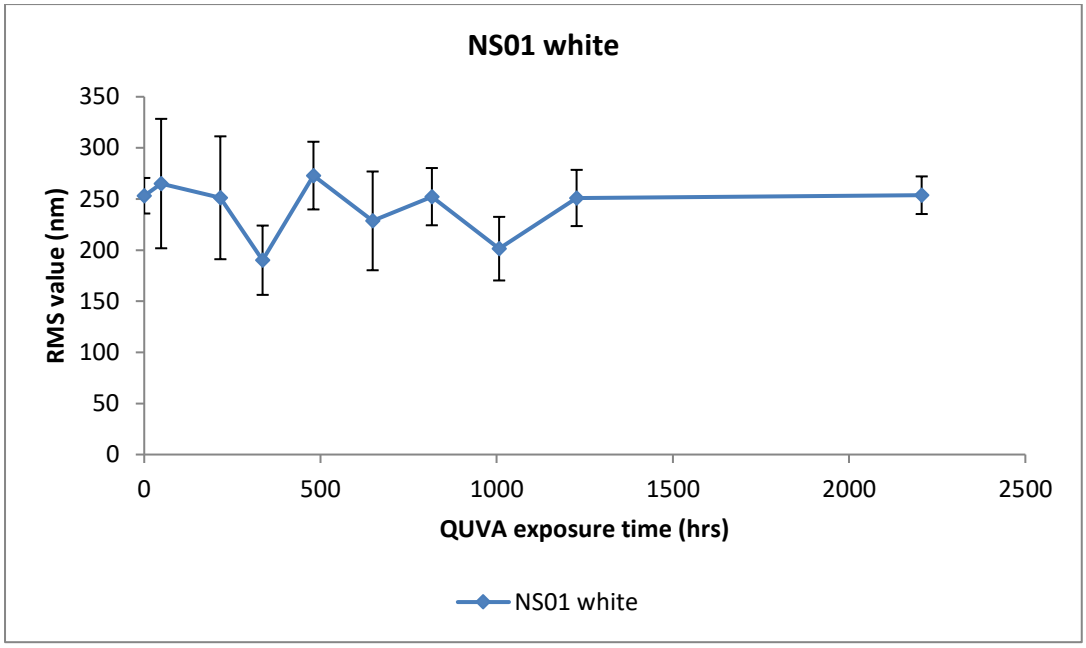

Figure 4.4: RMS values of NS01 white from QUVA exposure

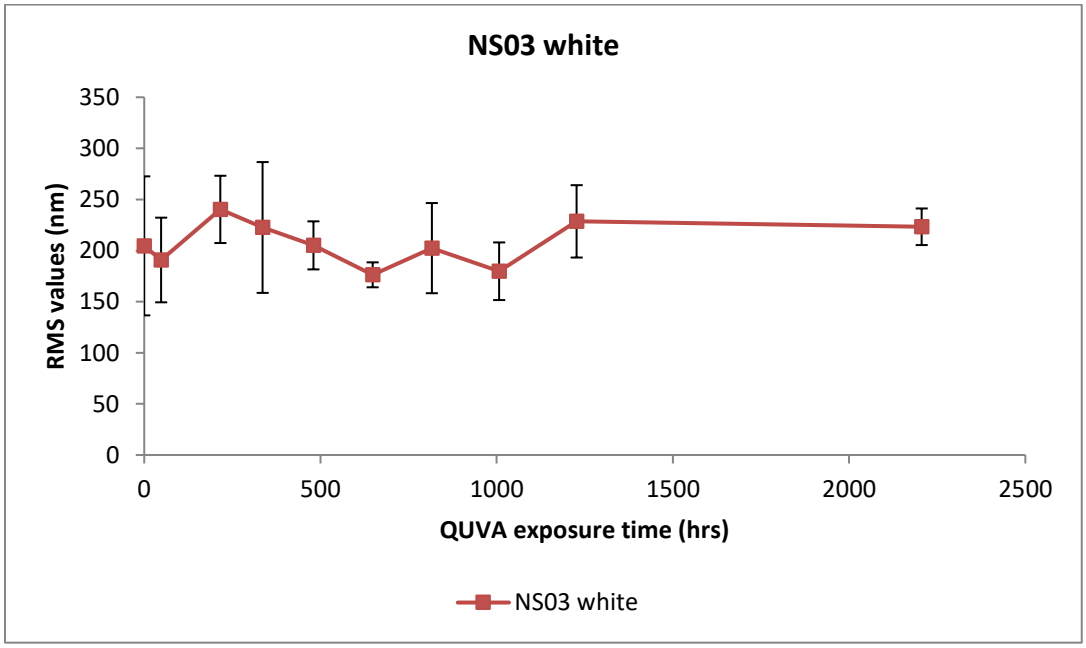

Figure 4.5: RMS values of NS03 white from QUVA exposure

After looking at the sudden drop in gloss retention for NS03 clear yet, a very stable NS03 white it becomes vital to carry out chemical analysis for each sample to understand what has caused this rapid change. Sole analysis of the physical state of the coil coating is not considered sufficient in determining the causes of failure within the expected lifetime of the coating. If there are certain elements in the new formula of the NS03 that cannot coexist it needs to be addressed, hence photo-acoustic Fourier transform infrared spectroscopy (PA-

FTIR) is used. PA-FTIR enables the analysis of the chemical make-up as stated in chapter 2 Following are the results obtained from PA-FTIR.

4.3 Analysis of the chemical make-up using photoacoustic Fourier transform infrared spectroscopy

4.3.1 Analysing PA-FTIR spectra

The key to analysing any FTIR spectra is to single out the bonds in the chemical formula which have a known presence in the spectra. For example, all polyester coil coatings have OH groups present in the formulation and the corresponding peak is a broad peak at 3000-3700cm^{-1}. In addition to understanding which chemical group owns a spectroscopy band area it is equally important to know what can happen to the spectra if there are chemical changes for that particular group.

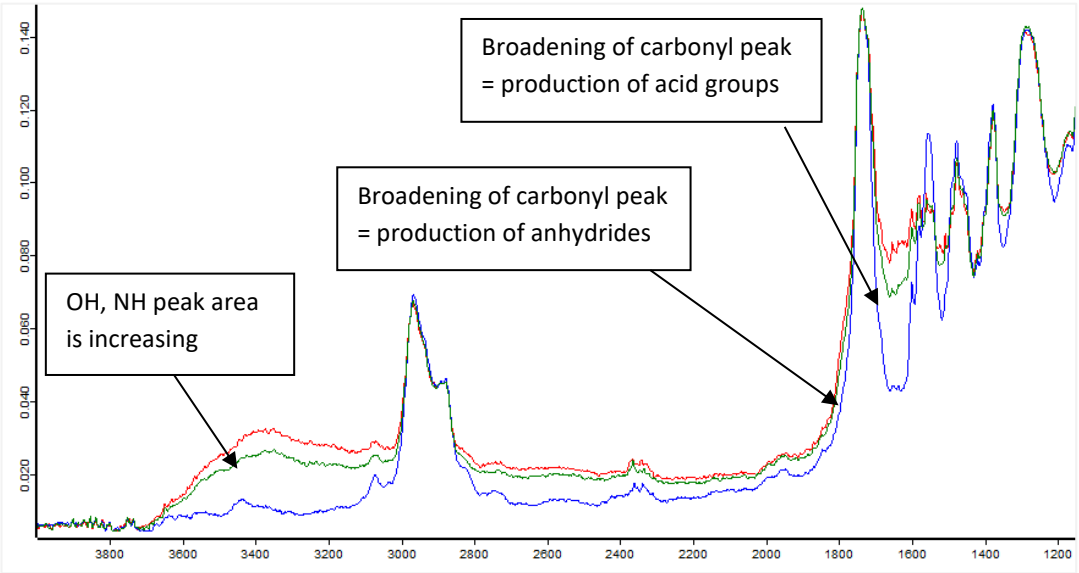

Figure 4.6: FTIR spectra of NS01 clear to demostrate peak changes as a function of exposure time

After observing the spectra in figure 4.6 of NS01 clear over exposure time, changes in relative peaks can be seen. The peak which is taken to represent the OH, NH chemical group increases in area over time when there is an increase in the production of OH NH group because of photo-oxiadtion. Another example here is that of the carbonyl peak. We see the peak broadens from the base of the peak on either side and this is the key characteristic linked to the production of anhydrides and acids. Similarly, there are key features which can be observed visually when analysing spectra whilst others need numerical analysis.

Table 7 and 8 were put together to show the band assignment of various chemical groups found within the spectra of NS01 and NS03. Band assignments can be found in books, papers and chemical analysis software. However, these are not specific to the sample being analysed hence the deviation of the table. The chemistry of the components making up this sample was known therefore, with the help of the coating specialist James Maxted and Chris Lowe at Beckers Ltd, Liverpool, UK, it was not so challenging to overrule band assignment suggestions which did not fit the chemical makeup.

Table 10: FTIR band assignment for NS01 (Larkin et al, 1988, Zhang. W,2009, Wang. X, 2012 and Marchewka et al, 2002)

Band Position (cm^{-1})	**NS01 Band Assignment**
3700-3200	OH vibration
3072	CH vibration in CH_3
2965	CH from all over
2890	CH_2 asymmetric stretch
2877	CH_2 symmetric stretch
1734	Carbonyl
1600 + 1580	Aromatic ring of polyester
1553	Melamine (1550-1555)
1475 1375 1250 1165	CH_2/CH_3 scissoring CH_2/CH_3 vibration CH_2/CH_3 rocking CH_2/CH_3 wagging
1278	C-O
1125 + 1075	C=O
975	CH_2/CH_3 vibration
915	Residual methoxy group
815	Triazene ring in melamine
745	Out of plane deformation in Orthothyalate

Table 8: FTIR band assignment for NS03 ((Larkin et al, 1988, Zhang. W,2009, Wang. X, 2012 and Marchewka et al, 2002)

Band Position (cm^{-1})	**NS03 Band Assignment**
3700-3200	OH vibration
3072	CH vibration in CH_3
2961	CH_3 asymmetric stretch
2934	CH2
2900	CH_2 asymmetric stretch or CH3 sym
2856	CH_2 symmetric stretch
1733	Carbonyl
1610	Isophthalic
1598	Orthophthalate
1457	CH2/CH3 scissoring
1357	CH2/CH3
1280	C-O
1097/1075	C=O or C-O
732	Isophthalic

To quantify photo-oxidation, the percentage of hydroxyl group and the percentage of melamine loss are calculated. The quantification method used to calculate the percentage OH involves normalising the OH band against the neighbouring CH band ($Ratio_{OH}$) before subtracting it from the normalised OH band of various weathered intervals and then dividing it through by the normalised OH band standard time at 0hrs exposure time.

From figure 4.7 and 4.9 the approximate band limits can be seen. These limits define the area of the CH band and the OH band and the ratio is determined using equation 4.1.

$$Ratio_{OH} = A_{OH} / A_{CH} \quad \text{(Eq4. 1)}$$

Where, A_{OH} = the area of the OH band and A_{CH} = area of the CH band.

At 0 hours; Ratio $_{OH\text{-}STD} = A_{OH\text{-}0hrs} / A_{CH\text{-}0hrs}$

At any QUV-A exposed hrs; Ratio $_{OH\text{-}QUV} = A_{OH\text{-}QUV} / A_{CH\text{-}QUV}$

Therefore, OH % is calculated using equation 2

$$OH\ \% = \frac{Ratio_{OH-QUV} - Ratio_{OH-STD}}{Ratio_{OH-STD}} \quad \text{(Eq4. 2)}$$

Where, OH % = formation of hydroxyl group due to the QUV-A exposure.

Figure 4.7 shows an example of the melamine and the corresponding CH (methylene) peak chosen to calculate the percentage melamine loss. Similarly, to calculate the percentage melamine loss, the melamine band must be normalised against the CH band however, this time the peak height is used instead of the peak area (eq 4.3).

$$\text{Ratio}_{Mel} = H_{Mel} / H_{CH} \quad \text{(Eq4.3)}$$

Where, H_{Mel}= peak height of melamine band and H_{CH} = peak height of CH band.

$$MEL\ \% = \frac{Ratio_{Mel-STD} - Ratio_{Mel-QUV}}{Ratio_{Mel-STD}} \quad \text{(Eq4.4)}$$

Where, MEL % = decomposition of the melamine cross-linker over QUV-A exposure time.

This method of melamine quantification is well known however, during this research it was discovered that the CH band adjacent to the melamine peak was unstable after exposure. If a peak is unstable the results of normalising against an unstable peak may not be reliable. To compensate for this, another stable peak was selected for this normalisation and the initial CH peak was also normalised against another peak to monitor how it changes over time. The closest stable peak to the melamine peak was a C-O peak.

The spectrum in figure 4.7 is of NS01 clear, unexposed i.e. at 0hr exposure. The highlighted peaks are the peaks used for FTIR analysis on all NS01 samples and the corresponding peak limits (wavenumbers) and analysis method are listed in table 9. NS01 and NS03 (figures 4.7 and 4.8) spectra show the same components however the peaks vary slightly due to the chemical makeup of each coating which effects the environment of the components. Therefore, it is important to analyse each spectrum individually to ensure the automated integration in the software is integrating within each peak limit.

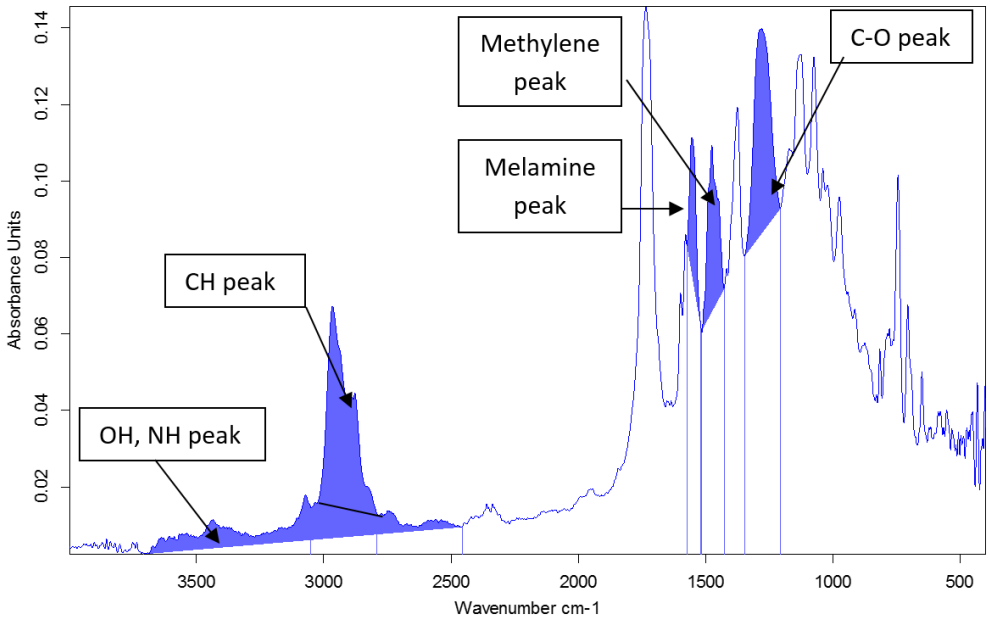

Figure 4.7: FTIR spectrum for NS01 clear showing the peaks used for analysis

Table 9: NS01 peaks used for FTIR analysis

NS01 Peak label	Approximate Peak wavenumber (cm^{-1})	Analysis method
OH,NH	3700 – 2450	Area integration
CH	3050 – 2790	Area integration
Melamine	1550	Peak height
Methylene (CH2/CH3)	1500-1430	Area integration
C-O	1345-1200	Area integration and peak height

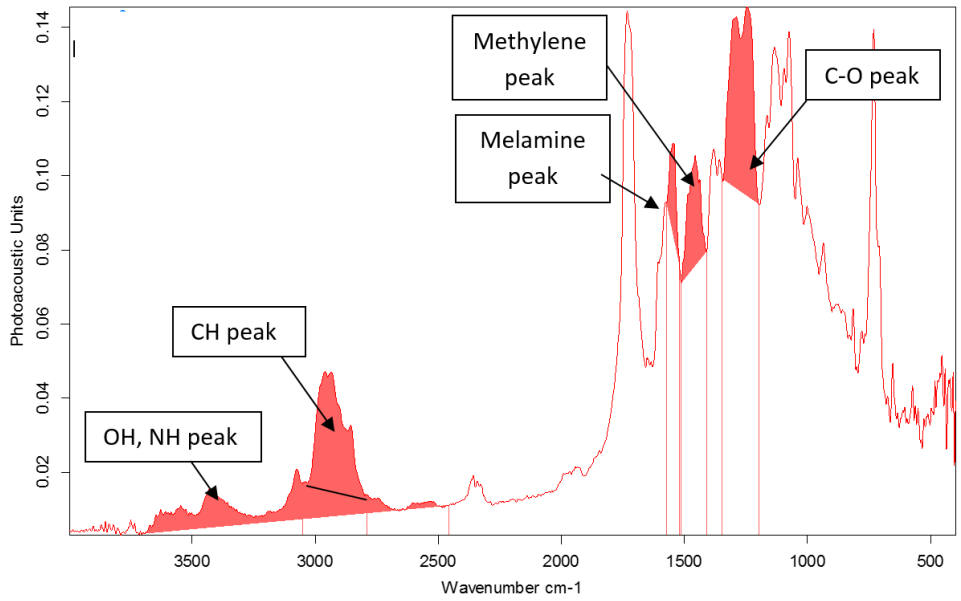

Figure 4.8: FTIR spectrum for NS03 clear showing the peaks used for analysis

Table 10: NS03 peaks used for FTIR analysis

NS03 Peak label	Approximate Peak wavenumber (cm^{-1})	Analysis method
OH,NH	3700 – 2450	Area integration
CH	3050 – 2790	Area integration
Melamine	1550	Peak height
Methylene (CH2/CH3)	1510-1410	Area integration
C-O	1345-1200	Area integration and peak height

4.3.2 PA-FTIR Spectra analysis

Before carrying out the peak analysis, analysis of the spectra was done. From the spectra we can see the change in certain peaks. For example, from the NS01 clear spectra the photo-oxidation can be seen in figure 4.9, and if the area is looked at in more detail the increase in –OH/-NH peak area, 3700- 2450cm^{-1} becomes more obvious (figure 4.10). On the opposite side of the spectra there seems to be small change in the melamine peak, 1550cm^{-1} and methylene peak, 1500-1430cm^{-1} for NS01 clear, again a closer look at the area of interest confirms this (figure 4.11). On the other hand, the NS03 clear spectra (figure 4.12) shows a clear increase in photo-oxidation, 3700-2450cm^{-1}. However, in comparison to NS01 the breakdown of the methylene peak, 1510-1410cm^{-1} and the melamine peak, 1550cm^{-1} is severe. Figure 4.13 shows the degraded peaks.

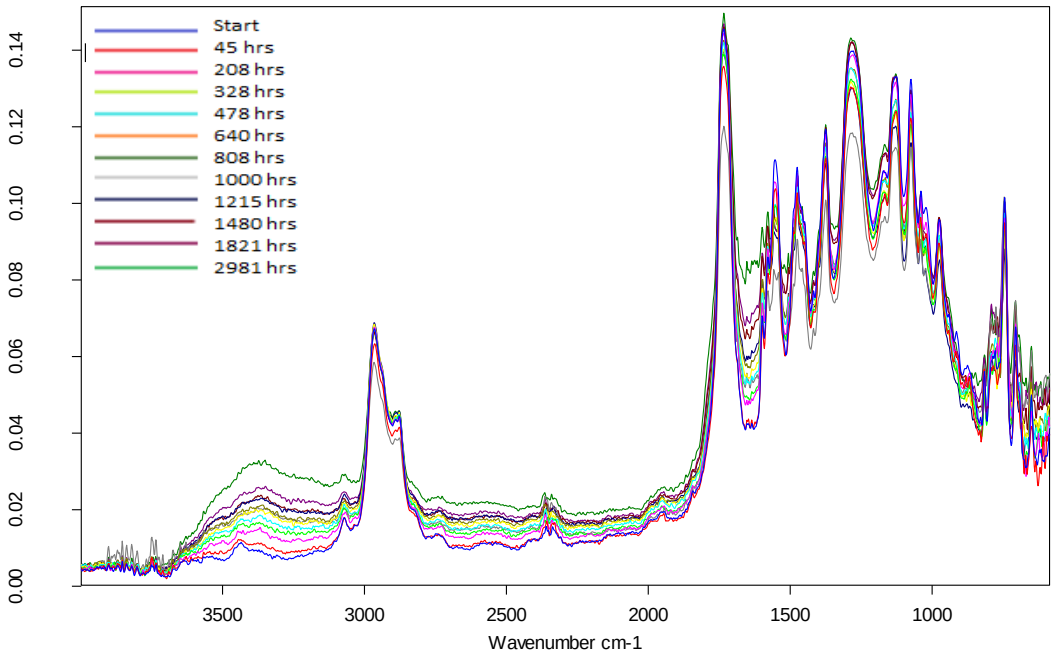

Figure 4.9: FTIR spectra of NS01 clear samples at various exposure hours

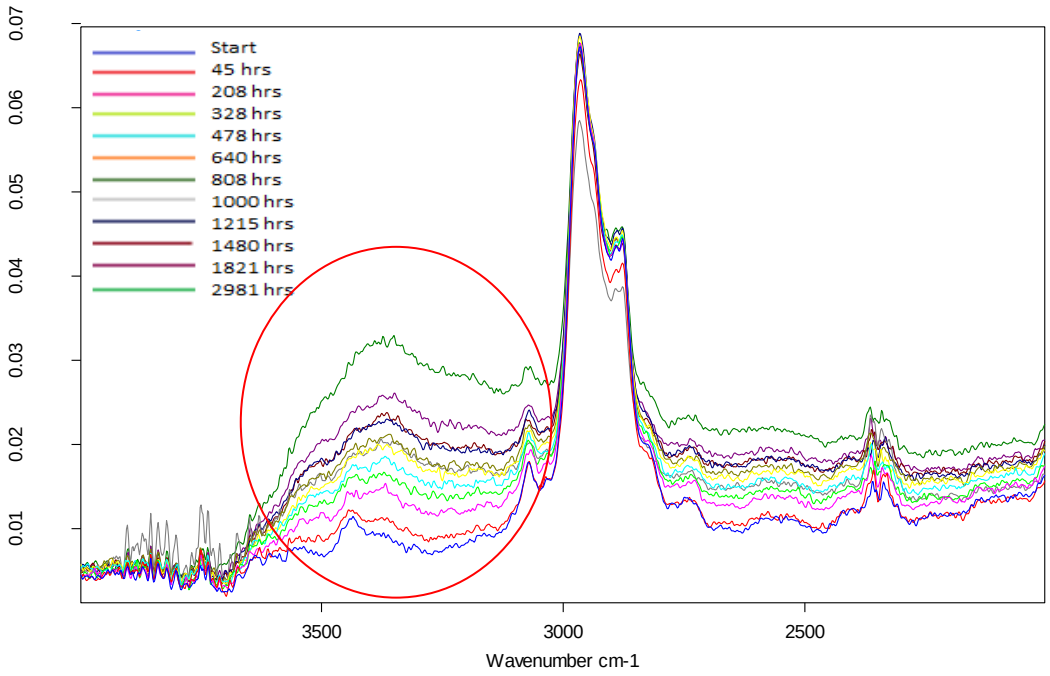

Figure 4.10: Photo-oxidation of NS01 clear after QUVA exposure

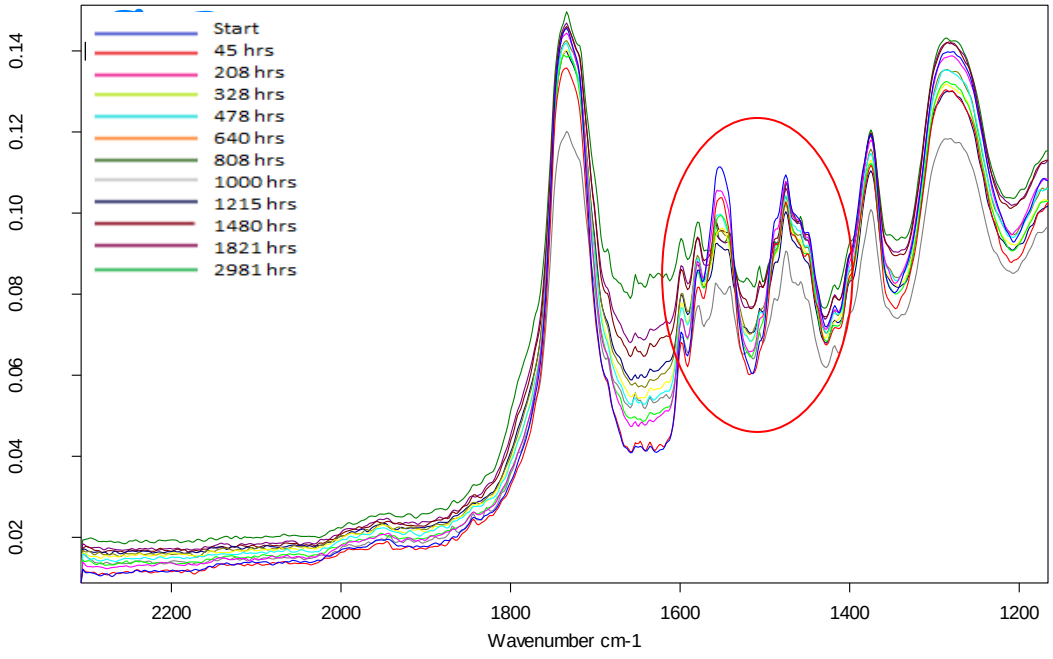

Figure 4.11: Melamine peak and CH peak spectral analysis for NS01 clear after QUVA exposure

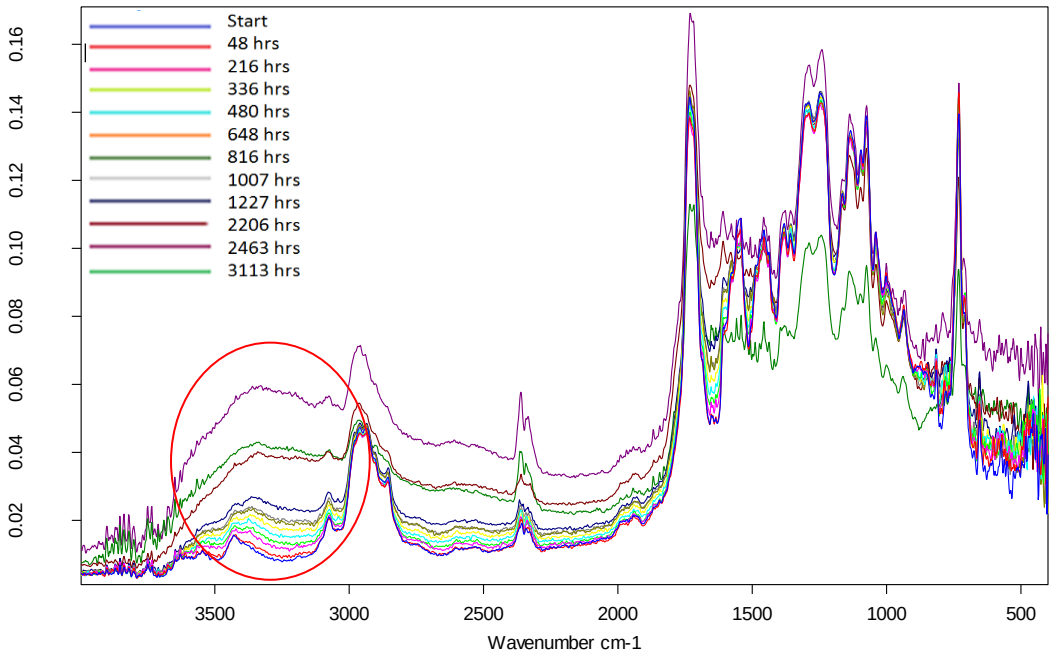

Figure 4.12: FTIR spectra of NS03 clear samples at various exposure hours

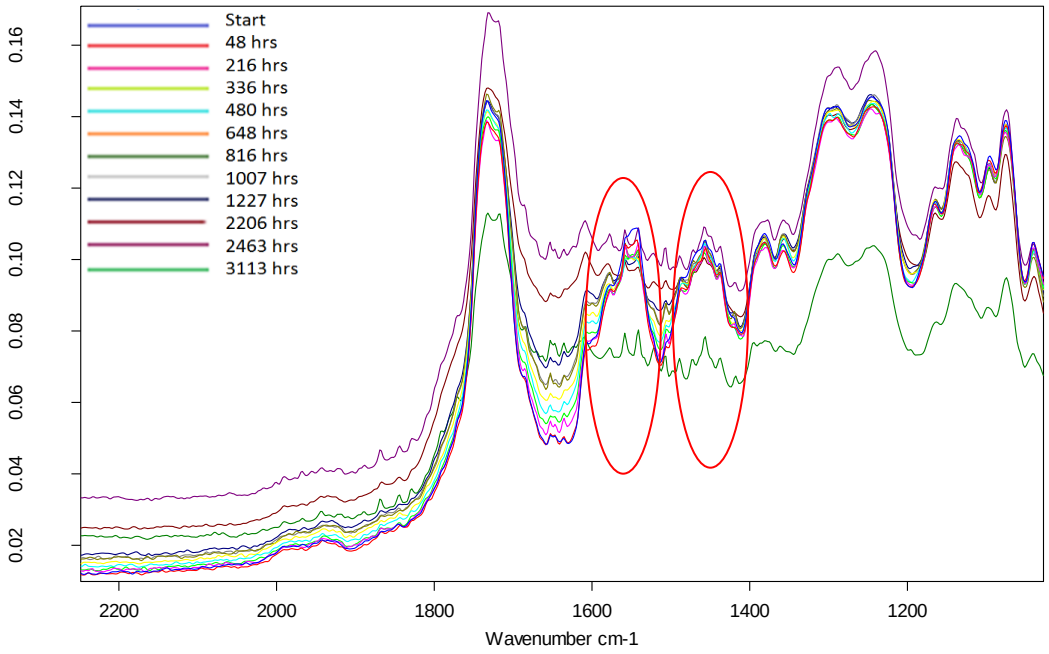

Figure 4.13: The degradation of the melamine and CH peak in NS03 clear after QUVA exposure

4.3.3 PA-FTIR RESULTS FROM PEAK ANALYSIS

As stated earlier, thorough peak analysis was carried out to investigate the method of degradation of each coating. A degradation method specifically examined by PA-FTIR is photo-oxidation. This is because photo-oxidation produces hydroxyl groups and results in a change in the environment surrounding the triazine ring in the crosslinker- melamine. This is measured as melamine loss.

Figure 4.14 displays the results of the area integration of the –OH,-NH peak with the CH peak, with respect to time. It can be observed that for each coating the percentage of hydroxyl groups increases which can confirm that photo-oxidation is taking place. It is apparent that the standard coating NS01 clear is undergoing considerably more photo-oxidation than NS03 clear, which is the bio-based formulation. NS03 clear shows an increase of 89% at the end of the exposure period whereas NS01 shows an increase of 281%. Having seen the photo-oxidation data, NS03 clear out-performs the standard NS01 clear and could be a perfect formulation to be used as an exterior coating. However, even without being readily susceptible to photo-oxidation the physical degradation of the coating is worse off than that of the standard.

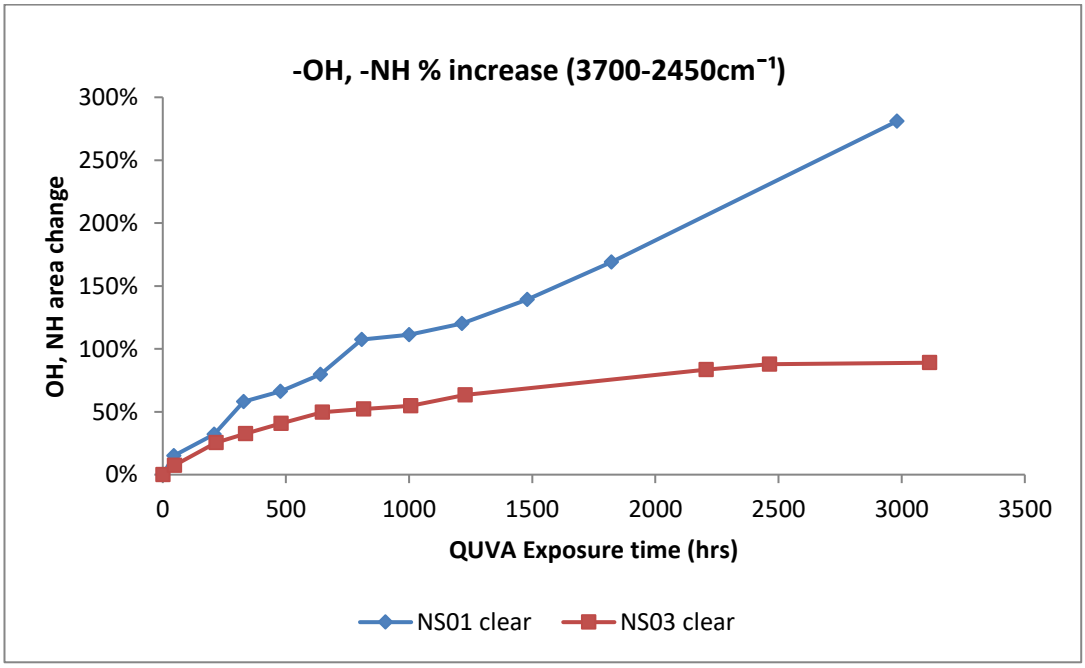

Figure 4.14: -OH, -NH peak analysis against time for NS01 and NS03 clear

The percentage of melamine loss is also shown in figure 4.15. The melamine peak height was normalised against the C-O peak as the typically used CH peak i.e. methylene peak was unstable. From the data, NS01 clear has a more gradual melamine loss. The melamine loss here refers to the change in the triazine region. The change in this region is associated to changes occurring in the crosslinking environment of the melamine crosslinker. NS01 clear shows a melamine loss from 100% to 84% over 1480hrs, almost half of the exposed lifetime and then further reduces to 75% by the end of the maximum exposure hours of 2981 hrs.

NS03 clear on the other hand has a greater melamine loss. After 1227hrs the melamine loss is 44%. By the end of the exposure hours at 3113hrs it reduces to 33%. This is a significant loss. It seems as the crosslink network is more susceptible to attack for NS03 clear compared to NS01 clear, which does not have significant melamine loss in comparison.

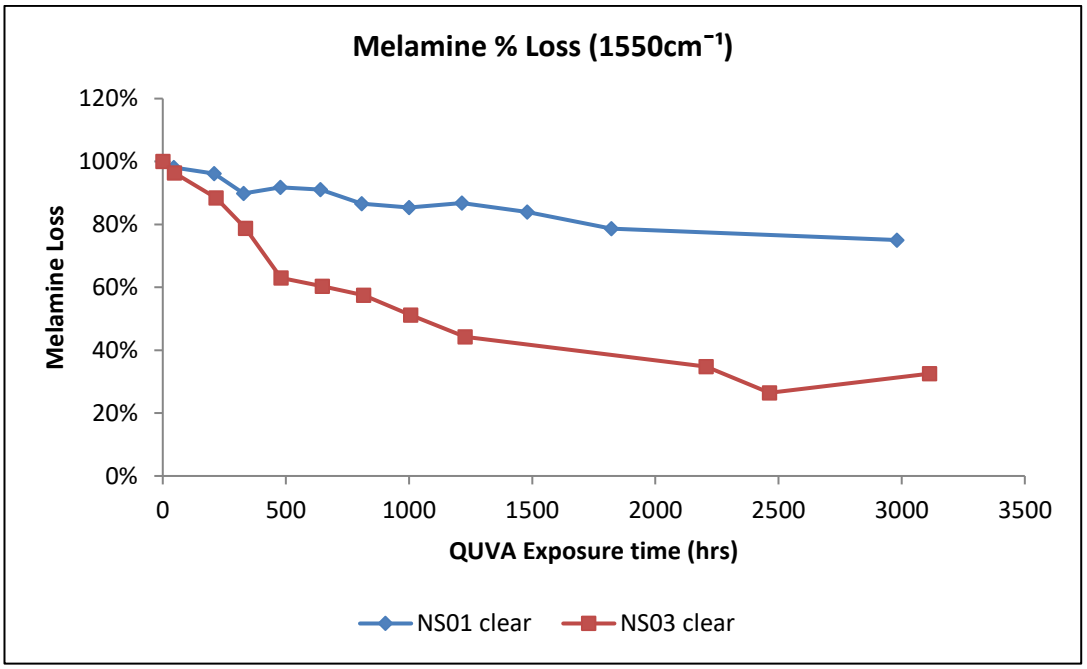

Figure 4.15: Melamine peak analysis against time for NS01 and NS03 clear

In the same region of the melamine crosslink network, changes in the methylene group are detected. This peak is usually used to normalise the melamine peak as it is quite stable in comparison to its crosslinked chemical environment. When subjected to UV exposure a typical coil coating polyester will experience minimal change in this area. This was also expected from the partially bio-sourced formula of NS03. However, it can be seen in figure

4.16 that significant changes take place just after 1000hrs which is less than half of the overall testing period of 3113hrs.

.

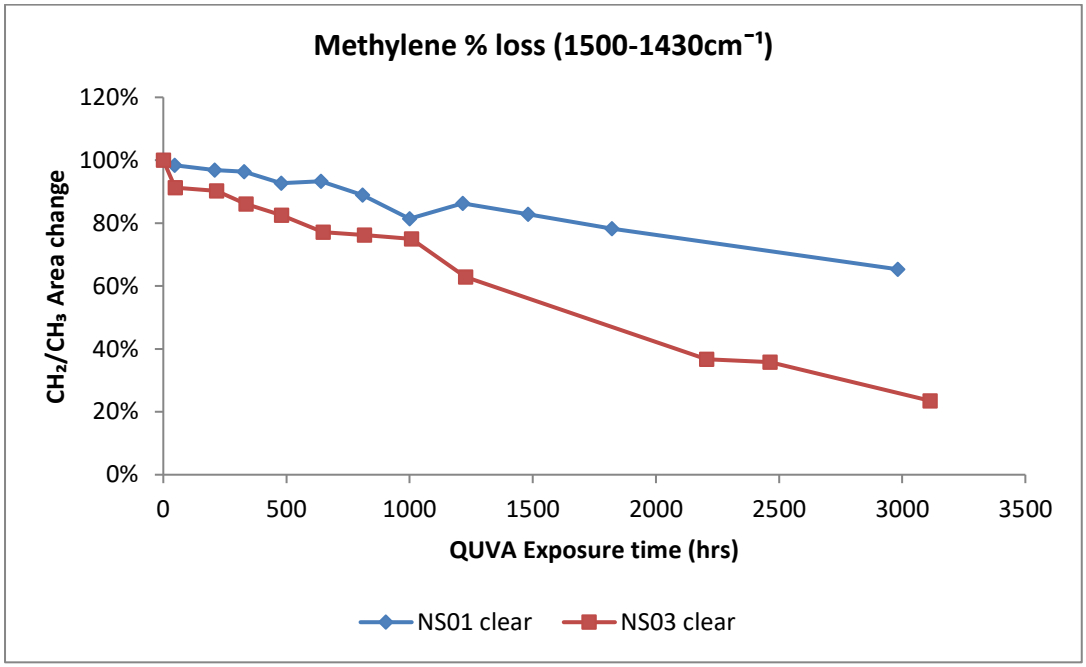

Figure 4.16: Methylene peak analysis of NS01 and NS03 clear

The peak analysis of the white coatings can be seen below. Initially there is an increase in –OH/-NH peak area of NS01 white but after approximately 1000hrs an increase in NS03 white supersedes NS01 white. However, the 90% approximate increase in peak area for NS01 and NS03 white coatings (figure 4.17) seems trivial compared to the 280% increase of the NS01 clear coating. In comparison the clear coating NS03 white has shown a similar increase.

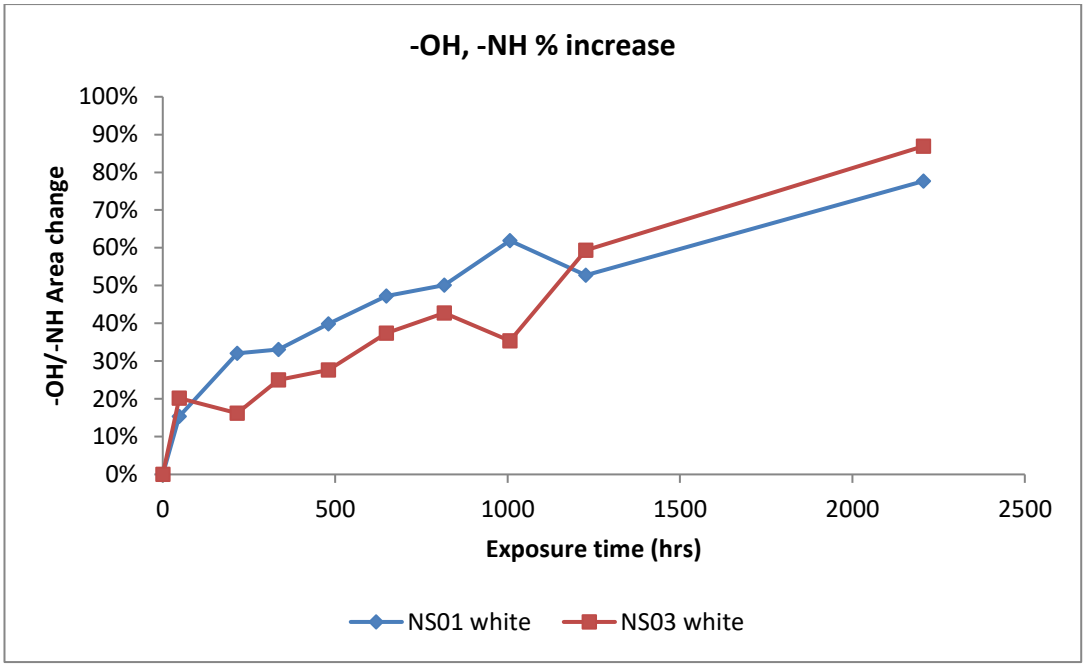

Figure 4.17: -OH/NH peak analysis of NS01 and NS03 white

The melamine and methylene loss for both white coatings is comparable, and clearly a drastic improvement from that of the clear counterparts, as seen in figure 4.18 and 4.19 respectively.

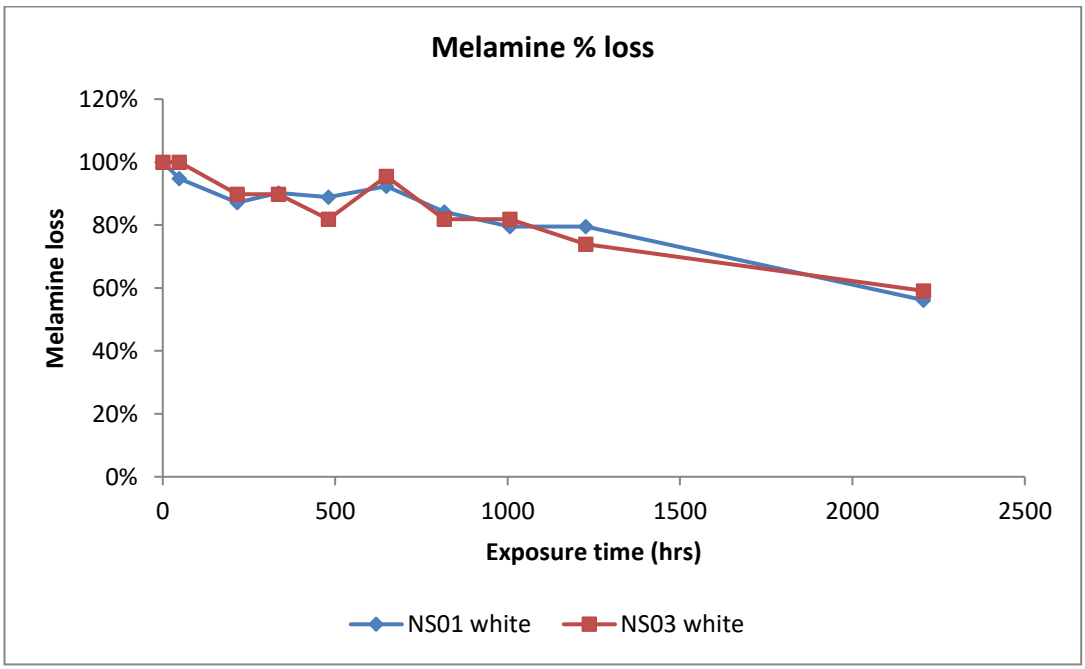

Figure 4.18: Melamine peak analysis of NS01 and NS03 white

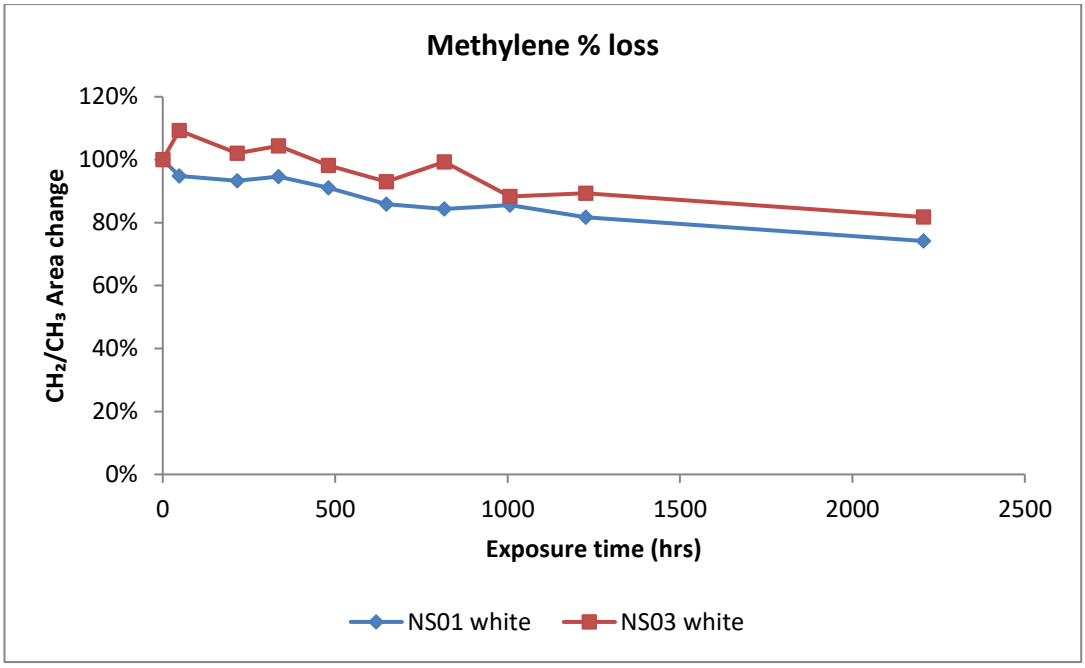

Figure 4.19: Methylene peak analysis of NS01 and NS03 white

4.4 Surface analysis using scanning electron microscopy

Scanning electron microscopy (SEM) was carried out with a stage tilt of 75˚. A head on view of the sample surface could not give as detailed information about the surface topography hence, the sample was tilted using a sample holder specifically designed in the Queen Mary University of London workshop.

SEM on the QUVA samples, NS01 clear, NS03 clear, NS01 white and NS03 white, unexposed and exposed at maximum hours was carried out. The images are presented below in to compare the surface before and after exposure.

Figure 4.20 displays a) the unexposed surface image of NS01 clear and b) the surface exposed at 2981 hours. The unexposed sample surface is relatively flat. Hardly any raised features were seen across the whole sample. Whereas, the exposed sample had multiple 3D structures scattered around. It is clear the structures are a part of the coating and perhaps a result of some physical degradation of the coating. These features are what most likely give rise to the increased RMS value detected using AFM.

Figure 4.21 shows both the unexposed and exposed sample of NS03 clear. The unexposed sample shows a flat surface like the unexposed NS01 clear sample, as expected. The exposed sample however looks completely different. The NS01 clear exposed sample did have some

3D structures appearing on the surface but the surrounding surface area looked unaffected. Contrary to this the complete surface of the NS03 clear exposed sample seems to have completely deteriorated. Again, the roughness is supported by the increased RMS values from AFM imaging.

The unexposed white samples of both NS01 and NS03 figure 4.22 a) and figure 4.23 a) respectively do not appear to have a completely uniform plane. An uneven surface could be the result of incorporating pigment into the formulation. Where, NS01 white has a slightly uneven texture on the surface with an indent, NS03 white looks rather rough. After exposure however, NS01 white seems to have developed 'holes' whereas NS03 white has a consistent roughness across the surface. The developed holes and indents across a surface also increase the initial and final root mean square roughness.

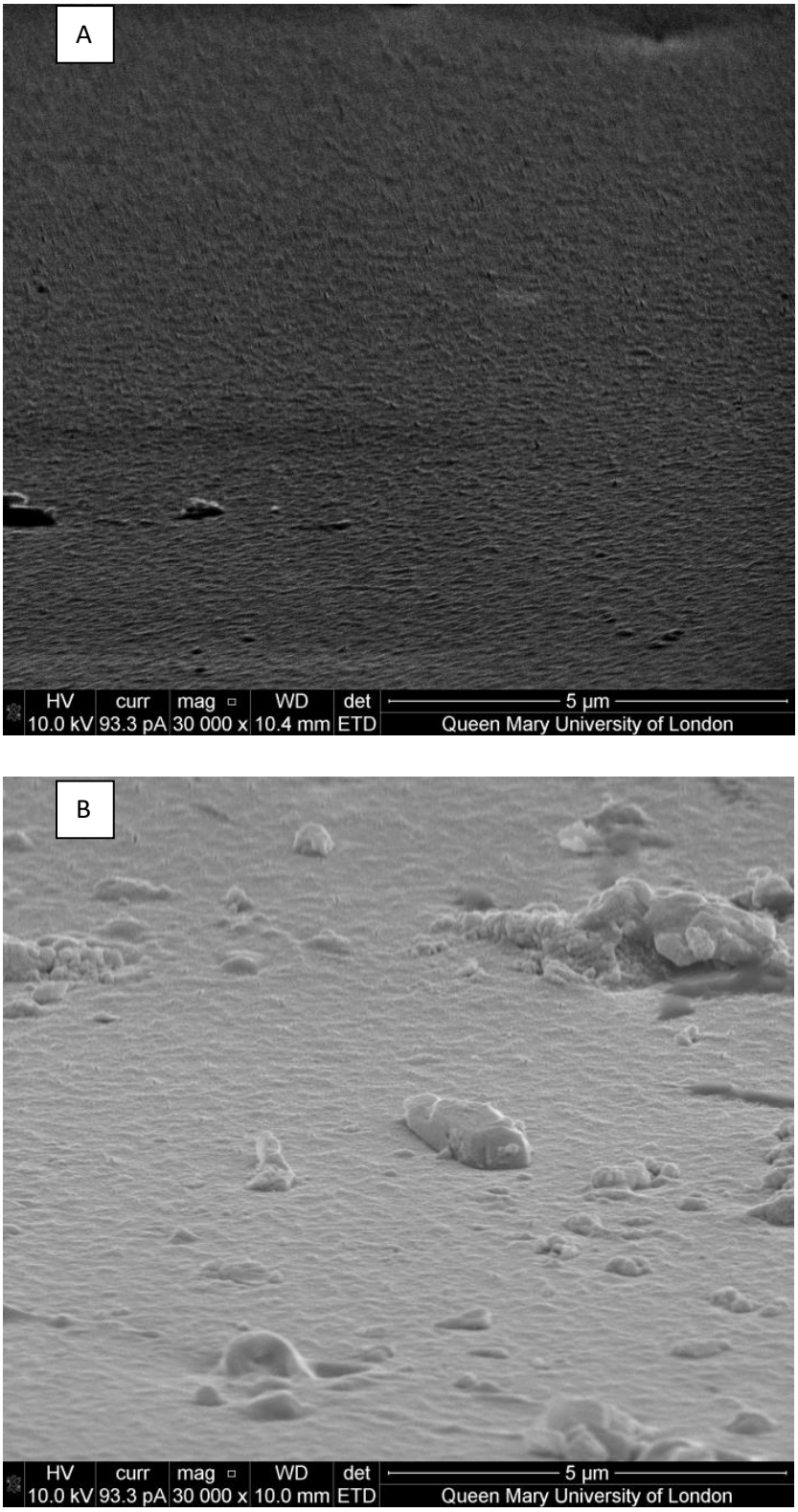

Figure 4.20: Surface analysis od a) NS01 clear, unexposed and b) NS01 clear, exposed at 2981hrs

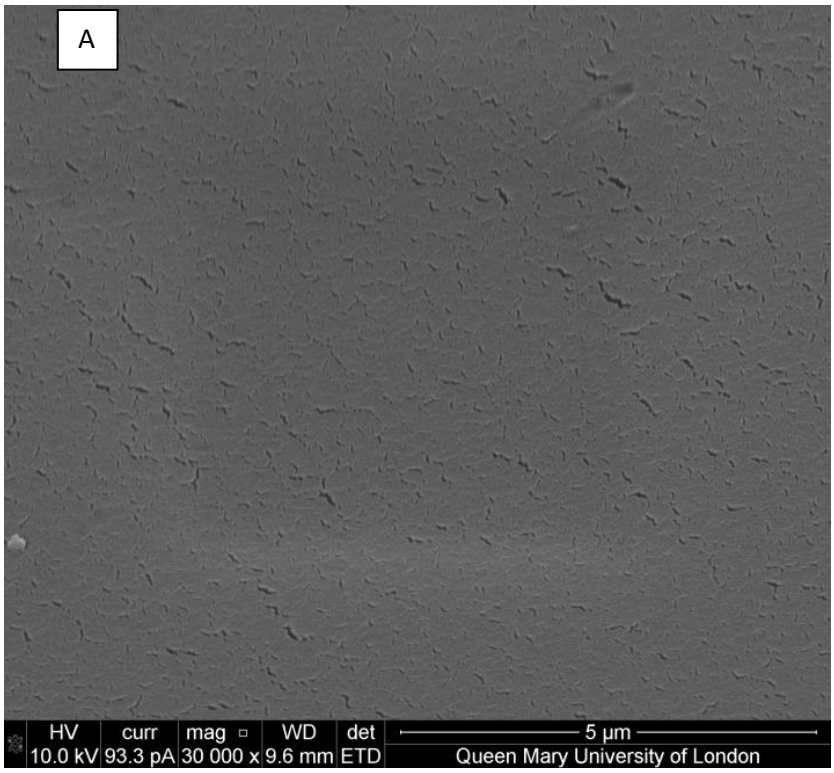

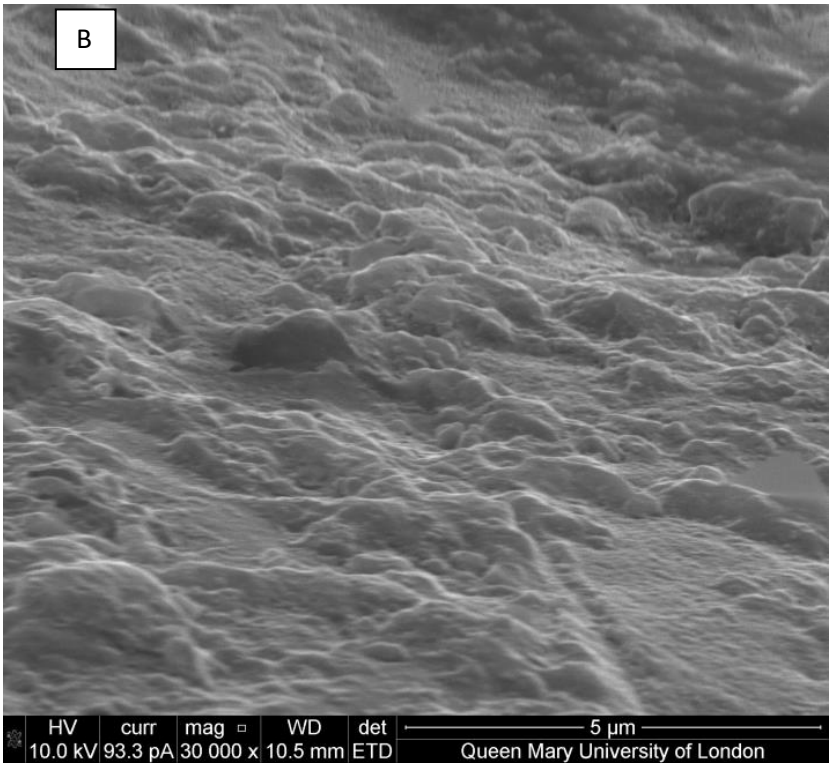

Figure 4.21: Surface analysis of a) NS03 clear, unexposed and b) NS03 clear, exposed at 3113 hrs

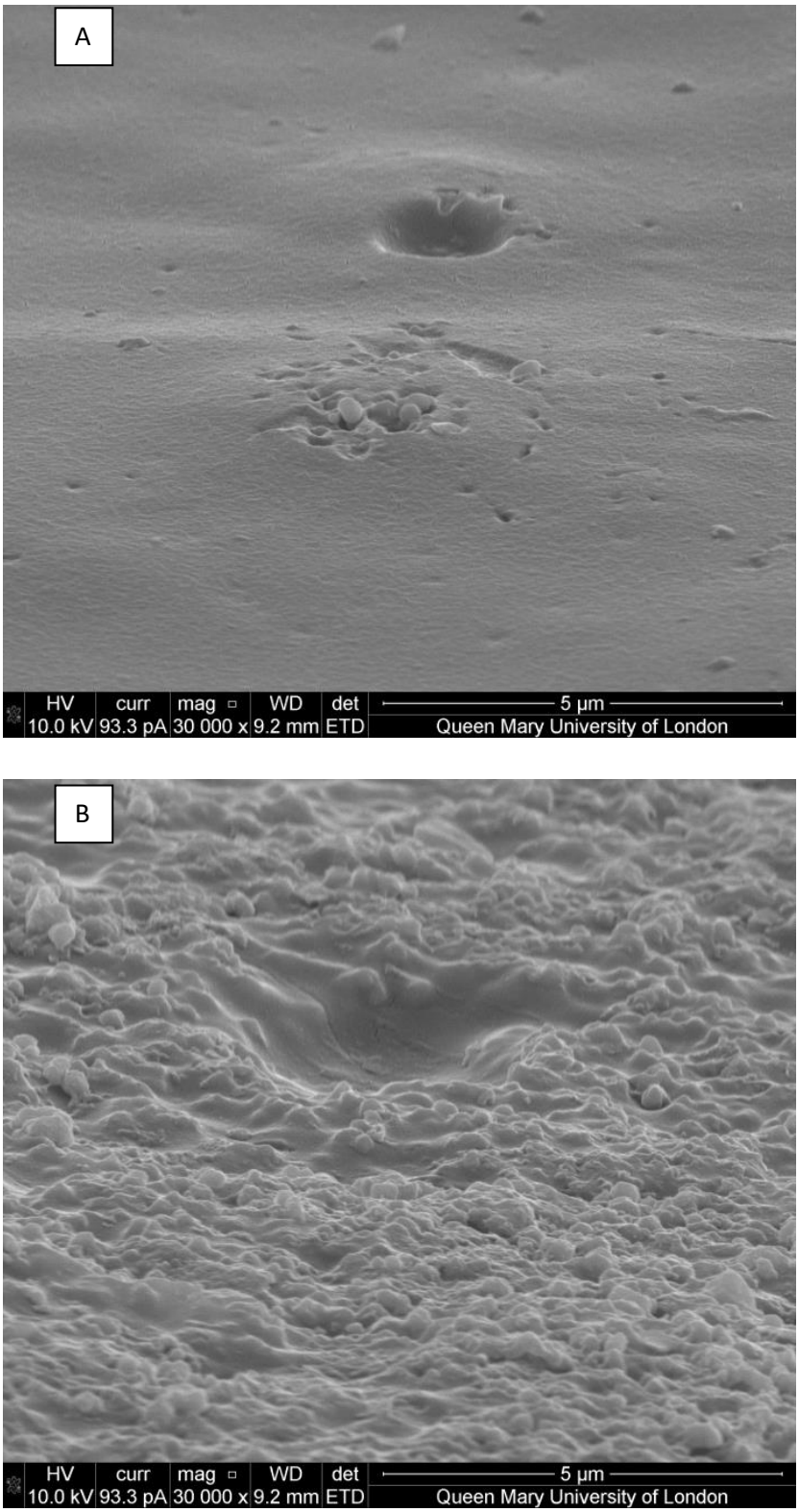

Figure 4.22: Surface analysis of a) NS01 white, unexposed and b) NS01 white, exposed at 2206 hrs

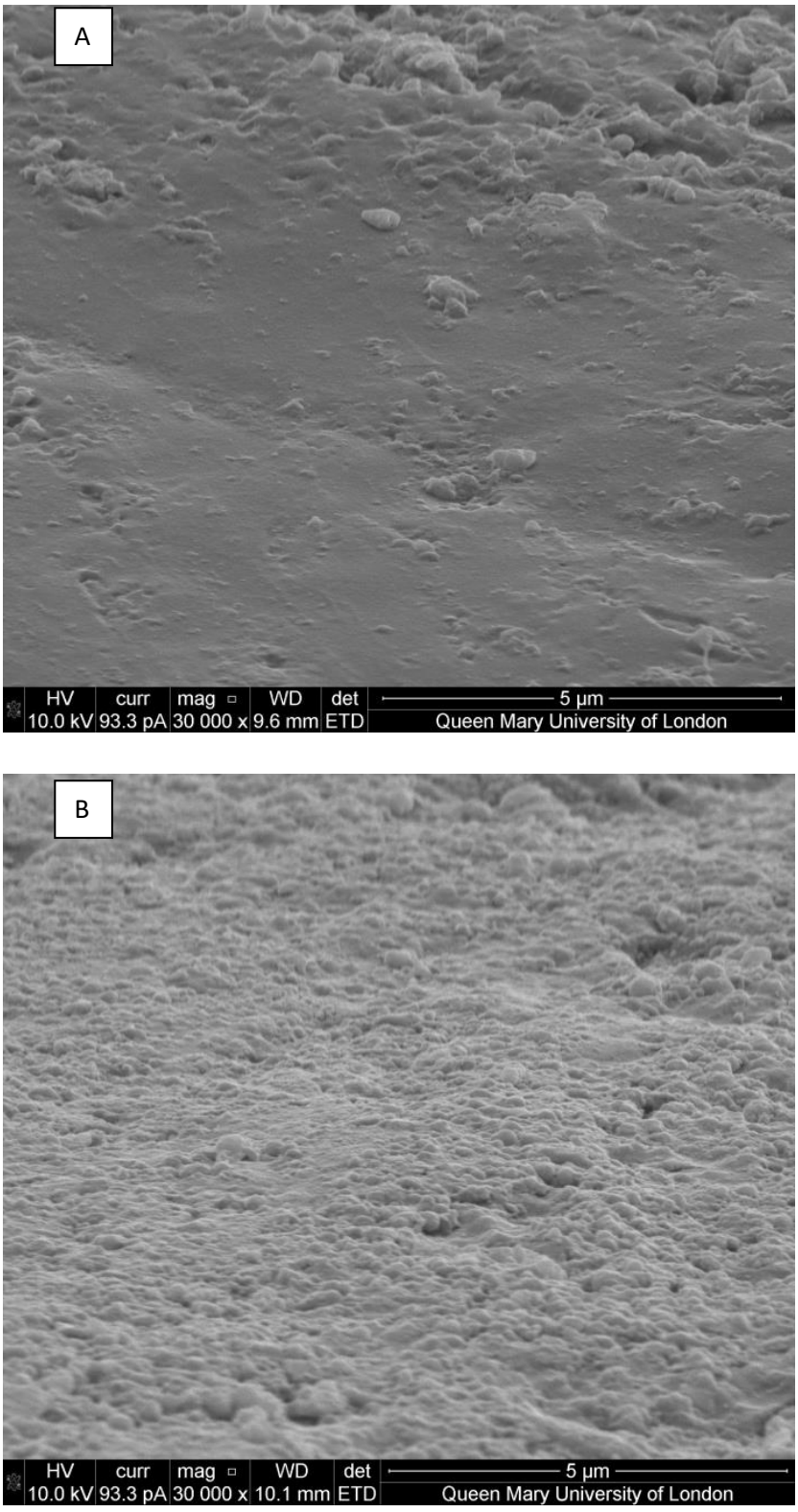

Figure 4.23: Surface analysis of a) NS03 white, unexposed and b) NS03 white, exposed at 2206 hrs

4.5 Conclusion of experimental results

From the data so far, it appears that NS01 clear has an overall better performance than NS03 clear. The reason for using NS01 to compare against is that it is the standard coil coating formulation which is being used and the performance of the coating is well known. NS03 clear was doing rather well as an exterior coating in comparison to NS01 until 1200hrs exposure. AFM which was used to characterise the surface topography also found that at the 1200hr mark the roughness increases significantly for NS03 clear. SEM images show the development of holes or pits on the surface of the coating at the same time interval. Physical degradation of the coating takes place when the binder and resin disintegrate which is interlocked with the chemical degradation, i.e. the breakdown of chemical bonds within the coating.

The gloss retention for NS03 starts off to be better than NS01 but once it reaches 1200hrs of exposure it decreases dramatically, suggesting the physical manifestation of degradation. It can be concluded that severe physical degradation begins at this point. The chemical analysis shows that photo-oxidation is prevalent in the NS01 clear coating hence, cannot be the reason for the physical degradation of NS03 clear. There is however, a noticeable change in the crosslink environment of the melamine crosslinker and the methylene peak disintegrates quickly, perhaps suggesting another degradation mechanism is the cause of failure at the critical 1200hr mark. As for the NS01 and NS03 white formulation, the addition of the titanium pigment appears to stabilise the white coatings as shown by the various experiments carried out.

This chapter only includes the results and a brief description of the findings. Further discussion on the degradation performance can be found in chapter 6.

5. Results from natural weathering of NS01 and NS03 coatings in Florida

Chapter 4 dealt with samples which were artificially weathered using a QUVA machine. In this chapter the focus will be on the samples that were tested in Florida. The weather conditions in Florida were ideal for testing against outdoor exposure of the coatings and it is a common place to carry out natural weathering tests. The coatings were applied to panels, prepared as described in chapter 3. The panels were sent to Florida and kept on the exposure site for two years. At regular time intervals coupons were cut out of the panel, labelled and sent back to the company for further analysis. As stated earlier, it is not common practice to investigate early exposure time as the rate of degradation is slow. However, when you have a new coating formulation it becomes vital to monitor the early stages of degradation. It can be that neglecting the earlier exposure time may result in losing key information about how the coating performs, and if it does not perform well, when does it begin to fail, may go unanswered. Not knowing when a coating begins to fail limits your understanding about the coating's performance. Understanding the onset of degradation can enable a quicker response in revising the formulation and re-testing it. Keeping these points in mind it was decided that for the first 12 months the sample would be analysed frequently. Every 2 months the coupons cut out from the sample were sent to Beckers Ltd, Liverpool and then forwarded to Queen Mary University to be analysed. After 12 months the samples were cut at 18months and then 24 months completing 2 years of exposure.

5.1 investigating gloss retention

The first measurement taken from the samples was using the gloss meter to analyse the gloss retention of each coating in the clear and white formulations. Figure 5.1 a) shows that the gloss retention for NS01 clear remains constant up until 18 months at approximately 100%. After 18 months the gloss retention decreases by 10%. NS03 clear also follows a similar trend to NS01 clear. It remains almost constant until 18 months after which it drops by 30%, 20% more than NS01 clear. This could be the start of the significant decline in gloss retention that was seen for the QUVA exposed sample at 1200hrs, in chapter 4, section 4.1.

In figure 5.1 b), we see a similar trend for NS01 white and NS03 white. The gloss retention for NS01 white remains consistent at 100% until 18 months after which we see a 3% drop which is not very significant and the degradation pattern cannot be predicted for the future exposure. The QUVA data shows superb gloss retention, therefore, it is hopeful the same is repeated in natural weathering.

In addition to the above, NS03 white also shows outstanding gloss retention until month 18, above and equal to 100%. After 18 months the gloss retention value drops from 100% to 89%, 8% more than NS01 clear. Again, there is nothing to suggest that this small change in gloss retention will result in a great loss.

a)

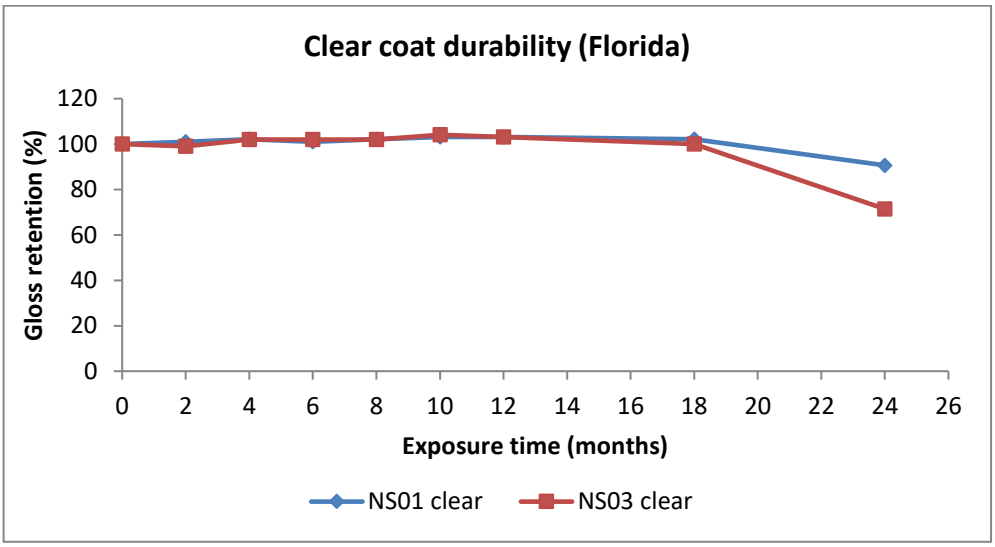

b)

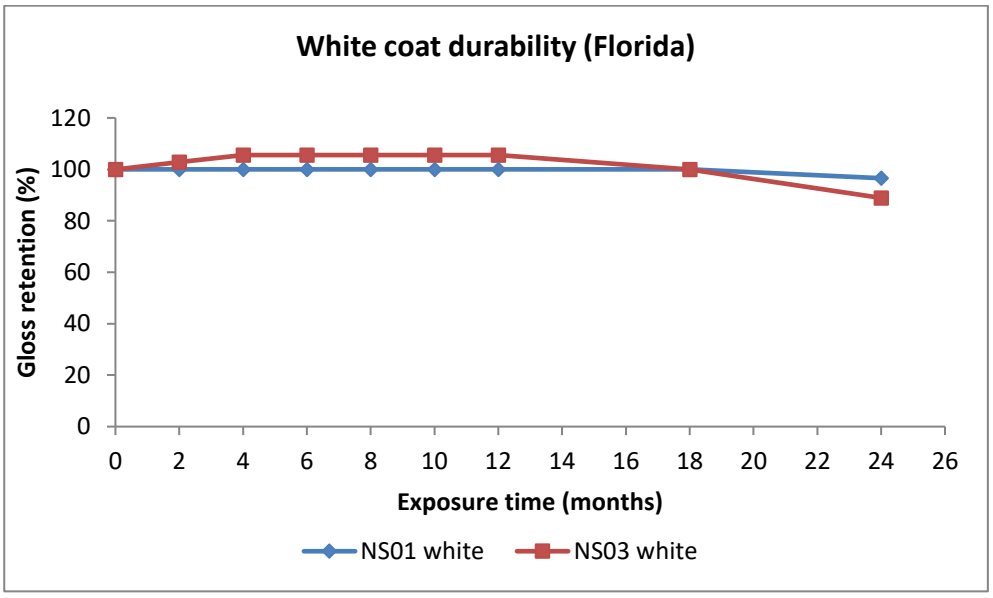

Figure 5.1:a) Gloss retention of clear coatings and b) Gloss retention of white coatings after Florida exposure

5.2 Analysis of the surface roughness using AFM

Atomic force microscopy was used to analyse the topography of the samples. Figure 5.2 demonstrates how the RMS value remains relatively steady with exposure time for NS01 clear. The RMS value varies within approximately 100nm over the whole exposure period of 24 months. In the first four months of exposure there is a decrease in the RMS value from an average value of 109nm to 54nm after which the RMS value increases and reaches 148nm over the next six months. The roughness then began to decrease again and an average RMS value of 48nm was reached before increasing again after 18 months of exposure. The values here is not what is of significance, as the trend could be following what we see in the 500hrs of exposure for the QUVA data as the measured RMS values fluctuate without dramatic variation and are localised around the average value. NS03 clear shows a similar RMS trend to NS01 clear where the RMS values do not show a steep increase or decrease over time, so the surface roughness does not vary considerably.

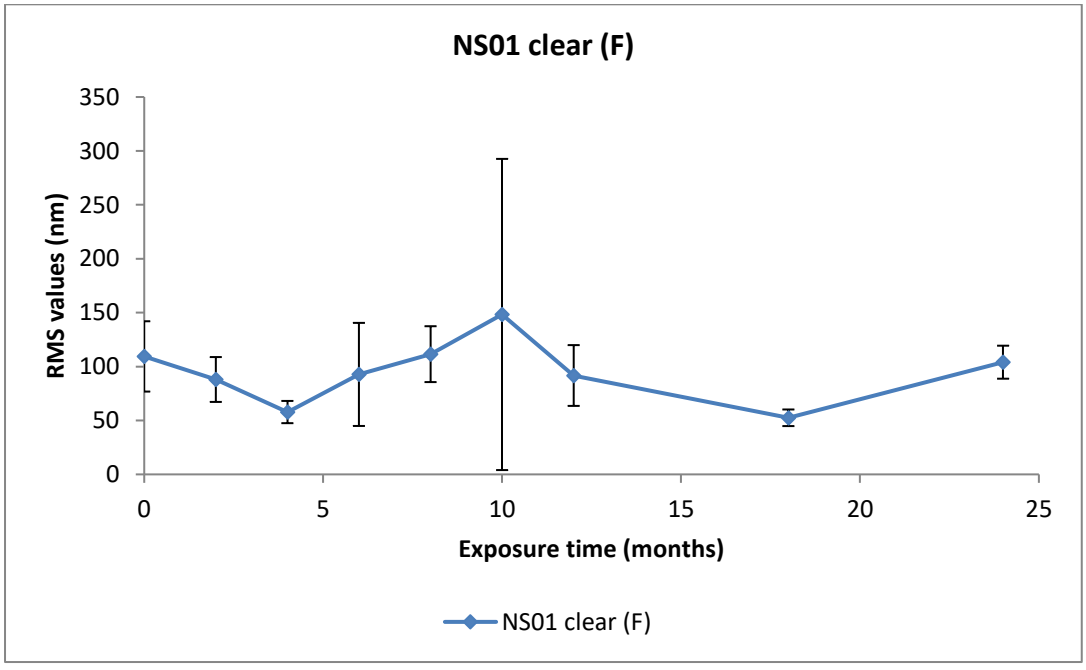

Figure 5.2: RMS value of NS01 clear after Florida exposure

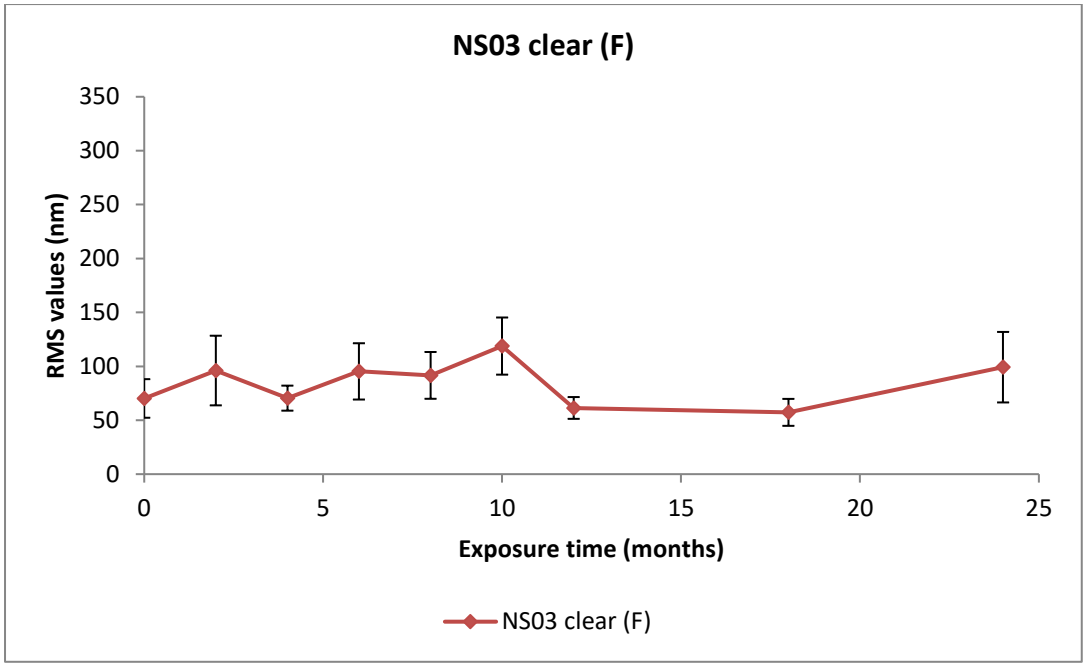

Figure 5.3: RMS values of NS03 clear after Florida exposure

After investigating the clear coats for NS01 and NS03, AFM was carried out on the white coatings, figure 5.4 and figure 5.5 respectively. It was found that the initial starting RMS value which is essentially measuring the surface roughness is higher than that of the clear coats. Where NS01 clear has an average starting RMS value of 109nm, NS01 white has a value of 253nm. Similarly, NS03 clear starts with 63nm whereas NS03 white starts with 209nm. The increased surface roughness is owed to the addition of titanium dioxide, TiO_2 pigment. The white surface which appears to be smooth to the naked eye is not as smooth as the clear coat. The pigment adds an extra dimension to the coating hence why the starting surface roughness is greater, at least twice as much of the clear coat. However, even whilst touching the surface, the surface is relatively smooth.

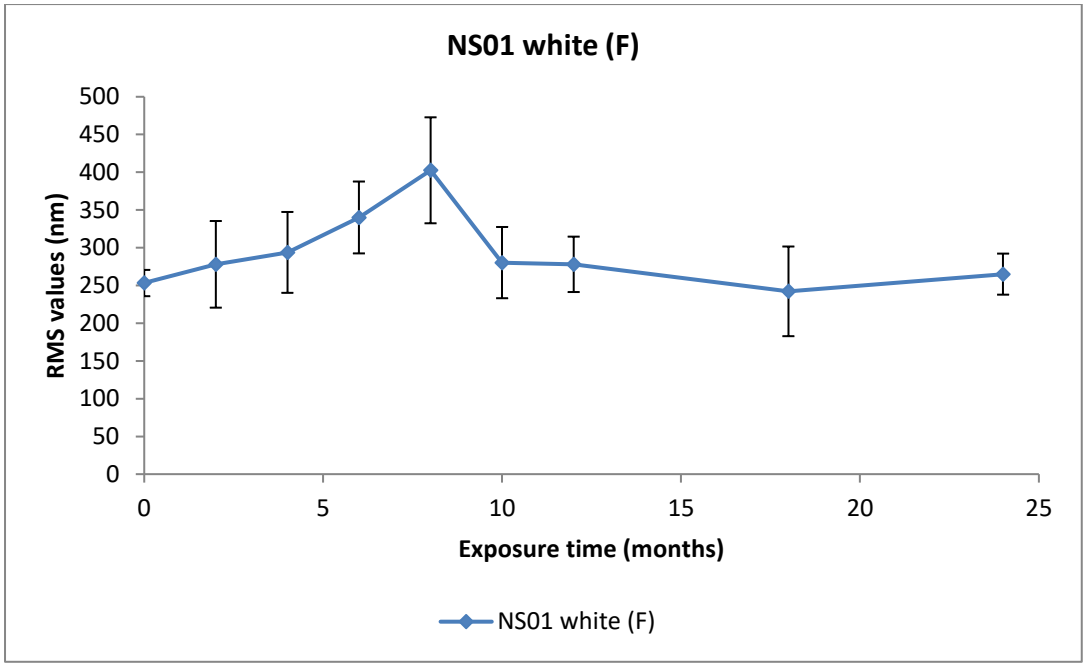

Figure 5.4: RMS value of NS01 white after Florida exposure

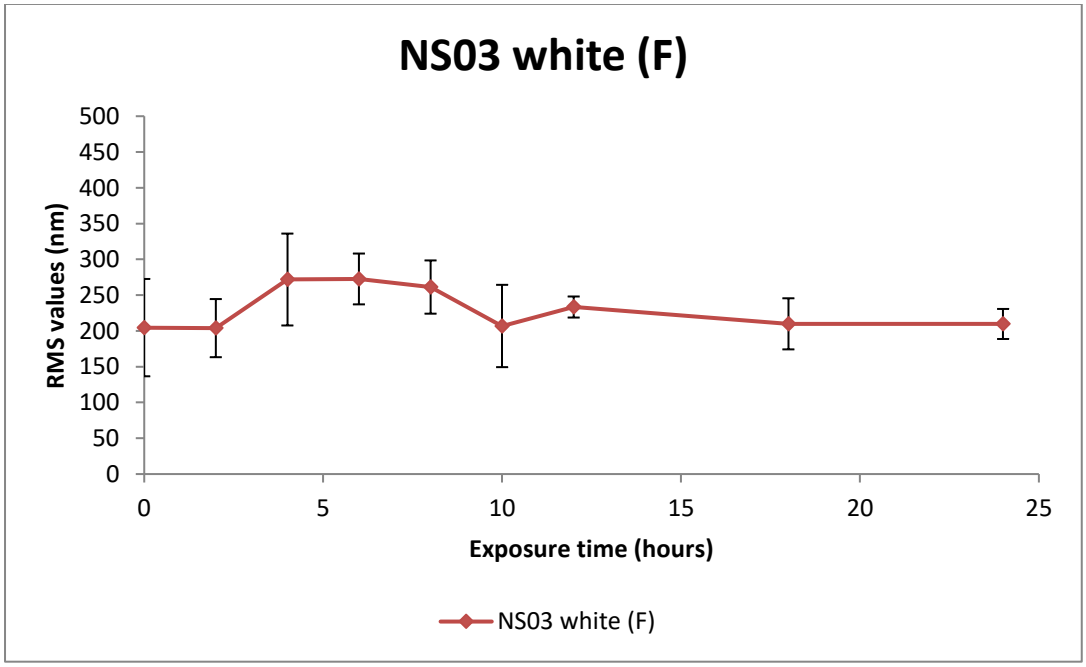

Figure 5.5: RMS value of NS03 white after Florida exposure

5.3 Analysis of the chemical make-up using photoacoustic Fourier transform infrared spectroscopy

The PA-FTIR data analysis procedure of the Florida exposed samples is the same as that of the QUVA exposed samples. The details of the analysis technique is described in Chapter 4, section 4.3.1. The peaks used to analyse the data are also the same as the formula is identical, only the exposure conditions have changed. Firstly, analysing the spectra of NS01 clear (circled in figure 5.7) suggests there is an increase in the –OH,-NH peak and a deterioration of the melamine peak (circled in figure 5.8). It is hard to determine the changes taking place in the methylene peak from the spectra alone.

NS03 clear also displays similar results to NS01 clear, figure 4.9. An increase in –OH,-NH peak is observed from figure 5.10. Figure 5.11 displays the changing crosslinked environment around the melamine crosslinker. The melamine peak is seen to disintegrate however, changes in the CH peak are difficult to observe. After examining the visible peak changes peak analysis was carried out on the spectra of both samples over all exposure time. The peak analysis data follows.

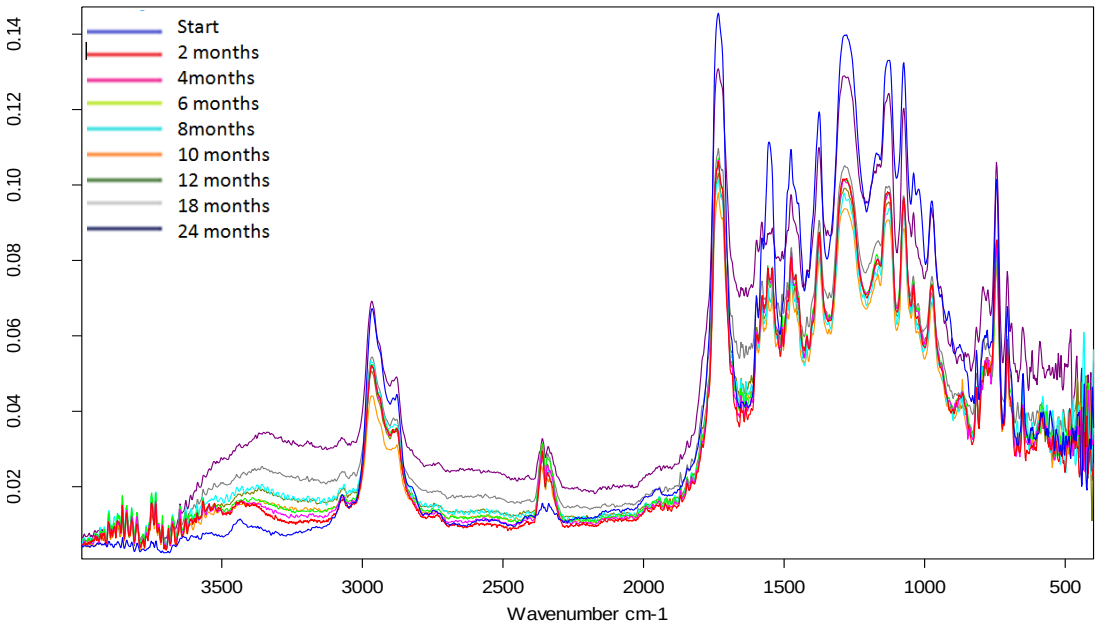

Figure 5.6: PA-FTIR spectra off samples exposed in Florida for NS01 clear

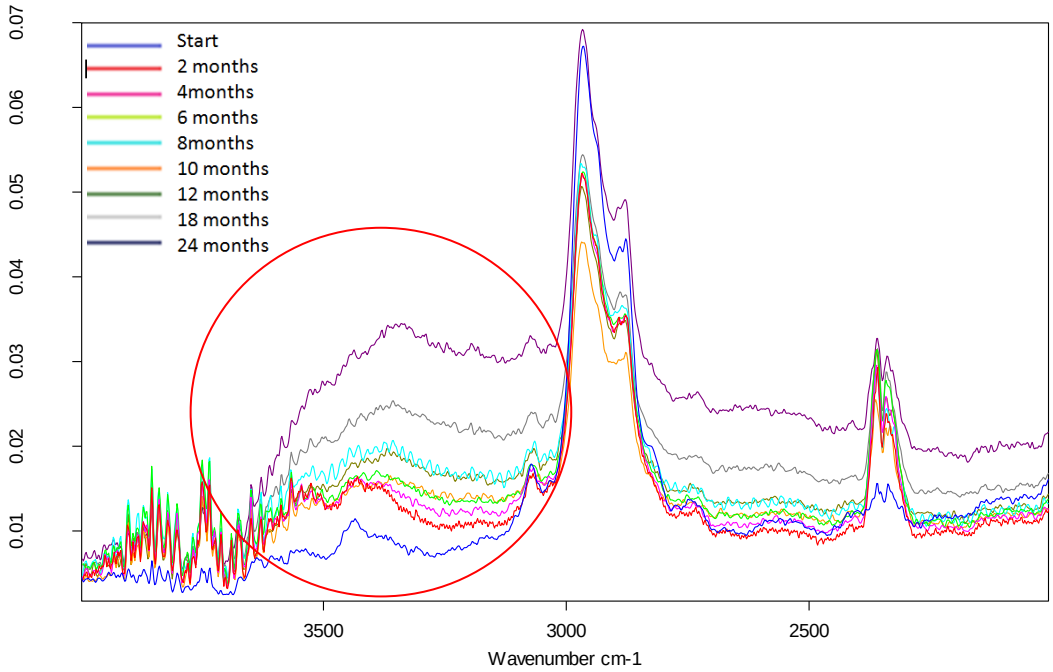

Figure 5.7: Changes in the -OH,-NH peak for NS01 clear sample

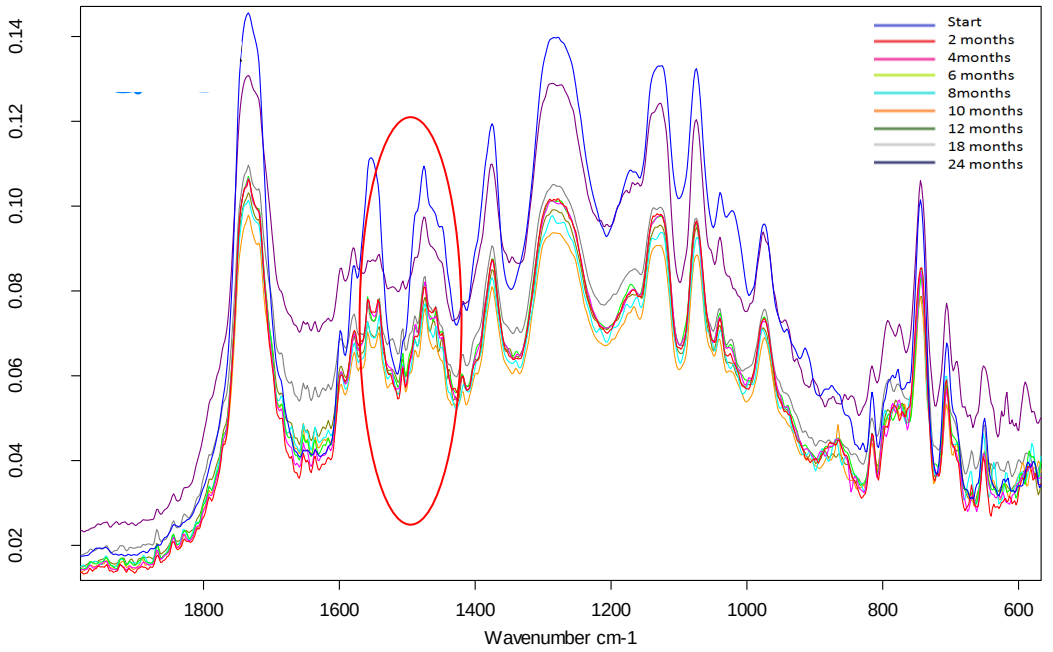

Figure 5.8: Changes in the melamine peak for NS01 clear sample

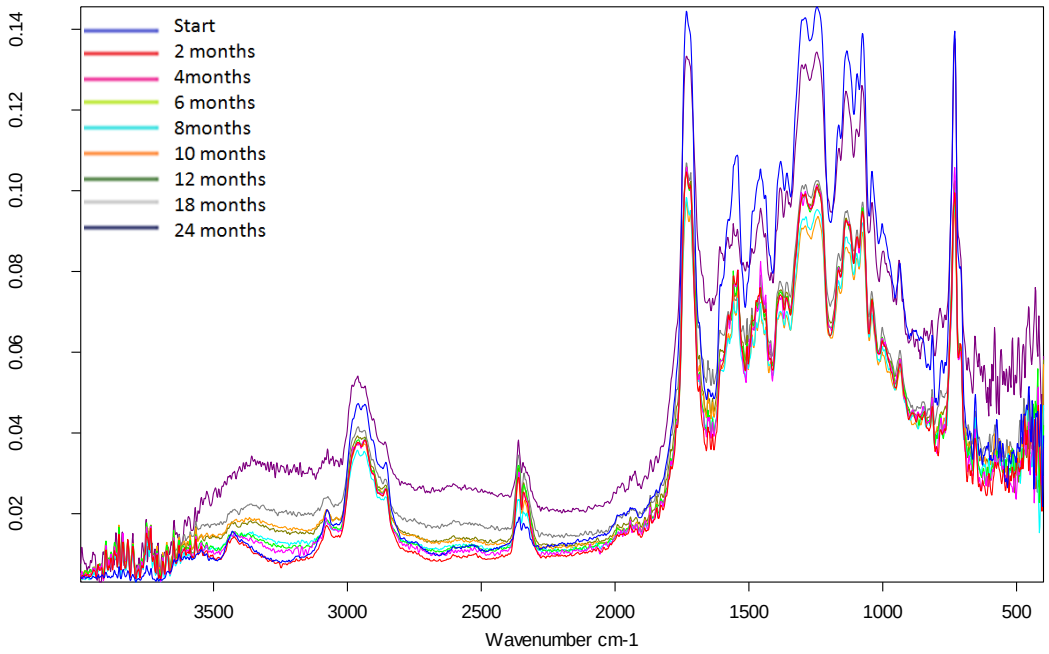

Figure 5.9: PA-FTIR spectra of all samples exposed in Florida for NS03 clear

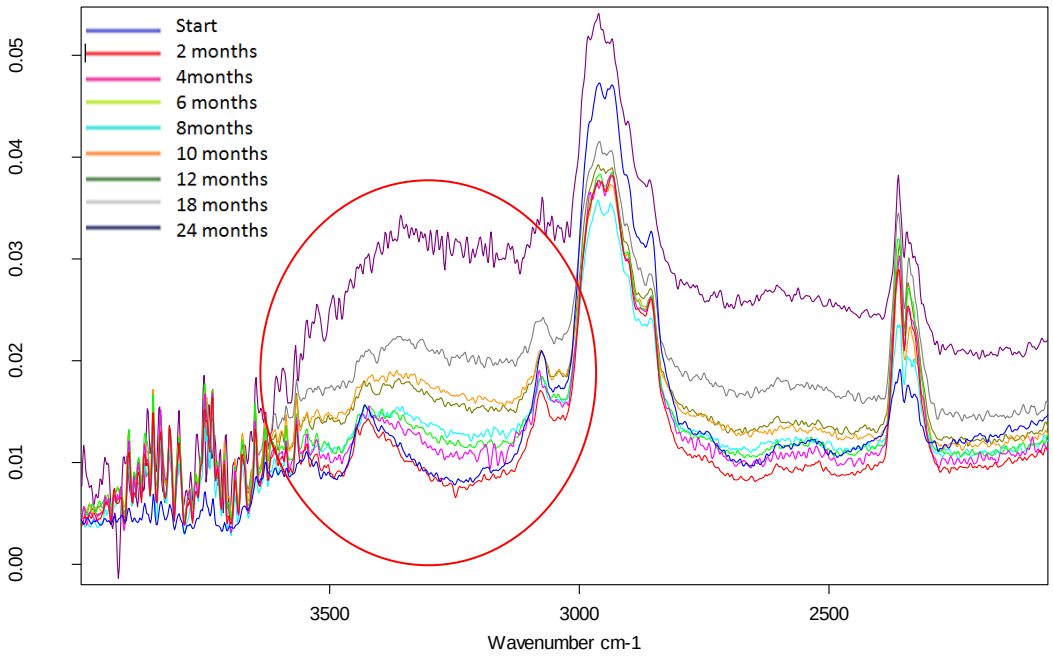

Figure 5.10: Changes in the OH peak for NS03 clear

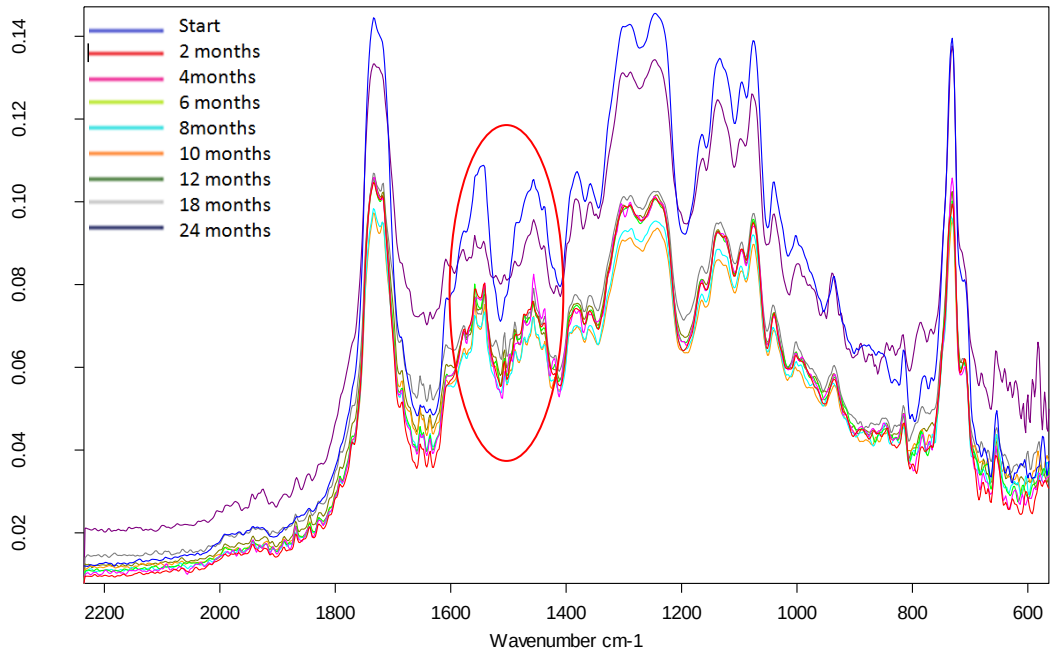

Figure 5.11: Changes in the melamine peak for NS03 clear

Having carried out the peak analysis on the –OH,-NH peak, a continuous increase in the peak area was found. Figure 5.12 shows a greater increase in the peak area of NS01 clear from 0% to 331% after 24vmonths. NS03 clear closely follows the same trend except the increase in –OH,-NH peak is from 0 to 276%. Within the 24 months of exposure there is no sign of the increasing OH production stabilising. Accelerated testing is done to get the bigger picture of how the coating reacts to UV exposure. Hence, the data of 24 months of natural exposure may be equal to the initial increase we see in the QUVA data and perhaps will stabilise has the exposure period continued. This however, cannot be confirmed at this stage but is worth considering. The melamine and methylene loss for NS01 and NS03 also seem to be closely following each other. What is worth noting is that NS03 clear shows a melamine loss from 100% to 40%, 20% less than NS03 clear after 24 months and this is consistent with the change in the –OH,-NH peak. However, the methylene peak which showed a similar degradation rate for both coatings up until 18 months is reversed. At 18 months the methylene area for NS03 clear decreases from 73% to 50% whereas for NS01 clear it decreases from 67% to 59%.

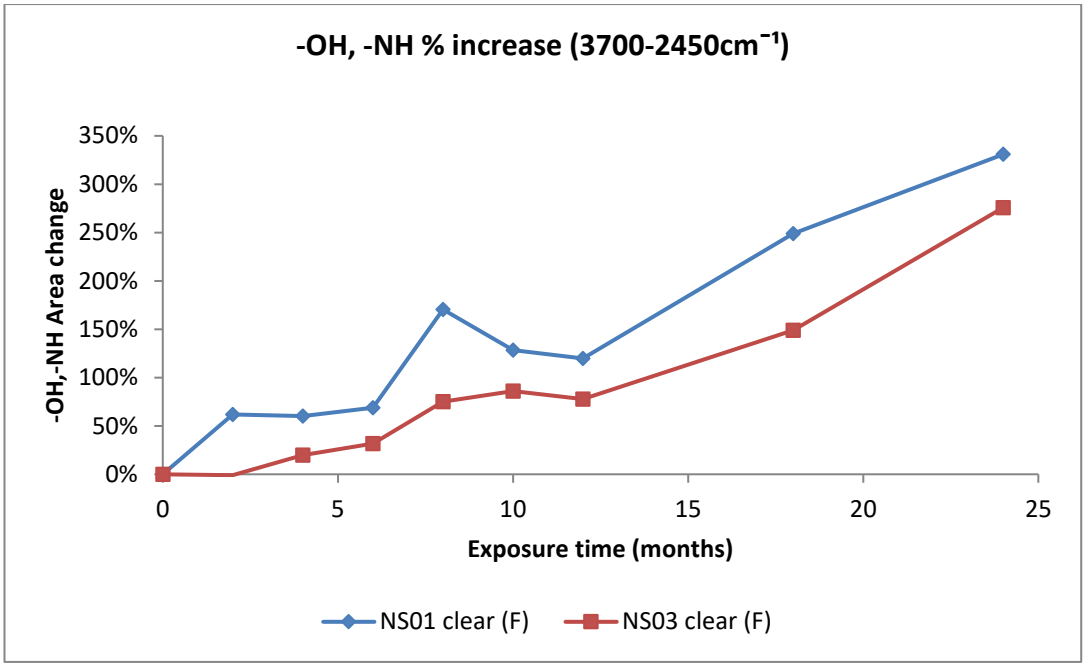

Figure 5.12: -OH, -NH peak analysis against time for NS01 and NS03 clear

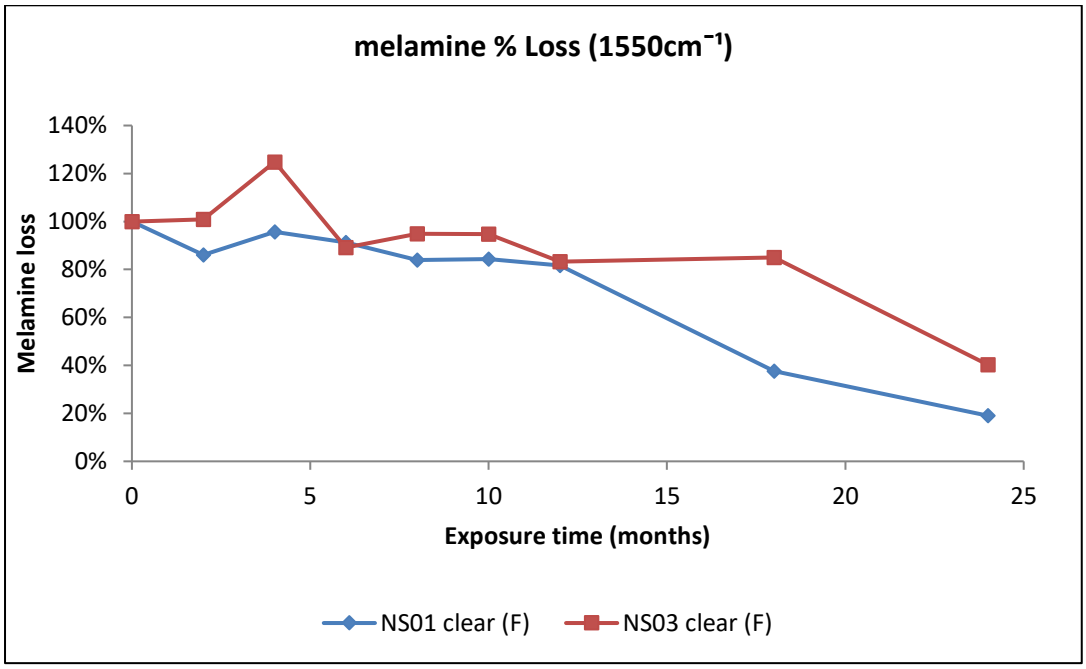

Figure 5.13: melamine peak analysis of NS01 and NS03 clear

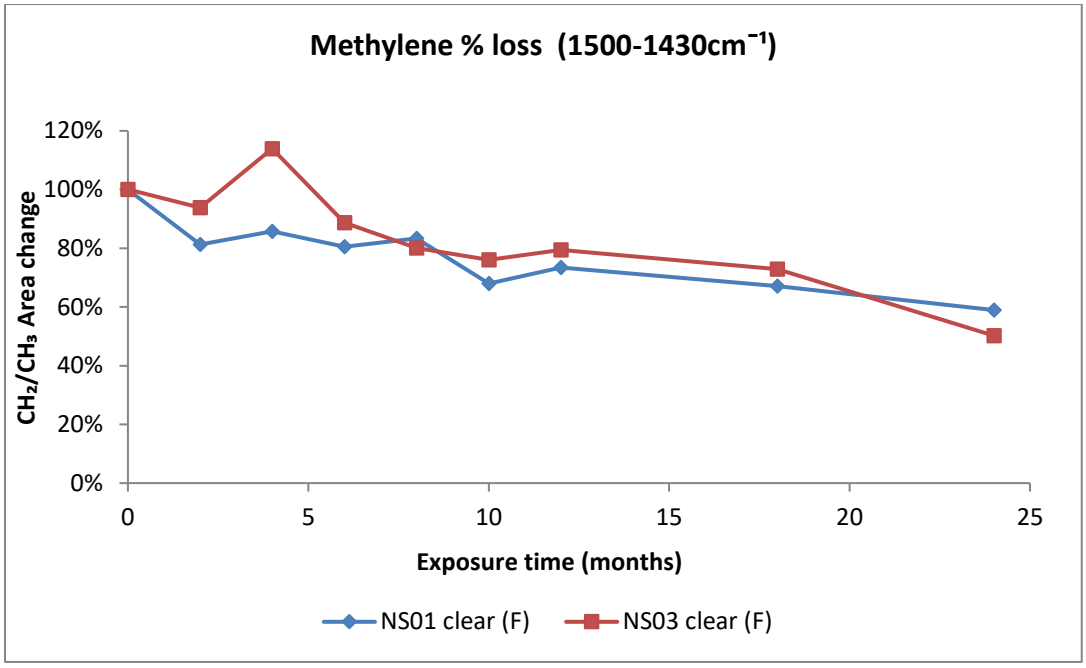

Figure 5.14: Methylene peak analysis of NS01 and NS03 clear

Looking at the data in figure 5.15, of NS01 white and NS03 white, an increase of approximately 50% can be seen for both coatings after 24 months of exposure for the –OH/-NH peak. This is notably low in comparison to the clear coatings which showed 250-300% increase in peak area over the same period. No significant change is visible in the spectra of NS01 white and NS03 white except for some increase in the –OH/-NH peak (figure 5.18 and 5.19 respectively). Similarly, the methylene loss (figure 5.16) and melamine loss (figure 5.17) for the white coatings is compressed. Over the same exposure period the loss is 20% at most for the white coatings and the only difference between the clear and white samples is the addition of the rutile titanium dioxide. Perhaps this is the reason of the stabilised coating against UV exposure. The degradation performance is closely analysed in the following chapter, chapter 6.

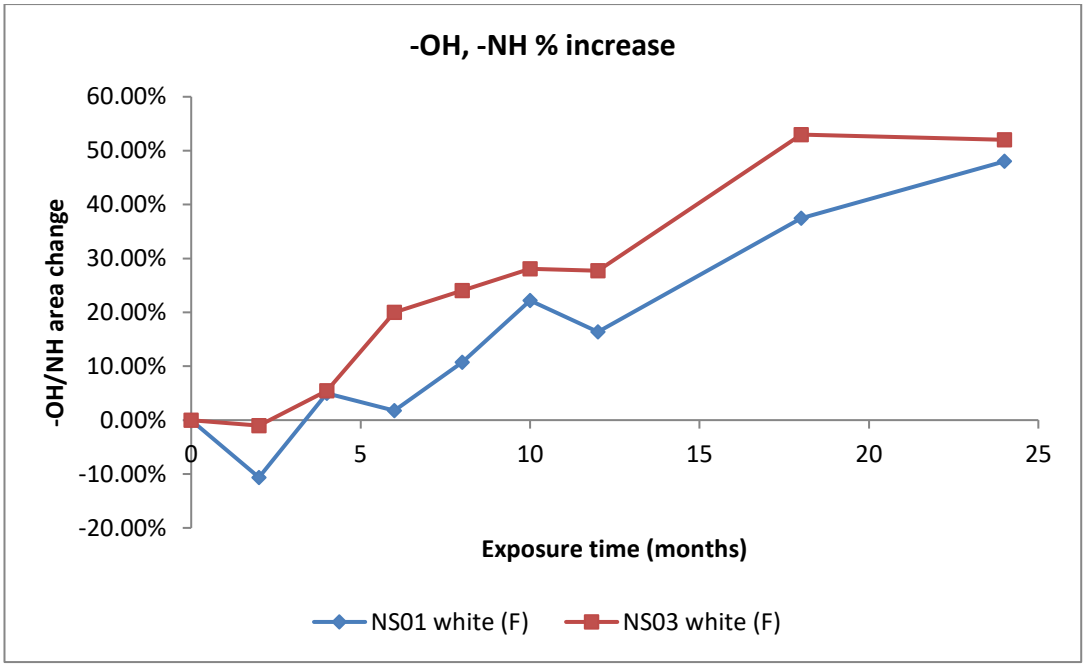

Figure 5.15: -OH/-NH peak analysis of NS01 and NS03 white

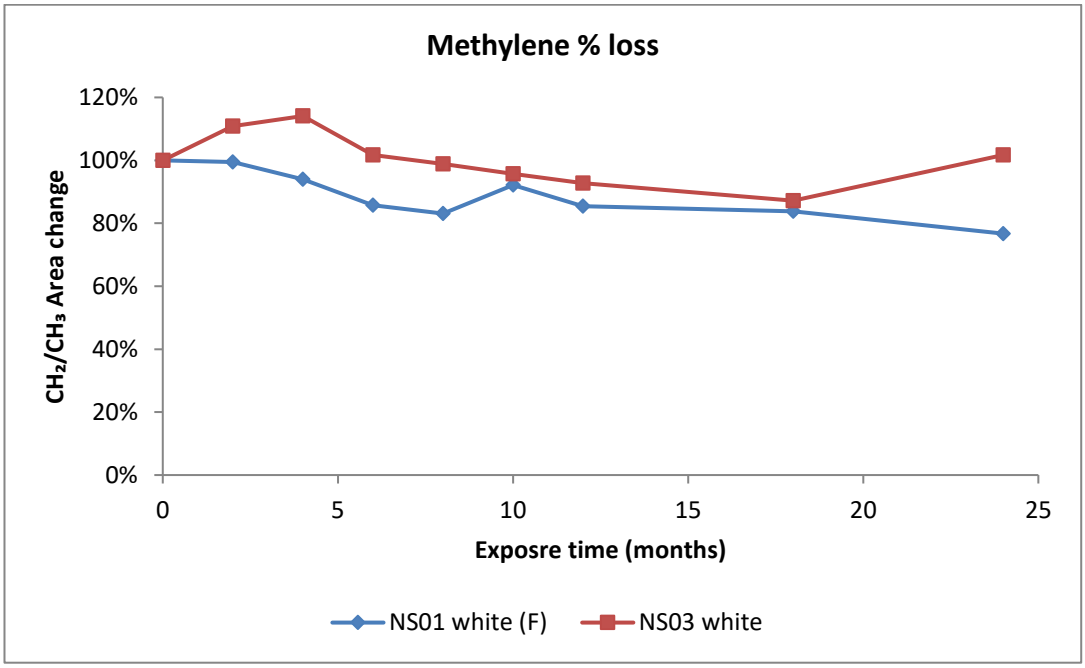

Figure 5.16: Methylene peak analysis of NS01 and NS03 white

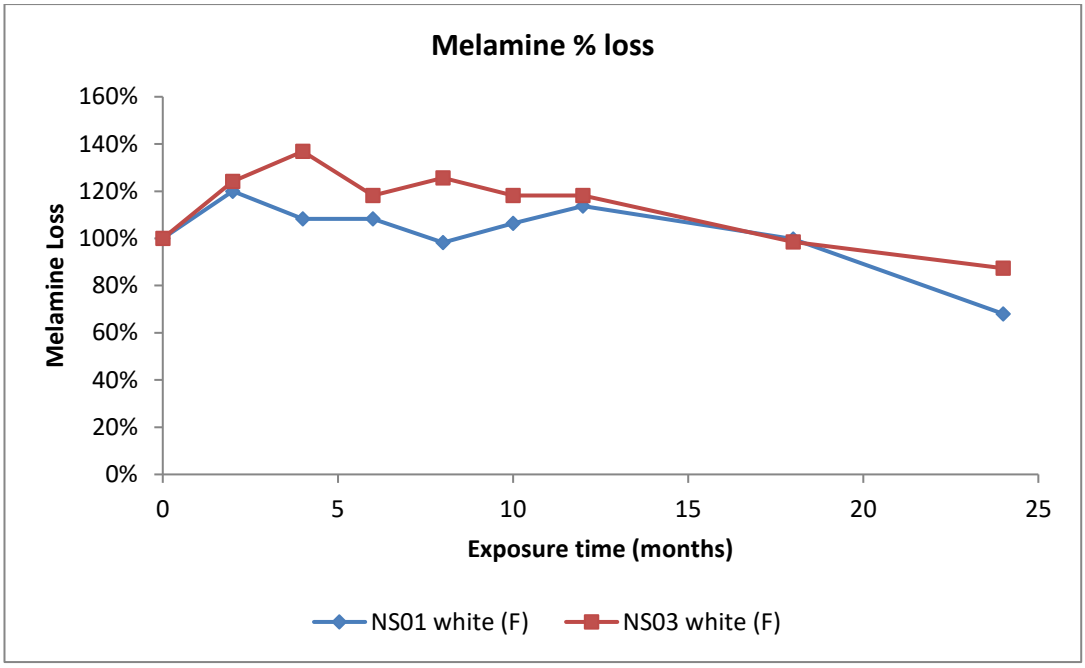

Figure 5.17: Melamine peak analysis for NS01 and NS03 white

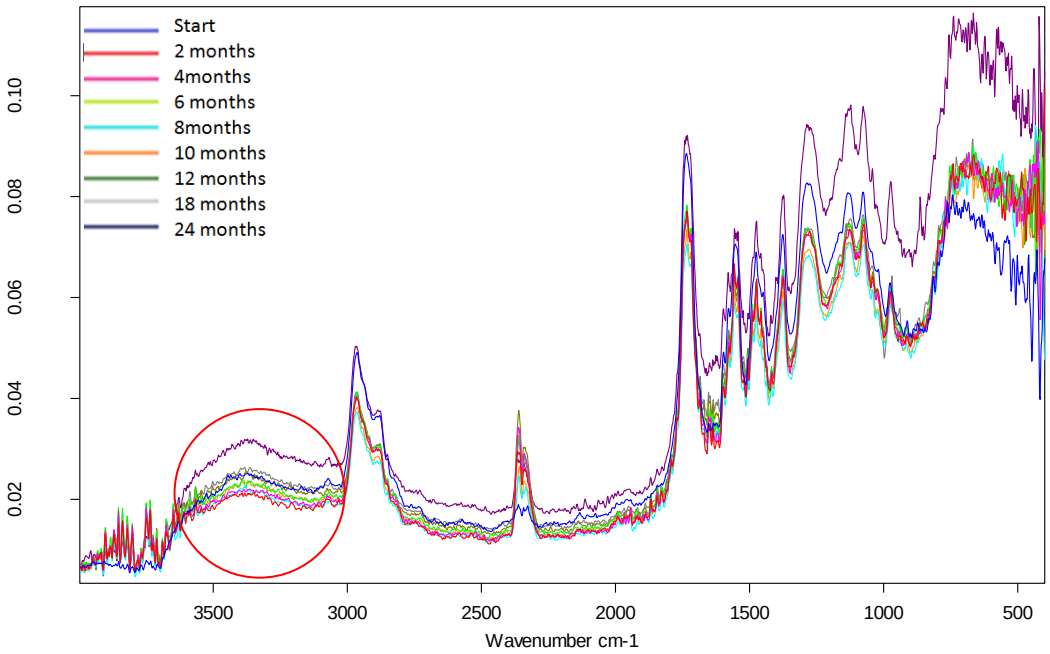

Figure 5.18: PA-FTIR spectra of all NS01 white samples exposed in Florida

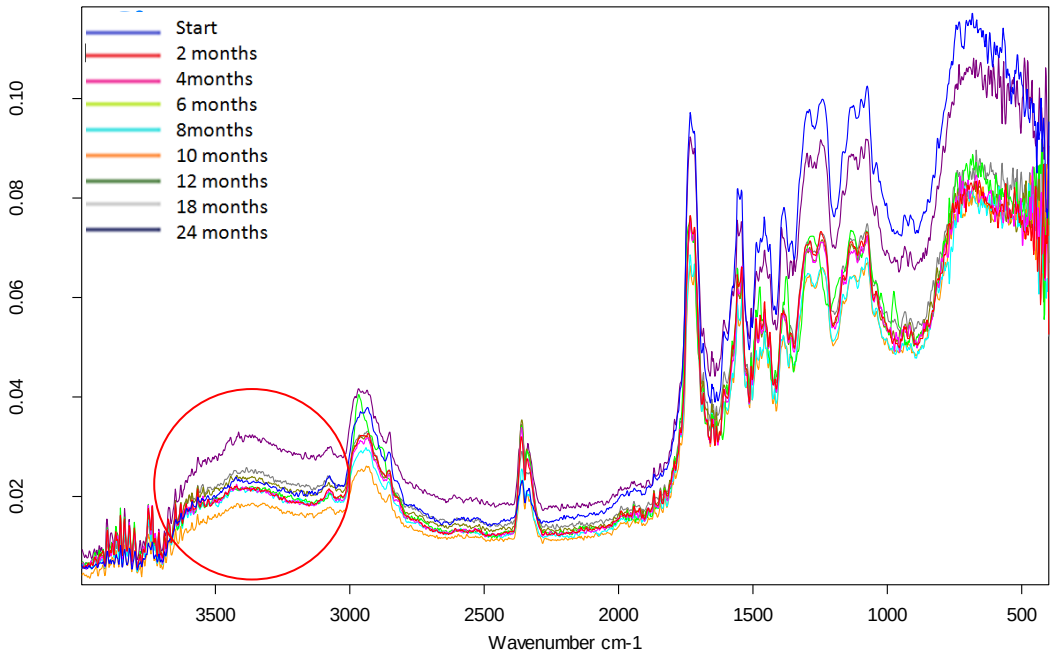

Figure 5.19: PA-FTIR spectra of all NS03 white samples exposed in Florida

5.4 Surface analysis using scanning electron microscopy

Scanning electron microscopy (SEM) was carried out at a tilt of 75˚ as highlighted in chapter 4 the significance of tilting the sample is because a head on view of the sample surface could not give detailed information about the roughness of the surface. Again, the sample was tilted using a sample holder specifically designed in the Queen Mary University of London workshop. SEM was carried out on samples, NS01 clear, NS03 clear, NS01 white and NS03 white, unexposed and exposed for 24 months. The images enclosed are for the clear samples only as they showed greater chemical changes as well as changes in physical properties such as roughness and gloss retention than the white samples.

Figure 5.20 displays a) the unexposed surface image of NS01 clear and b) the surface exposed at 24 months. The topography of the unexposed sample surface is relatively flat. On the other hand, the exposed sample shows some preferential degradation. The noticeable scratches on the surface and slightly raised features do not add to the RMS value detected using AFM. Figure 5.21 shows both the unexposed and exposed sample of NS03 clear. The unexposed sample shows a flat surface similar to the unexposed NS01 clear sample, as expected. The exposed sample shows indents in the surface however; regardless of this the remaining surface is intact and not degraded. It may be owing to this that the RMS value shows no significant change.

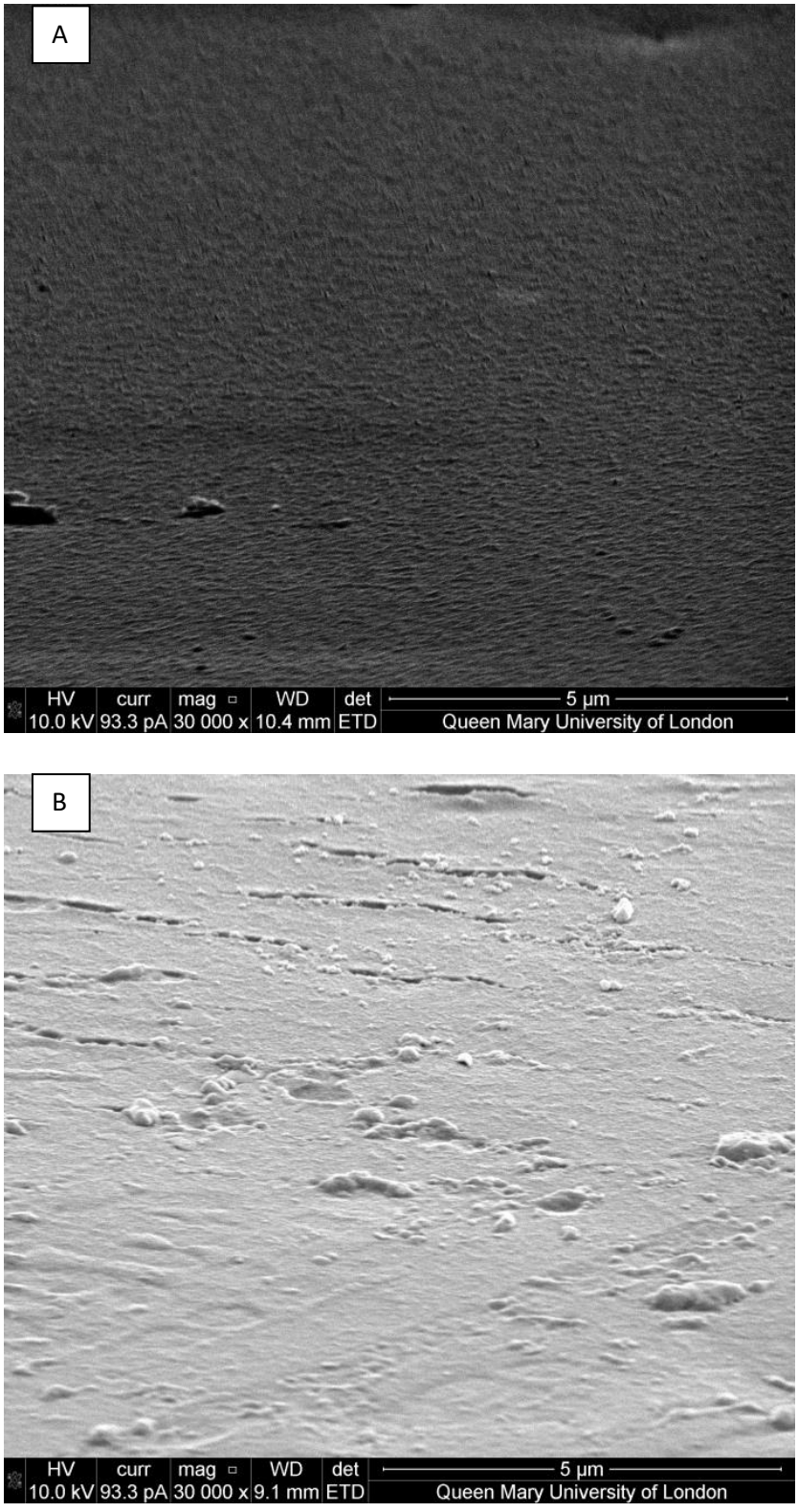

Figure 5.20: Surface analysis of a) NS01 clear, unexposed and b) NS01 clear, exposed at 24 months

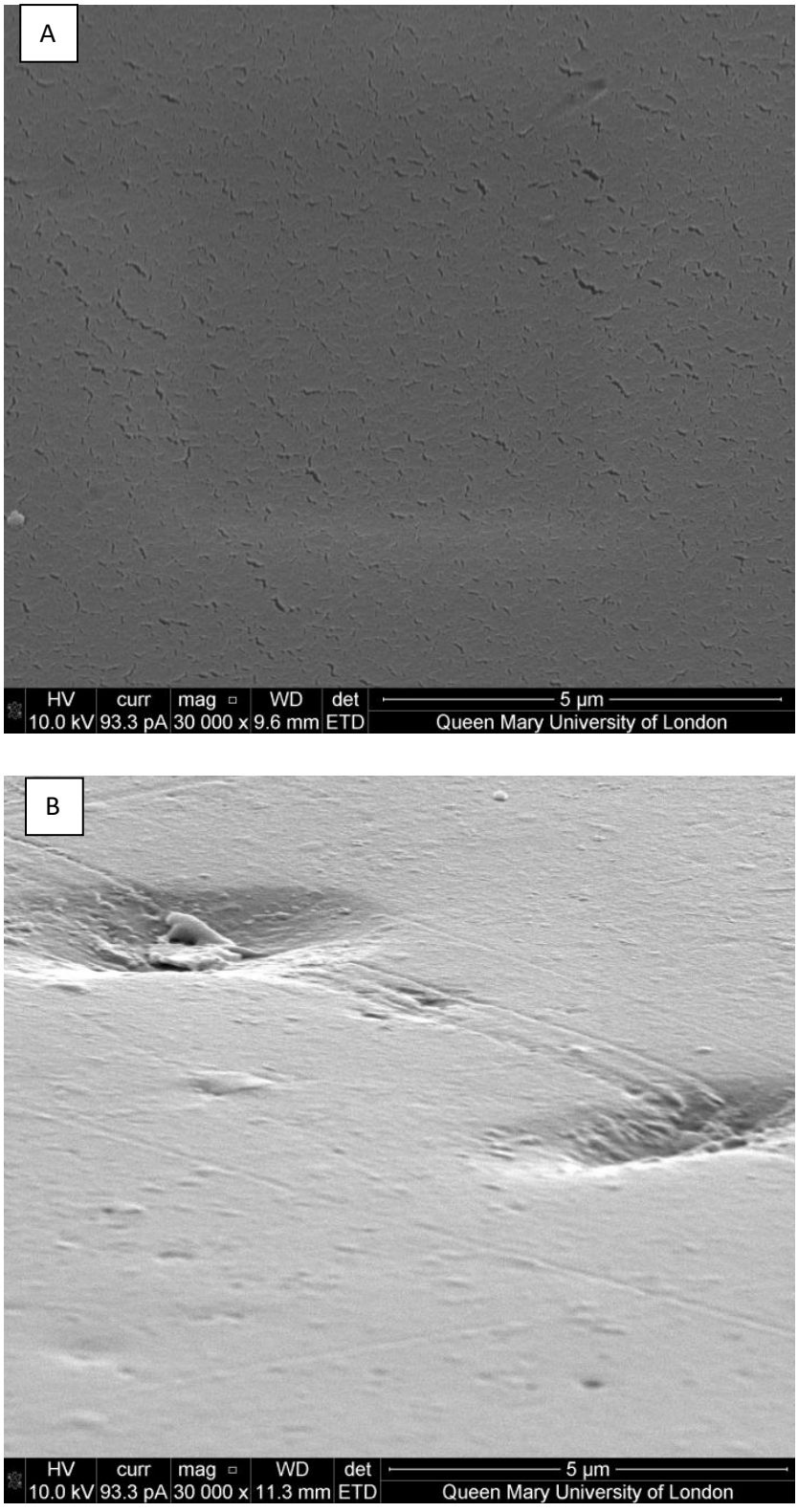

Figure 5.21: Surface analysis of a) NS03 clear, unexposed and b) NS03 clear, exposed at 24 months

5.5 Conclusion of experimental results

QUVA weathered samples are accelerated tests done to predict the service life of an industrial coating by close analysis of the degradation mechanism(s). Accelerated tests give an indication of how the coating will perform when exposed to external environments. In this chapter the experimental results for naturally weathered samples have been analysed to correlate with the data obtained from the accelerated weathered samples.

Gloss retention of NS01 clear and NS03 clear is greater than 80% for the first 18months, after which we see the onset of a reduction. This reduction is not detrimental yet but is predicted to keep reducing after this point if the coating follows the trend observed for the QUVA weathered samples. Addition of TiO_2 to the formulation, in NS01 and NS03 white improved the gloss retention, and at 24 months, is when we see the gloss to reach 80%. The surface roughness is also affected by the addition of TiO_2. The pigment adds an extra dimension to the coating as it sits close to the surface and within the bulk material. Therefore, the initial roughness for the white samples is greater than the clear samples. After 24 months of exposure there is no significant increase in RMS values hence, the coating has not physically degraded beyond the initial observed roughness.

SEM images, however, show the formation of some features on the surface of NS01 and some indentation on the surface of NS03. This could be due to the rapid chemical degradation observed in PA-FTIR data. The data shows a 250% increase in the percentage of Oh/NH groups detected at the surface after 24months natural exposure in Florida. A similar rate of OH/NH production is observed for NS01 clear after QUVA exposure hence the two testing methods positively correlate and the extent of degradation of NS01 clear can be predicted.

On the other hand, the results of NS03 clear differ for QUVA and Florida exposed samples. After maximum QUVA exposure the percentage increase in OH/NH groups was 89%, significantly lower than 250% detected after 24months exposure in Florida. This unexpected performance could be a result of higher UV and moisture exposure in natural Florida weather. UV irradiation could trigger cleavage of bonds producing radicals and subsequent oxidative chemical reactions which produce hydroxyl groups. The timely QUVA moisture and humidity cycles only attempt to reflect the natural weather but in reality other factors affect degradation in a natural environment.

Further detail on the degradation performance of the coatings can be found in chapter 6.

6. Degradation performance of polyester based coil coatings and partially bio-sourced polyester coatings

The purpose of this research was to analyse how a new coil coating formulation performs as an exterior coating, specifically under UV exposure. The idea was to introduce sustainable coil coatings into the market with minimal use of petroleum-based resin. To begin with three formulations were under study; a polyester coating with a fully petroleum-based resin, NS01, a fully bio-sourced resin in NS02 and lastly a NS03 which made use of a partially bio-sourced resin. The resin was the only part of the formulation which was altered, the resin was crosslinked with the hexamethoxy methyl melamine crosslinker. NS01 was kept as the standard as it is the current selling formulation for coil coatings.

In this chapter the main point of discussion is how NS03, a partially bio-sourced polyester coating performed in comparison to NS01 as NS02 completely degraded in the artificial testing and therefore further analysis was not carried out. The white NS01 and NS03 coatings have the same formula as their clear counterparts, except they have the addition of coated rutile titanium dioxide (TiO_2), the pigment which gives it the white colour. The results of analysis carried out on the artificially tested samples using a QUVA machine are reported in chapter 4 and the results for analysis on the samples carried under natural weathering tests carried out in Florida are reported in chapter 5. The degradation performance was assessed through a series of experiments to quantify the physical and chemical degradation taking place after exposure. The artificial testing does not depict the exact conditions in natural exposure of the coating. However, it does give an approximate measure of how the coating will react.

It was seen that after QUVA exposure the gloss retention for NS01 clear saw a steady decrease whereas after 24 months of exposure in Florida the gloss retention was still good. NS03 clear on the other hand shows better performance until 1200hrs of QUVA exposure, after which it declines rapidly. Figure 6.1 displays the surface images of NS03 clear at the start (a), after 1007hrs of QUVA exposure (b) and after 1227 hours of QUVA exposure. From the images a change in the surface topography, from a completely uniform surface to one with various features is seen.

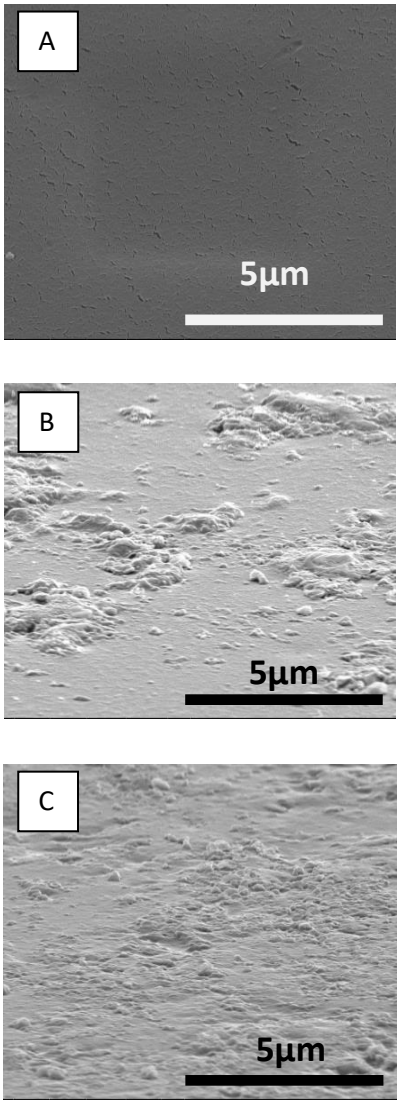

Figure 6.1: NS03 clear a) 0hrs exposure, b) 1007hrs exposure and c) 1227hrs exposure

SEM images in figure 6.2 (a), show that after 1007 hours of exposure the surface of the sample has started to abrade. Majority of the surface was found to be relatively flat however, scattered along the surface were 3D structures which could be a result from physical degradation of the surface. At 1227 hours (figure 6.2 (b)) of exposure the complete surface is noticed to roughen significantly with a few dips in the sample surface which later form pits.

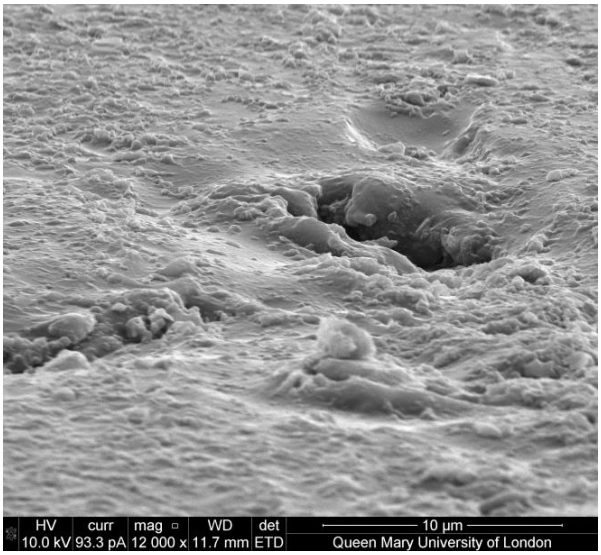

Figure 6.2: SEM images of NS03 clear samples showing the formation of 'holes' or 'pits'

It is after these periods of exposure (1227hrs) that the dramatic increase in root mean square roughness and the percentage of gloss loss is observed and after using SEM to analyse the surface it becomes apparent that the observed change was due to the deterioration of the sample surface. The gloss retention has a positive correlation with the surface roughness as the change in the surface topography can influence the amount of gloss reflected. The gloss meter is used to read the gloss of each sample. This is done by the reflection of light in the gloss meter. If light is reflected from a smooth surface there is almost 100% reflection from the surface as there is no scattering of the ray of light as there is no interference in the path of reflection. The roughness of the surface of a sample can cause the light to scatter, as shown in figure 4.6. The uneven sample surface introduces points of interference upon which when encountered the rays of light scatter in many directions. Thus, the light measured by the gloss meter is a reflection of the surface topography and the two measurements correlate positively indicating that if the surface remains intact the gloss retention will also be improved.

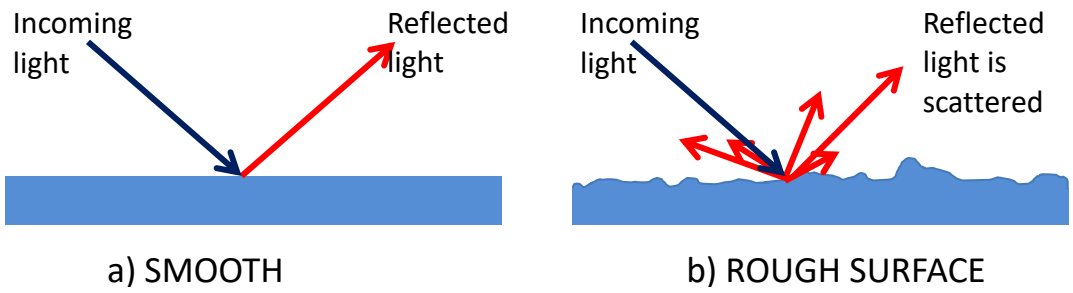

Figure 6.3: How light is reflected from a) a smooth surface and b) a rough surface

The roughness seen in the SEM images as stated earlier was reflected in the RMS value calculated by the AFM software. The change in roughness is also depicted in the 3D images presented in figure 6.4. From figure 6.4 (a) the topography of the surface shows a relatively uniform surface with some 3D structures whereas from figure 6.4 (b) we see the whole surface is beginning to roughen. After 2206 hours the surface becomes extremely rough. The formation of holes and pits also become obvious in the 3D topography images of different areas on the surface of the sample exposed up to 2206 hours (figure 6.5 (a) and (b)).

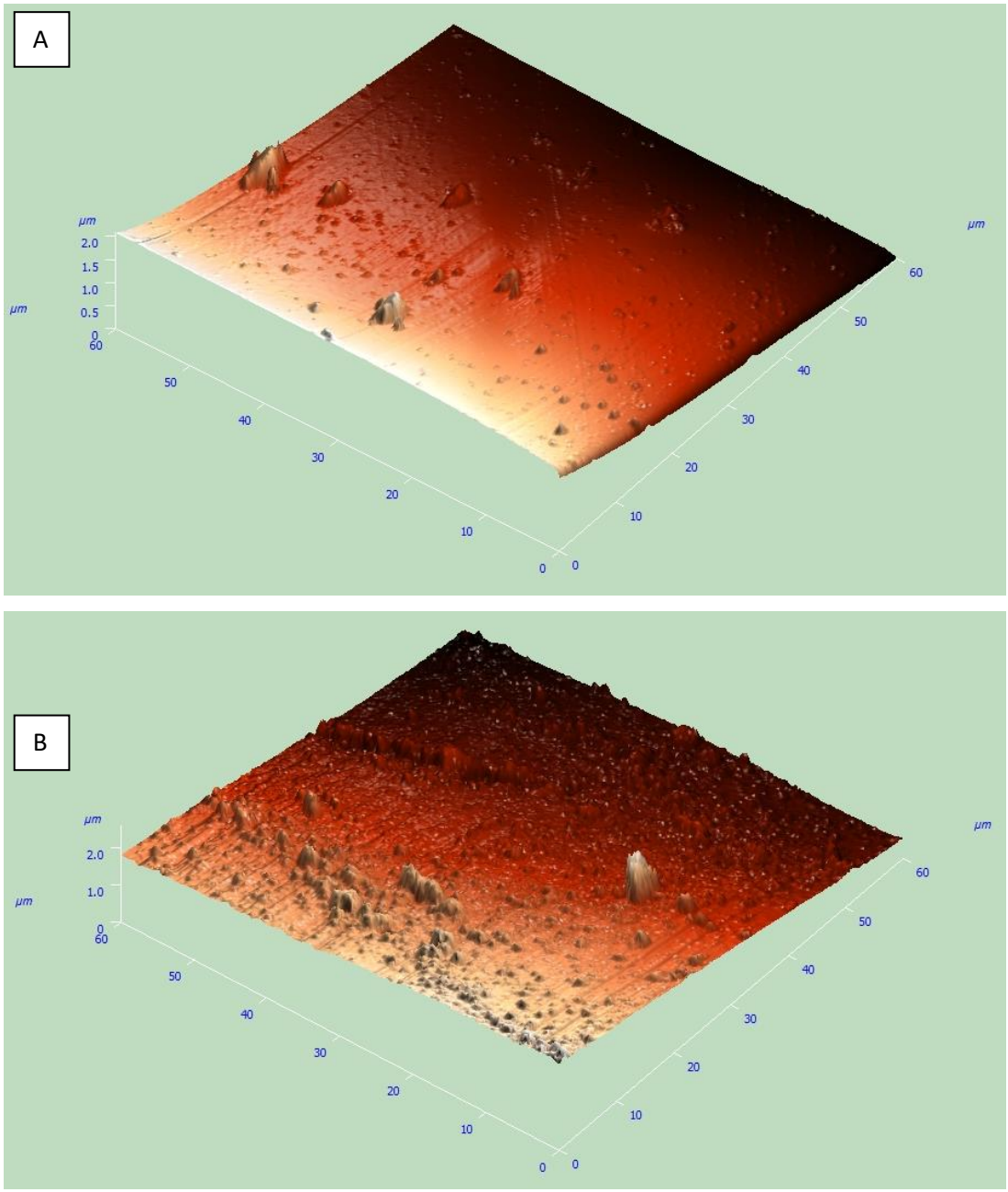

Figure 6.4: 3D AFM image of NS03 clear exposed at a) 1007hrs and b) 1227hrs

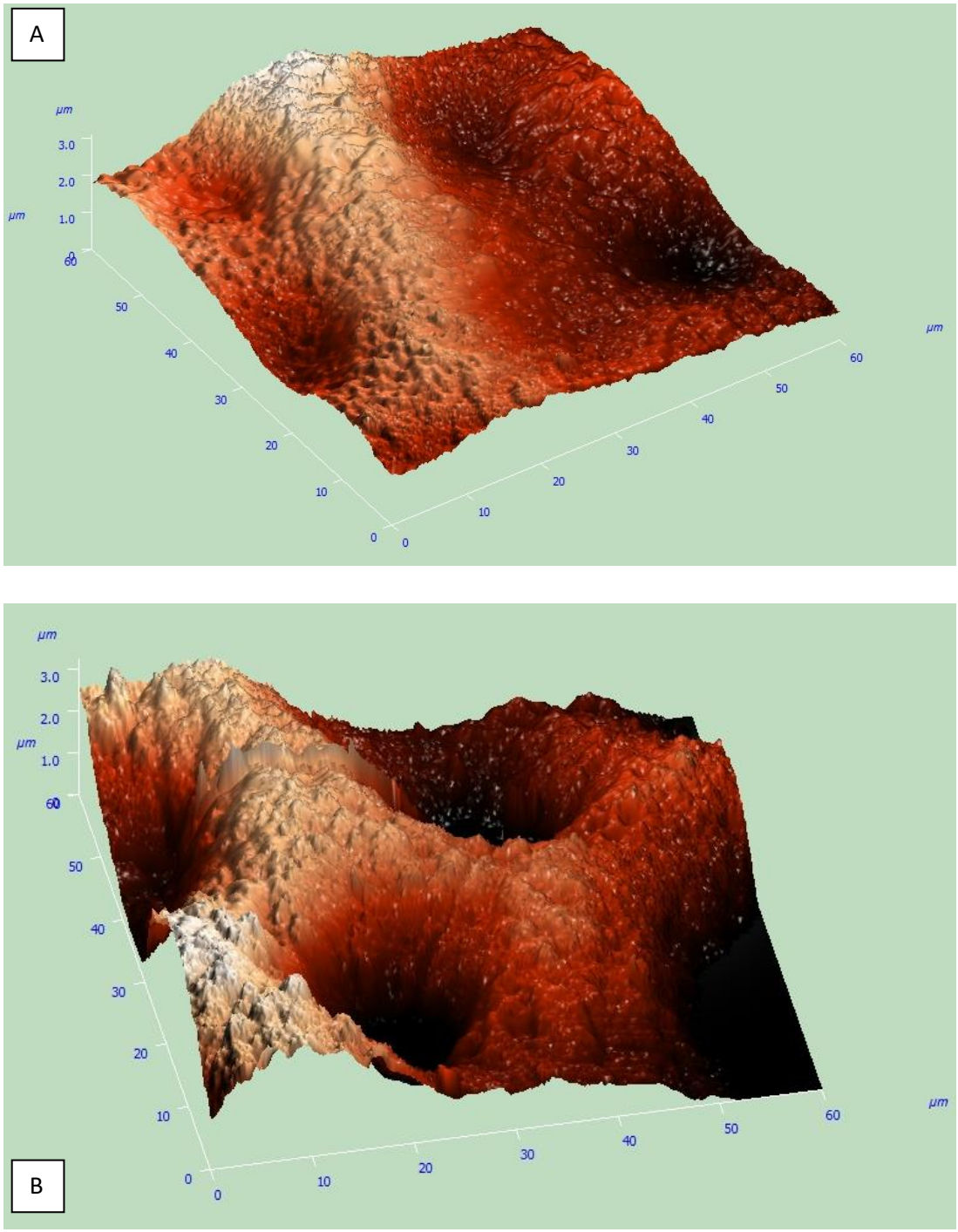

Figure 6.5: a) and b) 3D AFM image of NS03 clear exposed from different areas of the sample

Another important point to note is the consistent behaviour of NS03 clear after approximately 1200hrs of QUVA exposure with the gloss retention, the AFM roughness and the chemical degradation. The chemical degradation examined via PA-FTIR suggests that the coating does not degrade solely due to photo-oxidation. The NS03 clear coating which is initially stable regarding photo-oxidation shows a great loss in melamine and an even greater

unexpected loss in methylene percentage. NS03 resin has long chain aliphatic portions which is the cause of rapid degradation after the 1200hrs. The breakdown of the aliphatic chains is evident through the methylene peak change (CH_2/CH_3) and the calculated loss from 100% to approximately 20%. After the degradation initiation time (up to 1200 hrs) the breakdown of the methylene groups causes the surface to deteriorate rapidly. The breakdown of the polyester resin could be due to UV irradiation. This is seen in the Florida exposed samples, which show an increase in OH/NH groups, suggesting that significant degradation is taking place in the natural environment, even though the same rate of increase in OH/NH is not observed in the QUVA samples.

Another form of degradation which affects coil coatings is hydrolysis – the cleavage of chemical bonds due to the addition of water. Amides and Esters undergo hydrolysis. In a trans-esterfication reaction, hydroxyl groups in polyesters crosslink with the methoxy groups on melamine side chains producing ether links. The hydrolysis of an ester produces carboxylic acid and alcohol. In the case of polyester/melamine resin, the hydrolysis of the ether linkage results in the production of melamine methylol groups which can decompose into amine groups and formaldehyde (Batista et al, 2011). The production of amines would lead to an increase in the –OH/-NH peak but the NS03 resin seems to resist hydrolysis and photo-oxidation better than NS01, in the absence of titanium dioxide.

The specific reason for the enhanced photo-oxidation resistance of the NS03 clear is not apparent. However, it may be due to the lack of 'short-chain aliphatic di-acids' in the bio-based binder or it is a possibility that the aromatic acid used in the formulation has better UV stability and may also be greater in resisting hydrolysis (Reichmanis et al, 1993). To hypothesise an exact degradation mechanism, one needs to be aware of the exact composition of the bio-sourced resin. Having discussed the possibilities with the development team at Beckers, Ltd, a possible mechanism to describe this degradation pattern was discussed. It is known that the bio-based polyester resin contains long chain aliphatic monomers and it may be that prior to exposure a chain "*gives rise to weak pseudo-cyclic conformations"* (Siyab et al, 2016) and the hydrophobicity is also known to increase with increasing carbon chain length (Liu et al, 2006). This concept was also illustrated. Figure 6.6 shows that under increased temperature, UV, moisture and stress, the pseudo-cyclic conformation may straighten out making protons more susceptible to free radical attack.

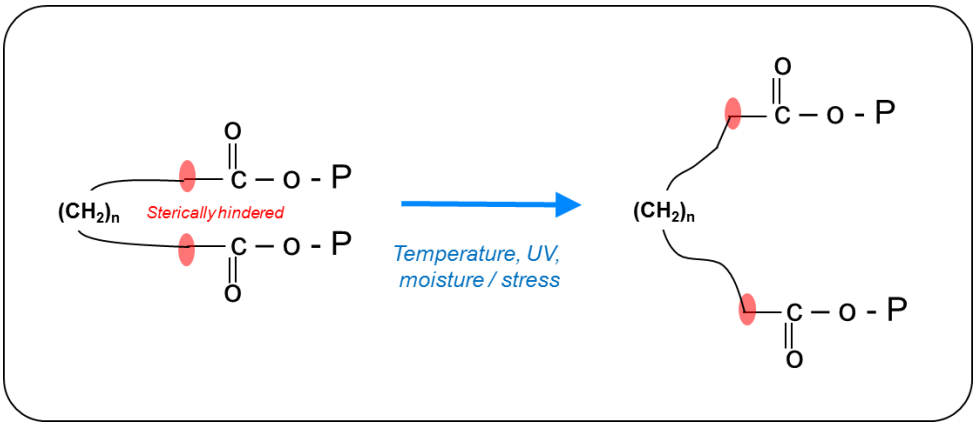

Figure 6.6: Proposed mechanism for NS03 clear degradation behaviour (Siyab et al, 2016)

The addition of rutile titanium dioxide in the white coatings has shown to stabilise the formulation. Pigments such as titanium dioxide and zinc oxide, can limit the penetration of UV light energy thus provided UV stabilisation (Mark F.M, 2007). This is evident from the extended gloss retention, improved surface roughness, i.e. the surface is less rough as formation of pits and holes is minimized, along with stabilised melamine and methylene loss and decreased area change in the –OH/-NH peak. The improved surface roughness of NS03 white can be seen from the 3D in figure 6.7 in comparison to figure 6.5.

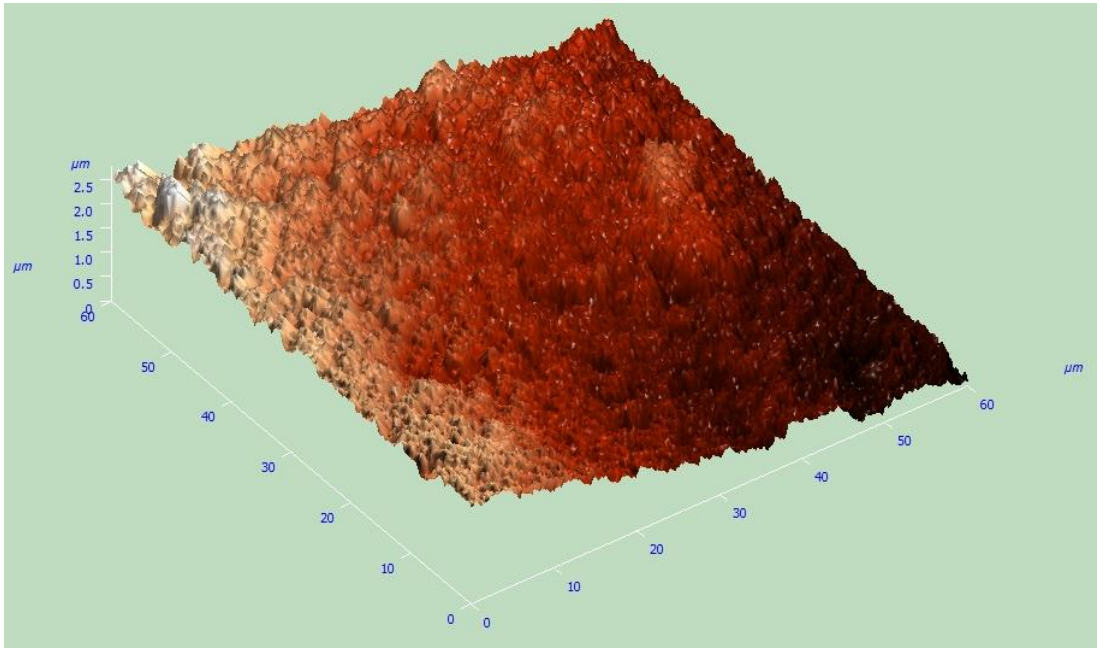

Figure 6.7: 3D AFM image displaying the roughness of NS03 white after maximum exposure hours (2206)

Accelerated weathering is by no means a replacement for natural weathering; however, it does assist in predicting the behaviour of coatings in an extreme environment. Though the coating used in industry may be pigmented, this research focuses a great deal on the clear coatings. As has been demonstrated, the white coatings were unable to give an in-depth insight into how the new bio-based resin, NS03 would perform. The white coatings showed an overall much more stable degradation performance.

The Florida exposed samples; in comparison to the QUVA exposed samples show a fraction of the degradation as can be seen in chapter 5. The surface analysis displays a fairly stable surface even after degradation in regard to gloss retention and AFM roughness. The FTIR results for the clear coatings show the unfolding degradation account. The increase in –OH/-NH peak and melamine loss describes the initial photo-oxidation of both NS01 and NS03 clears. However, the methylene disintegration seen for the QUVA samples is not seen in the clear Florida samples. On the other hand, 2 years of natural exposure of the NS01 and NS03 white coatings do not show evidence of severe degradation to predict the degradation route of these coating except the commencing of photo-oxidation can be seen.

6.1 Conclusion

From the FTIR data of the QUVA exposed samples; we can conclude that the NS03 clear is relatively stable in the initial hours of exposure, where it is performing better than NS01 clear. After approximately 1200hr it seems the photo-oxidation stabilises but a change in the crosslinker environment causes the coating to degrade severely. The proposed reason for degradation by a mechanism other than photo-oxidation is the attack on the crosslinked region as oppose to the resin itself. This attack causes a breakdown of the longer aliphatic chains which is why there is a significant melamine loss and methylene loss. At the 1200hr mark where the chemical degradation is witnessed it is also the same time at which there is a peak in physical degradation of the surface. This is evident from the reduction in gloss retention and an increased surface roughness, calculated using AFM root mean square roughness. After this peak in chemical and physical degradation NS03 deteriorates rapidly, a cause for concern for industrial application. NS01 however, shows typical degradation via photo-oxidation.

7. Development of techniques to spatially map chemical degradation in coil coatings using focused ion beam and chemical force microscopy

Further to the discussion in chapter 6 the next step to better understand the manifestation of chemical changes into physical changes is to determine whether the extent of photo-oxidation can be measured in the depth profile. Zhang et al (2009a) used Step Scan Photo-Acoustic Fourier Transform Infrared Spectroscopy (SSPA-FTIR) to depth profile multi-layered clear and pigmented coil coatings. It was concluded that SSPA-FTIR was most suitable for the clear Polyethylene Terephthalate (PET) sample but was not so accurate for the pigmented Polyvinylidene Fluoride (PvdF) sample primarily since the inorganic pigments in the coating extended the thermal diffusion depth. The method was only used to identify the layers in the multi-layered polymer coatings and not to spatially map any chemical changes.

In another study, Gonon et al (2001) used photo-acoustic spectroscopy with a step-scan interferometer to depth profile a photo-oxidised polymer and to quantify its extent of degradation. This method can be used to obtain the spectral depth profiling by varying the modulation frequency alone, however it is difficult to extract the depth information from the resultant spectra. The concentration of the chemical groups is not homogenous throughout the thickness of the sample as can be seen in (figure 7.1). For the peak at 1717cm^{-1} the intensity is maximised at a low modulation frequency of 50Hz whereas at 1600 cm^{-1} the intensity remains inversely proportional to the modulation frequency. Therefore, for any further analysis a reference peak which is homogenous through the thickness of the sample needs to be selected to get a ratio between two absorption bands along with checking if the intensity of the spectra obtained is independent of the modulation frequency. Nevertheless, taking the physical property of the sample and geometry into account a 'Rosencwaig model' adopted by the researchers can be used to determine the conditions needed to make quantitative analysis of the sample possible. Overall, it was found that where infrared spectroscopy of opaque samples is particularly difficult, photo-acoustic detection is useful to get the infrared spectrum of the sample. Moreover, the depth-profile of oxidation can be established using this method between 5 and 35μm.

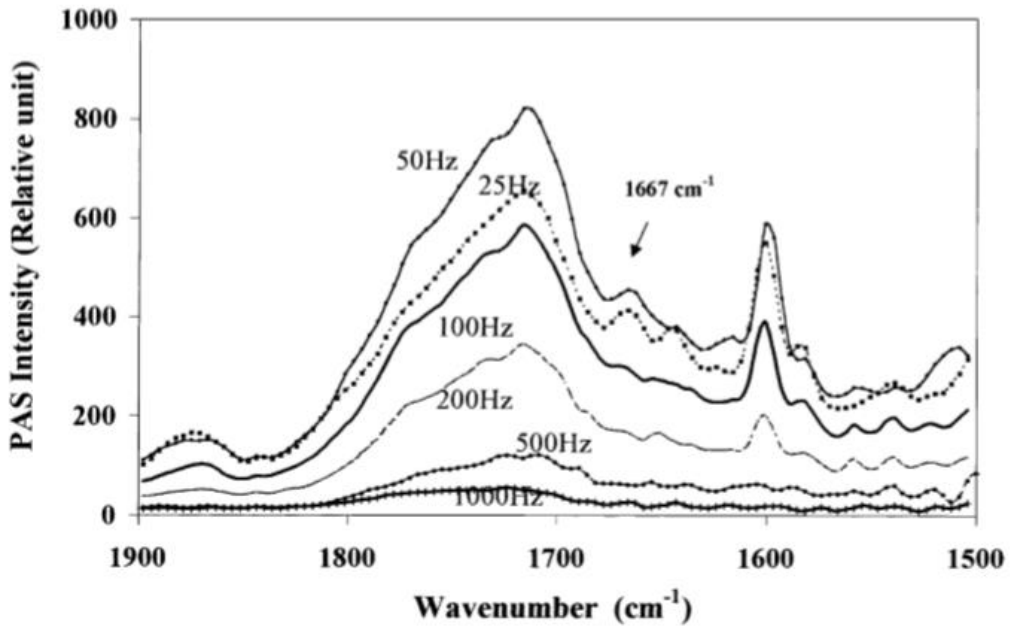

Figure 7.1: PA-FTIR spectra of a photo-oxidised polymeric material fro modulation frequencies between 25 to 1000Hz, Gonan et al, (2001).

Having noted that SSPA-FTIR can possibly be a useful tool to depth profile chemical changes, there is still the factor of looking at the bulk of the sample at a certain 'calculated' depth and not being able to chemically map the heterogeneity of the degradation. Furthermore, SSPA-FTIR technique is not widely available on latest FTIR equipment, so a different method was developed in order to depth profile and attempt to map the chemical degradation and link it to the physical degradation that can be seen on the surface of coil coatings.

To do this, two separate techniques were used. Focussed ion beam (FIB) microscopy technique, was utilised to mill to create a depth profile before chemical analysis could be carried out. Areas at calculated depths were cleared and polished to generate relatively flat surfaces upon which the second technique, chemical force microscopy (CFM) could be performed. However, before the two techniques were put to practice preliminary work was carried out to test the material suitability and validity of the method. In theory, the concept of CFM works and earlier studies (Sinniah et al, 1996) has shown the significance of using a liquid medium. Papastavrou and Akari (1999) used lateral force measurements in CFM to detect hydroxyl groups in two solvents, water and hexadecane. This study used gold samples prepared using micro-contact printing to get Self-Assembly Monolayers (SAM) of different terminations namely OH and CH_3 groups. The clarity of the pattern is shown on the lateral scan (figure 7.2) produced in hexadecane where the square regions are SAMs with terminal

OH-groups and the surrounding the substrate is terminated with CH_3 groups. The square regions are bright due to higher friction between the OH-tip and the OH-groups on the sample. Representative force-distant curves and adhesion force histograms are shown for different areas on the same sample. It can be seen that they are in agreement with the lateral force image. The force-displacement and adhesion data for the OH-terminated area (figure 7.2, a) and b)) show a strong friction contrast which is distinctly different to data for the CH_3 terminated area (figure 7.2, c) and d)).

Papastavrou and Akari (1999) discovered that hexadecane was shown to allow clear interpretation of the contrast over water as a medium which was achieved through lateral force measurements. The contrast in lateral force measurements or 'friction contrast' can be influenced by monolayer perfection or hydration forces other than the interaction of the functional groups, hence one must be cautious when interpreting the results.

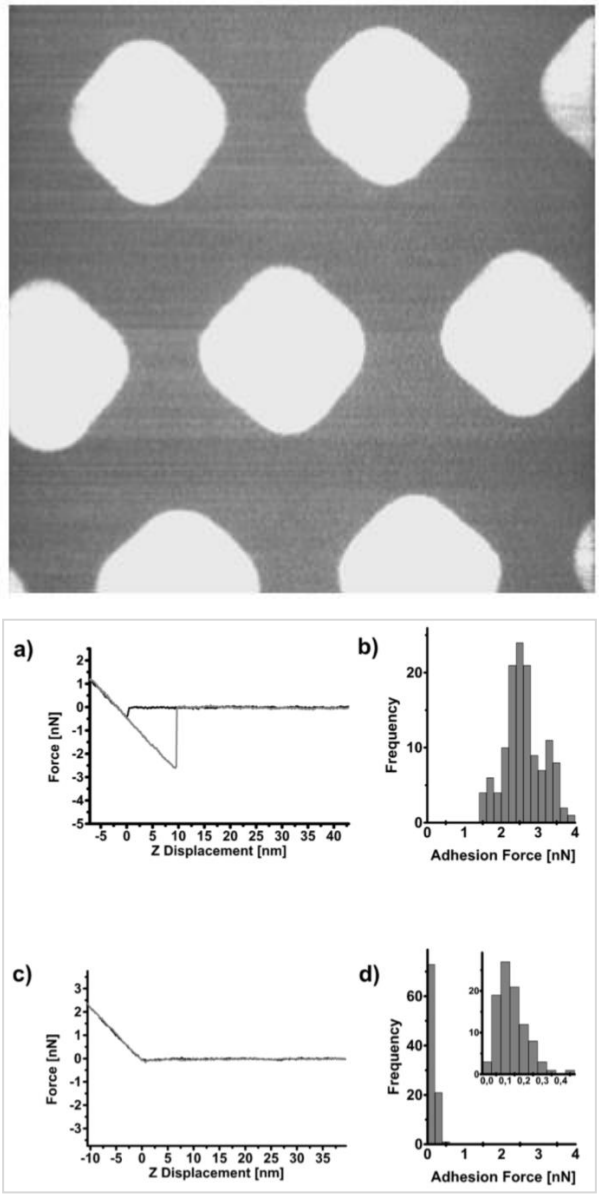

Figure 7.2: Lateral force image of SAMs on gold substrate. (a) Force-displacement curve measured for the OH-tip and OH-terminated area, (b) Adhesion data on OH-terminated area, (c) Force-displacement curve measured for the OH-tip and CH_3-terminated area, (d) Adhesion data on CH_3-terminated area, Papastavrou and Akari (1999).

AFM probes can be functionalized with many different chemical groups. The chemical group chosen is based on the interaction with the surface chemical group in question. For hydroxyl groups, OH-modified tips have the greatest interaction. Leng and Jiang (2002) carried out dynamic simulations of adhesion and friction in chemical force microscopy between the tip and the substrate both modified with SAMs of OH and CH_3 terminal groups. The results obtained show that the OH/OH adhesion force and surface energy is four times larger than the CH_3/ CH_3 interaction due to the formation of hydrogen bonds.

Lateral imaging for CFM has been conducted by many to detect chemical groups. However, the use of lateral-force based CFM for soft biological or polymer samples may be limited as; "*(1) shear forces in contact mode scanning can dominate chemical forces and preclude chemically sensitive imaging and (2) tip-induced deformations that occur in contact mode may also damage samples*" (Noy et al, 1998). A way to essentially eliminate these factors arising from using contact mode is to use tapping mode. Tapping mode uses an oscillating tip under free oscillation amplitude. When brought close to the sample surface, the oscillating tip changes from a free amplitude to a fixed set-point and is therefore maintained through the feedback loop. As with phase-imaging mentioned earlier the attractive force generates a phase-lag and according to this, the image is produced. This method will enable high-resolution imaging like that obtained from contact mode with minimal or no sample deformation.

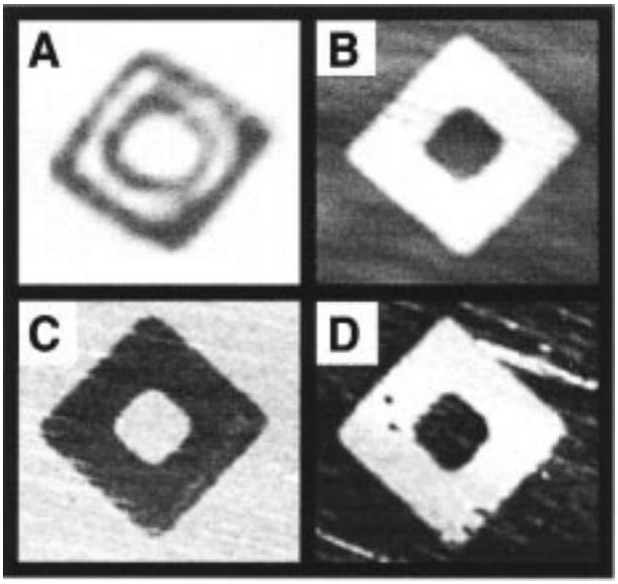

Figure 7.3: (a)Condensation figure of a water droplet condensed onto the COOH terminated area (the darker area) surrounded by CH_3 terminated area, (b) Friction map obtained with COOH-terminated tip where area of high friction (COOH) are light and surrounding area of CH_3 is of low-friction therefore darker, (c) phase lag map of a COOH-terminated tip and (d) phase lag map of a CH_3-terminated tip- dark area corresponds to greater phase lag, Noy et al (1998).

Noy et al (1998) were one of the first groups to carry out tapping mode CFM at a time where it was more common to use lateral force imaging for chemical sensitive imaging. Through their research, phase-lag imaging was evidently successful. Figure 7.3 displays their work in which the substrate had two areas each terminated with a chemical group, the squared

pattern being terminated with COOH and the surrounding area terminated with CH_3. First an optical condensation image was captured (figure 7.3(a)). A water droplet condensed on the COOH-terminated area (appearing as a light ring on top of the dark area) as from the two chemical groups, COOH is hydrophilic. Following the condensation, a clean area was used to carry out lateral force imaging in ethanol using a COOH-terminated tip. The COOH groups on the tip show high friction with the COOH groups due to the stronger COOH/COOH interaction as oppose to CH_3/COOH interaction. In a lateral force image high friction appears light and low friction appears dark as can be seen in figure 7.3(b). This also ties in with the results from the optical condensation image. After lateral force imaging, phase-lag images were obtained by carrying out tapping mode CFM. Figure 7.3(c) displays the image derived from using a COOH-terminated tip and 7.3(d) is the resultant image from using a CH_3-terminated tip. In a phase-lag image a darker area represents greater phase-lag whereas the lighter area denotes weaker interaction and therefore a smaller phase-lag, which is confirmed by both images. Therefore, tapping mode is a successful tool to map chemical interactions. The contrast on the lateral force image is opposite to that of the phase-lag image, however, this is only due to the way chemical information is interpreted and displayed and does not refute the concept of tapping mode CFM to generate chemical-sensitive data.

In this research, phase imaging was used to spatially map the surface chemistry. Phase imaging is sensitive to surface stiffness/softness and the adhesion between the tip and the surface (Bailey et al, 2013 and Advanced surface microscopy, Inc). Phase images are generated due to the phase-lag produced by the attractive force between the tip and the surface chemistry or regions with different compositions, generally in tapping mode AFM or CFM.

As there is no distinct pattern on the surface of the samples in this research, it will not be immediately evident from phase images whether the strength of the chemical interaction is strong or weak. To carry out chemical sensitive imaging to detect the production of hydroxyl groups and confirm the increase of photo-oxidation degradation with increased exposure hours -as deduced from the FTIR chemical analysis, OH-terminated tips were utilised. To demonstrate how effective the tip-sample interaction would be and to verify the method some preliminary work was carried out and will be highlighted in the following section.

7.1 Preliminary work

Preliminary work was carried to demonstrate CFM with a control surface. Further work could only be carried out if this technique was able to pick up -OH chemistry on the sample surface. Detecting -OH groups would indicate the extent of photo-oxidation. -OH production increases with photo-oxidation as the exposure time progresses, as discovered in chapter 4, figure 4.14. The samples were prepared via micro-patterning. Branches of OH groups were micro-patterned onto glass slides as can be seen in the figure 7.4 below. The slides were then analysed using chemical force microscopy in two separate environments in order to determine the best conditions to conduct the research on NS01 and NS03 formulations.

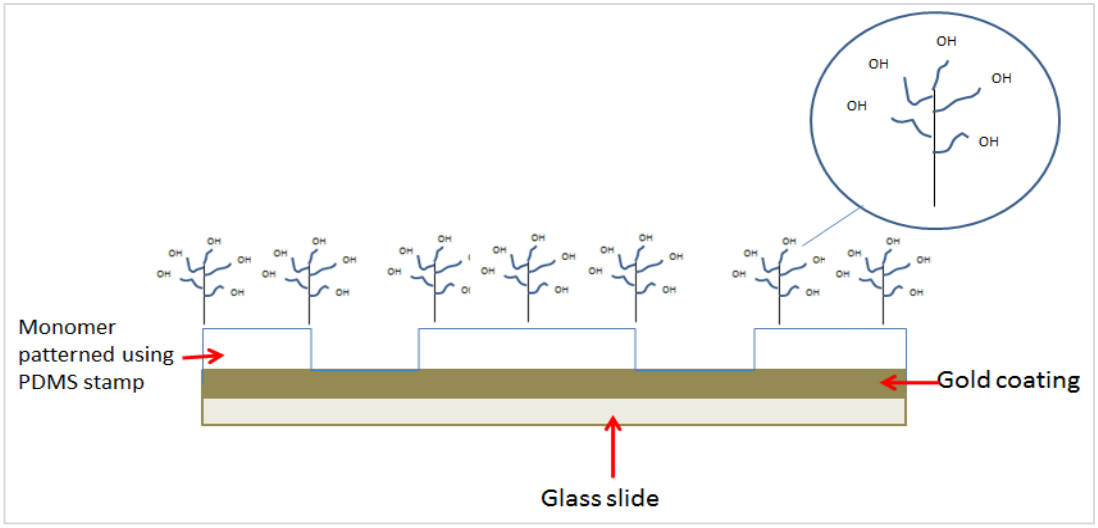

Figure 7.4: A schematic drawing of the micro-patterned substrate with OH-terminated brushes

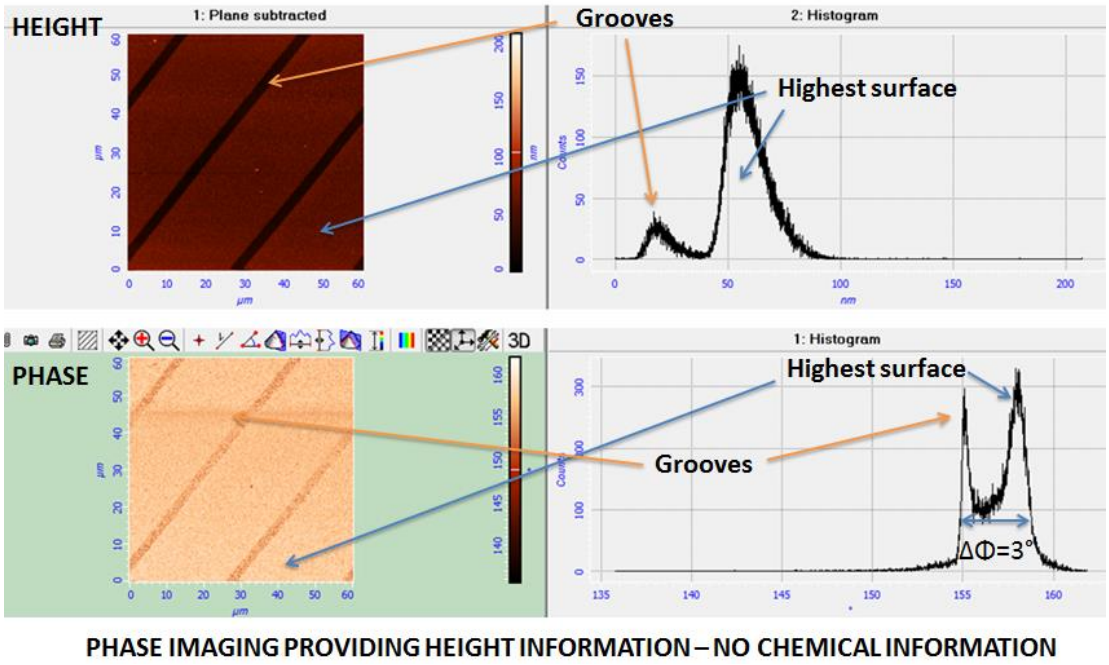

Figure 7.5: CFM Phase-imaging on OH-terminated sample using OH-terminated tip in air.

The first experiment involved doing CFM in air. However, as can be seen in figure 7.5 above, no chemical information was retrieved. The height of the peaks in the phase data is the same for both the grooves and the OH branches. A layer of water vapour builds up on top of the OH brushes and the rest of the sample surface building a liquid layer, as demonstrated in figure 7.6, hence interfering with the OH-OH interaction. The modified tip is therefore picking up chemical interactions from the same liquid layer resulting in no difference in chemical interaction. Van der Vegte and Hadziioannou (1997) ensured all adhesion measurements they carried out in chemical force microscopy were performed in a liquid either ethanol or water to "*avoid the appearance of a meniscus between tip and sample due to adsorbed water, which gives rise to uncontrolled capillary forces that mask the true introduced tip-sample interaction*." Noy et al (1998) also used a fluid solution during chemical force microscopy to eliminate the role of capillary forces in masking chemical interactions.

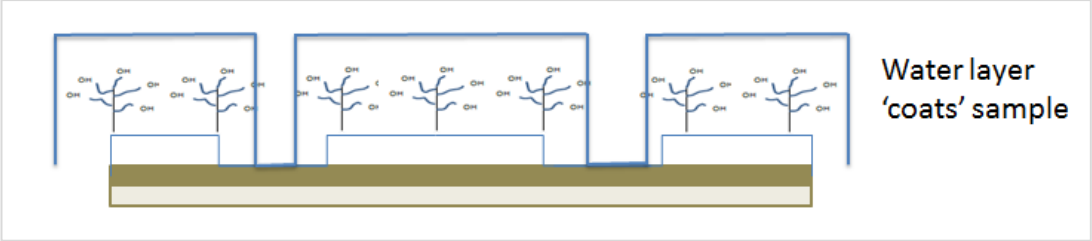

Figure 7.6: A schematic drawing demonstrating how a 'water layer' can form over the OH brushes and mask the tip-sample interaction.

The second experiment involved carrying out CFM on the same micro-patterned samples, however, this time immersed in hexadecane. Hexadecane has a very similar viscosity to water, but it is non-polar. Therefore, any chemical interaction is solely between the OH group on the branches and the modified tip. The results confirm the chemical interaction as a relatively large phase change can be seen with a single broad peak. This shows that the area on the glass slide without OH branches is not displayed on the phase image as it was not interacting with the modified tip. The corresponding phase and height data can be seen in figure 7.7.

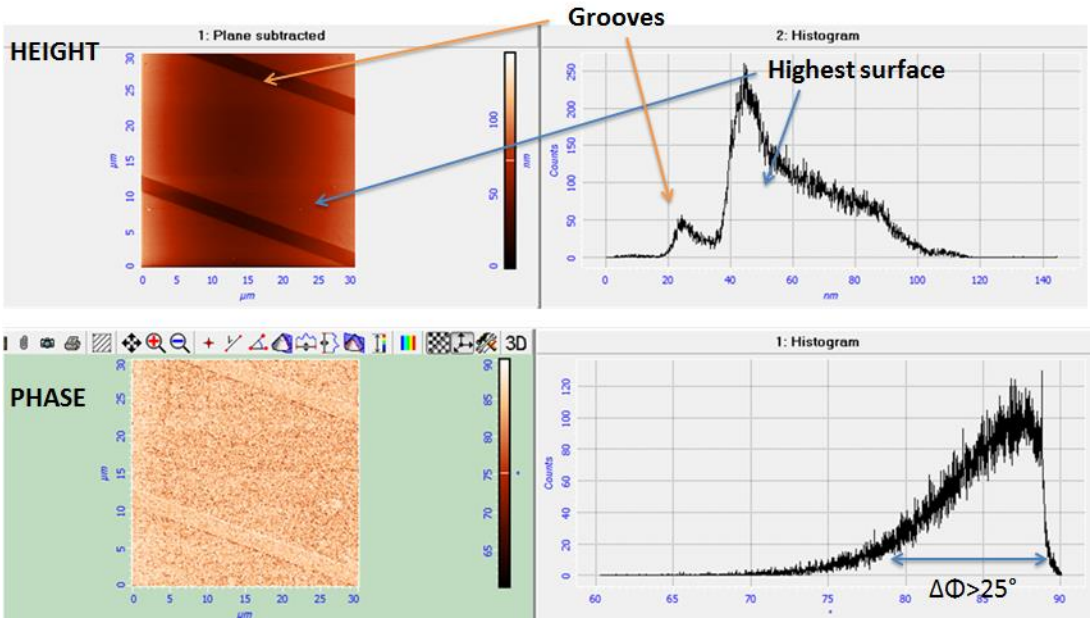

Figure 7.7: CFM Phase-imaging on OH-terminated sample using OH-terminated tip in hexadecane.

7.2 Repeating measurements on the surface of the sample

Repeat measurements were carried out on the sample surface of a fresh sample obtained from a separate NS01 clear coated panel to check if one scan was representative of different areas of the sample. Three separate areas were scanned on the sample, each 60µm × 60µm. Each area contained 256 × 256 pixels which is 65536 measurements. With such a sample size one scan may be justified and relied upon but to prove this, yet three separate areas were scanned. Figure 7.8 below shows the data of each area that was scanned. The plot shows the phase counts in each area. The phase as stated earlier is a measure of the chemical interaction. The chemical interaction on the standard unexposed sample should be uniform throughout the sample surface and generate a single peak which may or may not be broad according to the different types of OH-containing groups present. It can be seen from figure 7.8 that carrying out CFM on three different areas yields the same chemical information regardless of how strong or weak the chemical interaction is. The main concept of obtaining such data is to see how the peak broadens and calculate the phase change which will indicate if there is an increase or decrease in hydroxyl containing groups on the sample measured. The phase change of each area here has a phase change of 5˚. So, after carrying out further measurements on the same sample, it can be stated that the chemical information obtained is consistent with this method. Hence, one scan with 65536 measurements is sufficient to conclude the outcome of each sample.

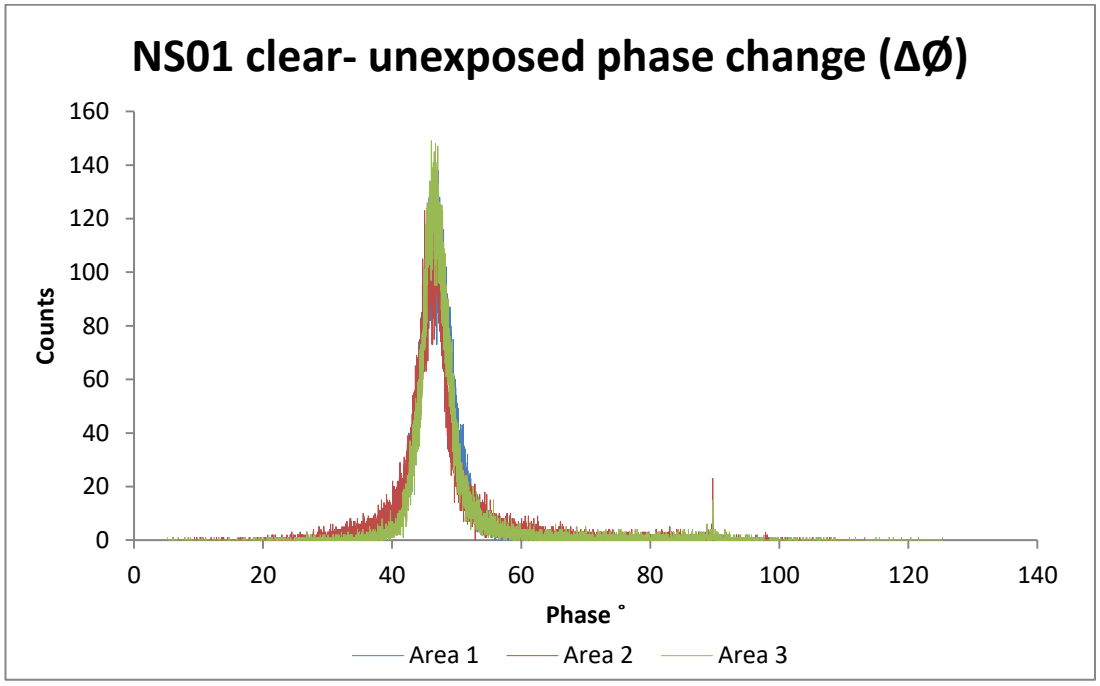

Figure 7.8: CFM phase-data on three separate areas of the same sample

7.3 Chemical force microscopy on the surface of the sample

Phase contrast AFM is a form of tapping mode AFM whereby an oscillating cantilever, near its resonance frequency, allows the tip to periodically contact the sample surface for a short duration in each oscillation cycle. A feedback loop is used to maintain a set-point amplitude whilst the AFM tip is scanned over the sample surface. A phase lag is generated between the driving signal (a sine wave) and the cantilever response (Haugstad. G, 2012) whilst scanning the sample surface which generates a phase contrast signal in the form of a phase change in degrees. The phase changes are related to energy dissipation whilst the tip is interacting with the sample (Bailey et al, 2013, Marcus et al, 2003 and Nguyen et al, 2001).

Chemical force microscopy, CFM follows the same principle as phase contrast AFM except a functionalised AFM tip is used and the phase lag is produced due to the chemical interaction between the functional group on the tip and the corresponding tip on the sample surface as detailed in chapter 2 section 2.5.1.2- chemical force microscopy. Scanning the sample surface with a functionalised tip produces a height and a phase image, figure 7.9.

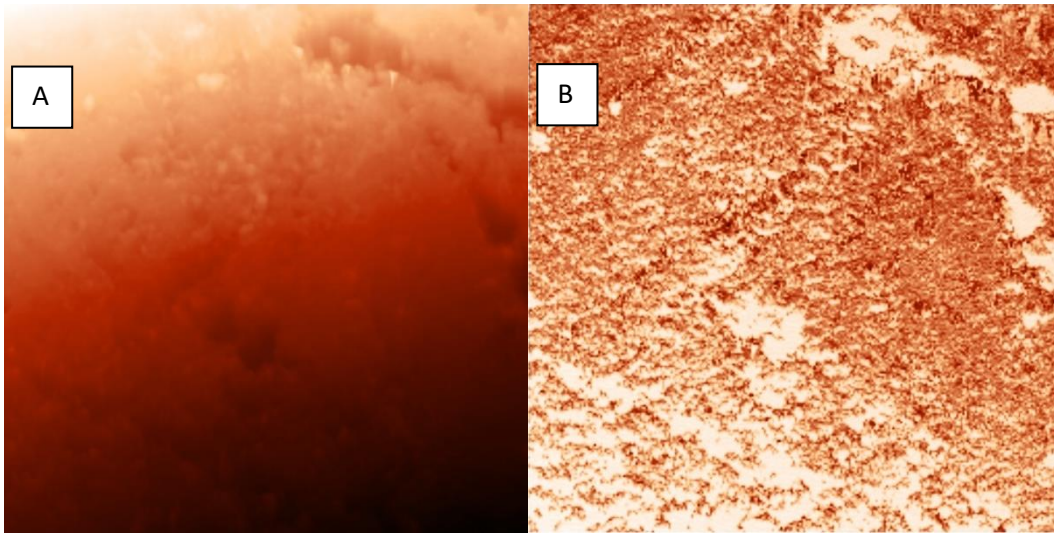

Figure 7.9: An example of a a) plane corrected height image and b) phase image

AFM software 'Nova' is used to analyse the data. Using an analysis feature on the AFM software, the height image is plane corrected so only the topographical data is present in the analysis. The surface roughness can then be extrapolated. An RMS value is obtained along with a histogram to display the results using the software. Note, that the peak and RMS value generated is an average of the whole sample area of 20µm × 20µm which is 256 x 256 data points and a total of 65,536 data points per sample.

Following the preliminary work on the control samples, CFM was carried out on the surface of NS01 at the start i.e. 0hrs exposure, figure 7.11. The results confirmed that the phase lag (calculated by taking the difference at half peak height) in the height image was less than that of the phase image. The height image shows a single peak which refers to the roughness being pretty much the same across the sample area. This was expected as the sample had not been exposed hence the roughness should be uniform across the sample surface. On the other hand, the phase image picked up peak changes. The phase data which refers to the chemical interactions between the chemical groups on the modified tip and those on the sample surface is picking up the presence of hydroxyl groups on the surface of the sample. The phase data shows more than a single peak which demonstrates the variation of the chemistry on the surface of the sample.

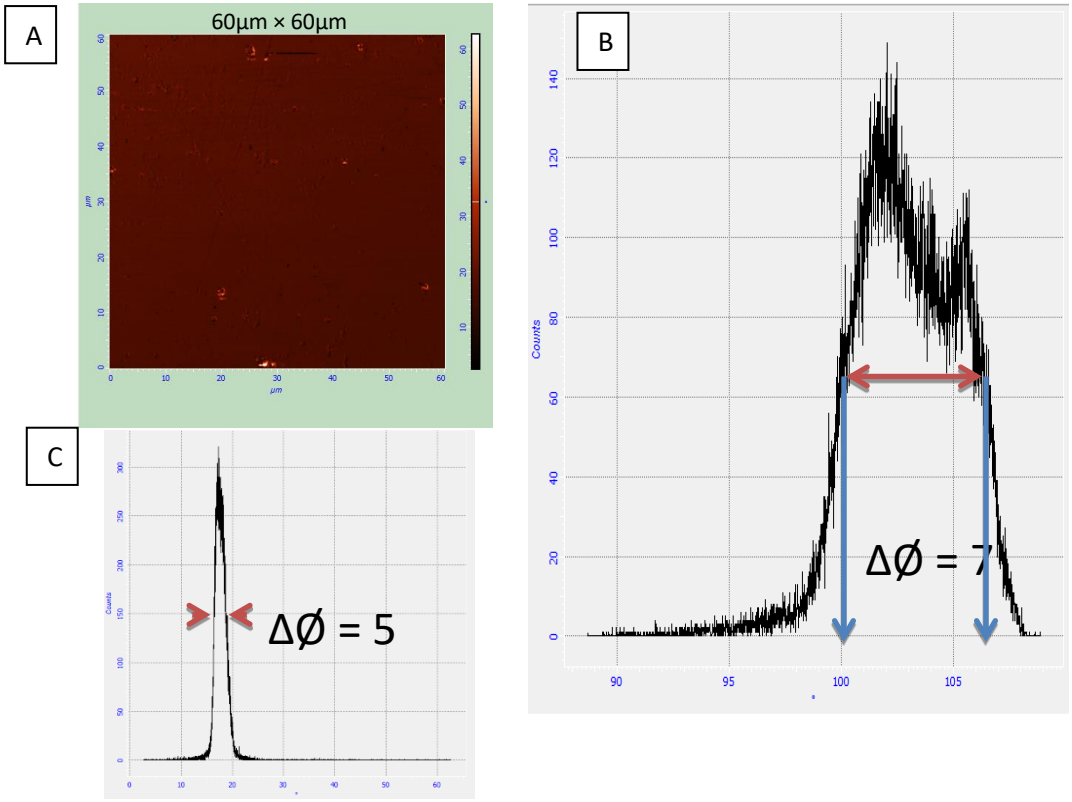

Figure 7.10: a) Phase image on unexposed NS01 sample b) Data from the height image of the unexposed sample and c) Data from CFM on the surface of NS01 unexposed sample

It would be an ideal if the OH-terminated tip could only pick up the production of hydroxyl groups due to photo-oxidation. The formation of hydrogen bonds between OH/OH groups however will not differentiate between the O-H groups in alcohols, carboxylic acids or any other chemical group. Hence, when the OH-interaction is measured, the attractive forces will be greater leading to a greater phase-lag and a broader peak on the histogram data of the phase-image (chemical interaction) in comparison to the histogram data of the height image (topography or roughness), as shown in figure 7.10.

After carrying out CFM on the surface of unexposed NS01 clear- the starting sample, it was repeated on unexposed NS03 clear along with 2 exposed NS01 and 2 exposed NS03 clear samples. Chemical analysis of the surface of the coatings was completed on samples before exposure, almost halfway of their QUVA exposure lifetime and at the maximum QUVA exposure hours.

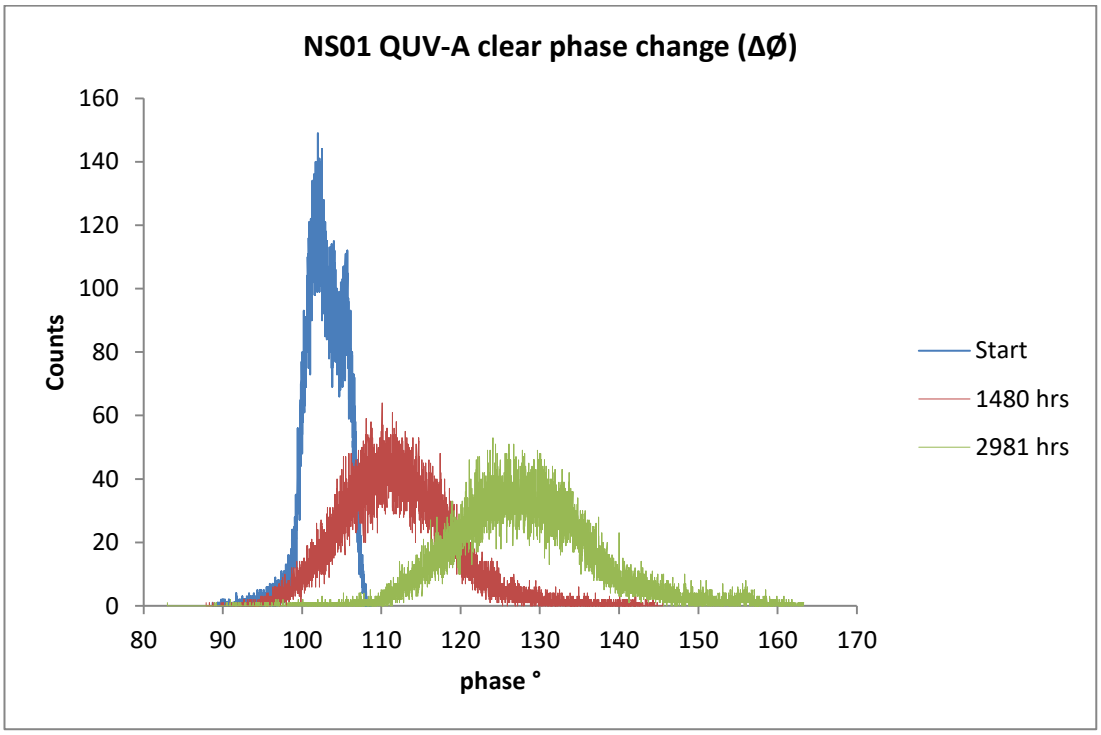

Figure 7.11: CFM on surface of NS01 clear at 0, 1480 and 2981 hrs

Figure 7.11 displays the phase data obtained on the surface of NS01 clear samples which were unexposed at the start and then exposed at 1480 and 2981hrs. At the start, the unexposed sample generates a sharp and narrow peak whereas the 1480hrs and 2981hrs

exposed samples generate flat and broad peaks. The significance of the type of peak was discussed earlier; a broader peak signifies a greater phase change and therefore it can be deduced more OH-groups are detected as the exposure time increases. The broad peaks for 1480hrs and 2981hrs are still single peaks hence the type of -OH containing chemical groups detected must be the same. Table 11 confirms the phase change of the peak at the different exposure time and again it is evident that the greatest phase change is recorded for 2981hrs at 20˚. At 1480hrs exposure time the phase change is 15˚ and the unexposed sample at 0hrs exposure has a phase change of 7˚.

Chemical sensitive phase imaging of NS03 clear is shown in figures 7.12 and 7.13. High spatial resolution of the images allows data variation to be seen using coloured pixels; darker areas correspond to stronger interaction between surface chemistry and the chemical groups attached to the probe. At 0hrs and 1227 hours, the 3D height images (figures 7.12a and 7.13a) show that topography is not completely uniform with features at a maximum height of 2µm but not much variability in coloured pixels is seen. On the other hand, the phase image (figures 7.12c and 7.13c) of the same scan area displays a lot of variability- representing the range of the phase angle. The range is shown to be consistent across the scan area, hence the chemical interaction is consistent across the surface.

At 0hrs the presence of -OH groups on the surface without QUVA exposure shows a single peak, as expected (figure 7.12d). The phase change for both NS01 and NS03 at the start was approximately 7˚. The degradation for NS03 clear exposed at 1227hrs is uniform (figure 7.13c). However, figure 7.13d shows another peak emerging. No additional peaks are observed for NS01 exposed samples in figure 7.11. Is this due to presence of other -OH containing chemical groups? Further analysis and comparison to NS03 clear exposed at 3113hrs will help understand this concept better.

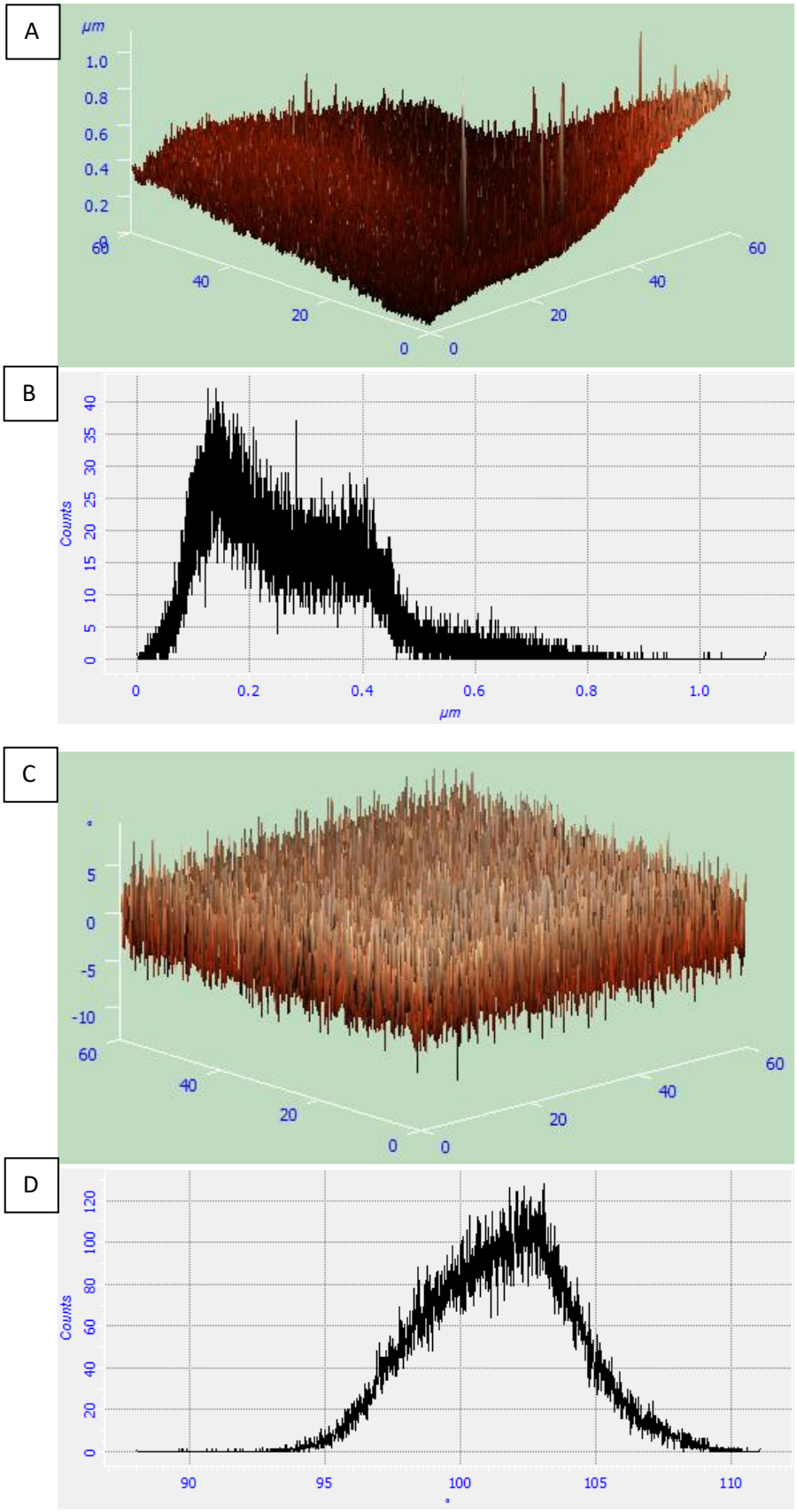

Figure 7.12: Chemical force microscopy of NS03 0hrs a) 3D height image, b) average height data, c) 3D phase image and d) phase angle data to calculate the phase change

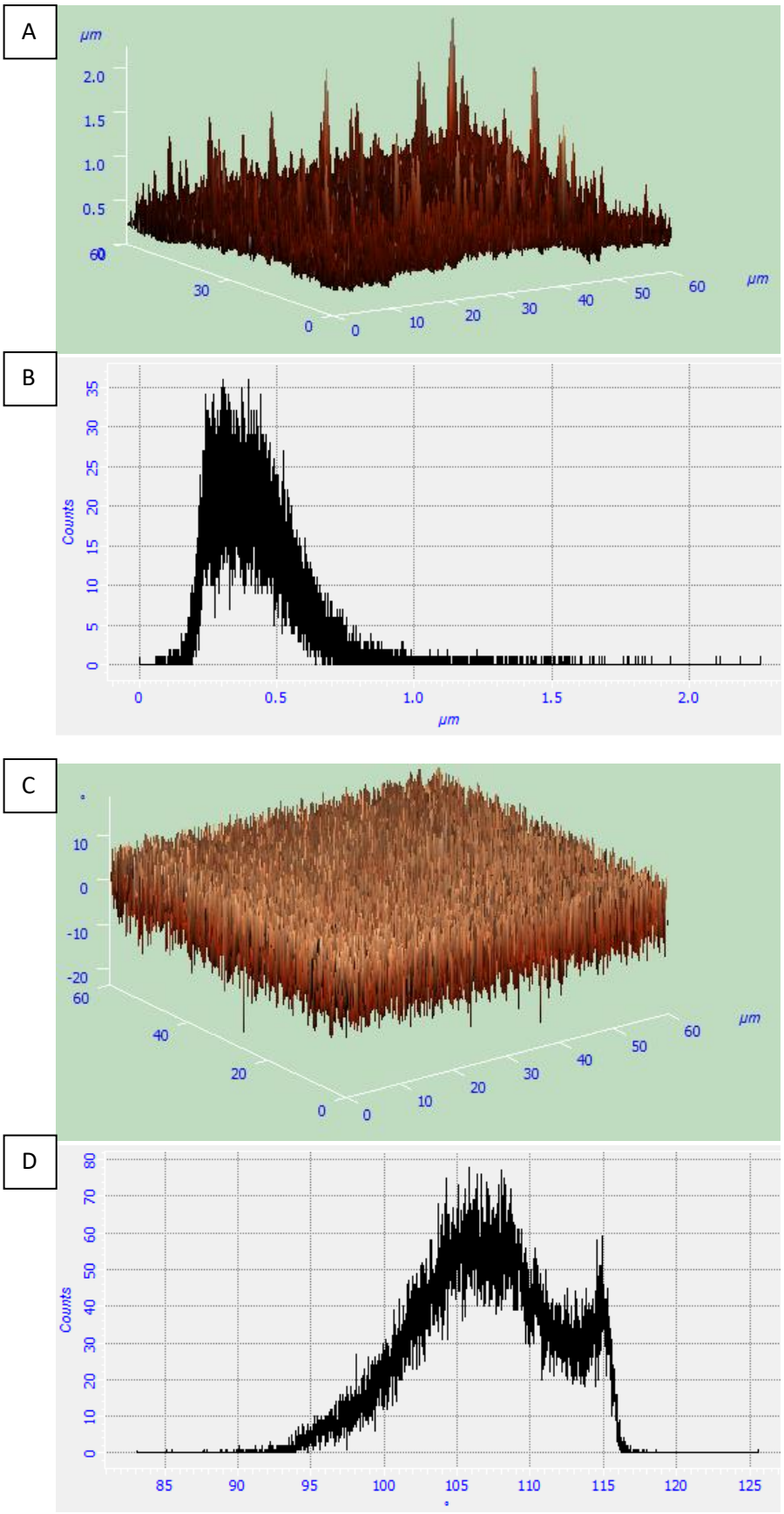

Figure 7.13: Chemical force microscopy of NS03 1227hrs a) 3D height image, b) average height data, c) 3D phase image and d) phase angle data to calculate the phase change

For NS03 clear at 3113hrs, areas of the coating disintegrated forming pits on the surface, shown in figure 7.14a. Despite the inconsistency of the coating, chemical interaction is detected across the whole surface. This could be due to chemical interactions being picked up from another chemical group below the coating or the remains of the coating itself. The corresponding 3D phase image, figure 7.14b displays what seems to be a large difference in the phase angle between the surface of the sample and areas with pits. But, looking at the scale of the phase image and the resultant histogram- figure 7.14c, the 'pits' have a phase angle in the range of 120-125˚ and chemical interaction detected in these areas is minimal in comparison (see histogram, figure 7.14c) to the rest of the sample surface and it is also not prominent in the data.

This chemical interaction could be confused with topography. Further analysis of a 20 x 20µm area (figure 7.15) within the 60 x 60µm area demonstrates that phase image is independent of topography and therefore the phase image is a good representation of the chemical change on the surface of the coatings.

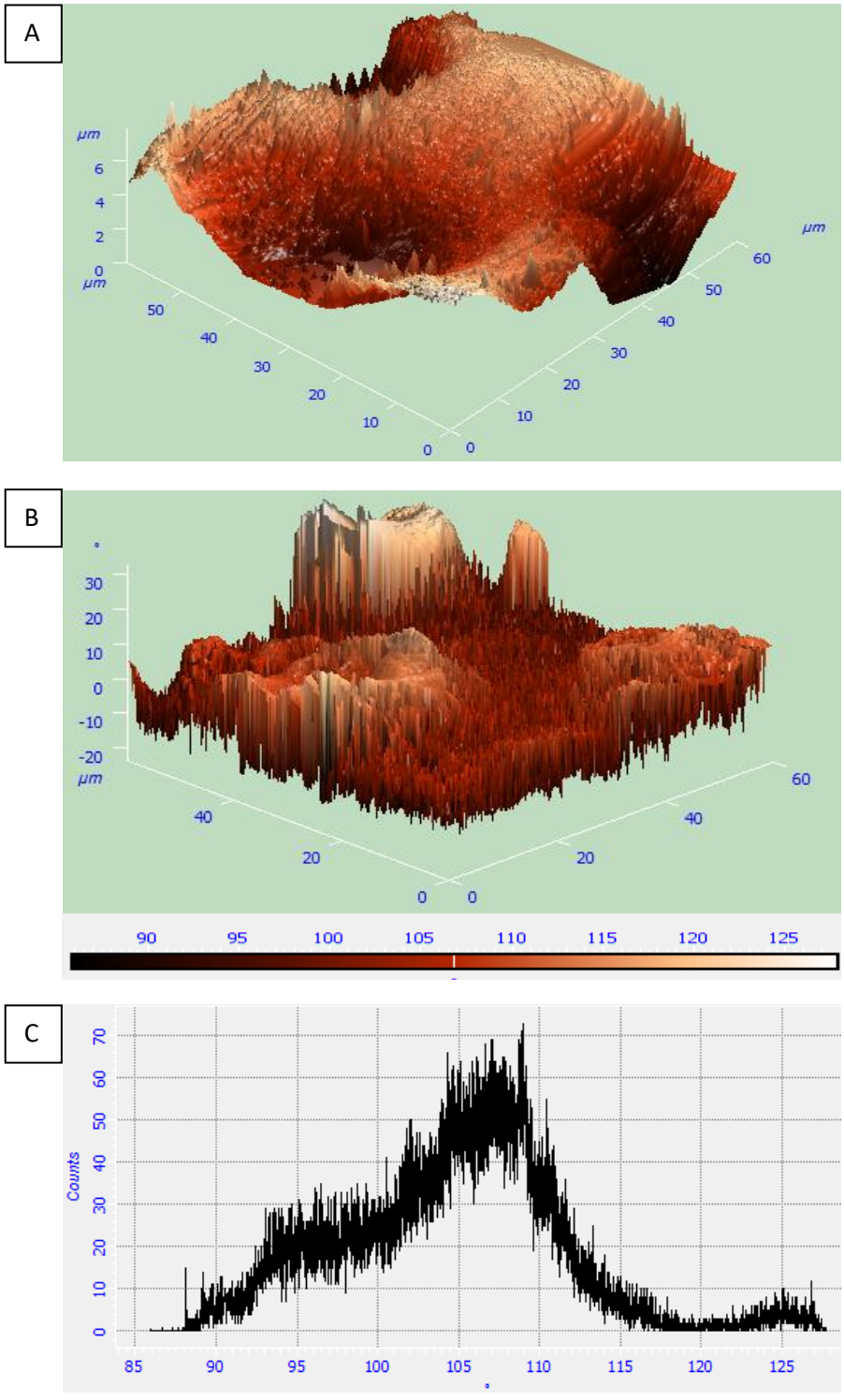

Figure 7.14: Chemical force microscopy of NS03 1227hrs a) 3D height image, b)3D phase image and c) phase angle data to calculate the phase change

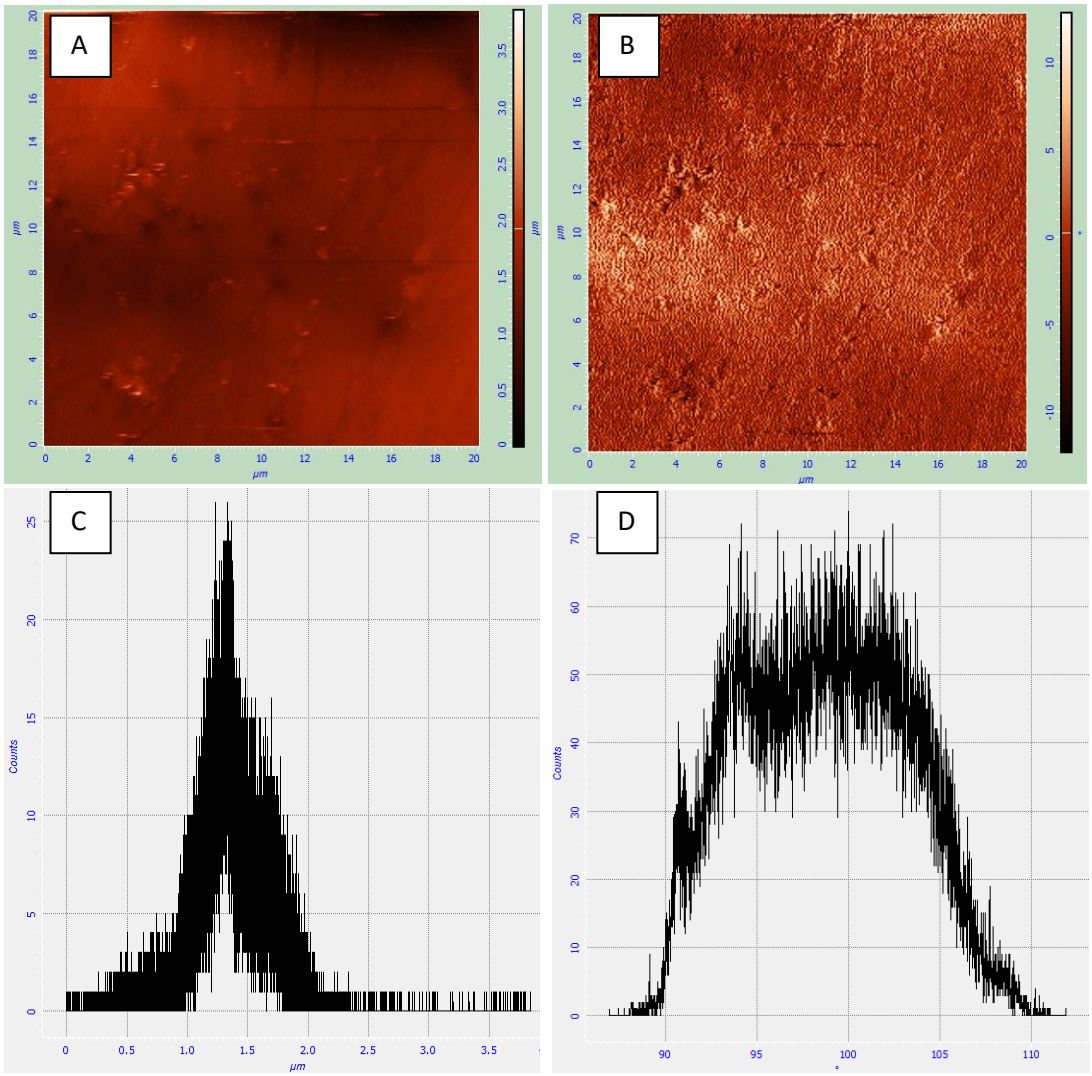

Figure 7.15: Chemical force microscopy of NS03 3113hrs, 20×20µm a) 3D height image, b)3D phase image and c) average height data d) phase angle data to calculate the phase change

Line analysis where each line represents 256 data points was carried out. Degraded NS03 (3113hrs) surface shows chemical sensitivity is consistent even where topography changes in the x-cross section, figure 7.16. The presence of the coating on the sample surface yields stronger chemical interaction whether the coating thickness is uniform or not.

Figure 7.17 shows that areas where a strong interaction is not present results in a small phase lag and therefore a small phase angle measurement which also corresponds to the area where coating is not detected in the height image (figure 7.17a) The chemical force probe is height independent and the resultant image reflects the chemical groups picked up from the surface of the coating.

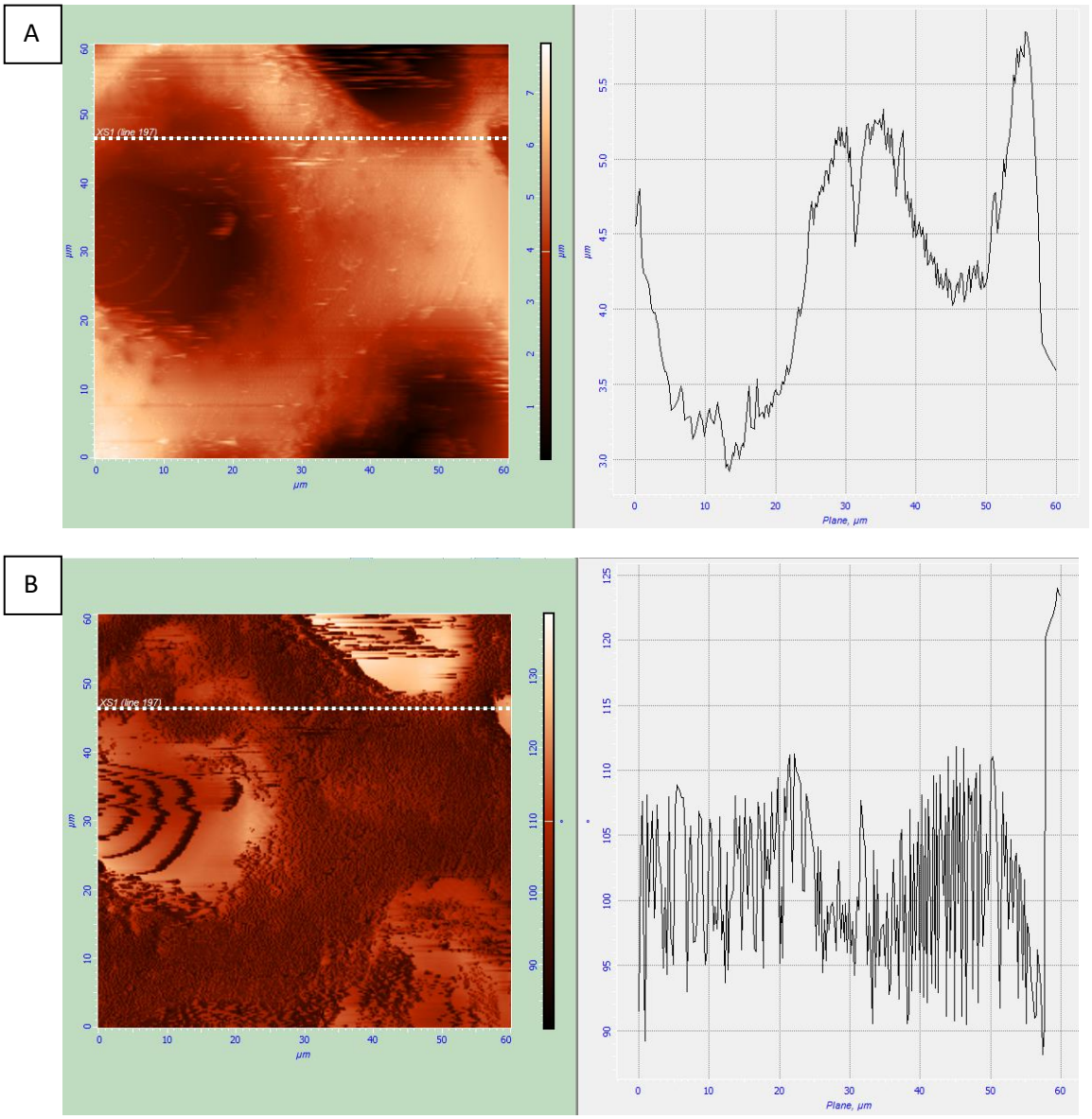

Figure 7.16: X-cross section analysis of NS03 3113hrs a) height image and line analysis and b) phase image and line analysis.

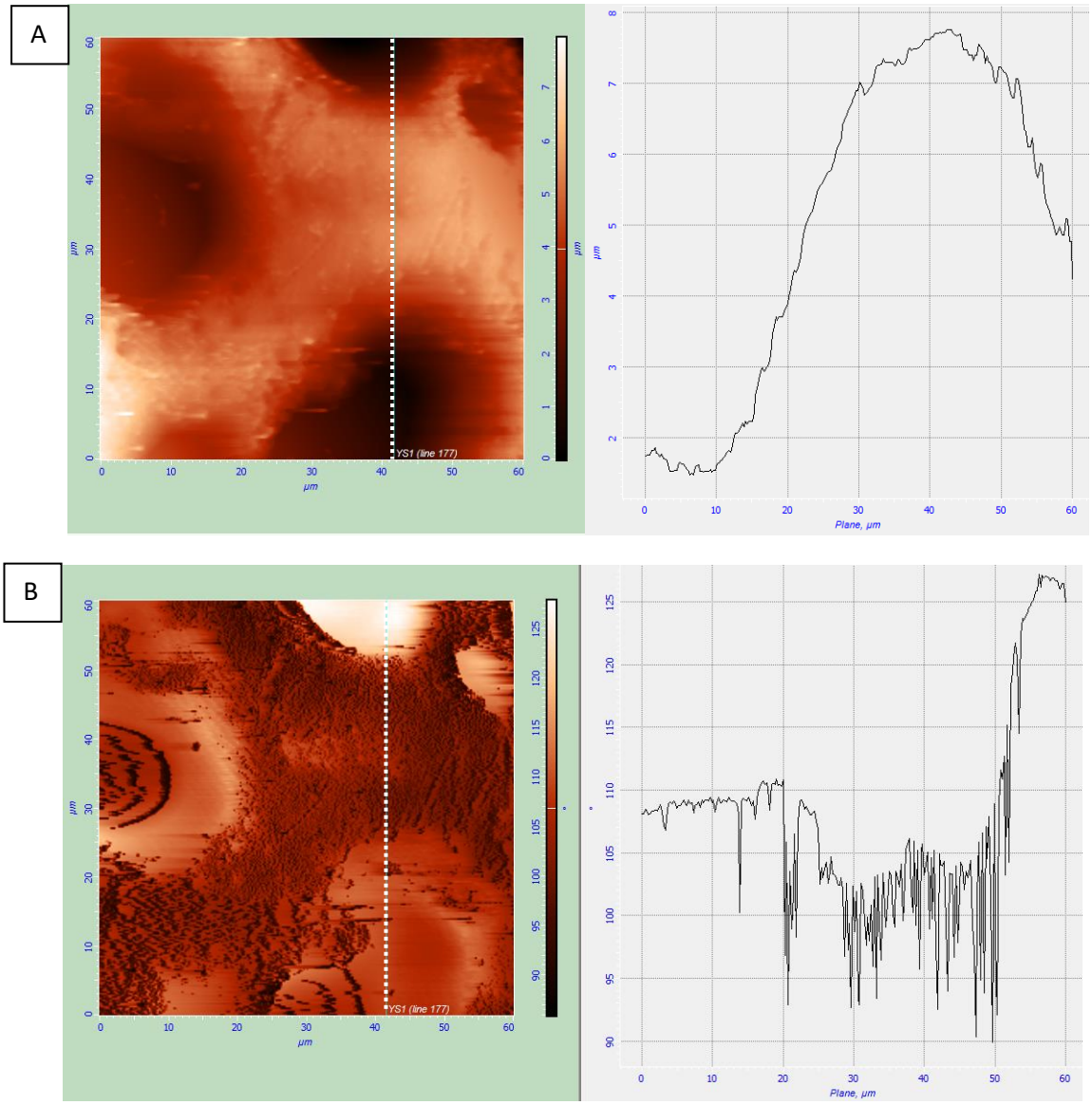

Figure 7.17: Y-cross section analysis of NS03 3113hrs a) height image and line analysis and b) phase image and line analysis.

Table 11: A summary of CFM phase data on the surface of NS01 and NS03 clear samples

Sample			
NS01 clear		NS03 clear	
Exposure time (hrs)	Phase Change (Φ˚)	Exposure time (hrs)	Phase Change (Φ˚)
0	**7** ± 5.8	0	**7** ± 6.7
1480	**15** ± 16.6	1227	**10** ± 12.3
2981	**20** ± 23.2	3113	**16** ± 12.2

Table 11 summarises the phase change of the surface of NS01 clear and NS03 clear coatings at 3 different exposure times. NS03 clear shows the same phase change at the surface of the unexposed sample as the NS01 clear sample. At 1227hrs the phase change for NS03 clear increases to 10˚ and after maximum exposure (3113 hours) the phase change increases to 16˚. It can be seen, that despite NS03 clear being exposed for more hours the phase change is greater for NS01 clear. This indicates that there is greater chemical change taking place on the surface of NS01 clear once the surface is exposed. As discussed earlier the phase change is related to the hydrogen bonding between the OH/OH groups and a by-product of photooxidation is the production of hydroxyl groups. An increased phase change shows that more hydroxyl groups are detected on the surface of NS01 clear. This correlates with FTIR peak analysis and photo-oxidation data (figure 4.14) where a significant increase is seen in the ON,NH peak area. Polymer irradiation in air produces radicals which give rise to oxidative reactions in the presence of oxygen. The result of such oxidative reactions are the formation of carbonyl and/or hydroxyl groups. The Carbonyl group is found to be relatively stable from FTIR data hence it was used as a normalising peak. Therefore, irradiation of the coatings took place in the form of photo-oxidation yielding hydroxyl groups and not carbonyl groups.

NS03 clear data also shows a phase change, figure 7.18 can shed some more light on the values for the phase change obtained for NS03 clear sample. The phase change reflects the strength of the chemical interaction and not the number of chemical groups interacting with probe tip, this is determined by the peaks in the histogram. -OH attached to different chemical groups will give rise to different peaks and depending on the strength of the interaction with the probe tip the height of each peak will vary.

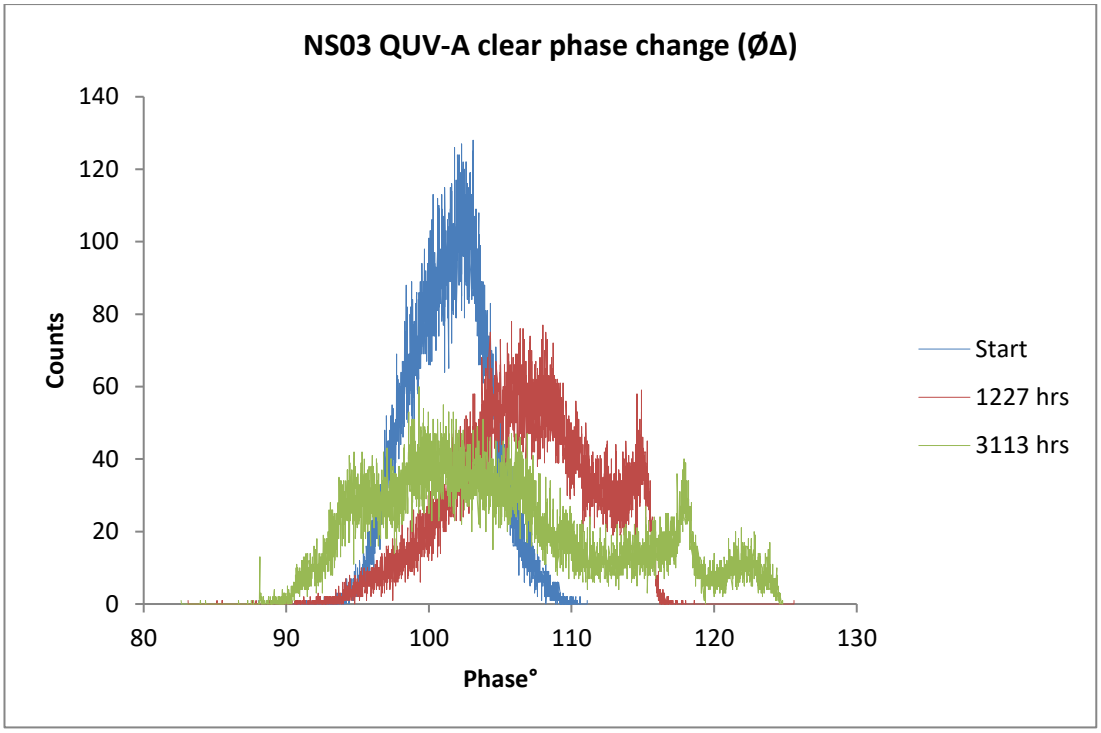

Figure 7.18: CFM on surface of NS03 clear at 0, 1227 and 3113hrs

Having analysed NS01 clear phase data, NS03 clear was also analysed to compare the amount of hydroxyl groups picked up. What may seem obvious from looking at data in table 8; the phase change is greater for NS01 exposed sample so most amount of photo-oxidation takes place when NS01 clear is exposed as oppose to NS03 clear, is it also an indication to the difference in degradation mechanism for NS03 clear? It is confirmed in chapter 4 that NS01 clear has an increased rate of photo-oxidation than NS03 clear. The production of hydroxyl groups calculated through the integration of the OH,NH peak area from FTIR data at 2981 hrs is 281% whereas for NS03 clear at 3113hrs is 89%, yet NS03 loses gloss quicker than NS01 and the surface degrades significantly more developing 'holes' or 'pits'.

The theory of NS03 degrading via another mechanism other than photo-oxidation is also suggested in chapter 4. After looking at the phase data the concept becomes almost visible. Figure 7.18 depicts the presence of other OH-containing chemical groups on the surface of NS03 clear at 1227hrs and more so at 3113hrs. The formation of more peaks across the phase shows the attraction of the OH terminated tip to OH-groups, possibly bonded in different ways, giving rise to different levels of attraction and suggesting the presence of chemical groups which were not present before exposure and therefore before degradation. It is after the degradation the rise of these peaks is noticed and, perhaps the peaks are a result of or

the by-product of the degradation or breakdown of the coating. Unfortunately, the OH-terminated tips cannot differentiate between OH groups bonded in different chemical groups, so the interaction between the tip and any chemical group containing OH is presented on one plot by the NOVA software.

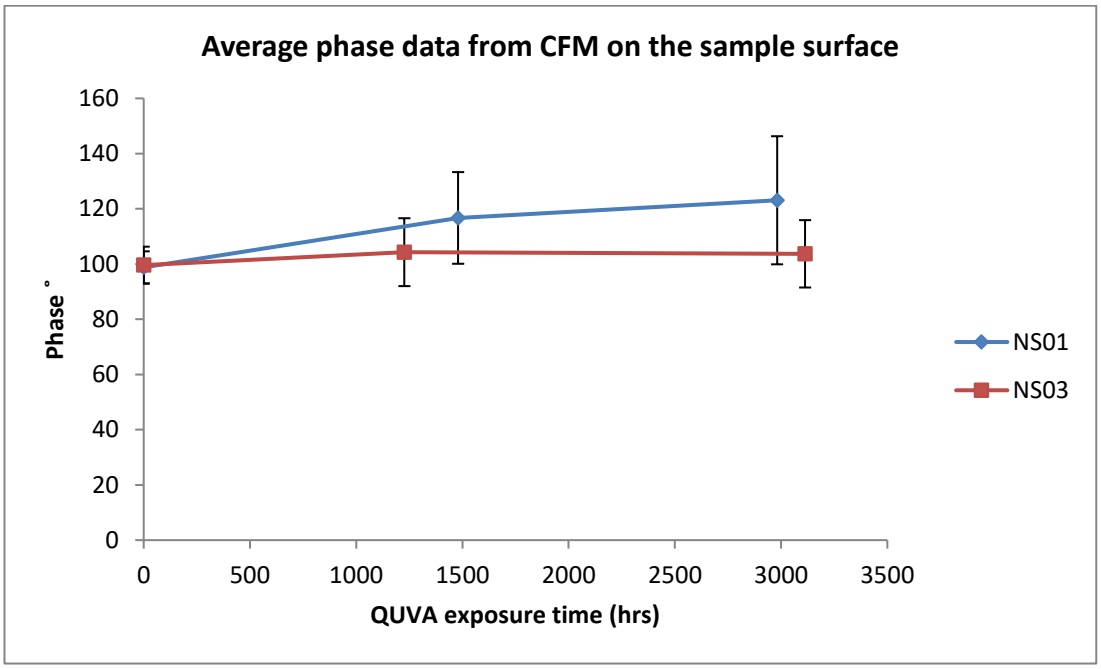

Figure 7.19: Average phase data from CFM on sample surface of NS01 and NS03, with calculated error

Figure 7.19 includes the average phase value from the phase data with a standard deviation of the 65536 collected phase measurements. It can be seen, that the standard deviation increases with exposure time. However, the increase here is not an error in measurement rather an expected increase due to the nature of the experiment. An increase in OH-groups generates a broader peak due to the interaction causing a phase lag and therefore a greater measurable phase change. It is because of this the values deviate greatly from the mean phase measurement. Though the deviation is expected, the calculated standard deviation also supports the fact that NS01 clear after maximum exposure hours of 2981hrs has greater phase change than the maximum exposure hours of NS03 clear on the surface.

The next section reports on the attempt to depth profile using focused ion beam and CFM.

7.4 Using the focus ion beam

Focused ion beam (FIB) microscopy has gained a lot of popularity as a sample preparation technique allowing samples to be cross sectioned or, structures such as beams to be made within the sample and further analysed using other experimental techniques. Some of the experimental techniques used are atomic force microscopy, AFM, energy dispersive spectroscopy, EDS and transmission electron microscopy, TEM. In this research FIB was used to cross section and then mill steps into the sample for depth profiling. In this section the importance of ion beam and sample interaction and FIB settings are discussed.

To use FIB to prepare soft materials such as polymers, it is important to use the correct settings and to do this, one must understand the ion beam and sample interaction as samples may become damaged or destroyed if the correct settings are not applied. Majority of the research evaluating the ion beam and sample interaction has been carried out on silicone models showing that any damage to the sample is based upon the accelerated voltage applied to the ion beam along with the angle of the incidents beam to the sample (Brezna et al., 2003)

Brostow et al (2007) used SEM and FIB milling to characterise polymer-metal hybrids. A transversal cut was created in the sample using FIB to image the dispersion of the metal within the polymer matrix. They found that FIB can cause damage to the material, such as cracking of the edges due to rapid changes in temperature at the site of interest due to the gallium ions. The parameters were optimised to minimise any damage. For example, by changing the beam overlapping to 0% from the 50% they were originally using they found that there was no cracking in the sample.

A considerable amount of research has been done on examining the effects of FIB exposure on various materials (Abdel-Salam et al, 2011, Brezna et al, 2003, Brostow et al, 2007, Giannuzzi. L.A and Stevie. F.A, 1999, Koizumi et al, 2003 and Oshima et al, 2007).

Bailey et al (2013) focused on finding the optimum FIB conditions to use with soft materials by evaluating FIB induced damage. They investigated the effect of gallium ion implantation on the surface of polycarbonate. The implantation would induce elastic modulus changes at the surface of the material and therefore could be imaged using phase contrast AFM also known as AFM phase imaging. FIB energies of 5, 10, 15, 20, and 25keV with a beam current of 0.5nA were used to mill the final surfaces of the trenches in the sample surface after majority of the material was quickly removed at a higher energy of 30keV. Using high beam currents caused a ‘melt-like damage’ at the target surface hence why they opted to keep the

beam current below 7nA. Once the sample had been prepared it was transferred to the AFM stage. The AFM was used in a 'semi-contact/tapping' mode being able to provide both topographical (using the topography images to calculate the root mean square, RMS surface roughness) and mechanical information in the form of a phase signal. Figure 7.20 shows the resultant phase shift angle and RMS roughness at the surface of the sample in relation to the different beam energies used to mill the trenches. It indicates that there was a large variability in the phase shift for the surface that was prepared using FIB energy of 5keV and that the surface roughness was also the highest at this FIB milled surface. It was expected that a rougher surface would give rise to a greater phase shift as the phase shift is "*strongly dependent on the contact area between the AFM probe and the sample surface*." The data also shows that the surface milled between 15keV-25keV not only reduced in surface roughness but converged to the phase shift value of the bulk material at 0keV. Bailey et al (2013) state that a decrease in the phase shift due to FIB energies below 20keV indicates stiffening of the polycarbonate surface and if the FIB energy used to mill the surface is greater than 25keV (as figure 7.20 shows the phase shift value starting to increase at this particular FIB energy) would produce a phase shift angle which is above the value of the bulk material due to softening of the polycarbonate surface.

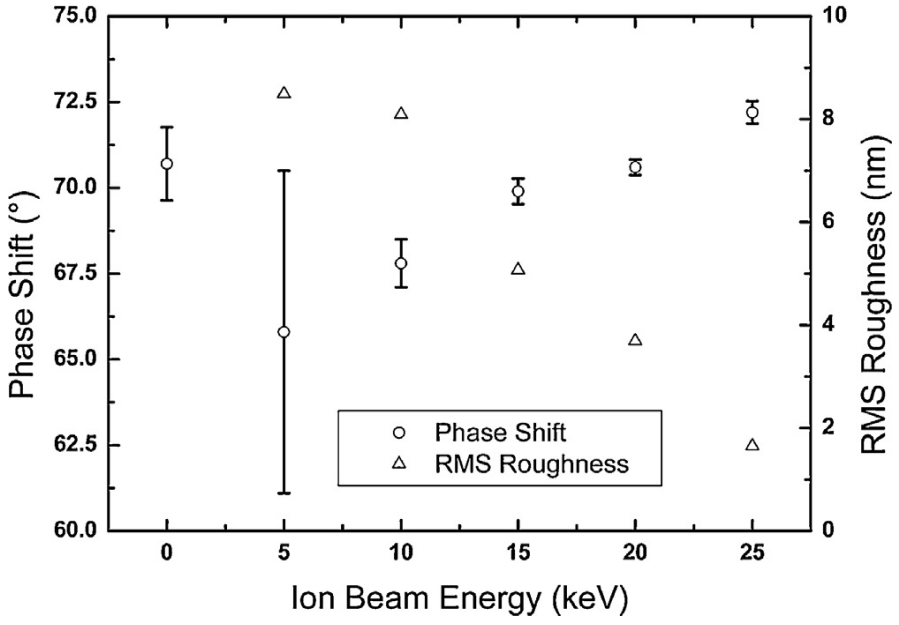

Figure 7.20: A Plot showing the relationship between the beam energies used to FIB mill platinum coated polycarbonate and the resulting AFM phase shift angle and RMS roughness measurements from AFM. 0KeV represents the bulk polycarbonate material (Bailey et al, 2013).

The changes observed to the mechanics of the polycarbonate surface in this research are supported by mechanisms highlighted in earlier literature (Abdel-Salam et al, 2011, Koizumi

et al, 2003 and Oshima et al, 2007). For example, Abdel-Salam et al, (2011) studied the structural modifications in proton irradiated polycarbonate samples using various characterisation techniques such as: FTIR spectroscopy, X-ray diffraction and mechanical properties. They found that the carbonyl group (C=O) degrades due to proton irradiation and was the most sensitive chemical group to proton irradiation. Proton irradiation has been found to be useful in inducing desired modifications of polymers and have suitable application in biosensors and microelectronics but may also lead to other unwanted processes such as "*production of primary and secondary radicals, formation of double bonds and transformation on C-C bonds*," (Singh. L and Samra K.S, 2008). You can also get molecular chain scission, rearrangement of bonding or radical induced crosslinking taking place in polymers due to ion radiation. This is because the ion beams have enough energy to break C-C and C-H bonds that can form free radicals and subsequent crosslinking to neighbouring polymer chains (Bailey et al, 2013 and Singh.L and Samra K.S, 2008).

If the above chemical changes take place within the polymer coatings under investigation in this research, a true analysis of the degradation of the coating cannot be achieved. The purpose of the research is to be able to quantify the extent and the mechanism of degradation the coating is subjected to. If, due to ion irradiation, free radicals are formed, chain scission occurs, or transformation of various bonds takes place, this may lead to further degradation of the samples. To minimise the chances of ion irradiation effecting the results it is vital to investigate the factors that affect ion irradiation and if there are optimum parameters that can be used to use FIB with polymers.

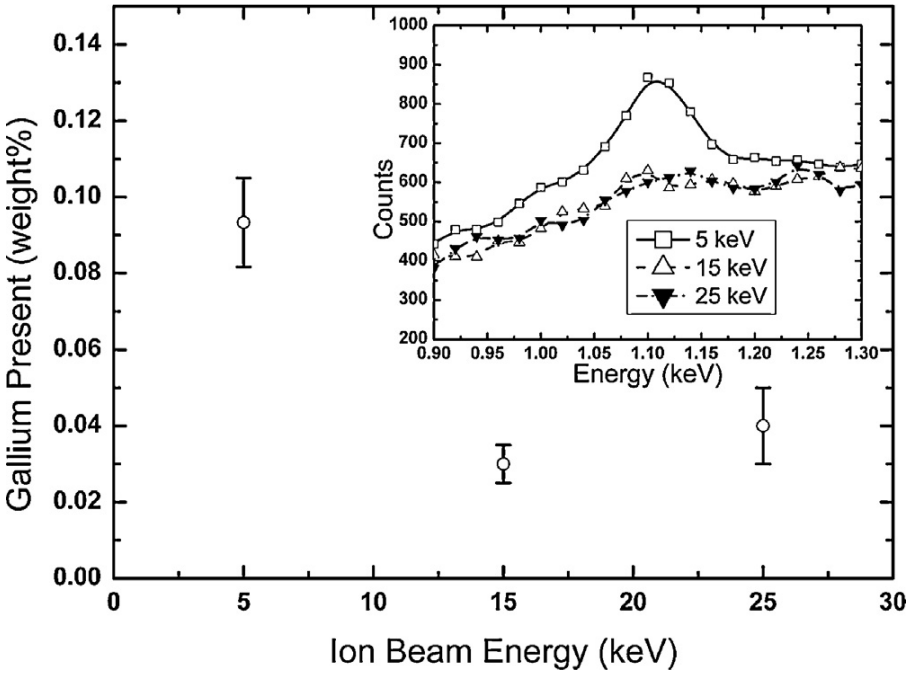

Figure 7.21: Plot showing Ga+ content variation with ion beam energy used to mill PC surfaces. The main plot shows the weight % of Ga+ as calculated by the EDS software, taken from the EDS spectra insert for the different FIB milled surfaces showing the Ga peak at 1.1keV (Bailey et al, 2013).

Bailey et al, (2013) carried out energy dispersive spectroscopy (EDS) to determine if Ga+ ions had been implanted on the surface of the FIB milled samples. EDS is used to carry out elemental analysis to find the composition of a material. The sample is exposed to an electron beam and EDS measures the energy of X-rays that are emitted from the sample. The energies are specific to each element present in the sample and because of which the composition of the sample can be determined. The software supporting EDS was used to calculate the weight percentage of Ga+ ions from each sample area milled using different FIB energies. Figure 7.21 is a plot of the weight percentage of the Ga+ ions present in the samples milled at FIB energies of 5, 15 and 25keV. The results show that more Ga+ ions are present on the surface of the sample milled at a lower FIB energy, at 5keV whereas, at higher FIB energies of 15keV and 25keV there was less Ga+ ions present on the surface. This data supports the phase shifts seen in figure 7.20 where lower beam energies have low phase shift values due to the reduced sputter yield. The beam energy is too low to sputter the sample material effectively and therefore being responsible for Ga+ ions implantation into the sample surface and hence, increasing the elastic modulus of the surface, which is picked up by the phase contrast imaging. In conclusion the research demonstrated that to prepare polymer samples using FIB microscopy higher energy of up to 25keV is required to reduce

the effect of Ga+ implantation on the mechanics of the surface of the sample and to get a true representation of the original sample properties.

Ngo et al, (2017) found the dual beam system of FIB and SEM a useful technique to study the cross-sections of pre-painted metal. The cross-section milled using the FIB could reveal information regarding the quality of the coating using secondary and backscattered electron images. For example, checking the adhesion of the coating to the substrate or how the pigment has been dispersed in the coating. The thickness of the coating using FIB and SEM could also be measured accurately once a cross section had been achieved, as this would cause less damage to the sample than other mechanical sectioning techniques. However, they found that the greatest drawbacks to this method was that it is extremely time consuming and that some surface damage can occur due to charging of the surface, as well as the production of artefacts due to redeposition. However, there are ways to minimise these problems. One of the methods adopted in this research was to 'polish' the surface using a low beam current of 7.5nA and an accelerating voltage of 16kV after removing the bulk of the material quickly at a high FIB energy of 30kV or a combination of 16kV with a beam current of 42nA. They did this to "*produce a smooth surface and also to remove any of the Ga+ ions embedded in the coating during the milling process*."

On the other hand, Kim et al (2011) found that beam heating as well as ion bombardment could limit the usefulness of FIB for sample preparation for transmission electron microscopy (TEM). FIB microscopy is also useful for easy cross-sectioning of various materials to be used in conjunction with TEM but with materials such as polymers and biological structures, which have low heat conductivity it is found that beam heating could damage the surface of the sample. Kim et al (2011) analysed the effect of ion beam damage on a block copolymer by varying the ion beam currents and the sample temperatures. The research concluded that beam heating in polymers could be limited if the beam current was kept low, ≤ 100pA during milling.

Overall, it can be concluded that various parameters effect the amount of ion irradiation / Ga+ implantation taking place on the sample surface during sample and beam interaction. This can be reduced by keeping a low beam current, FIB energies between 15 and 25keV and 'polishing' the sample after removing the bulk material quickly.

Having done chemical force microscopy on the surface of exposed samples with increasing time exposure and seeing a relative increase in the phase change, the next step was to determine whether this technique can be useful to verify how the chemical change varies with depth. To access the depth profile, steps were cut into the sample using a focused ion beam (FIB), Figure 7.22. A Focused Ion Beam (FIB) allows material from the sample to be removed with high spatial precision by using gallium, Ga-ions to facilitate this. Greater detail on how the focus ion beam works can be found in section 2.5.5. Once the sample is milled it can then be transferred to the atomic force microscope to carry out CFM.

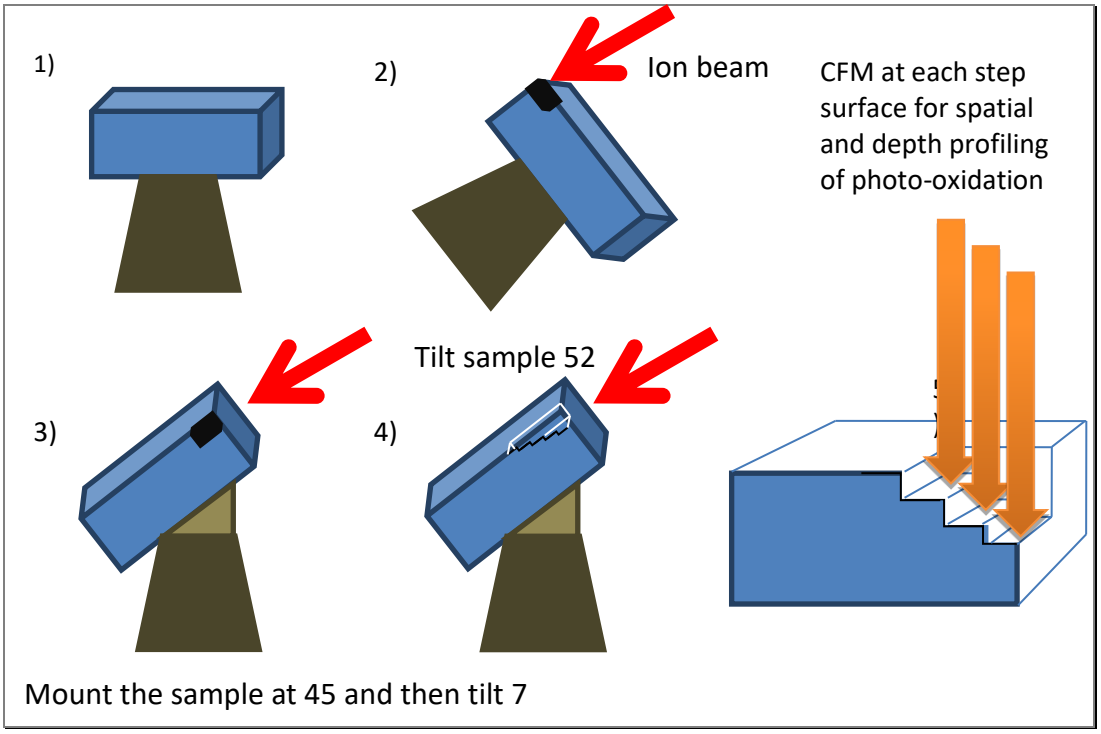

Figure 7.22: Method of cutting steps into the sample using FIB

Each step was approximately 30µm × 30µm and were cut at the following depths; 3µm, 6µm and 9µm. The step size and depth were kept constant regardless of the starting thickness at each exposure time. This can be seen in figure 7.23.

To mill into a sample the sample must be tilted to 52˚ as shown in step 2 of figure 7.22. At this stage a straight cut is performed to get a clean plane in the depth profile. This is necessary to get the best milling results when the steps are milled perpendicular to the

cleaned area. As a lot of material was to be removed the initial milling was done at 30kV and then followed up with a ‘polish’ at a lower FIB energy and beam current. After this step the sample is rotated 180˚, so steps are milled into the horizontal plane. The sample it rotated to enable the cleanest edge in the steps to be the one on the sample surface. With trial and error, it was found that each sample required a unique tilt angle along with the 45˚ pre-tilt on the sample stage (step-3 in figure 7.22) to ensure the steps; a series of rectangular shapes milled in parallel to each other with the same dimensions in horizontal and vertical planes but different dimensions for the z-plane, were successfully milled within the top coating. The tilt had to ensure the sample was parallel to the ion beam to sputter the sample. Each sample was flat and had a unique curvature on the surface or was slightly concave. Hence, the angle had to compensate for the extra feature on the sample so the surface being milled resulted in being parallel to the ion beam. The tilt variation was +/- 3 on-top of the 52˚ total tilt.

After the correct angle was obtained a series of rectangular shapes were drawn, each corresponding to the set dimensions of 30×30µm with varying depths as seen in figure 7.23.

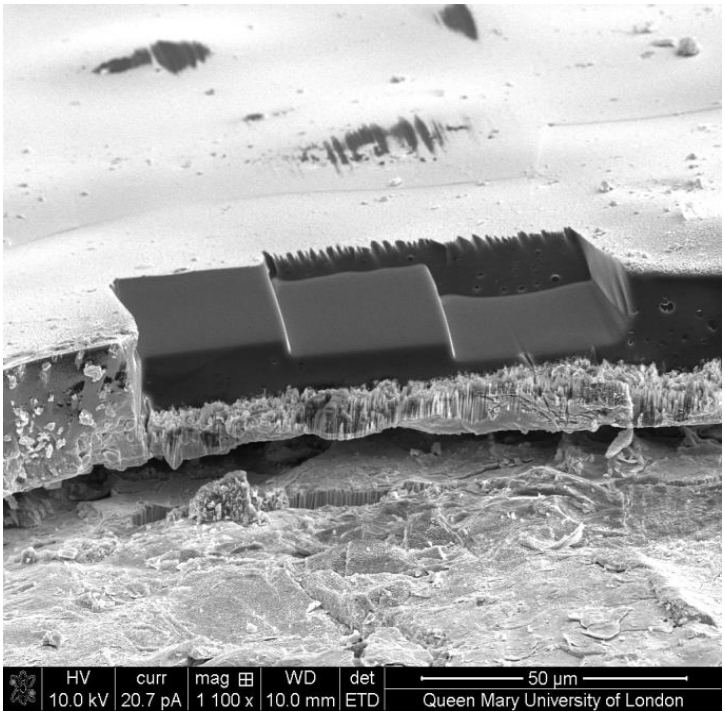

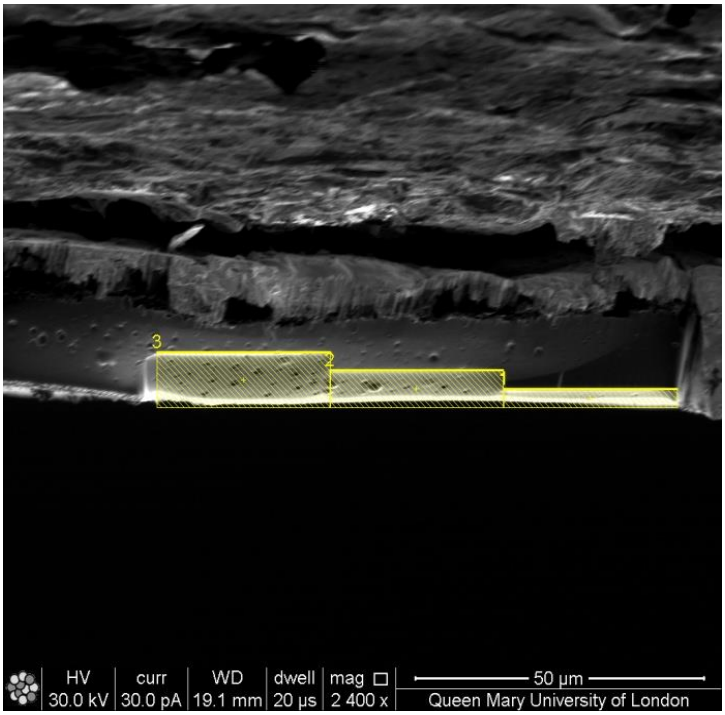

Figure 7.23: Steps in NS01 clear coating exposed at 2981hrs

7.5 Results and Discussion

Analysing and interpreting the surface chemical changes with respect to time generated interest into how the depth of the sample is related to this. Time restrictions did not allow for steps to be milled and analysed further for the sample exposed at 1480 hours. It was important to prioritise which samples should be further examined. Priority was given to compare an unexposed sample with a sample exposed to the maximum QUVA cycles.

NS01 clear (2981hrs) was the first sample to be milled and examined using CFM. Below are the supporting images to show a phase image with the corresponding data as a histogram. The data is analysed by calculating the peak width at half peak height.

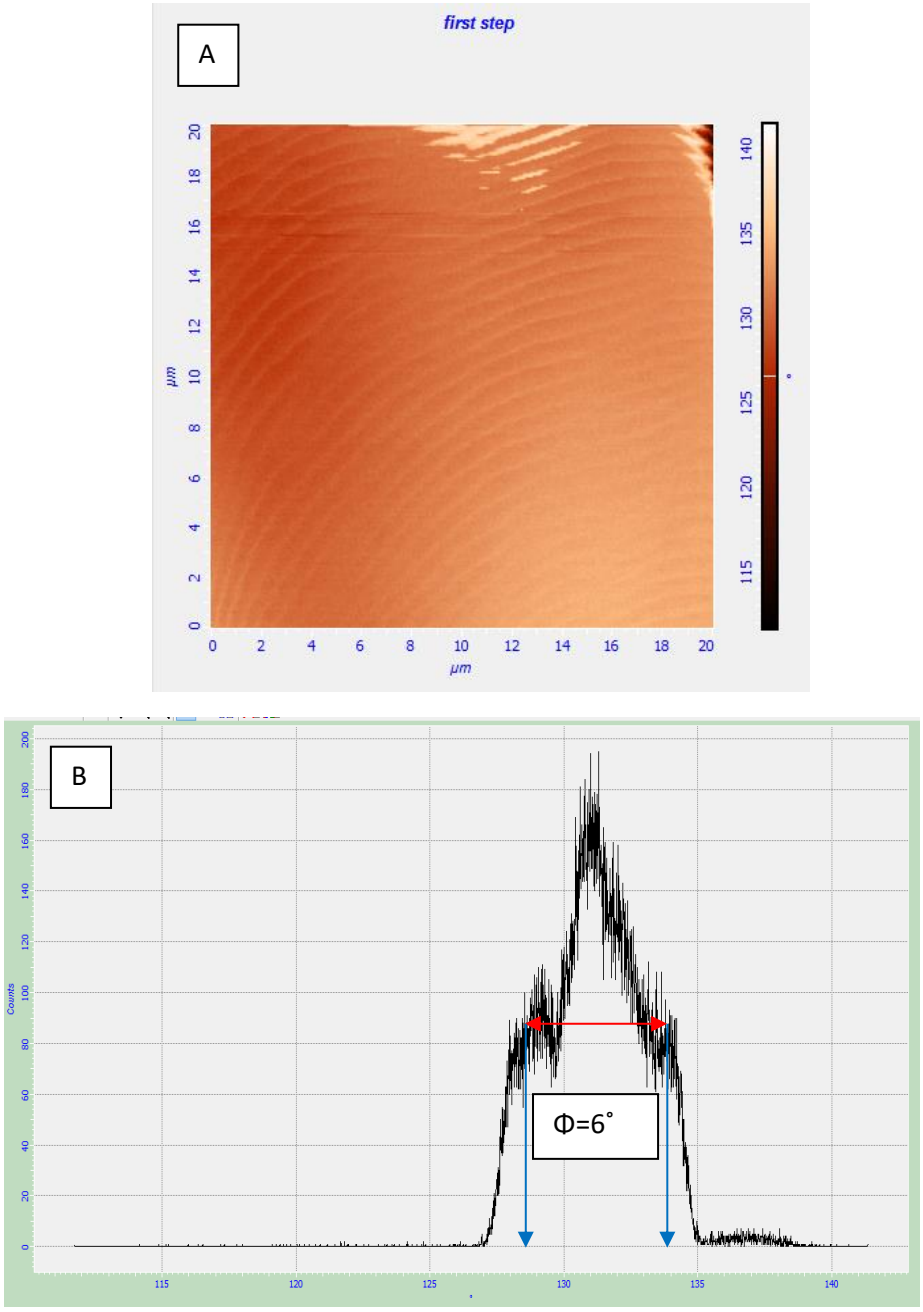

Figure 7.24: CFM on first step, approximately 3µm deep a) phase image and b) phase data

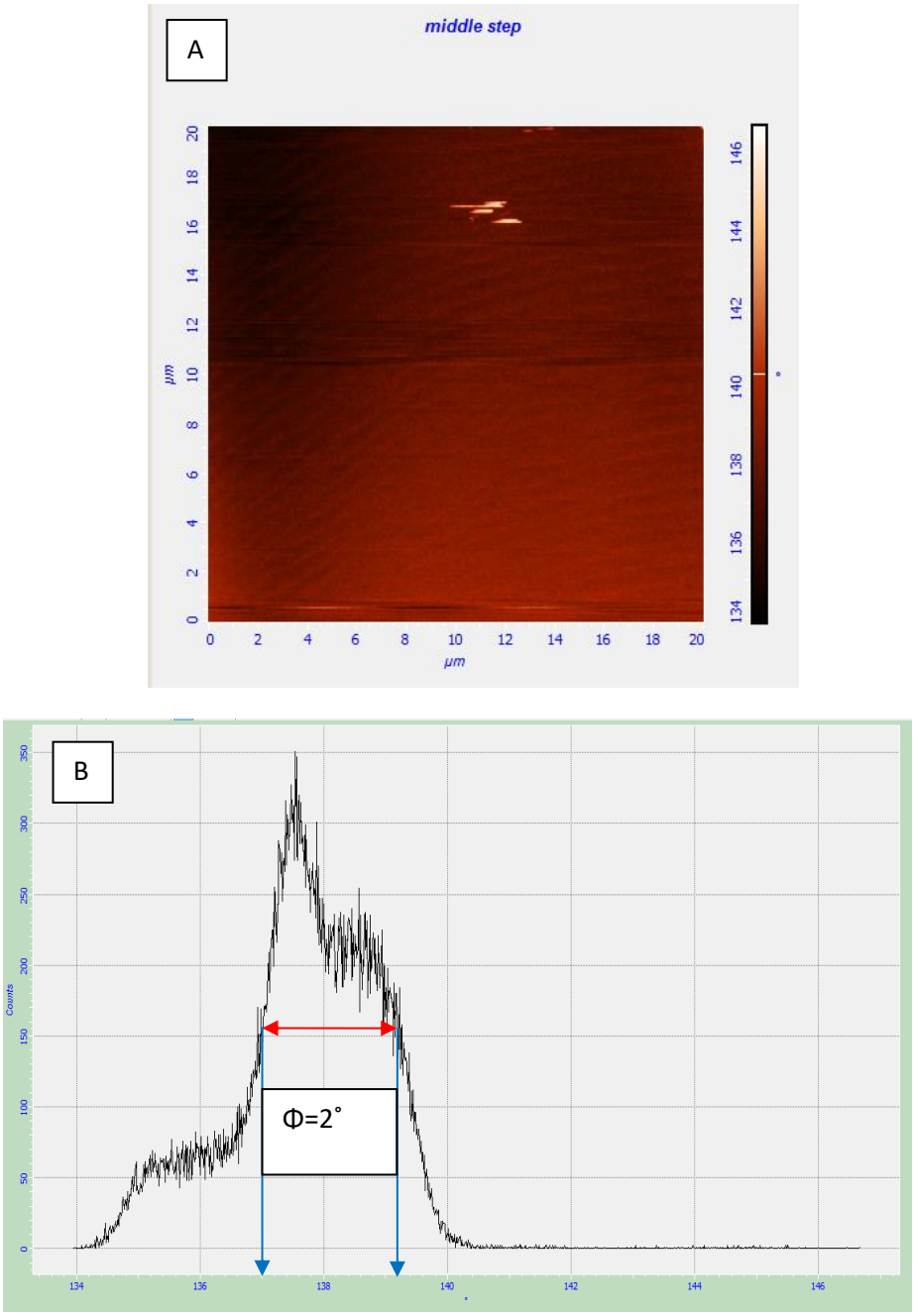

Figure 7.25: CFM on middle/second step, approximately 6µm deep a) phase image and b) phase data

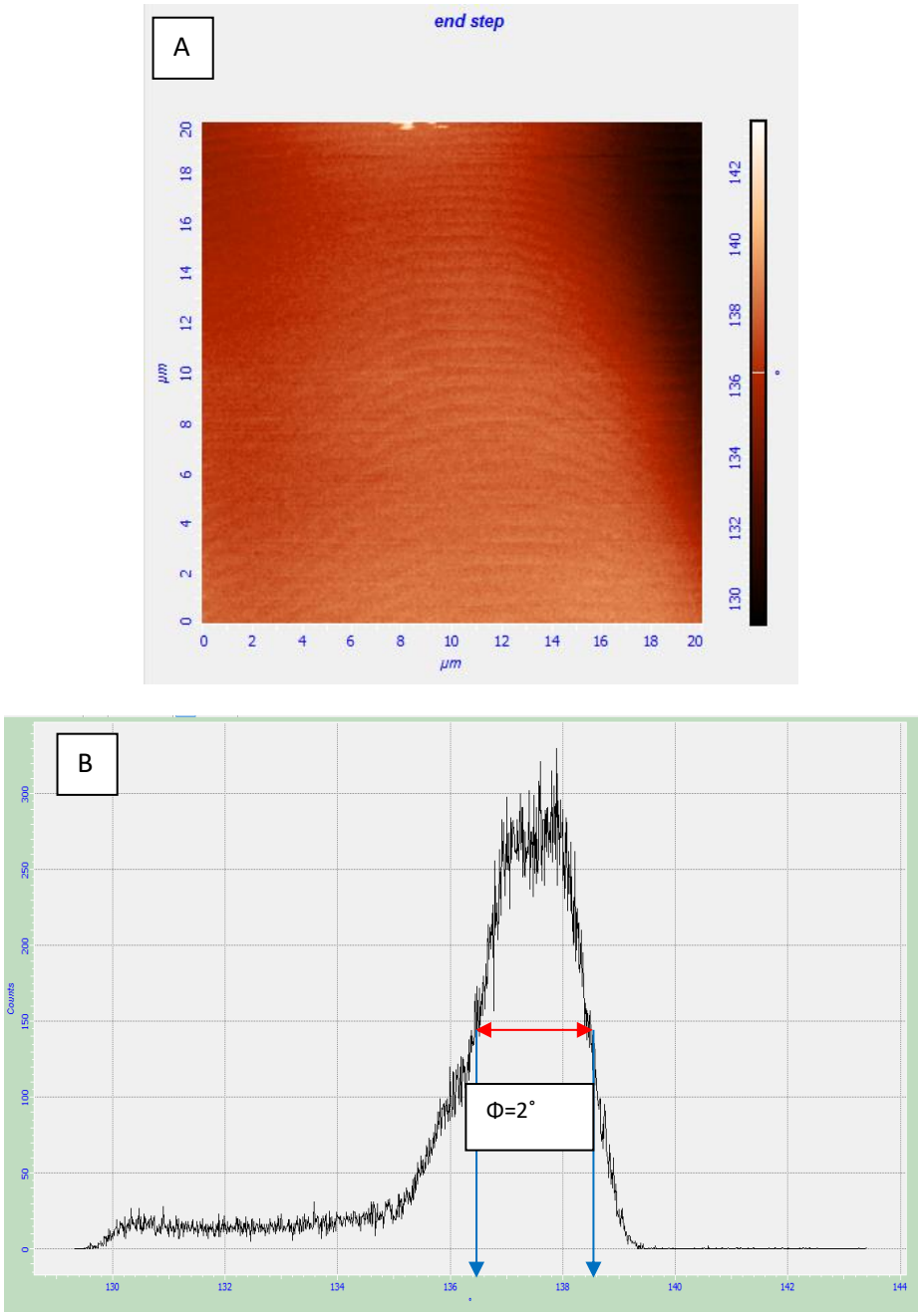

Figure 7.26: CFM on third step, approximately 9µm deep a) phase image and b) phase data

Table 12 displays the results of the phase difference obtained from chemical force microscopy at 0, 1480 and 2981 hours of exposure of NS01 clear. Various areas within the coating were analysed to investigate the degradation in the depth profile owing to the steps. At 0hrs the sample had not been exposed to any natural or artificial weathering conditions, hence, theoretically, phase difference should stay constant, provided the coating is chemically homogeneous throughout the coating thickness. However, there will be some polymer irradiation effect even when not exposed to extreme weathering conditions. The

surface of the unexposed sample shows a phase difference of 7˚ which then increases to 9˚, 3µm below the surface. Another 3µm deep, so at 6µm the phase difference value decreases to 6˚ and remains the same at a depth of 9µm.

From the phase difference of the surface of the sample exposed up to 2981hrs through to 3µm, the value has dropped significantly. With increasing depth, the chemical heterogeneity decreases from 20˚ to 6˚ and further decreases to 2˚ at 6µm depth and remains constant thereafter. This suggests that the chemical degradation does not go beyond the 6µm depth after 2981 hours of QUVA exposure hence why the phase difference remains constant. However, this is relative to the real time coating thickness. Upon exposure, erosion of the coating takes place. Hence, it is possible we have lost a few microns depth of the coating at 2981hrs after exposure and the surface results here are equivalent to the 6 or 9 microns depth of the 0hrs exposed sample and the sub-surface is the deepest of the bulk sample hence the phase change is minimal.

It may be understood that the bulk of the sample will not have oxidised at all as the surface is subject to some exposure even if it is not deliberately exposed in the QUVA machine or an external weathering site such as Florida. Therefore, the phase value at the greatest depth can be expected to be relatively smaller than that of the unexposed sample surface. This idea is supported by O'Donnell, J.H(1989) and Reichmanis et al (1993) as oxygen is more readily available at the external surfaces, therefore any oxidative reactions will be faster if not limited to the external surface i.e. the surface of the coating sample, causing there to be a difference in molecular modifications in the bulk.

Table 12: Phase change with depth over 3 different exposure times for NS01 clear

Exposure time (hrs)	NS01 Phase Change (Φ˚)			
	Depth (µm)			
	Surface*	3	6	9
0	7	9	6	6
1480	15			
2981	20	6	2	2

*Values are relative to real time coating thickness which may vary after exposure and the depths correspond to this given thickness.

From table 13 it can be observed that the NS03 clear 3113 hours exposed sample phase change decreases with depth. The phase change calculated at the surface of the sample is

twice as much as the 3µm sub-surface. Reduced phase change refers to the minimised chemical interaction. Thus, if the phase change has decreased there must be less OH-containing chemical groups below the surface suggesting degradation may penetrate the surface except it does not occur at the same pace as it does on the surface of the sample.

In addition to the above, at maximum exposure for each sample the results show that NS03-3113hrs exposed sample does not plateau once a certain depth is reached like NS01-2981hrs exposed sample. For NS01 at a depth of 6µm and 9µm the phase change remains constant suggesting photo-oxidation may be limited to the top 6µm of the bulk whereas for NS03, the phase change reduces from 7˚ at 6µm to 5˚ at 9µm. The decreasing phase change could again indicate the presence of OH-chemical groups being produced due the degradation mechanism of this specific coating and not a sign of photo-oxidation which is limited to a few microns below the surface.

Table 13: Phase change with depth over 3 different exposure times for NS03 clear

Exposure time (hrs)	NS03 Phase Change (Φ˚)			
	Depth (µm)			
	Surface*	3	6	9
0	7	4	5	5
1227	10			
3113	16	8	7	5

7.6 Analysis of the technique

Using the focus ion beam (FIB) to mill the steps into the samples proved to be successful, however, the process of milling and imaging was not without challenge. In fact, it became a process of trial and error until the reasons for failed milling were identified and correctly resolved. The problems that were presented were unique to each sample. For some samples the edge of the coating was delaminated (caused from the hole puncher used to cut out coupons) and raised as can be seen in figure 7.22 and therefore, the milling of the steps could not be carried out on that edge until a flat edge was located or the raised material was cleared using the FIB. However, the removal of the material is very time consuming, the removal of so much material may not be useful if the area behind the raised surface is also uneven or affected due to excessive milling.

During FIB milling you can also get molecular chain scission, rearrangement of bonding or radical induced crosslinking taking place in polymers due to ion radiation. This is because the ion beams have enough energy to break C-C and C-H bonds that can form free radicals and subsequent crosslinking to neighbouring polymer chains. This would affect the analysis of the samples as subsequent crosslinking and molecular chain scission will alter the true degradation effect. However, as stated previously in section 7.4, various conditions were employed to minimise the damage induce by the focus

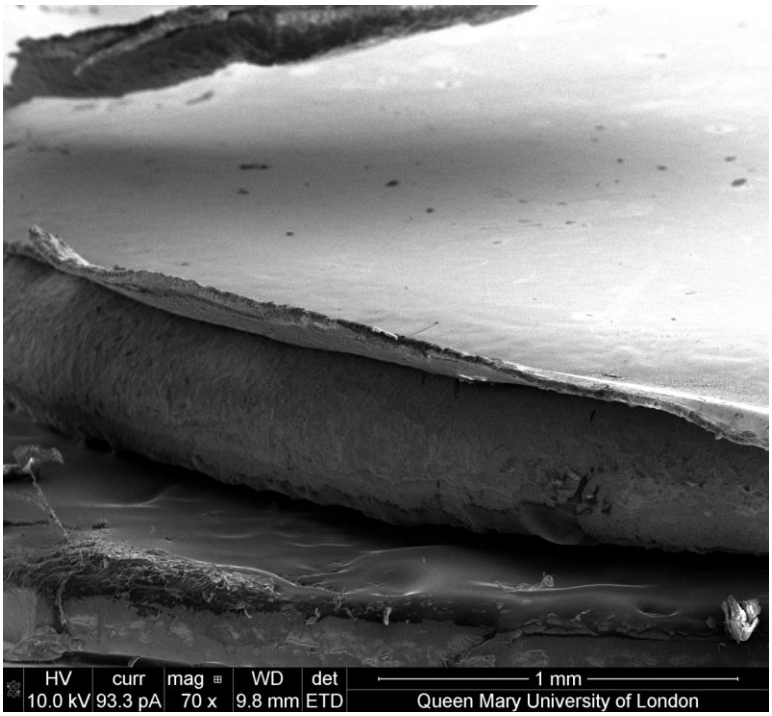

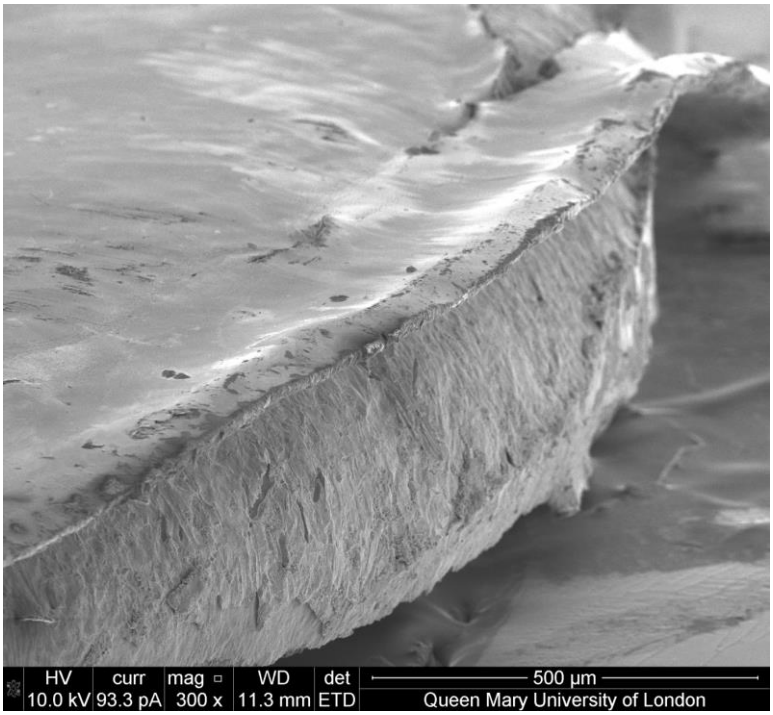

Figure 7.27: SEM images of a coating delaminated from the edges of the substrate

Another difficulty encountered with the sample was that as the sample was exposed, the thickness of the sample was not uniform throughout. Some areas of the surface may be indented or raised compared to the surrounding area. This made milling particularly difficult as when the initial cut was made to the sample to get a straight edge to mill the steps this was not obvious until the area was cleared and tilted to check how even the sample thickness was (figure 7.28). Initially, this problem was not known and hence an attempt was made to mill the steps. The steps started to mill well until it was found that the ion beam was not parallel to a part of the sample due to it being raised so a part of steps was milled under the coating surface as shown in figure 7.29.

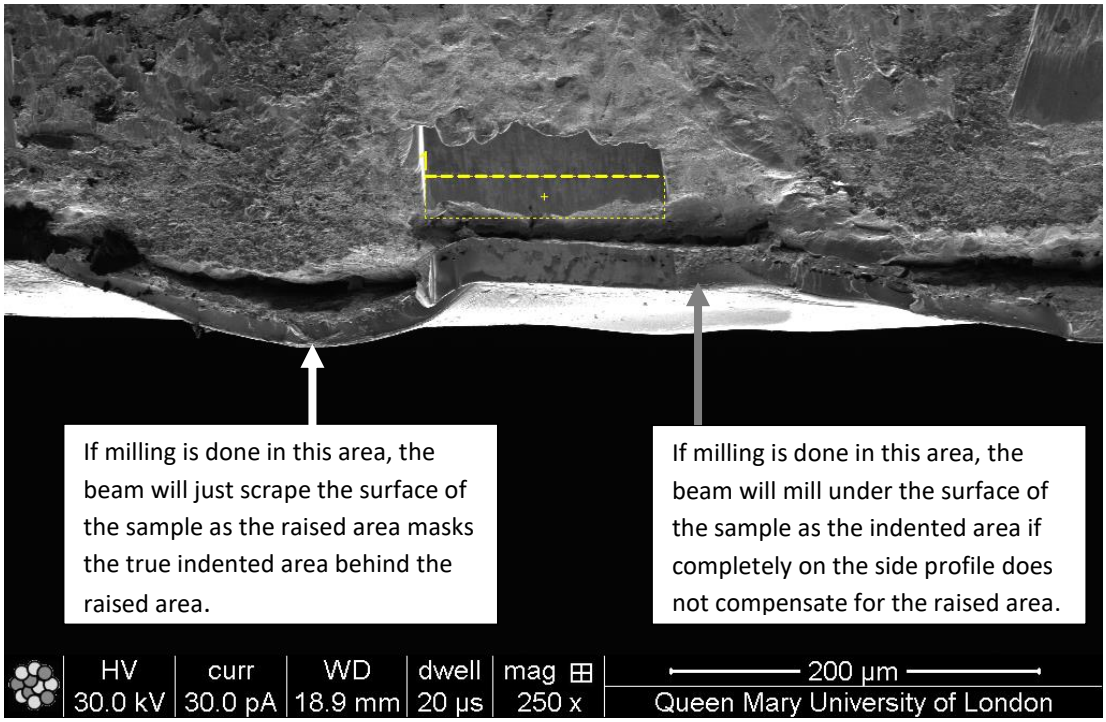

Figure 7.28: SEM image of the side profile of a coating showing the inconsistent thickness of the coating

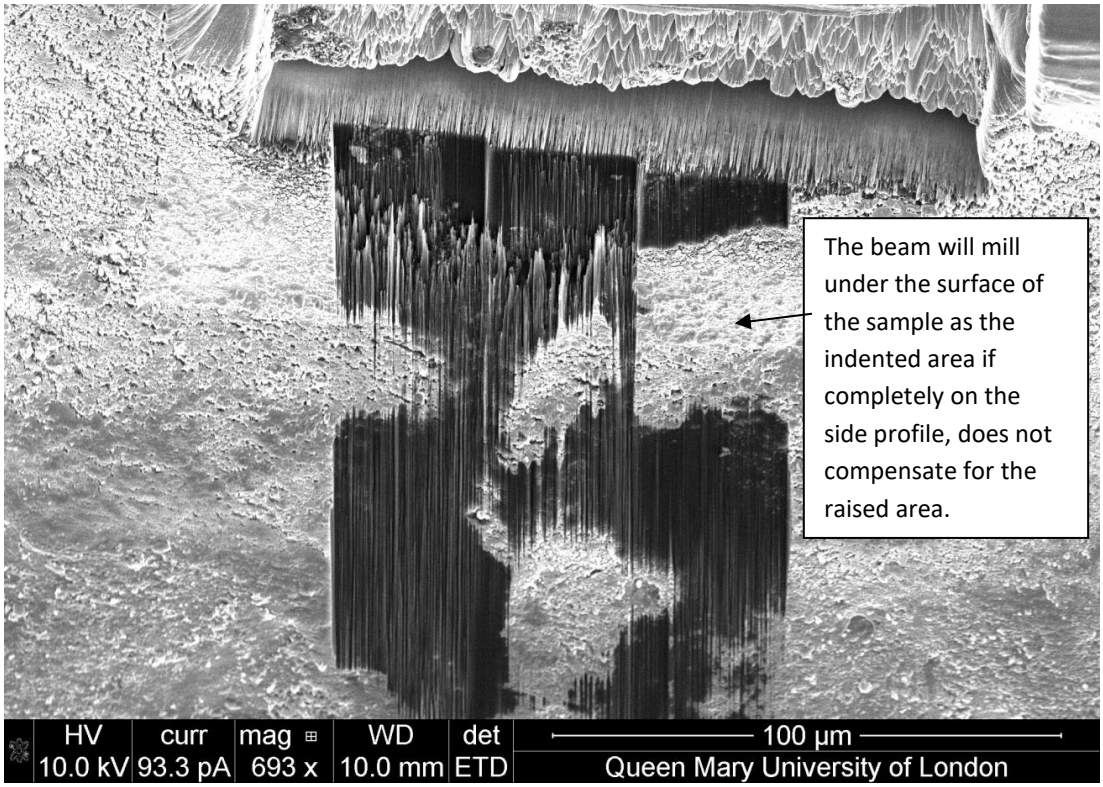

Figure 7.29: SEM image of the steps milled under the surface of the sample

To correct the above problem of inconsistent sample thickness an extra 1µm was added to each step and placed just over the known edge of the sample to compensate for any raised surface which, as can be seen in figure 7.30. It is not visible in the side profile of the coating. This methodology proved successful and steps were successfully milled, particularly for NS03 clear after 3113hrs exposure which took many months of trial and error to mill. Some samples also had cracks at the edge of the sample. Perhaps this was due to the mechanical strain the sample underwent when punches were taken from a sample panel. A special hole puncher was used to get a disc which is compatible to carry out a variety of analysis.

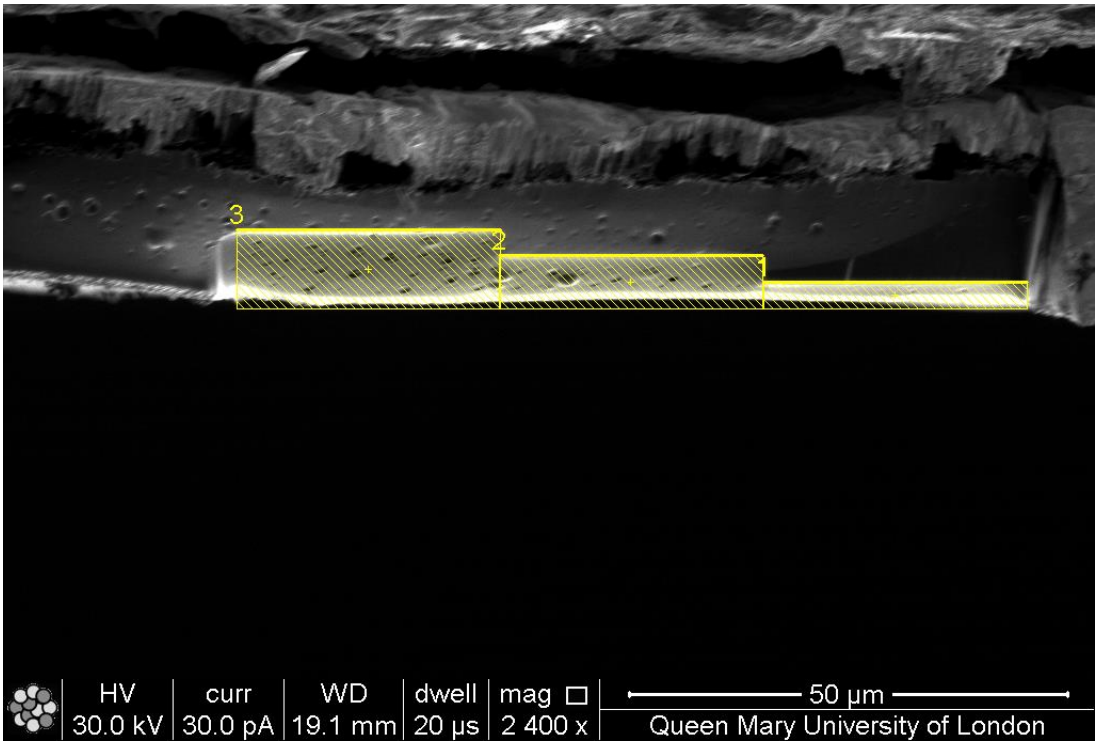

Figure 7.30: SEM image showing a method developed to overcome inconsistent thickness of a sample in to successfully mill steps

Furthermore, the FIB technique used was prone to drifting. Drifting results in the ion beam milling away from the required area and damaging the surrounding area. Drifting of the ion beam takes place due to various factors yet it is hard to prevent. Some of the factors include charging of the sample and thermal instability. When this happens a 'drift correction' can be activated from the software. However, this mode is not particularly useful if there is no contrast of a feature against the background. Drift correction works by focusing on a feature against its background in the selected frame area to be milled, using the feature as a marker. The software is unable to locate the same area without a marker. Refocusing on the area and

correcting the drift becomes impossible if there is no contrast between the marker(feature) and the background. The only precaution one can take is to manually correct the drift by constantly checking the progress of the milling and as soon as drifting becomes apparent, stopping are re-starting the milling procedure after adjusting the template to fit the area required to be milled. It cannot be stated when the sample will drift so it is important to remain at the instrument and not to let the milling run its due course in your absence. A single shape mill can take hours as a rough mill is first carried out and then refined to get the cleanest edge possible.

Another hurdle to overcome is comparing and milling a specific depth in the coating. Especially, milling the 'steps' required in this research to carry out depth profiling as they require to be milled at various depths. Direct comparison of depths in different samples is also challenging as it is dependent upon thickness of the coating at the time of measurement. The exposed samples provided are prone to erosion because of which, the real time thickness does not reflect the depth of an unexposed sample. When 3µm of an unexposed sample is milled, it is certain that the depth is 3µm from the surface. But when the same depth is milled for an exposed sample it cannot be guaranteed that the area is 3µm from the initial surface. The top few microns of the sample could have eroded because of degradation of the surface upon exposure.

There were also limitations for chemical force microscopy. CFM could not be carried out until the steps were milled. The chemically modified probes bought from a company had a shelf-life of one use. Once the chemically modified probe was unpackaged, it had to be used regardless if the CFM imaging was successful or not. The company advised not to store the probes as the probes were sensitive to contamination. To avoid contamination, precautions were taken to discard any used probes after single use. Many researchers use the cost-effective method of chemically modifying probes themselves. However, due to the restricted time on hand to complete this research the decision was taken to purchase the probes from company who specialise in the manufacture of such tips. It would be useful to develop a technique for chemically modifying the probes for future work to not be limited by the number of available attempts.

Despite limitations mentioned earlier, a technique has been developed to depth profile, a technique which has been shown to be effective. The CFM data correlates with the findings of chemical and physical degradation using SEM, AFM, Gloss test and PA-FTIR.

7.7 Concluding remarks

The mechanism to primarily cause degradation in NS01 clear is photooxidation, supported by PA-FTIR data. Photooxidation causes roughness of the surface with increasing exposure time, evident in NS01 RMS data, see figure 7.31c. SEM images (figure 7.31a) and AFM images (figure 7.31b) illustrate the extent of physical degradation taking place on the surface of the coating but found no delamination or peeling of the coating from the substrate. CFM links the chemical and physical degradation as successful chemical pick-up of OH groups using CFM enabled the production of -OH groups during photooxidation to be detected on the surface of the sample. CFM results agree with chemical data obtained via PA-FTIR. Both methods of chemical analysis highlight the production of hydroxyl groups which are a result of photo-oxidation and subsequent oxidative reactions.

CFM data is independent of topography however, the height distribution across the sample surface is also monitored during CFM- supporting the root mean square roughness data obtained from AFM; with increasing exposure time, surface roughness increases depicting the degradation of the coating.

The roughening surface physically affects the appearance of the coating as the gloss retention reduces with QUVA exposure time, a phenomenon directly linked with surface roughness, as explained in chapter 6, refer to figure 6.3.

The physical manifestation of the chemical degradation is summarised in figure 7.31 to get a better picture of the extent of degradation for NS01 clear.

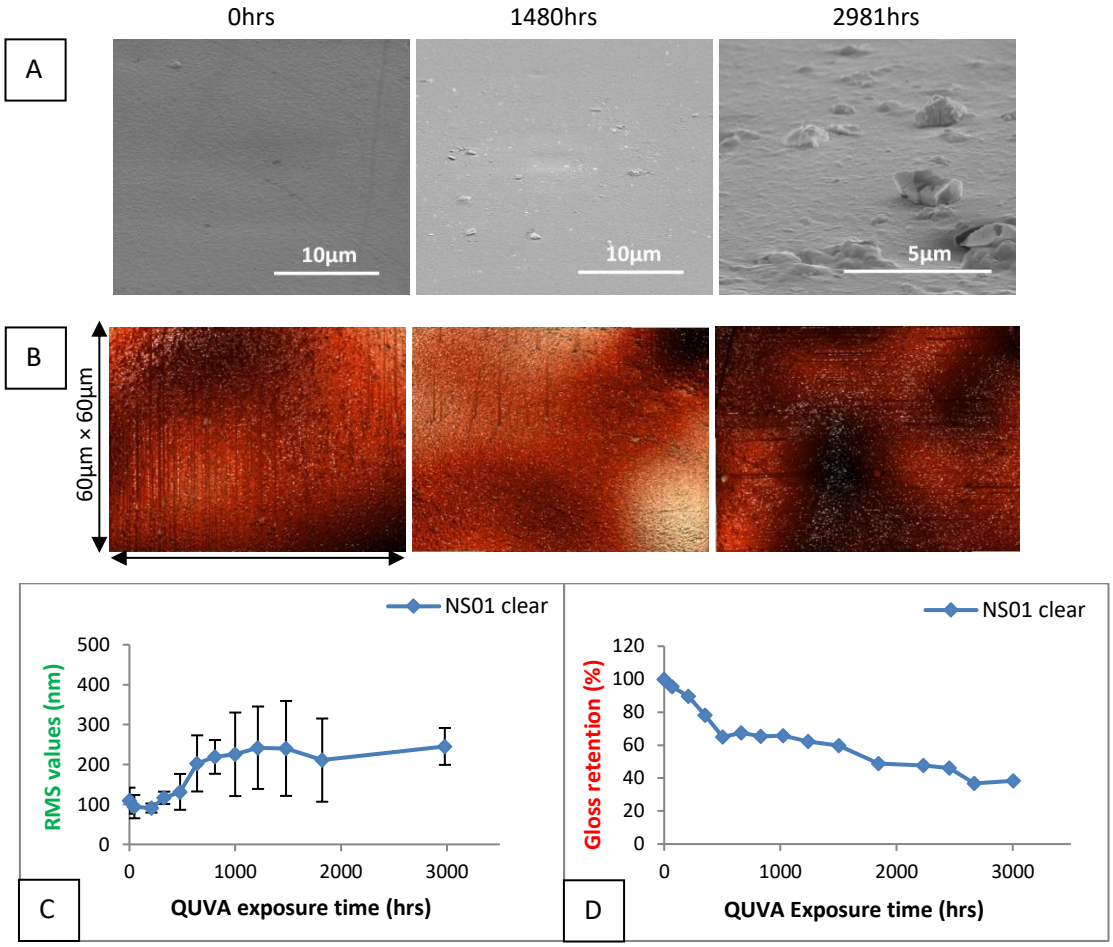

Figure 7.31: Data summary of NS01 clear a) SEM Images, b) AFM height images, c) RMS roughness data and d) Gloss retention data.

PA-FTIR data for NS03 clear shows some photooxidation taking place but it is not the main mechanism of degradation. The production of -OH groups is evident but significantly less compared to NS01 clear. However, changes are detected in other chemical groups such as the triazene ring in the crosslinker melamine along with and amount of methylene, CH_2/CH_3 groups. The percentage of melamine loss is due to breakage of the ester bond between crosslinker and polyester whereas percentage methylene loss indicates the chemical breakdown of the long carbon chain in the backbone.

In addition to the above, noteworthy changes were seen after approximately 1200hours of exposure. This 'step change' is consistent in SEM images (figure 7.32a), AFM images (figure 7.32b), RMS (figure 7.32c) and gloss data(figure 7.32d). After 1200hrs NS03 clear deteriorates rapidly. SEM and AFM images show the formation of 'holes' in the sample

surface, which cause the surface to roughen (shown in figure 7.32a and b). This physical degradation manifests over exposure time.

The percentage of melamine loss is consistent but the changes in methylene correlate positively with the 'step change' observed at 1200hrs. This shows that although photooxidation takes place in NS03 another degradation mechanism is responsible for the severe surface degradation beyond 1200hrs.

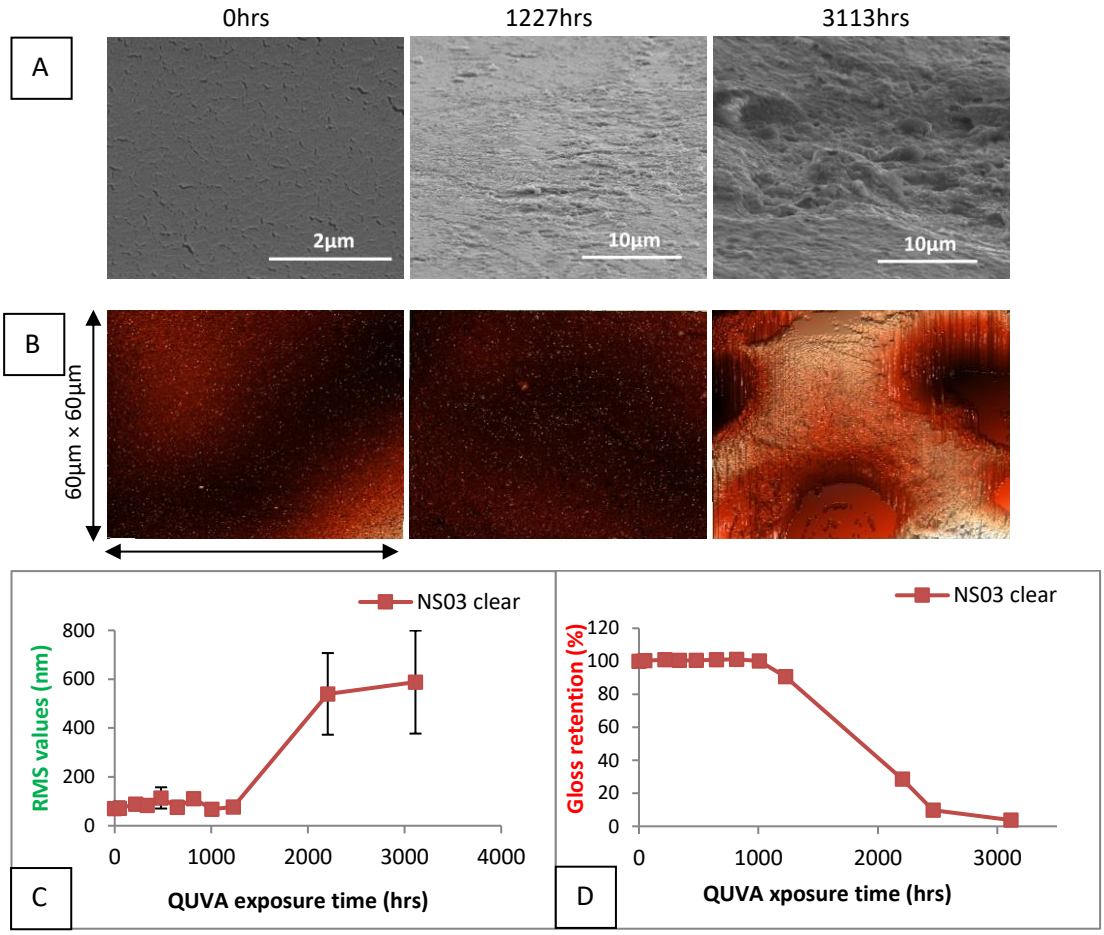

Figure 7.32: Data summary of NS03 clear a) SEM Images, b) AFM height images, c) RMS roughness data and d) Gloss retention data.

CFM supports NS03 degrading via another degradation mechanism. The data shows the formation of additional peaks in the chemical pickup of -OH groups. These chemical groups could be a product of the molecular breakdown within the bulk coating once photo-oxidation or polymer irradiation initiate the degradation at the surface of the coating.

Carrying out CFM on the surface of the sample can now be recognised as a method to detect photo-oxidation after exposure or identify the formation on OH-containing chemical groups. Follow up work can be carried out to distinguish between the interaction of the OH-

terminated tip and various OH-containing chemical groups. Some of these ideas are discussed in the following chapter.

To conclude, the application of FIB and CFM together for researching the degradation of coil coatings has not been done prior to this so this study and therefore much of the experimental procedure have need to be developed. Since the use of the techniques together is new in this field of research, it does need to be developed further. In this research the technique was verified first and then applied to obtain reliable data. Precautions were also taken to validate the results obtained. However, this can be a considered a pilot study which can be built upon. Full effort was made to ensure a method was developed to better understand the relationship between the physical and chemical degradation.

8. Summary and future work

The need for a sustainable environment is at the forefront of the scientific and political community at a time of increasing urbanisation and at a time where the effect of climate is being realised. It is clear that we should act immediately in order to stabilize our economies and environment by means of a sustainable policy. One such way is to use the world's resources efficiently. The coil coating industry has heavily relied upon petroleum-based resins and it is in the matter of everyone's interest if the petroleum resources could be replaced with sustainable equivalents. Having bio-based resins in a petroleum dominant industry could set a precedent. Hence, Beckers Ltd, have initiated this research in order to find out how suitable new bio-based coatings can be.

In this research three coatings with different resin formulations were examined. The petroleum-based coating NS01, was kept as a standard reference as it is a successful commercial coating formulation, used for many years. NS02 was a fully bio-sourced resin crosslinked with melamine and NS03 used a partially bio-sourced resin in its coating formulation. The coatings were first examined without any pigments as clear coatings and later examined with pigment as white coatings. The coatings were subjected to natural weathering in Florida and artificial weathering using a QUV A machine in a laboratory.

NS02 clear was found to deteriorate rapidly over the QUVA exposure hours. It was deemed unfit for the use as a coil coating, so it was excluded from further research. NS01 clear showed a steady degradation rate and NS03 clear started off to be more durable than NS01clear in the initial 1200hours of exposure after which it also degraded significantly. Characterization of the surface of the sample involved measuring gloss loss, imaging the surface using SEM and probing the surface to replicate the surface topography using AFM. The average gloss retention and RMS value for NS01 clear over the QUVA hours was better than NS03 clear. NS03 which demonstrated better resistance to physical degradation at first was found to deteriorate rapidly later. This pattern was consistent with the AFM data and the surface examination using SEM. Both techniques revealed an increase in surface roughness and it is also observed at the same critical mark. Chemical degradation was investigated using PA-FTIR and from the data it was seen that NS01 clear degraded via photo-oxidation whereas the photo-oxidation in NS03 clear was rather stable. Instead a dramatic loss of methylene groups was witnessed along with melamine loss. It became apparent the NS03 clear had a significant induction period before the methylene groups broke down and

the chemical environment around the cross-linker was disturbed, resulting in severe surface degradation. However, the Florida data did not show the same extent of degradation for either coating. This was expected as the artificial weathering conditions are extreme and hence produce accelerated weathering result. In regard to the pigment, the NS01 and NS03 formulations stabilize significantly for both QUVA and Florida sample. TiO_2 is known to provide UV stability to a coating system hence the results were not uncharacteristic.

A novel approach was taken to spatially map chemical degradation. CFM was first carried out on the surface of unexposed samples and samples exposed at maximum QUVA exposure hours. The results from CFM were in agreement with the conclusion that NS03 clear does not degrade solely via photo-oxidation as the amount of hydroxyl groups detected on the surface of NS03 clear was less than NS01 clear. The production of hydroxyl groups is a key to determining the photo-oxidation of the coating and is usually characterized using FTIR. The PA-FTIR data for NS03 also showed significantly less hydroxyl production through the analysis of the –OH,-NH peak at 3700-2450cm^{-1}. The use of FIB to enable the depth profiling of the samples was something new and has not been done in coil coating research. The technique had some limitations hence, it is work in progress. The technique did prove to be useful, however; the need to be able to distinguish between OH-containing groups arises, so the spatial mapping can portray the exact degradation. The CFM work on the surface proved to be helpful, it is through CFM the micro and macro changes could be linked.

For future work, the improvement of the CFM-FIB technique may be useful in bridging the gap between the chemical degradation to physical manifestation. This is important for the coil coating industry as it would mean fewer assumptions are being made regarding how chemical breakdown is translated into surface deterioration.

Another important point to note is that the bio-sourced resin has not been exploited before. Hence, future work could include gathering extra data on longer exposure time of natural weathering to be able to comment on how the coating performs for longer periods and if the same degradation mechanism is utilised.

Furthermore, a mechanism was suggested of how long chains in the NS03 resin straighten out under stress and high temperatures in the presence of moisture. What would be a great breakthrough if this mechanism could be tested in the future to see if the hypothesis is true or not.

Overall, NS03 demonstrates great resistance to degradation at first. If this can be improved, then the NS03 formulation could prove to be a viable solution for a future sustainable material based coating. Applications for domestic appliances have already been considered. For further information regarding the use and purpose of bio-based coil coatings, please refer to Siyab et al (2016).

References

ABDEL-SALAM. M.H, NOUH. S.A, RADWAN Y.E and FOUAD. S.S., Structure and mechanical investigation of the effect of proton irradiation in Makrofol DE 7-2 polycarbonate, Materials Chemistry and Physics, 2011, **127**, 305-309.

ADVANCED SURFACE MICROSCOPY INC, available at: https://www.asmicro.com/applications/phase.html

BAILEY. R.J, GUERTS. R, STOKES. D.J, JONG. F and BARBER. A.H, Evaluating focused ion beam induced damage in soft materials, Micron, 2013, **50**, 51-56

BATISTA M.A.J, MORAES R.P, BARBOSA J.C.S, OLIVEIRA P.C and SANTOS A.M, Effect of the polyester chemical structure on the stability of polyester-melamine coatings when exposed to accelerated weathering, Progress in Organic Coatings, 2011, **71**, 265-273

BIGGS. S, LUKEY C.A, SPINKS G.M, and YAU .S, An atomic force microscopy study of weathering of polyester/melamine paint surfaces, Progress in Organic Coatings, 2001, **42**, 49-58.

BINNIG. G, QUATE. C.F and GERBER .Ch, Atomic Force Microscope, Physical Review Letters, 1986, (**56**), 930-933.

BINNIG. G and ROHRER.H, Scanning Tunneling Microscopy, Surface Science 126, 1983, 236-244.

BREZNA. W, WANZENBOCK. H, LUGSTEIN. A, BERTAGNOLLI. E, GORNIK. E and SMOLINER. J, Focussed ion beam induced damage in silicon studied by scanning capacitance microscopy. Semiconductor Science and Technology, 2003, **18**, 195–198.

BROSTOW. W, GORMAN. B.P. and OLEA-MEJIA. O, Focused ion beam milling and scanning electron microscopy characterization of polymer plus metal hybrids, Materials Letters, 2007, **61**, 1333–1336.

CAPELLA.B and DIETLER. G, Force-distance curves by atomic force microscopy, Surface Science reports, 1999, **34**, 1-104.

CHEMISTRY EXPLAINED. Available at: http://www.chemistryexplained.com/Hy-Kr/Hydrolysis.html

COCUZZI D.A, PILCHER G.R, Ten-year exterior durability test results compared to various accelerated weathering devices: Joint study between ASTM International and National Coil Coatings Association, Progress in organic coatings, 2013, **76**, 979-984

FAUCHEU .J, WOOD K.A, SUNG .L, MARTIN J.W, Relating gloss loss to topographical features of PVDF coating, Journal of Coating Technology Research, 2006, **3** (1), 29-39.

FEI, An introduction to electron microscopy, FEI.com , 2010, 1-37

GIANUZZI. L.A. and STEVIE. F.A, A review of focussed ion beam milling techniques for TEM specimen preparation, Micron, 1999, **30**, 197-204.

GERLOCK J.L, PETERS C.A, KUCHEROV A.V, MISOVSKI T, SEUBERT C.M, CARTER R.O and NICHOLS M.E, Testing accelerated weathering tests for appropriate weathering tests for appropriate weathering chemistry: ozone filtered xenon arc, Journal of coatings technology, 2003, **75**, 35-45.

GESENHUES. U, Influence of titanium dioxide pigments on the photodegradation of poly(vinyl chloride), Polymer degradation and stability, 2000, **68**, 185-196.

GESENHUES .U, Al-doped TiO_2 pigments: influence of doping on the photocatalytic degradation of alkyd resins, Journal of photochemistry and photobiology A: Chemistry, 2001, 139, 243-251.

GONON. L, MALLEGOL. J, COMMEREUC. S and VERNEY. V, Step-scan FTIR and photo-acoustic detection to access depth profile to photooxidized polymer, Vibrational Spectroscopy, 2001, **26**, 43-49.

GU .X, NGUYEN .T, SUNG .L, VANLANDINGHAM M.R, FASOLKA M.J and MARTIN J.W, Advanced Techniques for Nanocharacterization of Polymeric Coating Surfaces, Journal of Coating Technology Research, 2004, **1** (3), 191-200.

GU .X, SUNG .L, KIDAH .B, OUDINA .M, CLERICI .C, HU .H, STANLEY .D, BYRD W.E, JEAN J.Y.C, NGUYEN .T, MARTIN J.W, Multiscale physical characterization of an outdoor-exposed polymeric coating system, Journal of Coating Technology Research, 2009, **6** (1), 67-79.

HAUGSTAD. G. Atomic Force Microscopy : Understanding Basic Modes and Advanced Applications, Wiley, 2012. ProQuest eBook Central, http://ebookcentral.proquest.com/lib/gmul-ebooks/detail.action?docID=894402. Created from gmul-ebooks on 2018-10-08 07:47:18. Page 19

JALILI .N and LAXMINARAYANA .K, A review of atomic force microscopy imaging systems: application to molecular metrology and biological sciences, Mechatronics, 2004, **14,** 907-945.

JR, W.D.C, Corrosion and degradation of materials, 2007 In: Materials science and engineering an introduction, 7th Edition, John Wiley and Sons, 655-658.

KIM. S, PARK. M.J, BALSARA. N.P, LIU. G and MINOR. A.M, Minimization of focused ion beam damage in nanostructured polymer thin films, Ultramicroscopy, 2011, **111**, 191 -199.

KOIZUMI. H, ICHIKAWA. T, TAGUCHI. M, KOBAYASHI. Y and NAMBA. H, Chemical effects of heavy ion beams on organic materials, Nuclear Instruments and Methods in Physics Research B, 2003, **206**, 1124-1127.

LARKIN P.J, MAKOWSKI M.P, COLTHUP N.B, and FLOOD L.A, Vibrational analysis of some important group frequencies of melamine derivatives containing methoxymethyl, and carbamate substituents: mechanical coupling of substituent vibrations with triazine ring modes, Vibrational Spectroscopy, 1988, **17**, 53-72.

LATIF. A, Nanofabrication using focused ion beam, PhD thesis, University of Cambridge, 2000.

LI. Y, HAYASHI. A, SAITO. M, VACHA. M, MURASE. S and SATO. H, Degradation of aliphatic polyesters by vacuum ultraviolet irradiation, Polymer Journal, 2006, **38** (4), 395-399.

LIU .Y, LOTERO E, GOODWIN Jr J.G, Effect of carbon chain length on esterification of carboxylic acids with methanol using acid catalysis, Journal of Catalysis, 2006, **243**, 221-228.

MARCHEWKA M.K, Infrared and Raman spectra of melaminium chloride hemihydrate, Materials Science and Engineering, 2002, **B95**, 214-221.

MARCUS. M.S, ERIKSSON M.A, SASAKI D.Y AND CARPICK R.W, In-plane contributions to phase contrast in intermittent contact atomic force microscopy, Ultramicroscopy, 2003, **97**, 145-150.

MARK, H.M, *Encyclopedia of polymer science and technology*, 3rd edition, Hoboken, New Jersey, John Wiley & Sons, Inc, 2007, pg 1284.

MAVER. U, MAVER. T, PERSIN, MOZETIC. M, VESEL. A, GABERSCEK. M and STANA-KLEINSCHEK. K, Polymer characterisation with the atomic force microscope, Polymer science, chapter 4, 113-132.

MAVER. U, VELNAR. T, GABERSCEK. M, PLANINSEK. O and FINSGAR. M, Recent progressive use of atomic force microscopy in biomedical applications, Trends in analytical chemistry, 2016, **80**, 96-11.

MEJIA .O, OLEA-CARDODO .O and LOPEZ-CASTANARES, FIB-SEM Combination Technique for Characterizacion of Polymer Composites, Current Microscopy Contributions to Advances in Science and Technology, 2012, 1060-1065.

NANOSCIENCE, available at: http://www.nanoscience.com/education/afm.html

NGO. S, LOWE. C, LEWIS. O and GREENFIELD. D, Development and optimisation of focused ion beam/ scanning electron microscopy as a technique to investigate cross-sections of organic coatings, Progress in Organic Coatings, 2017, **106**, 33-40.

NGUYEN. T, GU. X, VANLANDINGHAM. M, GIRAUD. M, DUTRUC-ROSSET .R, RYNTZ. R AND NGUYEN. D, Characterization of coating system interphases with phase imaging AFM, Reprinted from the 24th Annual Meeting of the Adhesion Society. Proceedings, TheAdhesion Society, February 2001, Williamsburg, VA. Adhesion Society, Blacksburg, VA, Emerson, J. A., Editor, 68-70 pp, 2001.

Noy. A, Frisbie C.D, Rozsnyai L.F, Wrighton M.S and Lieber C.M, Chemical Force Microscopy: Exploiting Chemically-Modified Tips To Quantify Adhesion, Friction, and Functional Group Distributions in Molecular Assemblies, J. Am. Chem. SOC. 1995,**117**, 7943-7951.

NOY. A, SANDERS. C.H, VEZENOV. D.V, WONG. S.S and LIEBER. C.M, Chemically-sensitive imaging in tapping mode by chemical force-microscopy: relationship between phase lag and adhesion, Langmuir, 1998, **14**, 1508-1511.

O'DONNELL. J.H, Radiation chemistry of polymers, The Effects of Radiation on High-Technology Polymers, American chemical society, 1989, 1-13.

OSHIMA. A, MURATA. K, OKA. T, MIYOSHI. N, MATSUURA. A, KUDO. H, MURAKAMI. T, KATOH. E, WASHIO. M and HAMA. Y, Heavy ion beam induced phenomena in polytetrafluoroethylene, Nuclear instruments and methods in physics research B, 2007, 265, 314-319.

PHANEUF. M.W, Applications of focused ion beam microscopy to materials science specimens, Micron, 1999, **30**, 277-288.

PAPASTAVROU. G and AKARI. S, Specific detection of interactions between uncharged surfaces in different solvents: high-resolution imaging by chemical force microscopy, Nanotechnology, 1999, **10**, 453-457.

REICHMANIS. E, Frank. C.W, O'Donnell. J.H, Hill. D.J.T, Radiation effects on Polymeric materials, Irradiation of Polymeric materials, American chemical society, 1993, 1-8.

REUTELER. J, FIB artefacts and how to overcome them, 2016. Available at:

http://www.eu-f-n.org/cms/wp-content/uploads/2017/07/tutorial_joakimreuteler_fib-artifacts-and-how-to-overcome-them_2017-05-24.pdf

RODRIGUEZ. F, *Principles of polymer systems*, 4th edition, Taylor & Francis, 1996, 49-62.

SCHEEPERS M.L, MEIER R.J, MARKWORT .L, GELAN J.M, VANDERZANDE D.J and KIP B.J, Determination of free melamine content in melamine-formaldehyde resins by Raman spectroscopy, Vibrational Spectroscopy, 1995, **9**, 139-146.

SCHNABEL .W, *Polymer Degradataion- Principles and Practical Applications*, Hanser publishers, 1992.

SINGH. L and SAMRA. K.S., Opto-structural characterization of proton (3 MeV) irradiated polycarbonate and polystyrene, Radiation Physics and Chemistry, 2008, **77**, 252–258.

SINNIAH. S.K, STEEL. A.B, MILLER. C.J and REUTT-ROBEY. J.E, Solvent Exclusion and Chemical Contrast in Scanning Force Microscopy, J. Am. Chem. Soc. 1996, **118**, 8925-8931

SIYAB. N, TENBUSCH. S, WILLIS. S, LOWE. C and MAXTED. J, Going Green: making reality match ambition for sustainable coil coatings, J. Coat. Technol. Res, 2016.

VAN DER VEGTE. E.W AND HADZIIOANNOU. G, Scanning force microscopy with chemical specifity: an extensive study of chemically specific tip-surface interactions and the chemical imaging of surface functional groups, Langmuir, 1997, **13**, 4357-4368.

VERNON-PARRY. K.D, Scanning electron microscopy: an introduction, Analysis, lll-Vs Review, **13** (4), 40-44.

VOLKERT C.A and MINOR A.M, Focused ion beam microscopy and micromachining, MRS Bulletin, 2007, 32, 389-399

WANG. X, Polyester based Hybrid organic coatings, PhD Thesis, University of Akron, 2012.

WASHIO. M and HAMA. Y, Heavy ion beam induced phenomena in polytetrafluoroethylene, Nuclear Instruments and Methods B, 2007, **265**, 314–319.

WICKS Z.W.Jr, JONES F.N and PAPPAS S.P, *Organic Coatings- Science and Technology*, 2nd edition, John Wiley & Sons, 1999.

ZHANG W.R, LOWE. C, and SMITH .R, Depth profiling of coil coating using step-scan photoacoustic FTIR, Progress in Organic Coatings, 2009a, **65**, 469-476.

ZHANG W.R, LOWE. C, and SMITH .R, Depth profiling of clear coil coating by confocal Raman microscopy, Progress in Organic Coatings, 2009b, **65**, 141-148.

ZHANG W.R, ZHU T.T, SMITH .R, LOWE .C, An investigation on the melamine self-condensation in polyester/melamine organic coating, Progress in Organic Coatings, 2010, **69**, 376-383.

ZHANG W.R, ZHU T.T, SMITH .R, LOWE .C, A non-destructive study on the degradation of polymer coating 1: Step-scan photoacoustic FTIR and confocal Raman microscopy depth profiling, Polymer testing, 2012a, 31, 855-863

ZHANG W.R, HINDER S.J, SMITH .R, Journal of Coating Technology Research, 2011, **8** (3), 329-342.

ZHANG Y, BARBER .A, MAXTED .J, LOWE. C, SMITH .R and LI .T, The depth profiling of TiO_2, pigmented coil coatings using step scan phase modulation photoacoustic FTIR, Progress in organic coatings, 2012b – article in press.